

A microscopic image of rock salt crystals, showing a complex, branching, and porous structure. The crystals are light blue and white, with a central dark blue vein-like structure. The overall appearance is that of a highly textured, crystalline material.

Microfabrics and deformation mechanisms of Gorleben rock salt

Dissertation zur Erlangung des Doktorgrades der
Naturwissenschaften

vorgelegt am Fachbereich
Geowissenschaften / Geographie
der Johann Wolfgang-Goethe Universität
in Frankfurt am Main

von
Nicolas Thiemeyer
aus Frankfurt am Main

Frankfurt am Main (2015)
(D30)

Vom Fachbereich Geowissenschaften / Geographie der

Johann Wolfgang Goethe - Universität als Dissertation angenommen

Dekan: Prof. Dr. Ulrich Achatz

Gutachter: Prof. Dr. Gernold Zulauf
Dr. habil. Jörg Hammer

Datum der Disputation: 20.5.2016

*Dedicated to
Tanja*

Acknowledgements

Prof. Gernold Zulauf is sincerely thanked for giving me the opportunity to work in the Gorleben project. I am deeply indebted to his permanent support, critical remarks and his very pleasant nature, which made me feel very comfortable working in his group and the Geoscience department. He was always available for my requests. Most importantly, I am proud and grateful for all his trust in my work over many years.

Dr. Jörg Hammer is greatly acknowledged who has finally made this thesis possible with all the support from the BGR and his personal interest and encouragement. It was a pleasure to contribute to such an important subject and to work in a competent team of scientists. Especially his trust in my person and his open-minded attitude for new methods and techniques has significantly increased the meaning of my work and my enthusiasm. His support for my person and for many other scientists is far beyond the normal case.

Dr. Jörg Habersetzer essentially influenced my career. His expertise in CT imaging has offered me a new and extremely interesting research direction, which is now a major part in my life. Our shared findings and experiences collected in many hours working at the CT lab have considerably enriched my work. Due to his tremendous support and his pleasant and positive manner my passion for CT imaging has developed. During the entire time we have been working together, I have never felt like an assistant but more like his colleague honored with his confidence and entrusted responsibilities. His personality has inspired me.

Maximilian Pusch is kindly acknowledged for his help with all the rock salt samples and his fast and reliable support concerning questions and discussions. His enthusiasm and his skills considerably contributed to this thesis.

Michael Mertineit is thanked for critical discussions, many enriching EBSD sessions and important contributions to my work.

I would like to thank all the guys from the BGR in Hannover for fruitful discussions, interesting meetings, important tips and valuable talks, especially Dr. Christian Ostertag-Henning, Dr. Michael Schramm, Dr. Otto Schulze and Gerhard Mingerzahn.

Dr. Jolien Linckens is thanked for her help with the EBSD measurements, critical discussions and her pleasant nature. She was an awesome neighbor.

Mark Peinl has helped me a lot with all questions concerning IT, computers and CT data processing. His

Acknowledgements

friendly and reliable nature has significantly enriched my days in the laboratory.

Dr. Thomas Götte has supported me in all questions and techniques regarding fluid inclusions. His valuable remarks on fluid dynamics and his spontaneous participation in the project are kindly acknowledged.

Maria Bladt has supported my work in the lab preparing thick and thin sections. I really enjoyed all the experimenting and testing in order to successively improve the preparation techniques for rock salt.

Wolfgang Schiller is thanked for his help in all facets of microscopy.

Dr. Beverley Tkalcec is deeply thanked for her help concerning English. More importantly, our shared academic way has built a real friendship with her, the most positive and warm-hearted person I know.

Stuart, Filip and Thomas, thank you guys for all the non-scientific stuff.

My family is thanked for everything. All of you have supported the path I have chosen, and I am eternally grateful to have you.

Tanja, I am deeply grateful for all your support, patience and your love.

Abstract

This thesis presents microstructural investigations of rock salt from the central part of the Gorleben salt dome (Northern Germany). The main emphasis was to characterize the rock salt microfabrics, to identify operating deformation mechanisms in halite and anhydrite and to decipher the macro- and microstructural distribution of hydrocarbons, which have been encountered during the underground exploration of the salt dome.

The microfabrics of the *Knäuel*- and the *Streifensalz* formation indicate that strain-induced grain boundary migration has been active during deformation of halite. Crystal plastic deformation of halite is further documented by lattice bending, subgrain formation and minor subgrain rotation. Evidence for pressure solution of halite has not been found, but cannot be excluded because of the small grain size, the lack of LPO and the low differential stress (1.1 - 1.3 MPa) as deduced from subgrain-size piezometry. Solution precipitation creep was proven for intercalated anhydrite layers and clusters, which have been deformed in the brittle-ductile regime. Brittle deformation of anhydrite in terms of boudinage and fracturing was counteracted by viscous creep of halite which caused a re-sealing of fractures and a re-establishing of the characteristic sealing capacity of rock salt.

Hydrocarbons are mainly located along cross cut 1 West of the Gorleben exploration mine and are heterogeneously distributed in the rock salt. They are incorporated in the rock salt foliation in the form of streaks, dispersed clouds, clusters and isolated patches. On the micro-scale, hydrocarbons are trapped along grain boundaries of halite and/or anhydrite, in micro-capillary tubes of anhydrite and in pore space of the rare rock salt with elevated porosity (< 1.26 vol.-%). Such elevated porosities correlate with elevated hydrocarbon concentrations of several hundred ppm. The overall concentrations of hydrocarbons, however, are very low (< 0.05 wt.-%). Elevated porosity is depicted to be a remnant originating from an early stage of salt uplift when fluid and hydrocarbons have migrated and spread from the *Staßfurt-Karbonat* (z2SK) into the superjacent Gorleben *Hauptsalz*. During halokinesis and the strong reworking of the salt body hydrocarbons have been redistributed and dismembered resulting in the isolated present-day occurrences.

The distribution of hydrocarbons shows no relation to local variations in the rock salt fabric. The microstructures of hydrocarbon-bearing and hydrocarbon-free Gorleben rock salt are not distinguishable from each other. Likewise, the presence of hydrocarbons should not have influenced the mechanical behavior of the rock salt as indicated by the microfabrics studied and by geomechanical data. The pure amounts of hydrocarbons are too low for any detectable impact on the barrier properties of this part of rock salt. Although hydrocarbons have migrated into the Gorleben *Hauptsalz* during an early stage of salt uplift when the sealing capacity of rock salt was diminished, the major implication of their isolated distribution patterns is that the Gorleben rock salt was able to regain its sealing capacity during subsequent deformation and re-equilibration. Former migration pathways for fluid and hydrocarbons have been healed and do not exist anymore.

The application of X-ray computed tomography (CT) allows the 3D visualization and quantification of

Abstract

anhydrite, pore space and fluid phases located along grain-boundaries or trapped as intracrystalline inclusions. The 3D reconstruction of anhydrite clusters and pore space for the same sample reveals different spatial distribution patterns. This fact implies that anhydrite is not responsible for such elevated pore space in the rock salt studied, which has been largely closed during the polyphase deformation history of the Gorleben salt dome. High-resolution nanoCT scans ($\leq 1 \mu\text{m}$ voxel size) of single intra- and intercrystalline fluid inclusions in rock salt enable a characterization of gaseous, solid and liquid phases inside single fluid inclusions and give exact information on morphology and shape. The 3D reconstruction of grain boundary fluid inclusions allows the amount, volumes, surface areas or diameters of various types to be determined.

Non-destructive X-ray CT imaging is presented as very useful tool to characterize the structural inventory of rock salt. This non-destructive technique offers new perspectives for microstructural studies and for a wide range of research in structural geology, in general.

Kurzfassung

Die vorliegende Arbeit präsentiert mikrostrukturelle Untersuchungen an Steinsalz aus dem Zentralteil des Salzstockes Gorleben (Norddeutschland). Ein Schwerpunkt dieser Arbeit bestand darin, die Steinsalz-Mikrogefüge zu charakterisieren, aktive Deformationsmechanismen in Halit und Anhydrit zu identifizieren und die makro- und mikroskopische Verteilung von Kohlenwasserstoffen zu entschlüsseln, die während der Unter-Tage-Erkundung des Salzstockes angetroffen worden sind.

Die Mikrogefüge der *Knäuel-* und *Streifensalz-*Formation bezeugen, dass Strain-induzierte Grenzflächenwanderung während der Deformation im Halit aktiv gewesen ist. Kristallplastische Deformation von Halit ist zudem anhand von Gitterverbiegung, Subkornbildung und schwacher Subkornrotation dokumentiert. Evidenz für Drucklösung ist im Halit nicht festgestellt worden, kann jedoch aufgrund der geringen Korngröße, dem Fehlen einer kristallographischen Vorzugsorientierung und der anhand von Subkorn-Piezometrie ermittelten, geringen Differenzialspannungen (1,1 - 1,3 MPa) nicht ausgeschlossen werden. Lösungs-Fällungskriechen konnte jedoch in zwischengeschalteten Anhydritlagen und -knäueln nachgewiesen werden, die im spröde-duktilen Regime deformiert wurden. Der spröden Deformation von Anhydrit in Form von Boudinage und Rissbildung wurde durch viskoses Kriechen des Halits entgegengewirkt, wodurch Risse verheilten und eine Wiederherstellung des charakteristischen Abdichtungsvermögens des Steinsalzes erfolgte.

Kohlenwasserstoffe sind im Erkundungsbergwerk Gorleben hauptsächlich entlang von Querschlag 1 West lokalisiert und im Steinsalz heterogen verteilt. Sie folgen in ihrer Anlage der Steinsalzfoliation in Form von Schlieren, diffusen Wolken, Clustern und isolierten Flecken. Im mikroskopischen Maßstab liegen Kohlenwasserstoffe auf Halit- und Anhydrit-Korngrenzen vor sowie in Mikrokapillaren des Anhydrits und in Porenraum von Steinsalz, das in seltenen Fällen erhöhte Porositäten aufweist (< 1,26 Vol.-%). Letztere sind korrelierbar mit erhöhten Kohlenwasserstoff-Konzentrationen von mehreren hundert ppm. Die Gesamtkonzentration der Kohlenwasserstoffe ist jedoch sehr niedrig (< 0,05 Gew.-%). Erhöhte Porositäten werden als Relikte einer Frühphase des Salzaufstiegs verstanden, als Fluide und Kohlenwasserstoffe aus dem *Stäufurt-Karbonat* in das überlagernde *Hauptsalz* des Salzstockes Gorleben migrierten und verteilt wurden. Während der Halokinese und dem starken Verkneten des Salzkörpers wurden die Kohlenwasserstoffe umverteilt und auseinander gerissen, wodurch die heutigen, isolierten Vorkommen zu erklären sind.

Die Verteilung der Kohlenwasserstoffe ist nicht mit lokalen Variationen im Steinsalz-Gefüge korrelierbar. Die Mikrostrukturen von Kohlenwasserstoff-führendem und Kohlenwasserstoff-freiem Steinsalz zeigen keine Unterschiede. Somit sollte das Vorhandensein von Kohlenwasserstoffen keinen Einfluss auf das mechanische Verhalten des Steinsalzes gehabt haben, was durch die beobachteten Mikrostrukturen und durch geomechanische Daten bestätigt wird. Die reinen Gehalte an Kohlenwasserstoffen sind zu gering, um einen Einfluss auf die Barriere-Eigenschaften des Steinsalzes zu bewirken. Obwohl Kohlenwasserstoffe in einer Frühphase des Salzaufstieges, als das Abdichtungsvermögen des Salzes geringer war, in das Gorleben-Hauptsalz migrierten, implizieren die heute isolierten Verteilungsmuster, dass das Gorleben-

Kurzfassung

Steinsalz während der anschließenden Deformationsphasen sein Abdichtungsvermögen zurückerlangt hat. Ehemalige Migrationspfade für Fluide und Kohlenwasserstoffe sind verheilt und nicht mehr vorhanden.

Die Verwendung der Röntgen-Computertomographie ermöglicht eine 3D-Visualisierung und Quantifizierung von Anhydrit, Porenraum und Fluidphasen, die auf Korngrenzen lokalisiert sind oder als intrakristalline Einschlüsse vorliegen. Die 3D-Rekonstruktion von Anhydrit-Clustern und Porenraum der gleichen Probe ergibt unterschiedliche Verteilungsmuster. Dieser Aspekt impliziert, dass Anhydrit nicht für den erhöhten Porenraum im untersuchten Steinsalz verantwortlich ist, welcher während der mehrphasigen Deformationsgeschichte des Salzstockes Gorleben überwiegend geschlossen wurde. Hochauflösende nanoCT-Scans ($\leq 1 \mu\text{m}$ Voxelgröße) von intra- und interkristallinen Fluideinschlüssen in Steinsalz ermöglichen eine Charakterisierung von gasförmigen, festen und flüssigen Phasen innerhalb der Einschlüsse und geben exakte Informationen über Morphologie und Form. Die 3D-Rekonstruktion von Korngrenz-Fluiden erlaubt es, Mengen, Volumina, Oberflächen oder Durchmesser verschiedener Formen zu bestimmen.

Zerstörungsfreie Röntgen-Computertomographie erweist sich als sehr geeignete Methode, um das strukturelle Inventar von Steinsalz zu charakterisieren. Diese zerstörungsfreie Technik eröffnet neue Perspektiven für mikrostrukturelle Untersuchungen aber auch für ein breites Forschungsfeld der Strukturgeologie allgemein.

Table of contents

Chapter 1: Introduction of the thesis

1.1. Subject	16
1.2. Scope, study area and previous work	16
1.2.1. The Gorleben salt dome as a nuclear waste repository	16
1.2.2. The role of rock salt	18
1.2.2.1. Material properties	18
1.2.2.2. Deformation mechanisms in halite and rock salt	19
1.2.3. The Gorleben salt dome	21
1.2.3.1. Geological setting and structural evolution	21
1.2.3.2. Hydrocarbon occurrences	24
1.3. Sample material and methods	25
1.3.1. Rock salt samples	25
1.3.2. Methods and tools	26
1.4. Aims of the thesis	27
1.5. Structure of the thesis	27
1.5.1. Overview	27
1.5.2. Journal papers as contributions to the present thesis	28
1.5.3. Conference contributions	29
1.6. References	30

Chapter 2: Microfabrics and 3D grain shape of Gorleben rock salt: constraints on deformation mechanisms and paleodifferential stress

2.1. Introduction	38
2.2. Geological setting	40
2.3. Methods	42
2.3.1. Halite grain shape analyses	42
2.3.2. Microstructural investigations	43
2.3.3. Paleopiezometry	44
2.3.4. Electron backscatter diffraction (EBSD)	45
2.4. Results	45
2.4.1. Halite grain size and shape	45
2.4.2. Halite microfabrics, grain boundaries and fluid inventory	47
2.4.3. Halite subgrain fabrics and piezometry	49
2.4.4. Halite texture	52
2.4.5. Macro- and microfabrics of anhydrite	55
2.5. Discussion	59

Table of contents

2.5.1. Grain size and shape	59
2.5.2. Deformation mechanisms in Gorleben rock salt	61
2.5.3. Deformation mechanisms operating in anhydrite	63
2.5.4. Differences and similarities of the salt formations	65
2.6. Conclusions	65
2.7. Acknowledgements	66
2.8. References	66
Chapter 3: Deformation of thin layered anhydrite rocks within the Gorleben salt dome, Germany	
3.1. Introduction	75
3.2. Geological setup, sampling and methods	75
3.3. Results	77
3.3.1. Deformation behavior of individual zones	77
3.3.2. General observations	79
3.3.3. Strain analyses	82
3.4. Discussion	82
3.5. Conclusions	84
3.6. Acknowledgements	84
3.7. References	84
Chapter 4: Macro- and microscale distribution of hydrocarbons in the Staßfurt Hauptsalz of the Gorleben salt dome	
4.1. Introduction	89
4.2. Macroscopic observations regarding to the distribution of hydrocarbons in the Gorleben salt dome	89
4.3. 3D visualization of the hydrocarbon distribution in the Gorleben exploration mine	92
4.4. Microscopic studies of the hydrocarbon distribution in the Staßfurt Hauptsalz	95
4.5. Mineralogical and microstructural analysis of hydrocarbon-bearing rock salt	95
4.6. Conclusions	101
4.7. Acknowledgements	101
4.8. References	102
Chapter 5: Hydrocarbons in rock salt of the Gorleben salt dome – amount, distribution, origin and influence on geomechanical properties	
5.1. Introduction	104
5.2. Sampling and analytical methods	104

Table of contents

5.2.1. Sampling	104
5.2.2. Geochemical, microscopic and tomographic analyses	105
5.3. Results	105
5.3.1. Macroscopic distribution of hydrocarbons	105
5.3.2. Microscopic studies of hydrocarbon distribution	107
5.3.3. Confocal laser scanning microscope (CLSM)	107
5.3.4. Computed tomography	108
5.3.5. Organic geochemical studies	110
5.3.6. Laboratory geomechanical tests	110
5.4. Summary & Conclusions	111
5.5. Acknowledgements	113
5.6. References	113
 Chapter 6: Quantification and 3D visualization of pore space in Gorleben rock salt: constraints from CT imaging and microfibrics	
6.1. Introduction	116
6.2. Samples and methodology	117
6.2.1. Samples	117
6.2.2. CT imaging	118
6.2.3. Data processing	118
6.2.4. Microfabric studies	121
6.3. Results	121
6.3.1. CT imaging, 3D reconstruction and porosity quantification	121
6.3.2. Microfibrics and the distribution of fluids and pore space	124
6.4. Discussion	126
6.4.1. Limitations and uncertainties of CT quantification	126
6.4.2. Application of CT analysis on the relationship between porosity and hydrocarbon content	127
6.5. Conclusions	129
6.6. Acknowledgements	129
6.7. References	129
 Chapter 7: The application of high resolution X-ray computed tomography on naturally deformed rock salt: Multi-scale investigations of the structural inventory	
7.1. Introduction	134
7.1.1. CT imaging in the geosciences	134

Table of contents

7.1.2. CT imaging of rock salt	135
7.2. Geological background and microstructural characteristics of the rock salt samples	135
7.2.1. Sample localities	135
7.2.2. Anhydrite, pore space and fluid inclusions in rock salt	722
7.3. Methods	140
7.3.1. Sample preparation	140
7.3.2. X-ray computed tomography	140
7.3.3. Data processing	141
7.4. Results	143
7.4.1. Anhydrite distribution in rock salt on different scales	143
7.4.2. The relation between pore space and anhydrite distribution	143
7.4.3. Fluid phase reconstructions	146
7.4.3.1. Grain-boundary fluids of Asse rock salt	146
7.4.3.2. Fluid inclusions in Gorleben rock salt	146
7.5. Discussion	149
7.5.1. Filtering, image arithmetic and error estimation	149
7.5.2. Improving raw data set information in the sub-micron range	152
7.5.3. Implications and restricting aspects of rock salt CT measurements	152
7.6. Conclusions	154
7.7. Acknowledgements	155
7.8. References	155
Chapter 8: Summary and Conclusions	162
Chapter 9: Zusammenfassung und Schlussfolgerungen	169
List of Figures and Tables	175
Appendices	
Appendix A: Halite grain shape and subgrain data	
A1. Halite grain shape data	181
A2. Subgrain data	188
Appendix B: CT imaging at the nanoCT lab	
B1. CT imaging with the nanotom s at the Institute of Geoscience: Basic principles of CT imaging, a guideline for CT data acquisition and specific handling instructions.	194

Table of contents

B1.1. Introduction	194
B1.2. The scanning parameter sequence	194
B1.3. Representative CT scans on different scales	197
B1.4. Central questions regarding solid CT data acquisition	202
B1.5. References	203
B2. CT manual for the nanotom s	204
B2.1. MICROCENT	204
B2.2. Fokussierung des Röntgenstrahls	207
B2.3. Digitale Filter	211
CV	215

Chapter 1

Introduction of the thesis

Chapter 1: Introduction of the thesis

1.1. Subject

The present thesis examines the microfabrics and deformation mechanisms of Zechstein rocks of the Gorleben salt dome in Northern Germany. The main focus is set on the Hauptsalz group (z2HS), which forms the major portion of the Gorleben salt dome and consists of several rock salt formations. Since “rock salt”, defined as a crystalline aggregate primarily composed of halite (NaCl) (Jackson, 1997; Hudec and Jackson, 2007), acts as a quasi-impermeable natural seal due to its specific material properties, the Gorleben Hauptsalz group is considered to be used for a final nuclear waste repository.

Extensive underground research carried out in the Gorleben exploration mine revealed the presence of oil and gas (hydrocarbons) mainly distributed along cross cut 1 West at the 840 m exploration level. The presence of these hydrocarbons entailed further investigations in various disciplines concerning provenance, spatial distribution, potential influence on the rock salt barrier properties and significance for the fundamental safety assessment required for a potential nuclear waste repository. One of the major aims was to decipher the rock salt microfabrics in order to better understand the irregular distribution of the hydrocarbons and to determine whether microstructural characteristics can be found in hydrocarbon-impregnated and hydrocarbon-free rock salt. Therefore, traditional and modern analytical techniques were combined to investigate the Gorleben rock salt fabrics.

This chapter introduces the topic of nuclear waste storage in rock salt and, more specifically, in the Gorleben salt dome, including a brief review of the specific material properties, the geological setting of the study area and the previous work focusing on hydrocarbon occurrences. Furthermore, the sample material and the various methods used for the structural investigations are listed. Finally, the major aims and the overall structure of the thesis are presented.

Since single chapters of this thesis represent stand-alone, published articles and one submitted manuscript, it is inevitable that certain parts are repeated, such as the geological setting of Gorleben, methods applied or microstructural aspects of the rock salt samples.

1.2. Scope, study area and previous work

1.2.1 The Gorleben salt dome as a nuclear waste repository

Rock salt deposits are considered for nuclear waste disposal due to the characteristic barrier properties of rock salt, e.g. its sealing capacity in particular (e.g. Carter and Hansen, 1983; Hermann and Knipping, 1993; Hunsche and Hampel, 1999; Schulze et al., 2001; Powers and Holts, 2008 and references therein). The search for a suitable geological structure for constructing a final repository in Germany has now lasted for several decades and will continue in the future, since an adequate and satisfactory solution has not been found yet. The Gorleben salt dome in Northern Germany is considered to be one of the most adequate sites and is being discussed as a suitable repository. Although the scientific investigation

Chapter 1: Introduction of the thesis

has recently been stopped, Gorleben is officially still considered as a potential site, however, without drawing a predetermined conclusion on its suitability in the current political discussion. In the framework of nuclear waste disposal, the Gorleben salt dome represents a prime example how extensively the scientific exploration of a potential site must be performed in order to enable a solid consideration on potential hazardous aspects and FEP scenarios (Features, Events, Processes) for humans and the environment (e.g. Buhmann et al., 2008). In this context, geological investigations of potential sites play an essential role for estimating the future safety for a potential repository in natural formations, such as salt domes.

Since 1979 substantial investigations of the Gorleben salt dome have been performed including underground explorations starting in 1986 (BMW, 2008). Apart from the fact that the exploration of the Gorleben salt dome was interrupted due to a standstill agreement, officially declared by the government for the period from 2000 until 2010 (moratorium), substantial knowledge was gained about the internal and external structure of the Gorleben salt dome regarding the geology and hydrology of the overburden and the adjoining rock (Klinge et al., 2007; Köthe et al., 2007), the surface and the underground of the salt dome (Bornemann et al., 2008) and many other geotechnical aspects (Bräuer et al., 2011). Moreover, the safety assessment includes a geotechnical safety concept and a detailed repository design in case of installing a final repository (Weber et al., 2011a).

The construction of the Gorleben exploration mine was valuable for in-situ measurements and gave access to a very large amount of sample material preserved by numerous boreholes. During the technical and geological underground exploration oil and gas encountered in different stratigraphic formations of the salt dome have become a major focus of interest (Bornemann et al., 2008). Since hydrocarbons are natural constituents of salt rocks (e.g. Popp et al., 2002; Bornemann et al., 2008) underground drillings can be accompanied by oil and gas leakage, or in extreme cases by gas outbursts, causing serious problems to mine operators and even resulting in fatal accidents (e.g. Ehgartner et al., 1998, and references therein).

Apart from the safety aspects for miners, the presence of hydrocarbons in Gorleben entailed further questions regarding various aspects and potential processes, which have to be analyzed and evaluated in the theoretical case of storing heat-generating nuclear waste inside the salt dome (Weber et al., 2011b), for instance chemical reactions with waste casks and subsequent cask corrosion. For every process with a direct or an indirect effect on the barrier integrity, it needs to be clarified how the presence of hydrocarbons might negatively influence or complicate the barrier properties and therefore influence the entire safety assessment and the systematic concepts for nuclear waste storage in rock salt (Weber et al., 2011a, b). Besides potential effects arising from the presence of hydrocarbons, the origin, the transport and the present-day occurrence of hydrocarbons in the Gorleben salt dome are of major importance to understand and evaluate their distribution and, furthermore, their potential behavior in the case of storing heat-generating nuclear waste in the surrounding rock salt mass. In this

Chapter 1: Introduction of the thesis

framework, macro- and microstructural investigations of hydrocarbon-impregnated rock salt are of the utmost importance and contribute to a comprehensive safety analysis conducted in the Gorleben exploration mine.

1.2.2. The role of rock salt

1.2.2.1. Material properties

The basic idea of constructing nuclear waste repositories inside rock salt deposits is related to the specific rock salt properties. Rock salt is characterized by low permeability, low porosity, low water content (e.g. Sutherland and Cave, 1980; Carter and Hansen, 1983; Peach, 1991; Popp et al., 2007, 2012) and high thermal conductivity (Dreyer, 1974; Weber et al., 2013). Moreover, the rheological material properties include viscous flow and (self-)healing capacity under upper crustal conditions (e.g. Schulze et al., 2001, 2007; Chen et al., 2013), which guarantee a recovery from damage (e.g. Fischbeck and Bornemann, 1993). This ability of rock salt for recovery enables a (re-)establishing of a quasi-impermeable geological barrier over a relatively short amount of time. Regarding the viscous flow of rock salt at low temperature, potential sites for a repository were selected and cut in the massive Zechstein salt rock of the Staßfurt Series (z2, Chapter 1.2.3.1.) due to high creep rates of this salt sequence compared to other sequences (Hunsche et al., 2003; Hammer et al., 2012; Weber et al., 2013).

A short-term interruption of the rock salt sealing capacity is related to the underground excavation diminishing the geological integrity around the shafts and drifts. This excavation damage zone (EDZ) is characterized by dilatancy resulting in increased permeability and potential migration pathways for fluids in the EDZ (e.g. Borns and Stormont, 1989; Stormont and Daemen, 1992; Cristescu and Hunsche, 1998; Popp et al., 2001; Schulze, et al., 2001). However, the EDZ around the exploration mine at the 840 m level only extends into the rock salt wall by approximately 30 cm (Bräuer et al., 2011; Weber et al., 2013). When drifts are re-sealed with backfill, the geological integrity is re-established by the self-healing ability of rock salt due to the creep behavior and the humidity-assisted compaction (Popp and Minkley, 2008; Popp et al., 2010). The deformation behavior and operating deformation mechanisms in halite rocks are further reviewed in Chapter 1.2.2.2.

Apart from the favorable material properties of rock salt, there are further reasons why salt rock could be used for the deposition of waste in Germany. Firstly, salt beds, pillows or domes are distributed quite frequently in Northern Germany (Fig. 1.1) (e.g. Hudec and Jackson, 2007; Reinhold et al., 2008, 2014; Vackiner et al., 2013). Secondly, there is a comprehensive German and international experience in salt exploration and mining, and a large amount of results of rock salt repository research from the USA since the mid 1950's is available (e.g. the waste isolation pilot plant (WIPP), e.g. Powers and Holt, 2008). According to all these factors, rock salt certainly represents a suitable medium for nuclear waste storage in theory due to its qualifying material properties. However, a reliable safety assessment has to be carried out for every considered natural site due to the particular and unique, geological circumstances.

Chapter 1: Introduction of the thesis

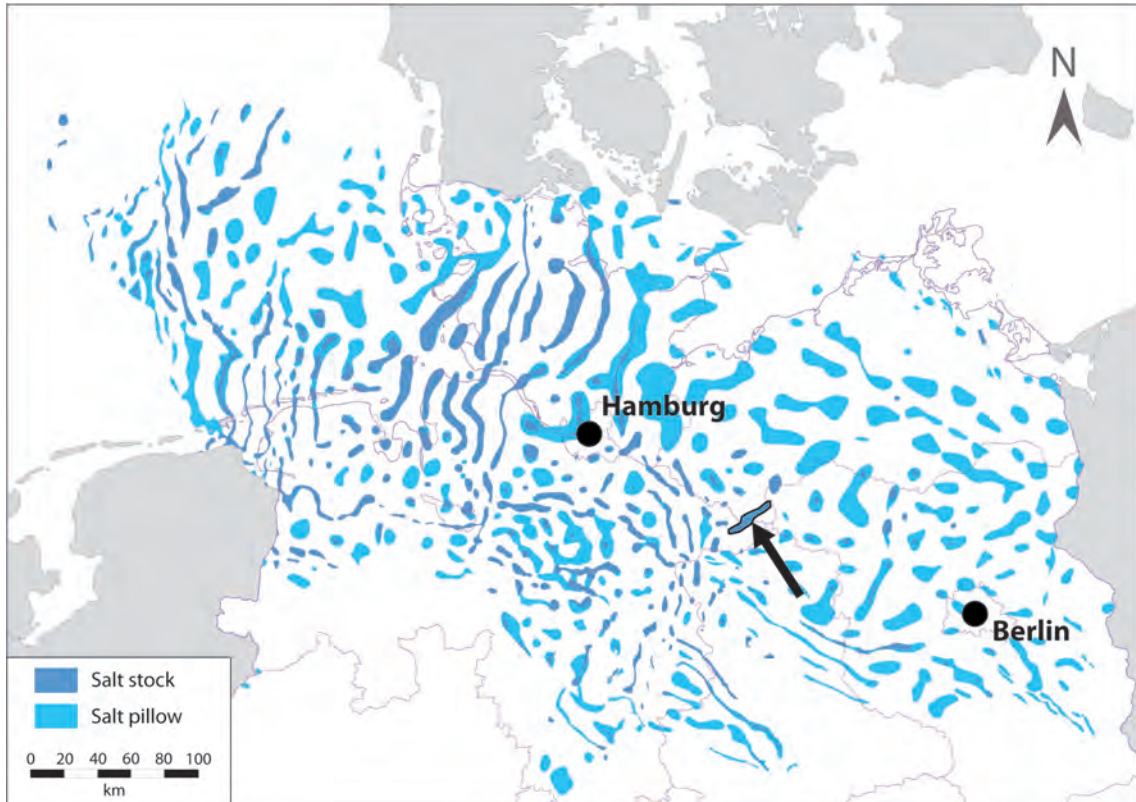


Fig. 1.1: Salt structures of Northern Germany. The NE-SW striking Gorleben salt dome (arrow) represents one of ca. 450 salt stocks and pillows mainly from the Upper Permian (Zechstein) (from BGR, modified; see e.g. Reinhold et al., 2008, 2014).

1.2.2.2. Deformation mechanisms in halite and rock salt

The material properties of rock salt listed above (Chapter 1.2.2.1.) are basically related to the deformation behavior of halite. In naturally deforming rock salt, a couple of deformation mechanisms can (co-) occur, which have recently been reviewed by Urai and Spiers (2007) (Fig. 1.2). Under natural halokinetic conditions (20-200 °C) the deformation behavior of rock salt is largely controlled by temperature, differential stress, confining pressure, grain size, amount of impurities and water content (Urai and Spiers, 2007, and references therein).

Dislocation creep results from glide and climb of dislocations within the crystal lattice causing a reduction of the internal strain energy of grains (e.g. Poirier, 1985). As a result, subgrains may develop, which reflect domains of homogeneous crystallographic orientation separated by boundaries with a low misorientation ($< 10^\circ$). The formation of subgrains as recovery mechanism is influenced by temperature, differential stress and strain rate, and furthermore by material properties, such as grain orientation, grain size and fluid content (e.g. Pennock et al., 2005). There is strong evidence that the pure formation of subgrains is able to accommodate significant amounts of strain (Linckens et al., submitted).

Rotation of subgrains may result in high-angle boundaries (misorientation angle $> 10^\circ$) and formation

Chapter 1: Introduction of the thesis

of new recrystallized grains, the latter with a lower amount of dislocations compared to the host grain. This process is called *subgrain rotation recrystallization* (SGR) (e.g. Drury and Urai, 1990). Additionally, the migration of a subgrain boundary through an area of cumulative lattice rotation is defined as *sub-boundary migration* and can also result in high-angle misorientations (Drury and Urai, 1990). A summary of SGR operating in minerals is presented in Drury and Pennock (2007) and the contribution of SGR recrystallization in Gorleben rock salt is investigated and discussed in Chapter 2.

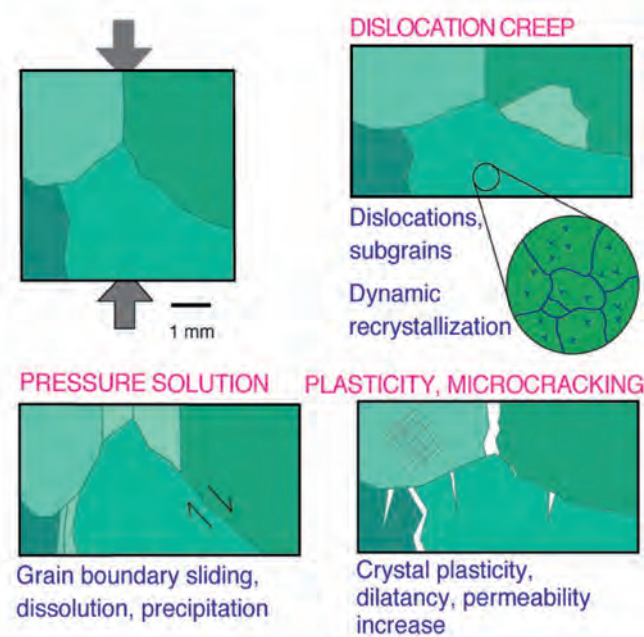


Fig. 1.2: Microstructural processes operating during deformation of halite (from Urai and Spiers, 2007). Shades of green represent differently oriented halite crystals.

Another potential deformation mechanism is *pressure solution*. Highly stressed parts of halite grains, such as domains adjacent to grain contacts, are prone for being dissolved. The dissolved material can be transported and removed by grain boundary fluids finally becoming re-deposited from the latter at sites of low stress (e.g. Schutjens and Spiers, 1999; Passchier and Trouw, 2005; Urai and Spiers, 2007). Evidence for solution precipitation creep has been found in salt glaciers of Iran (Talbot, 1981; Jackson and Talbot, 1986; Talbot et al., 2000) or in Zechstein rock salt from Neuhof salt mine in Germany (Schlöder et al., 2008).

Dynamic recrystallization in terms of (strain-induced) *grain boundary migration* (GBM) (Urai et al., 1986a, b) plays a significant role for the deformation of rock salt (e.g. Schenk and Urai, 2004; Ter Heege et al., 2005a, b; Schlöder, 2006). GBM is driven by differences in dislocation density across grain boundaries and significantly supported by grain boundary fluids (Peach et al., 2001; Urai and Spiers, 2007). The ductile (long-term) behavior of rock salt (Carter and Hansen, 1983; Carter et al., 1993) is already supported by

Chapter 1:

Introduction of the thesis

relatively low amounts of water (Urai et al., 1986a; Ter Heege et al., 2005a). Therefore, natural fluids should have a significant impact on rock salt deformation, because already small amounts of brine may result in mechanical weakening of rock salt (Urai et al., 1986a, b, Peach et al., 2001; Ter Heege et al., 2005a; Pennock et al., 2006; Urai and Spiers, 2007; Zhang et al., 2007).

Fracturing and intergranular slip of halite are related to volume increase (dilatancy) and thus occur under high differential stress and low effective confining pressure at uppermost crustal conditions. Fracturing and dilatancy also occur under (semi)brittle conditions in the EDZ (e.g. Borns and Stormont, 1989; Cristescu and Hunsche, 1998; Schulze, et al., 2001; Urai and Spiers, 2007). At deeper structural levels, where confining pressure is high, dilatant behavior and increased permeability can only be initiated by elevated fluid pressure (e.g. Schoenherr et al., 2007), although hydraulic fracturing is not expected to occur in z2HS rock salt as reported by Schulze et al. (2001) and Schulze (2013). In the case of dilatancy, the healing of open fissures in rock salt is ensured by the viscous flow and the precipitation of halite (Bornemann et al., 2008).

1.2.3 The Gorleben salt dome

1.2.3.1. Geological setting and structural evolution

The Gorleben salt dome in Northern Germany is situated halfway between Hamburg and Berlin (Fig. 1.1) and mainly consists of Upper Permian (Zechstein) rock salt formations. The Gorleben salt structure extends from NE to SW over a distance of approximately 14 km (Bornemann et al., 2008).

Stratigraphic sequences in the Gorleben area are mainly based on ca. 50 boreholes (e.g. Bornemann 1982; Bornemann and Fischbeck 1986) and include the Staßfurt (z2), Leine (z3) and Aller Series (z4). The z2 sequence is forming the central part of the salt dome while z3 and z4 are forming the margins (Fig. 1.3) (Weber et al., 2013). Sea water evaporation in the North German Basin during the Zechstein occurred in several cycles involving inflow of fresh sea water and subsequent isolation of the basin (e.g. Zhang et al., 2013). The preservation of primary bromide distribution in the Staßfurt (z2) and the Leine Series (z3) corresponds to a progressive evaporation phase (Bornemann et al., 2008). It is possible to correlate the stratigraphic sequences with potash mining sites and salt mines of Saxony-Anhalt (Weber et al., 2013), and although this correlation reveals relatively uniform sedimentation in the Zechstein Basin, thicknesses of the single series and formations can vary depending on the position within the specific salt structures (Bornemann et al., 2008). A simplified stratigraphic table of the main salt units is shown in Chapter 4.2. A further geological cross section of the salt dome and a top view of the 840 m level (exploration area 1) are presented in Chapter 2.2.

Zirngast (1996) combined drilling and reflection-seismic data to reconstruct the structural development of the Gorleben salt dome (Fig. 1.4). The investigation of the sedimentary fill of peripheral sinks allowed identifying 13 successive stages from the Late Buntsandstein (Röt) to the present day (see Jaritz, 1980; Zirngast, 1991). Altogether, 280 km³ of salt has flowed into the salt dome since the beginning of diapirism

Chapter 1: Introduction of the thesis

and more than 60 % of the initial source salt beds with an original thickness of ca. 1150-1400 m have moved upwards into the dome (Zirngast, 1996). Zirngast further calculated the highest salt flow rates for the narrowest parts of the salt dome by 0.14 mm per year during the Late Cretaceous.

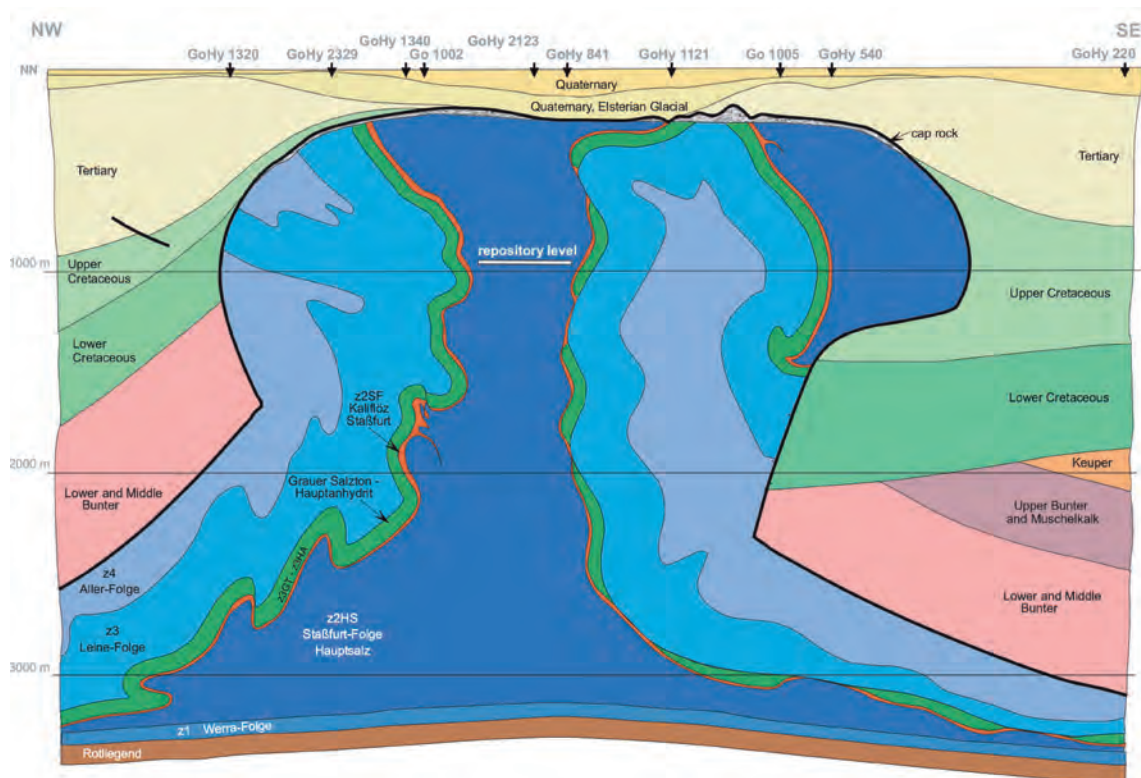


Fig. 1.3: Simplified cross section of the Gorleben salt dome (from Bornemann et al., 2008) with the central part composed by the Staßfurt series (z2). The repository level within z2HS corresponds to the exploration mine at the 840 m level. The black arrows at the top represent boreholes.

The lowest rate was determined for the most recent period (Miocene to Quaternary) by 0.03 mm per year. Furthermore, the theoretical rates of salt rise of the dome surface (salt table) were calculated by a maximum of 0.088 mm per year (Late Cretaceous) and by a minimum of 0.018 mm per year from the Miocene to the Quaternary. From the Malm to the Lower Cretaceous the salt pillow stage ended and the main diapir stage began by upward penetration through the overlying beds (Weber et al., 2013). Salt rise was generally counteracted by salt erosion and subsrosion (Zirngast, 1996). Today, the base of Zechstein salt is situated at a depth between 3200 and 3400 m. The top salt is around 250 m below ground level (Bornemann et al., 2008). Only minor regional tectonic stresses exist in the present days and no evidence for any major movement along active fault zones is given (Weber et al., 2013). Further information on salt flow rates and the structural geology of the Gorleben salt dome are described in Zirngast (1996) and Bornemann et al. (2008).

Chapter 1: Introduction of the thesis

Today, the Gorleben salt dome is covered by a cap rock with an average thickness of 30 m (Fig. 1.3). Quaternary sediments are resting on top of the cap rock and partly directly on top of the salt in the area of the Gorleben channel. Due to glacial erosion, this channel penetrated ca. 100 m into the salt dome at around 400.000 B.P. (Weber et al., 2013).

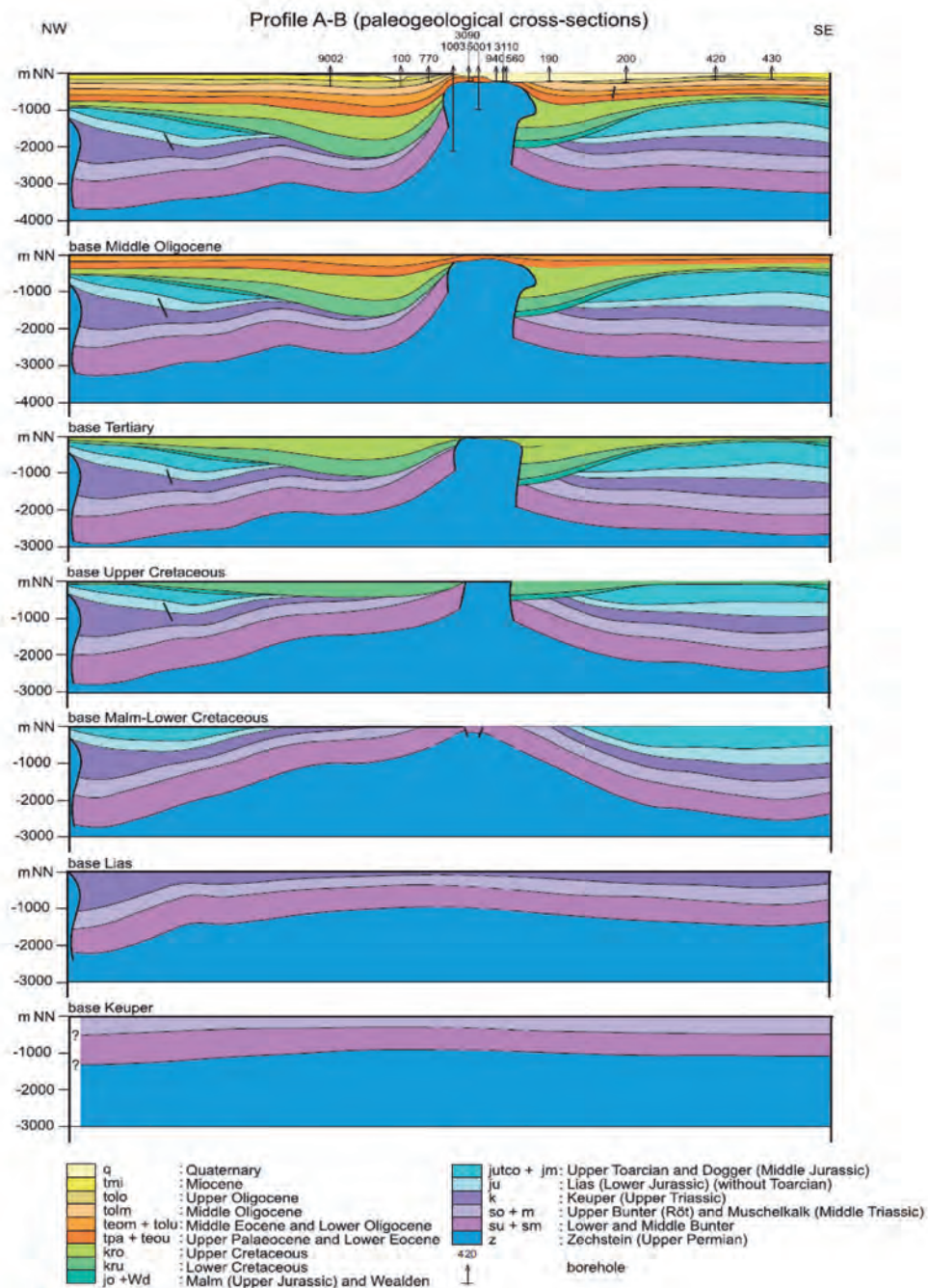


Fig. 1.4: Structural evolution of the Gorleben salt dome (from Bornemann et al., 2008). See text for explanation.

Chapter 1: Introduction of the thesis

1.2.3.2. Hydrocarbon occurrences

The sealing capacity of rock salt is a decisive factor for the entrapment of oil and gas in adjacent reservoir and source rocks (e.g. Parnell, 1994; Tang et al., 2004; Warren, 2006). However, hydrocarbons occur inside the rock salt structure as well, which is related to different scenarios. As a primary origin, organic matter of the sea water column is deposited in a shallow marine basin and is subsequently enclosed by precipitating minerals (e.g. halite) during the deposition of evaporites. As a consequence, organic (autochthonous) matter is directly trapped in rock salt (e.g. Tissot and Welte, 1984; Gerling and Faber, 2002; Weber et al., 2011b). As a post-sedimentary origin, the migration and entrapment of matured organic matter (oil and gas) from underlying or intercalated organic-rich source or reservoir rocks into top salts is a well known phenomenon (e.g. Schoenherr et al., 2007) and was also assumed for hydrocarbons found in the Gorleben salt dome (e.g. Siemann and Ellendorff, 2001; Gerling and Faber, 2002). Intercalated layers of carbonate or anhydrite rocks (“stringers”; see Van Gent et al., 2011) represent potential reservoirs for organic fluids inside rock salt formations (Peters et al., 2003; Al-Siyabi, 2005), which can be characterized by very high fluid pressures (Williamson, 1997). Since hydrocarbons are natural constituents of evaporites, rock salt deposits are often associated with the occurrence of hydrocarbons (Tissot and Welte, 1984; Popp et al., 2002) and occur in many salt mines in Northern Germany (e.g. Siemann, 2007; Bornemann et al., 2008).

However, in contrast to highly porous reservoir rocks, such as sandstones or carbonates, pure concentrations of oil and gas entrapped in rock salt are usually in the ppb range (Gerling et al., 1991). These very low amounts are mainly due to the high entry pressures and the low porosity and permeability of rock salt (e.g. Popp et al., 2001; Schoenherr et al., 2007). In the case of the Gorleben salt dome, the hydrocarbon occurrences are studied in respect to safety issues, primarily.

Hydrocarbons in the Gorleben exploration mine were encountered in various types of rocks and various stratigraphic units, for instance in anhydrite rocks or claystones, in the Kaliflöz-Staßfurt (z2SF) or in fault and fissure zones at the z2/z3 boundary (Bornemann et al., 2008). Due to a reworking and “squeezing” of the massive Hauptsalz group (z2HS) during salt uplift, the brines and gases were generally redistributed, particularly into the top salt or into the anhydrite-joint reservoirs (Weber et al., 2013). Due to this fact the average fluid content of the Gorleben Hauptsalz was quantified as less than 0.02 vol.-% (Bornemann et al., 2008, and references therein). Such very low fluid contents of naturally-deformed rock salt especially apply for domal salts (Carter and Hansen, 1983). The major occurrences of hydrocarbons in the Gorleben exploration mine are located along cross cut 1 West (Bornemann et al., 2008; Hammer et al., 2012, 2013), whereas impregnations along cross cut 1 East occur only subordinately (Hammer et al., 2013).

The first microstructural investigations of Gorleben Hauptsalz fabrics in the context of hydrocarbon impregnations were conducted by Fischer (2000), who determined very low hydrocarbon contents in the range of 0.02–0.03 %. The comparison between grain fabrics from hydrocarbon-free and hydrocarbon-

Chapter 1: Introduction of the thesis

bearing zones revealed slight discrepancies regarding halite grain size and halite grain elongation (Fischer, 2000), which were subsequently quantified by Popp et al. (2002) (Fig. 1.5). According to Popp et al. (2002), hydrocarbon-bearing zones revealed smaller halite grain size and more distinctly developed grain orientations compared to hydrocarbon-free zones. This idea was reassessed in the present thesis and extended by three-dimensional grain shape analyses, because the approach found by Popp et al. (2002) was only limited to one sample and therefore statistically not trustworthy. The relation between the Gorleben rock salt fabrics and hydrocarbon impregnations are illustrated in Appendix A (Figs. A1.2 and A2.2).

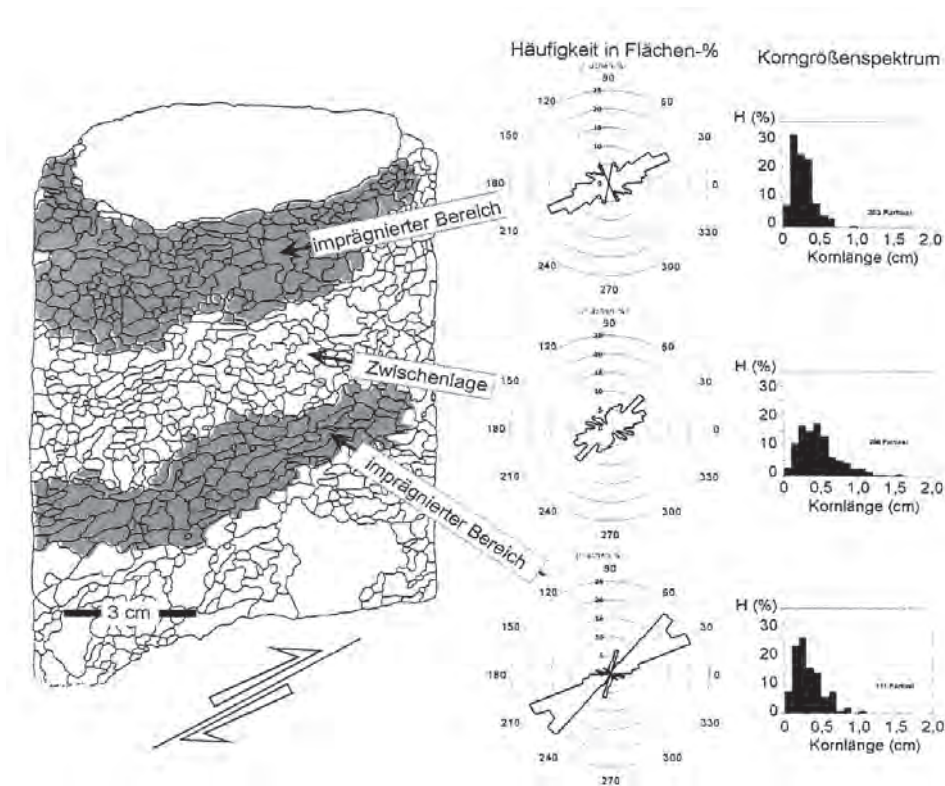


Fig. 1.5: Retraced halite grain masks from Gorleben Hauptsalz sample analyzed in respect to grain orientation and grain size (from Popp et al., 2002). Gray-shaded areas represent hydrocarbon impregnations.

1.3. Sample material and methods

1.3.1. Rock salt samples and stratigraphic formations

The majority of the samples investigated were collected from drill cores along cross cut 1 West and 1 East at the 840 m level (Exploration area 1) of the Gorleben salt dome. Altogether, 45 boreholes with a length of 6 to 9 m have been drilled in nearly constant distances into the Hauptsalz rocks as part of a

Chapter 1: Introduction of the thesis

further geological exploration of the salt dome (Hammer et al., 2012, 2013, 2015a, b; see Pusch et al., 2014, Chapter 4). As an exceptional case, the anhydrite rocks examined in Chapter 3 derive from the *Gorleben-Bank* (z3OSM).

The majority of the boreholes drilled in exploration area 1 cover the two lowermost units of the Hauptsalz (z2HS): The *Knäuelsalz* formation (z2HS1) and the *Streifensalz* formation (z2HS2). These two formations are the main constituents of the central part of the Gorleben salt dome (Fig. 2.1 in Chapter 2 and Fig. 4.4 in Chapter 4) and are mainly composed of halite (approx. 95 vol.-%) and anhydrite (approx. 5 vol.-%). The terms *Knäuel* (English: nodule or cluster) and *Streifen* (English: strip or band) are related to the characteristic anhydrite distribution. Especially the z2HS1 formation reveals strongly knotted and disrupted anhydrite clusters, which is why both formations are also described as salt tectonic breccia (Bornemann et al., 2008). The former anhydrite layers have been torn and disrupted due to the polyphase deformation during the salt uplift (Bornemann et al., 2008; see Chapters 2 and 7 for further details). A typical sampling sequence along cross cut 1 West is shown in Figure 2.1b (Chapter 2) or in Figure A2.1 (Appendix A).

1.3.2. Methods and tools

The data and results of the present thesis were obtained using various methods and tools. The major techniques for microstructural investigations of the rock salt fabrics are the following:

- 1) Polarized light microscopy using reflected, transmitted and ultraviolet (UV) light on etched or ground/polished thick and thin sections to analyze the rock salt microstructures. Etched sections were used to study the size and shape of halite subgrains, and fluorescence microscopy was used to trace hydrocarbons (Chapter 2).
- 2) Flat bed scanning of drill core segments to capture and retrace the halite grain masks used for geometric measurements and a reconstruction of 3D grain shape ellipsoids (Chapter 2).
- 3) Scanning electron microscopy (SEM) combined with Electron backscatter diffraction (EBSD) to analyze rock salt textures, lattice preferred orientation (LPO) and subgrain fabrics (Chapter 2). A comprehensive description of EBSD basics and typical examples is presented in Maitland and Sitzmann (2007).
- 4) Digital photography of rock salt drill cores under reflected, transmitted and ultraviolet light to characterize the rock fabrics and the distribution of fluorescing hydrocarbons, which was followed by a 3D visualization of the drill cores from cross cut 1 West and 1 East using an AutoCAD-based openGEO software (Chapter 4).
- 5) Non-destructive X-ray computed tomography (CT) to visualize and quantify mineral phases, porosity and (multi-phase) fluid inclusions (Chapters 5, 6 and 7). An overview of the technology and the application of CT imaging in the geosciences are illustrated and reviewed in Cnudde and Boone (2013).

Chapter 1: Introduction of the thesis

The analytical techniques listed above represent those techniques applied for microstructural investigations. Supplementary methods and tools concerning geochemical, geo-mechanical and mineralogical analyses are briefly presented in Chapters 3, 4 and 5.

1.4. Aims of the thesis

The present thesis mainly focuses on the fabrics and hydrocarbons in Gorleben Hauptsalz (z2HS). The major aim was to unravel the main deformation mechanisms in both halite and anhydrite operating during the deformation history of the Gorleben rock salt. Regarding the role of hydrocarbons, a main question to be solved was how the hydrocarbons are distributed within the rock salt on both macro- and microscopic scale and whether hydrocarbon-free and hydrocarbon-impregnated rock salt are different in grain fabrics as previously suggested by Popp et al. (2002) (Fig. 1.5). Apart from thick and thin section analyses, a major focus was on the application of high resolution X-ray computed tomography (CT) to quantify and visualize the structural inventory, anhydrite inclusions in halite matrix, fluid phases and potential fluid reservoirs, such as elevated porosities. The 3D visualization and quantification of different types and phases of fluid inclusions has been carried out for the first time. Since the CT lab at the Johann Wolfgang Goethe-University has recently been established, a summary and record of CT handling aspects and hands-on experience are included in the present thesis (Appendix B).

1.5. Structure of the thesis

1.5.1. Overview

Chapter 2 deals with operating deformation mechanisms of Gorleben z2HS1 and z2HS2 as derived from the microstructures and textures, the latter obtained using electron backscatter diffraction (EBSD). Based on the size of halite subgrains, the paleo-differential stress is determined, and the 3D geometry of the halite grain shape is derived from sectional grain shape masks. Detailed grain shape and subgrain data, as well as their relation to hydrocarbon contents are listed in Appendix A (Figs. A1.2 and A2.2). Furthermore, fluid distributions and the microstructures of anhydrite were investigated and used to unravel the operating deformation mechanisms.

Chapter 3 examines the deformation behavior of anhydrite rocks from the Gorleben-Bank (z3OSM) in the Gorleben salt dome. Individual zones of the Gorleben-Bank are studied in respect to microstructural characteristics.

Chapter 4 focuses on the distribution of the hydrocarbons in the z2HS. The hydrocarbon distribution is illustrated by means of fluorescence analyses of drill cores converted into a three-dimensional visualization of the hydrocarbon impregnations along cross cut 1 West and 1 East at the 840 m exploration level. Furthermore, the mineralogical composition of z2HS is analyzed.

Chapter 1: Introduction of the thesis

Chapter 5 enumerates basic facts about the amounts and the origin of the Gorleben hydrocarbons by combining results obtained in macro- and microstructural, geochemical and CT studies. Additionally, the influence of hydrocarbons on the geomechanical properties of hydrocarbon-bearing rock salt is discussed and important conclusions are drawn about the hydraulic integrity of the salt barrier.

Chapter 6 presents the results of X-ray computed tomography (CT) applied on rock salt. Particular attention was paid to elevated porosities of three samples representing outliers within the overall, very low porous Gorleben z2HS. The quantified porosities are compared to elevated hydrocarbon contents and are further analyzed by light microscopy in corresponding rock salt thick sections. This chapter represents a case study of CT imaging on Gorleben rock salt.

Chapter 7 gives an overview about the potential value of the CT imaging technique regarding a characterization of the structural rock salt inventory. Several CT examples are presented dealing with anhydrite and pore space distributions and 3D reconstructions of various types of fluid inclusions. Additionally, the first rock salt CT scans in the sub-micron range are illustrated. CT visualization and projection modes are explained and aspects of digital filtering are introduced and discussed. This chapter draws general conclusions for CT imaging of rock salt, but also includes essential information for the structural investigation of Gorleben rock salt in particular. Supplementary information about CT handling aspects and hands-on experience valuable for operators of the nanoCT lab at the Johann Wolfgang Goethe-University are summarized in Appendix B.

Chapters 8 and 9 comprise a summary, the main conclusions of the present thesis including a brief consideration of unsolved or open questions and potential future work regarding microstructural aspects of rock salt and the impact of hydrocarbon occurrences on its barrier properties. Important implications are formulated and the value of CT imaging is outlined.

1.5.2. Journal papers of this thesis

The following manuscripts have been published in peer-review journals of international standards. Three of these articles are first-authorships. The articles do not succeed here by publication date, but are arranged according to their individual content in order to form a structured thread through the thesis.

Chapter 2:

Thiemeyer, N., Mertineit, M., Linckens, J., Pusch, M., Zulauf, G., Hammer, J., 2016. Microfabrics and 3D grain shape of Gorleben rock salt: Constraints on deformation mechanisms and paleodifferential stress. *Tectonophysics* 676, 1-19.

Chapter 1: Introduction of the thesis

Chapter 3:

Mertineit, M., Hammer, J., Schramm, M., Kneuker, T., Thiemeyer, N., Zulauf, G., 2015. Deformation of thin layered anhydrite rocks within the Gorleben salt dome, Germany. In: Roberts, L., Mellegard, K., Hansen, F. (Eds.). *The Mechanical Behavior of Salt VIII*, Taylor & Francis Group, London, 99-107.

Chapter 4:

Pusch, M., Hammer, J., Kus, J., Klosa, D., Thiemeyer, N., Mingerzahn, G., 2014. Macro- and microscale distribution of hydrocarbons in the Staßfurt Hauptsalz of the Gorleben salt dome. *German Journal of Geosciences* 165 (1), 3-14.

Chapter 5:

Hammer, J., Pusch, M., Häher, C., Ostertag-Henning, C., Thiemeyer, N., Zulauf, G., 2015. Hydrocarbons in rock salt of the Gorleben salt dome – amount, origin and influence on geomechanical properties. In: Roberts, L., Mellegard, K., Hansen, F. (Eds.). *The Mechanical Behavior of Salt VIII*, Taylor & Francis Group, London, 69-75.

Chapter 6:

Thiemeyer, N., Pusch, M., Hammer, J., Zulauf, G., 2014. Quantification and 3D visualisation of pore space in Gorleben rock salt: constraints from CT imaging and microfabrics. *German Journal of Geosciences* 165 (1), 15-25.

Chapter 7:

Thiemeyer, N., Habersetzer, J., Peinl, M., Zulauf, G., Hammer, J., 2015. The application of high resolution X-ray computed tomography on naturally deformed rock salt: Multi-scale investigations of the structural inventory. *Journal of Structural Geology* 77, 92-106.

1.5.3. Conference contributions

Thiemeyer, N., Zulauf, G., Hammer, J., Habersetzer, J., 2014. The application of high-resolution X-ray computed tomography for naturally deformed rock salt. *GeoFrankfurt 2014*. Talk.

Mertineit, M., Müller, H.-H., Leiss, B., Schramm, M., Hammer, J., Henneberg, M., Thiemeyer, N., Zulauf, G., 2014. Microstructural and mineralogical-geochemical investigations on the transition zone z2-z3 of the Gorleben salt dome, Northern Germany. *GeoFrankfurt 2014*. Talk.

Thiemeyer, N., Pusch, M., Hammer, J., Zulauf, G., 2012. Microstructural investigation and CT imaging of hydrocarbon-bearing Gorleben rock salt: deformation mechanisms and fluid characteristics. *GeoHannover 2012*. Talk.

Thiemeyer, N., Zulauf, G., Hammer, J., 2014. Understanding strain accommodation in rock salt – an

Chapter 1: Introduction of the thesis

- evaluation of deformation mechanisms operating in Gorleben rock salt. GeoFrankfurt 2014. Poster.
- Thiemeyer, N., Pusch, M., Hammer, J., Zulauf, G., 2014. CT imaging of rock salt - Part I: 3D multi-scale analyses of the structural inventory. AAPG conference, Houston (Texas). Poster.
- Thiemeyer, N., Pusch, M., Hammer, J., Zulauf, G., 2014. CT imaging of rock salt - Part II: filtering and resolution limits. AAPG conference, Houston (Texas). Poster.
- Thiemeyer, N., Pusch, M., Hammer, J., Zulauf, G., 2014. CT imaging of rock salt - 3D multi-scale analyses of the structural inventory. GEOFLUIDS: Lubricants of the earth, Tübingen. Poster.
- Thiemeyer, N., Pusch, M., Hammer, J., Zulauf, G., 2012. Microfabrics and deformation mechanisms of hydrocarbon-bearing Gorleben rock salt. TSK 14, Kiel. Poster.

1.6. References

- Al-Siyabi, H. A., 2005. Exploration history of the Ara intrasalt carbonate stringers in the South Oman Salt Basin. *GeoArabia* 10 (4), 39-72.
- BMWi (Bundesministerium für Wirtschaft und Technologie) 2008. Endlagerung hochradioaktiver Abfälle in Deutschland - Das Endlagerprojekt Gorleben (Berlin, München), 64 pp.
- Bornemann, O., 1982. Stratigraphie und Tektonik des Zechsteins im Salzstock Gorleben. *Zeitschrift der Deutschen Geologischen Gesellschaft* 133, 119-134.
- Bornemann, O., Fischbeck, R., 1986. Ablaugung und Hutgesteinsbildung am Salzstock Gorleben. *Zeitschrift der Deutschen Geologischen Gesellschaft* 137, 71-83.
- Bornemann, O., Behlau, J., Fischbeck, R., Hammer, J., Jaritz, W., Keller, S., Mingerzahn, G., Schramm, M., 2008. Description of the Gorleben Site Part 3. Results of the geological surface and underground exploration of the salt formation. – BGR: 50 figures, 7 tables, 5 appendices; Hannover, 223pp.
- Borns, D. J., Stormont, J. C., 1989. The delineation of the disturbed rock zone surrounding excavations in salt. Rock mechanics as a guide to efficient utilization of natural resources, Proceedings of the 30th US Symposium on rock mechanics, Morgantown, 353-360.
- Bräuer, V., Eickemeier, R., Eisenburger, D., Grisseemann, C., Hesser, J., Heusermann, S., Kaiser, D., Nipp, H.-K., Nowak, T., Plischke, I., Schnier, H., Schulze, O., Sönnke, J., Weber, J. R., 2011. Description of the Gorleben site Part 4: Geotechnical exploration of the Gorleben salt dome. – BGR, Hannover, 176 pp.
- Buhmann, D., Mönig, J., Wolf, J., 2008. Ermittlung und Bewertung von Freisetzungsszenarien. Interim Report, Gesellschaft für Anlagen- und Reaktorsicherheit (GRS) mbH, ISBN 978-3-939355-07-6, 115 pp.
- Carter, N. L., Horseman, S. T., Russell, J. E., Handin, J., 1993. Rheology of rocksalt. *Journal of Structural Geology* 15 (9/10), 1257-1271.

Chapter 1:

Introduction of the thesis

- Carter, N. L., Hansen, F. D., 1983. Creep of rocksalt. *Tectonophysics* 92, 275-333.
- Chen, J., Ren, S., Yang, C., Jiang, D., Li, L., 2013. Self-healing characteristics of damaged rock salt under different healing conditions. *Materials* 6, 3438-3450.
- Cnudde, V., Boone, M. N., 2013. High-resolution X-ray computed tomography in geosciences: A review of the current technology and applications. *Earth-Science-Reviews* 123, 1-17.
- Cristescu, N., Hunsche, U., 1998. Time effects in rock mechanics. Series: Materials, modeling and computation. John Wiley & Sons (Oichester), 342 pp.
- Dreyer, W., 1974. Materialverhalten anisotroper Festkörper, Springer (Wien), 296 pp.
- Drury, M. R., Urai, J. L., 1990. Deformation-related recrystallization processes. *Tectonophysics* 172, 235-253.
- Drury, M. R., Pennock, G. M., 2007. Subgrain rotation recrystallization in minerals. *Materials Science Forum* 550, 95-104.
- Ehgartner, B., Neal, J., Hinkebein, T., 1998. Gas releases from Salt. Sandia report SAND98-1354, Albuquerque (New Mexico), 37 pp.
- Fischbeck, R., Bornemann, O., 1993. Hinweise auf Stofftransporte im Salzstock Gorleben aufgrund von kleintektonischen Untersuchungen und Brombestimmungen an halitischen Klutfüllungen. *Geologisches Jahrbuch A* 142, 233-256.
- Fischer, M., 2000. Gefügekundliche Untersuchung von Steinsalz im Hinblick auf die Verteilung und Bindungsform von Kohlenwasserstoffen und die Bestimmung des Volumenanteils der Kohlenwasserstoff-Einschlüsse. Diploma thesis Part 2, Universität Kiel, 60 pp.
- Gerling, P., Beer, W., Bornemann, O., 1991. Gasförmige Kohlenwasserstoffe in Evaporiten des deutschen Zechsteins. *Kali & Steinsalz* 10. 376-383.
- Gerling, P., Faber, E., 2001. Geologische Bearbeitung der Erkundungssohle (Geologie, Mineralogie, Geochemie): Dokumentation der chemischen Analysen von gasförmigen und flüssigen Kohlenwasserstoffen. BGR, unpubl. Report, 20 pp.
- Gerling, P., Faber, E., Wehner, H. (2002): Interpretation der chemischen Analysen von gasförmigen und flüssigen Kohlenwasserstoffen. - BGR-Bericht, Tagebuch-Nr. 12243/02: 82 S.
- Hammer, J., Pusch, M., Häger, A., Ostertag-Henning, C., Schlömer, S., Mingerzahn, G., Scheeder, G., Shao, H., Paul, B., Schulze, O., Zaretzki, B., Hesser, J., 2012. Untersuchungen von Kohlenwasserstoffen im Erkundungsbergwerk Gorleben. Interim report 2012, Federal Institute for Geosciences and Natural Resources, Hannover, 236 pp.
- Hammer, J., Pusch, M., Häger, A., Ostertag-Henning, C., Schlömer, S., Mingerzahn, G., Scheeder, G., Shao, H., Paul, B., Schulze, O., Zaretzki, B., Hesser, J., 2013. Untersuchungen von Kohlenwasserstoffen im Erkundungsbergwerk Gorleben. Interim report 2013, Federal Institute for Geosciences and Natural Resources, Hannover, 207 pp.
- Hammer, J., Pusch, M., Ostertag-Henning, C., Haeger, A., Schlömer, S., Scheeder, G., Shao, H., Paul,

Chapter 1: Introduction of the thesis

- B., Kus, J., Hesser, J., Blumenberg, M. 2015a. Untersuchungen von Kohlenwasserstoffen im Erkundungsbergwerk Gorleben. Final report 2014, Federal Institute for Geosciences and Natural Resources, Hannover.
- Hammer, J., Pusch, M., Häher, C., Ostertag-Henning, C., Thiemeyer, N., Zulauf, G., 2015b. Hydrocarbons in rock salt of the Gorleben salt dome – amount, origin and influence on geomechanical properties. In: Roberts, L., Mellegard, K., Hansen, F. (Eds.). *The Mechanical Behavior of Salt VIII*, Taylor & Francis Group, London, 69-75.
- Hermann, A. G., Knipping, B., 1993. *Waste disposal and evaporites – Contributions to long-term safety*. Springer (Berlin), 208 pp.
- Hudec, M. R., Jackson, M. P. A., 2007. Terra infirma: Understanding salt tectonics. *Earth-Science Reviews* 82, 1-28.
- Hunsche, U., Hampel, A., 1999. Rock salt – the mechanical properties of the host rock material for a radioactive waste repository. *Engineering Geology* 52, 271-291.
- Hunsche, U., Schulze, O., Walter, F., Plischke, I., 2003. *Projekt Gorleben. Thermomechanisches Verhalten von Salzgestein*. Final report, Federal Institute for Geosciences and Natural Resources, Hannover, 157 pp.
- Jackson, M. P. A., Talbot, C. J., 1986. External shapes, strain rates and dynamics of salt structures. *Geological Society of American Bulletin* 97 (3), 305-323.
- Jackson, J. A., 1997. *Glossary of Geology*, Fourth Edition. American Geological Institute, Alexandria, Virginia, 769 pp.
- Jaritz, W., 1980. Einige Aspekte der Entwicklungsgeschichte der Nordwestdeutschen Salzstöcke. *Zeitschrift der Deutschen Geologischen Gesellschaft* 131, 387-408.
- Klinge, H., Boehme, J., Grisseemann, C., Houben, G., Ludwig, R.-R., Rübél, A., Schelkes, K., Schildknecht, F., Suckow, A., 2007. Description of the Gorleben Site Part 1: Hydrology of the overburden of the Gorleben salt dome. BGR: 42 figures, 19 tables, Hannover, 220pp.
- Köthe, A., Hoffmann, N., Krull, P., Zirngast, M., Zwirner, R., 2007. Description of the Gorleben Site Part 2: Geology of the overburden and adjoining rock of the Gorleben salt dome. BGR: 59 figures, 4 tables, 1 appendix, Hannover, 145pp.
- Linckens, J., Zulauf, G., Hammer, J. (submitted). Experimental ductile deformation of halite to high strain by dislocation creep without dynamic recrystallization. *Journal of Geophysical Research*.
- Maitland, T., Sitzmann, S., 2007. Electron Backscatter Diffraction (EBSD) Technique and Materials Characterization Examples. In: Zhou, W., Wang, Z. L., (Eds.). *Scanning Microscopy for Nanotechnology – Techniques and Applications* (Springer), 522 pp.
- Parnell, J., 1994. *Geofluids: Origin, Migration and Evolution of Fluids in Sedimentary Basins*. Geological Society Special Publication 78, London, 372 pp.
- Passchier, C. W., Trouw, R. A. J., 2005. *Microtectonics*. Springer, Berlin, 366 pp.

Chapter 1: Introduction of the thesis

- Peach, C. J., 1991. Influence of deformation on the fluid transport properties of salt rocks. PhD thesis, Rijksuniversiteit te Utrecht, 238 pp.
- Peach, C. J., Spiers, C. J., Trimby, P. W., 2001. Effect on confining pressure on dilatation, recrystallization and flow of rock salt at 150 °C. *Journal of Geophysical Research* 106 (B7), 13315-13328.
- Pennock, G. M., Drury, M. R., Spiers, C. J., 2005. The development of subgrain misorientations with strain in dry synthetic NaCl measured using EBSD. *Journal of Structural Geology* 27, 2159-2170.
- Pennock, G. M., Drury, M. R., Peach, C. J., Spiers, C. J., 2006. The influence of water on deformation microstructures and textures in synthetic NaCl measured using EBSD. *Journal of Structural Geology* 28, 588-601.
- Peters, J. M., Filbrandt, J. B., Grotzinger, J. P., Newall, M. J., Shuster, M. W., Al-Siyabi, H. A., 2003. Surface-piercing salt domes of interior North Oman, and their significance for the Ara carbonate “stringer” hydrocarbon play. *GeoArabia* 8 (2), 231-270.
- Poirier, J. P., 1985. *Creep of Crystals*. Cambridge University Press, 260 pp.
- Popp, T., Kern, H., Schulze, O., 2001. Evolution of dilatancy and permeability in rock salt during hydrostatic compaction and triaxial deformation. *Journal of Geophysical Research* 106 (B3), 4061-4078.
- Popp, T., Fischer, M., Kern, H., 2002. Gefügekundliche Untersuchungen zur Verteilung von Kohlenwasserstoffen (KW) in Steinsalz. *Meyniana* 54, 131-154.
- Popp, T., Wiedemann, M., Kansy, A., Pusch, G., 2007. Gas transport in dry rock salt – implications from laboratory investigations and field studies. In: Wallner, M., Lux, K.-H., Minkley, W., Hardy Jr., H. R. (Eds.). *The Mechanical Behavior of Salt – Understanding of THMC Processes in Salt*, Taylor & Francis Group, 17-26.
- Popp, T., Minkley, W., 2008. Integrity of a salt barrier during gas pressure build-up in a radioactive waste repository – Implications from laboratory investigations and field studies. *REPOS SAFE 2007, International Conference on Radioactive Waste Disposal in Geological Formations*, Braunschweig.
- Popp, T., Brücker, D., Minkley, W., 2010. Pressure induced gas break through in rock salt – Implications from laboratory investigations and field studies. In: Zou, M. Z., Xie, H., Yoon, J. S., (Eds.). *Underground Storage of CO₂ and Energy*, Taylor & Francis Group, 139-147.
- Popp, T., Minkley, W., Salzer, K., Schulze, O. (2012): Gas transport properties of rock salt – synoptic view. - In: Bérest, P., Ghoreychi, M., Hadj-Hassen, F., Tijani, M. (Eds.): *Mechanical Behavior of Salt VII*: 143-154, Taylor & Francis Group, London.
- Powers, D. W., Holts, R. M., 2008. Lessons from early site investigations at the Waste Isolation Pilot Plant. In: Rempe, N. T. (Ed.): *Deep Geological Repositories: Geological Society of America Reviews in Engineering Geology* XIX, 81-95.
- Pusch, M., Hammer, J., Kus, J., Klosa, D., Thiemeyer, N., Mingerzahn, G., 2014. Macro- and microscale distribution of hydrocarbons in the Staßfurt Hauptsalz of the Gorleben salt dome. *German*

Chapter 1: Introduction of the thesis

- Journal of Geosciences 165 (1), 3-14.
- Reinhold, K., Krull, P., Kockel, F., 2008. Salzstrukturen Norddeutschlands 1:500.000, Federal Institute for Geosciences and Natural Resources, Hannover, 2 pp.
- Reinhold, K., Hammer, J., Pusch, M., 2014. Verbreitung, Zusammensetzung und geologische Lagerungsverhältnisse flach lagernder Steinsalzfolgen in Deutschland. Interim report 2014, Federal Institute for Geosciences and Natural Resources, Hannover, 98 pp.
- Schenk, O., Urai, J. L., 2004. Microstructural evolution and grain boundary structure during static recrystallization in synthetic polycrystals of Sodium Chloride saturated brine. Contributions to Mineralogy and Petrology 146, 671-682.
- Schléder, Z., 2006. Deformation mechanisms of naturally deformed rock salt. PhD thesis, RWTH Aachen, 158 pp.
- Schléder, Z., Urai, J. L., Nollet, S., Hilgers, C., 2008. Solution-precipitation creep and fluid flow in halite: a case study of Zechstein (Z1) rocks from Neuhoof salt mine (Germany). International Journal of Earth Sciences 97, 1045-1056.
- Schoenherr, J., Urai, J. L., Kukla, P. A., Littke, R., Schléder, Z., Larroque, J.-M., Newall, M. J., Al-Abry, N., Al-Siyabi, H. A., Rawahi, Z. (2007): Limits to the sealing capacity of rock salt: A case study of the infra-Cambrian Ara Salt from the South Oman salt basin. - AAPG Bulletin 91/11: 1541-1557.
- Schulze, O., Popp, T., Kern, H. 2001. Development of damage and permeability in deforming rock salt. Engineering Geology 61, 163-180.
- Schulze, O. 2007. Investigations on damage and healing of rock salt, in: Wallner, M., Lux, K.-H., Minkley, W., Hardy Jr., H. R. (Eds.), The Mechanical Behavior of Salt – Understanding of THMC Processes in Salt, Taylor & Francis Group, 33-44.
- Schulze, O., 2013. Geotechnische Laborarbeiten im Rahmen der Erkundung Gorleben. Laboruntersuchungen zu den thermo-mechanischen Eigenschaften von Steinsalz mit KW-Imprägnationen. Ergebnisbericht. Report, Bundesanstalt für Geowissenschaften und Rohstoffe, Hannover, 69 pp.
- Schutjens, P. M. T. M., Spiers, C. J., 1999. Intergranular pressure solution in NaCl: Grain-to-grain contact experiments under the optical microscope. Oil & Gas Science and Technology – Rev. IFP 54 (6), 729-750.
- Siemann, M. G., Ellendorff, B., 2001. The composition of gases in fluid inclusions of late Permian (Zechstein) marine evaporites in Northern Germany. Chemical Geology 173, 31-44.
- Siemann, M. G., 2007. Herkunft und Migration mineralgebundener Gase der Zechstein 2 Schichten in Zielitz. Kali und Steinsalz 3, 26-41.
- Stormont, J. C., Daemen, J. J. K. 1992. Laboratory Study of Gas Permeability Changes in Rock Salt during Deformation. International Journal of Rock Mechanics and Mining Sciences 29, 325-342.
- Sutherland, H. J., Cave, S. P. 1980. Argon gas permeability of New Mexico rock salt under hydrostatic

Chapter 1: Introduction of the thesis

- compression. *International Journal of Rock Mechanics and Mining Sciences* 17, 281-288.
- Talbot, C. J., Medvedev, S., Alavi, M., Shahrivar, H., Heidari, E., 2000. Salt extrusion rates at Kuh-e-Jahani, Iran: June 1994 to November 1997. *Geological Society Special Publication*, London, 174, 93-110.
- Talbot, C.J., 1981. Sliding and other deformation mechanisms in a glacier of Salt, S Iran. *Geological Society*, London, *Special Publications* 9, 173-183.
- Tang, L.-J., Jia, C.-Z., Jin, Z.-J., Chen, S.-P., Pi, X.-J., Xie, H.-W., 2004. Salt tectonic evolution and hydrocarbon accumulation of Kuqa foreland fold belt, Tarim Basin, NW China. *Journal of Petroleum Science and Engineering* 41, 97-108.
- Ter Heege, J. H., De Bresser, J. H. P., Spiers, C. J., 2005a. Rheological behavior of synthetic rocksalt: the interplay between water, dynamic recrystallization and deformation mechanisms. *Journal of Structural Geology* 27, 948-963.
- Ter Heege, J. H., De Bresser, J. H. P., Spiers, C. J., 2005b. Dynamic recrystallization of wet synthetic polycrystalline halite: Dependence of grain size distribution on flow stress, temperature and strain. *Tectonophysics* 396, 35-57.
- Tissot, B. P., Welte, D. H., 1984. *Petroleum formation and occurrence*, Springer (Berlin, Heidelberg), 699 pp.
- Urai, J. L., Spiers, C. J., Zwart, H. J., Lister, G. S., 1986a. Weakening of rock salt by water during long-term creep. *Nature* 324, 554-557.
- Urai, J. L., Means, W. D., Lister, G. S., 1986b. Dynamic recrystallization of minerals. In: Hobbs, B. E., Heard, H. C. (Eds.). *Mineral and Rock Deformation: Laboratory Studies – The Paterson Volume*, American Geophysical Union *Geophysical Monograph* 36, 161-199.
- Urai, J. L., Spiers, C. J., Peach, C. J., Franssen, R. C. M. W., Liezenberg, J. L., 1987. Deformation mechanisms operating in naturally deformed halite rocks as deduced from microstructural investigations. *Geologie en Mijnbouw* 66, 165-176.
- Urai, J. L., Spiers, C. J., 2007. The effect of grain boundary water on deformation mechanisms and rheology of rocksalt during long-term deformation. In: Wallner, M., Lux, K.-H., Minkley, W., Hardy Jr., H. R. (Eds.). *The Mechanical Behavior of Salt – Understanding of THMC Processes in Salt*, Taylor & Francis Group, 149-158.
- Urai, J. L., Spiers, C., J., Zwart, H., J., Lister, G., S., 1986. Weakening of rock salt by water during long-term creep. *Nature* 324, 554-557.
- Vackiner, A. A., Antrett, P., Strozyk, F., Back, S., Kukla, P., Stollhofen, H., 2013. Salt kinematics and regional tectonics across a Permian gas field: a case study from East Frisia, NW Germany. *International Journal of Earth Science* 102, 1701-1716.
- Van Gent, H., Urai, J. L., de Keijzer, M., 2011. The internal geometry of salt structures – A first look using 3D seismic data from the Zechstein of the Netherlands. *Journal of Structural Geology* 33, 292-311.

Chapter 1: Introduction of the thesis

- Warren, J. K., 2006. *Evaporites: Sediments, Resources and Hydrocarbons*. Springer, 1035 pp.
- Weber, J. R., Keller, S., Mrugalla, S., Wolf, J., Buhmann, D., Mönig, J., 2011a. Safety strategy and assessment for a German HLW-repository in salt. International High-Level Radioactive Waste Management Conference (IHLWMC), Albuquerque (New Mexiko), 8 pp.
- Weber, J. R., Hammer, J., Schulze, O., 2011b: Empfehlungen der BGR zur Berücksichtigung der Kohlenwasserstoff-Vorkommen im Hauptsalz des Salzstockes Gorleben im Rahmen einer vorläufigen Sicherheitsanalyse. Federal Institute for Geosciences and Natural Resources, Hannover, 28 pp.
- Weber, J. R., Mrugalla, S., Dresbach, C., Hammer, J., 2013. Preliminary Safety Analysis of the Gorleben Site: Geological Database – 13300. Conference Paper, WM2013 Conference, Phoenix (Arizona), 11 pp.
- Williamson, M. A., Murray, S. J., Hamilton, T. A., Copland, M. A., 1997. A review of Zechstein drilling issues. *SPE Drilling and Completion* 13 (3), 174-181.
- Zhang, X., Peach, C. J., Grupa, J., Spiers, C. J., 2007. Stress relaxation experiments on compacted granular salt: effects of water. In: Wallner, M., Lux, K.-H., Minkley, W., Hardy Jr., H.R. (Eds.). *The Mechanical Behavior of Salt – Understanding of THMC Processes in Salt*, Taylor & Francis Group, 159-166.
- Zhang, Y., Krause, M., Mutti, M., 2013. The formation and structure evolution of Zechstein (Upper Permian) Salt in Northeast German Basin: A review. *Open Journal of Geology* 3, 411-426.
- Zirngast, M., 1991. Die Entwicklungsgeschichte des Salzstocks Gorleben – Ergebnis einer struktureologischen Bearbeitung. *Geologisches Jahrbuch A* 132, 3-31.
- Zirngast, M., 1996. The development of the Gorleben salt dome (northwest Germany) based on quantitative analysis of peripheral sinks. In: Alsop, G. I., Blundell, D., Davison, I. (Eds.). *Salt Tectonics*, Special Publication of the Geological Society of London 100, 203-226.

Chapter 3

Microfabrics and 3D grain shape of Gorleben rock salt: Constraints on deformation mechanisms and paleodifferential stress.

Nicolas Thiemeyer¹, Michael Mertineit², Jolien Linckens¹, Maximilian Pusch², Gernold Zulauf¹, Jörg Hammer²

¹*Institute of Geoscience, Goethe-University Frankfurt am Main, Altenhöferallee 1, 60438 Frankfurt am Main, Germany.*

²*Federal Institute for Geosciences and Natural Resources (BGR), GeoZentrum Hannover, Stilleweg 2, 30655 Hannover, Germany.*

Abstract

The Permian *Knäuel*- and *Streifensalz* formations (z2HS1 and z2HS2) are main constituents of the Gorleben salt dome (Northern Germany) and show different amounts and distributions of anhydrite. The reconstruction of 3D halite grain shape ellipsoids reveals small grain size (3.4 ± 0.6 mm) and heterogeneous grain shapes in both formations, the latter attributed to the polyphase deformation of the rock salt during diapirism. The halite microfabrics of both formations indicate that strain-induced grain boundary migration was active during deformation. Crystal plastic deformation of halite is further documented by lattice bending, subgrain formation and minor subgrain rotation. Evidence for pressure solution of halite has not been found, but cannot be excluded because of the small grain size, the lack of LPO and the low differential stress (1.1 - 1.3 MPa) as deduced from subgrain-size piezometry.

Anhydrite has been deformed in the brittle-ductile regime by solution precipitation creep, minor dislocation creep and brittle boudinage. No continuous anhydrite layers are preserved, and halite has acted as a sealing matrix embedding the disrupted anhydrite fragments prohibiting any potential migration pathways for fluids. Thus, anhydrite should not have a negative effect on the barrier properties of the Gorleben rock salts investigated in our study.

Keywords: Microfabrics; Deformation mechanisms; Rock salt; Anhydrite; Grain shape ellipsoid, EBSD

[Tectonophysics 676, 1-19. DOI:10.1016/j.tecto.2016.02.046.](https://doi.org/10.1016/j.tecto.2016.02.046)

Chapter 2: Microfabrics and 3D grain shape of Gorleben rock salt: constraints on deformation mechanisms and paleodifferential stress

2.1. Introduction

The deformation behavior of rock salt is an important field of research for nuclear waste disposal (e.g. Bornemann et al., 2008; Hunsche and Hampel, 1999), for salt mining, for the localization of petroleum reservoirs in some salt structures (e.g. Schoenherr et al., 2007) and for understanding salt tectonics (e.g. Talbot and Jackson, 1987; Wagner and Jackson, 2011). For these reasons, microfabrics and related deformation mechanisms in halite have been intensely studied for naturally and experimentally deformed rock salt (e.g. Urai and Spiers, 2007, and references therein).

The rock salt deposits from the Gorleben salt dome (Northern Germany) attract major interest because the salt dome has been considered as a nuclear waste repository (e.g. Bornemann et al., 2008). Microstructural investigations of Gorleben rock salt are of major importance in the framework of a comprehensive characterization of these rocks. Regarding future evolution and safety aspects of the Gorleben salt dome, anhydrite in the form of layers, boudins and inclusions inside the rock salt is of major interest (e.g. Burchardt et al., 2011; Chemia et al., 2009). However, microstructural investigations of anhydrite are scarce for the Gorleben Hauptsalz group, which is targeted as potential medium for nuclear waste storage. Layers of anhydrite have been discussed to represent possible migration pathways for fluids (e.g. Zulauf et al., 2010), which is why the role of anhydrite is important to evaluate with respect to nuclear waste disposal.

Studying rock salt microstructures allows identifying the operating deformation mechanisms. For natural halokinetic conditions (20 - 200 °C) several deformation mechanisms should be considered. *Dislocation creep* results from glide and climb of dislocations within the crystal lattice causing a reduction of the internal strain energy of grains (e.g. Poirier, 1985). As a result, subgrains may develop, which reflect domains of homogeneous crystallographic orientation separated by boundaries with a low misorientation ($< 10^\circ$). The formation of subgrains as recovery mechanism is controlled by temperature, differential stress and strain rate, and furthermore by material properties, such as grain orientation, grain size and fluid content (e.g. Pennock et al., 2005). There are two processes that allow subgrains to be transformed into normal grains. One of these processes is related to the migration of a subgrain boundary through an area of cumulative lattice rotation defined as *sub-boundary migration* (Carter et al., 1993; Drury and Urai, 1990). The second process is *subgrain rotation*, which is a common mechanism to accommodate crystal plastic strain in rock-forming minerals (Poirier, 1985, and references therein). Subgrain rotation (SGR) recrystallization gradually transforms subgrain boundaries with low misorientations into high-angle grain boundaries generating new grains out of former subgrains (Drury and Urai, 1990; Poirier, 1985; Urai et al., 1986b). Drury and Pennock (2007) summarized the process of SGR in minerals. The critical angle for the switch from a low to a high-angle boundary is not exactly defined in the literature. In some cases a high-angle grain boundary is referred to a misorientation angle $> 10^\circ$ (Kleber, 1983; Trimby et al., 2000a, 2000b; White, 1977) or to an angle $>$

Chapter 2: Microfabrics and 3D grain shape of Gorleben rock salt: constraints on deformation mechanisms and paleodifferential stress

15° (Bestmann & Prior, 2003; Bestmann et al., 2005; Pennock et al., 2002). Drury and Urai (1990) point to a more sophisticated nomenclature, because several minerals show different transitions deduced by changes in the mechanical behavior and the transition angle is dependent on the boundary conditions. Based on results presented in the present paper, we will assume 10° as critical angle.

Evidence for weak to moderate subgrain rotation in rock salt has been observed and discussed in several studies (Desbois et al., 2010; Leitner et al., 2011; Pennock et al., 2002, 2005; Pennock and Drury, 2005; Schléder and Urai, 2005; Talbot, 1981; Trimby et al., 2000a, 2000b). However, pervasive SGR *recrystallization* has never been described from naturally deformed halite, although evidence can be drawn from experimentally deformed rock salt (e.g. Franssen, 1994; Guillopé and Poirier, 1979). Moreover, deformation experiments on halite single crystals indicate that the pure formation of subgrains is able to accommodate significant amounts of strain (Linckens al., under review).

Dynamic recrystallization in terms of (strain-induced) *grain boundary migration* (GBM) (Urai et al., 1986a, b) plays a significant role for the deformation of rock salt (e.g. Schenk and Urai, 2004; Schléder, 2006; Ter Heege et al., 2005a, b). GBM is driven by differences in dislocation density across grain boundaries and is significantly supported by grain boundary fluids, which should have a significant impact for rock salt deformation, because already small amounts of brine may result in mechanical weakening of rock salt (Peach et al., 2001; Pennock et al., 2006; Urai et al., 1986a, Urai and Spiers, 2007; Zhang et al., 2007). Since sedimentary and diagenetic fluid phases are common constituents of most salt deposits (e.g. Davison, 2009; Roedder, 1984; Talbot and Rogers, 1980; Závada et al., 2012), the ductile (long-term) behavior of rock salt is ensured (Carter and Hansen, 1983; Carter et al., 1993).

Pressure solution is active along grain boundaries involving grain boundary sliding (GBS) and dissolution/precipitation of halite (Schutjens and Spiers, 1999; Spiers et al., 2004; Urai and Spiers, 2007). By the presence of grain boundary fluids, highly-stressed parts of grains are dissolved (for instance at grain contacts) and material is transported and finally deposited at sites of low stress (e.g. Passchier and Trouw, 2005; Schutjens and Spiers, 1999; Urai and Spiers, 2007). The process of *solution precipitation creep* has been reported for salt glaciers of Iran (Jackson and Talbot, 1986; Talbot, 1981; Talbot et al., 2000) or Zechstein rock salt of the Neuhof salt mine in Germany (Schléder et al., 2008).

Fracturing and intergranular slip of halite are related to volume increase (dilatancy) and thus occur under high differential stress and low effective confining pressure at uppermost crustal conditions. Fracturing and dilatancy also occur under (semi)brittle conditions in the excavation damage zone (EDZ) around shafts or drifts (e.g. Borns and Stormont, 1989; Cristescu and Hunsche, 1998; Schulze, et al., 2001; Urai and Spiers, 2007). Brittle fracturing and related dilatancy result in increased permeability, which is important for fluid flow and barrier properties of salt deposits. Near-lithostatic fluid pressures can increase permeability of rock salt even at depths of a few kilometers (Schoenherr et al., 2007). However, a main mechanical property of rock salt is the potential for recovery (self-healing) even at upper structural levels. The viscous flow of rock salt at hydrostatic pressure counteracts crack propagation,

Chapter 2: Microfabrics and 3D grain shape of Gorleben rock salt: constraints on deformation mechanisms and paleodifferential stress

which reduces porosity and permeability by solution, re-precipitation and crystal plastic deformation of halite (Schulze et al., 2001; Schulze, 2007). Accordingly, hydraulic fracturing is not expected in Gorleben rock salt as shown by geomechanical studies (Hammer et al., 2015; Schulze et al., 2001).

The present paper focuses on the microfabrics of Gorleben rock salt. The major motivation is to analyze the variety of microstructures in order to identify operating deformation mechanisms which have been active during salt diapir emplacement. Furthermore, the microfabrics of anhydrite are examined to estimate its role for fluid transport and the deformation history of the salt dome. Deciphering halite and anhydrite microfabrics is important to specify the rock salt deformation behavior and to gain implications on rock salt sealing capacity during nuclear waste storage.

2.2. Geological setting

The Gorleben salt dome in Northern Germany consists of Upper Permian (Zechstein) rock salt formations, which have been investigated as a possible disposal zone for heat-generating nuclear waste since 1979 (Bornemann et al., 2008). The salt structure strikes from NE to SW over a distance of approximately 14 km (Bornemann et al., 2008). The Gorleben salt rocks started to rise upwards in the Triassic with a maximum rate of 0.14 mm per year during the Late Cretaceous (Zirngast, 1991, 1996). Today, the base of Zechstein salt is situated at a depth between 3200 and 3400 m. The top salt is around 250 m below ground level (Bornemann et al., 2008).

The core of the main anticline of the Gorleben salt dome consists of the *Stassfurt* division (z2), which is subdivided into several groups. The *Hauptsalz group* (z2HS) forms the main constituent in the Gorleben salt dome incorporating the *Knäuelsalz* (z2HS1), the *Streifensalz* (z2HS2) and the *Kristallbrockensalz* (z2HS3) formation (Fig. 2.1). The terms *Knäuel-* and *Streifensalz* are related to the characteristic distribution of anhydrite within these rocks. As described by Bornemann et al. (2008), z2HS1 is a dark-gray, medium- to coarse-grained rock salt characterized by formative amounts of anhydrite impurities present as disseminated inclusions, nodules and clusters (German language: *Knäuel*) mainly representing former anhydrite layers. Underground explorations and drill core analyses show a gradual transition over a few meters from z2HS1 to z2HS2. The latter is characterized by layers and strips (German language: *Streifen*) of anhydrite aggregates (≤ 0.05 m) mixed with halite alternating with almost pure halite layers (Bornemann et al., 2008). Crystal halite fragments up to several cm have also been used to distinguish both salt formations. These lumps occur more frequently in z2HS2, especially toward the top of the sequence (Bornemann et al., 2008). Primary halite fabrics, such as chevron and hopper crystals, are largely missing and restricted to z2HS3 (Pape et al., 2002).

Based on the characteristic macrofabrics the term salt-tectonic breccia for the z2HS group was established, since primary rock fabrics, such as bedding, were largely destroyed by mixing and homogenization during the salt uplift. For this reason, the amount of brines and gases of sedimentary

Chapter 2: Microfabrics and 3D grain shape of Gorleben rock salt: constraints on deformation mechanisms and paleodifferential stress

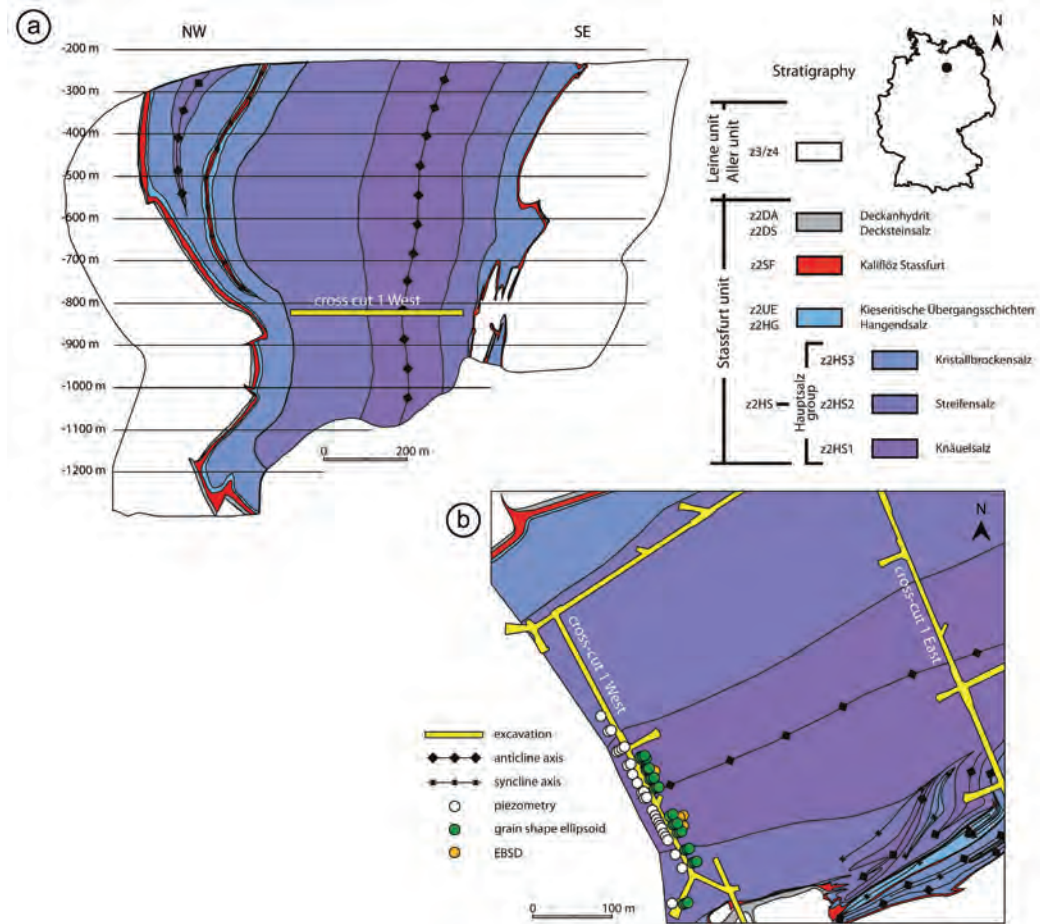


Fig. 2.1: Geology of the Gorleben salt dome (Northern Germany) in the area of the exploration mine after Bornemann et al. (2008). a) Cross section showing the main salt anticline and the composing salt formations. b) Top view of the 840 m exploration level with approximate sample positions. The detailed stratigraphy of Gorleben salt rocks is illustrated in Bornemann et al. (2008).

and diagenetic origin in Gorleben z2HS is very low. Due to the reworking and squeezing of the rocks, the brines and gases were redistributed, particularly into the top salts or into the anhydrite-joint reservoirs (Bornemann et al., 2008; Schramm, pers. comm.).

The structural development of the Gorleben salt dome was reconstructed by combining drilling and reflection-seismic data (Zirngast, 1996). The sedimentary fill of peripheral sinks allowed identifying 13 successive stages from the Late Buntsandstein (Röt) to the present day (Jaritz, 1980; Zirngast, 1991). Accordingly, 280 km³ of salt has flowed into the salt dome since the beginning of diapirism and more than 60 % of the initial source salt beds with an original thickness of ca. 1150-1400 m have moved upwards into the dome (Zirngast, 1996).

Chapter 2: Microfabrics and 3D grain shape of Gorleben rock salt: constraints on deformation mechanisms and paleodifferential stress

2.3. Methods

2.3.1 Halite grain shape analyses

Gorleben z2HS1 and z2HS2 samples from the Gorleben exploration mine (cross cut 1 West, 840 m exploration level) were analyzed regarding halite grain sizes, axial ratios and grain shape ellipsoids. A three-dimensional grain shape ellipsoid was calculated from multiple two-dimensional grain shape ellipses of differently trending and dipping planes using the software *Ellipsoid* (Launeau and Robin, 2005; Robin, 2002). Depending on the particular orientations and axial ratios (ARs) of all captured ellipses, the shape of the final ellipsoid is defined (oblate, triaxial, prolate shaped; Fig. 2.2a). In order to obtain the final ellipsoid, particular geometric information is required: i) the strike (α) and dip (Θ) of the analyzed plane, ii) the axial ratio of the grains (AR) and iii) the dip (φ) of the ellipse's long axis with reference to a horizontal line on the analyzed plane (rake; Fig. 2.2b).

The drill cores with a diameter of 7.2 cm were cut parallel to the drilling axis into quarters to obtain three perpendicular surfaces that were imaged with a flat bed scanner in order to capture the halite grain fabrics. The characteristic halite grain contours were outlined with Adobe Illustrator in order to create masks of the halite grain shapes by manual retracing of the grain boundaries (Fig. 2.2c, left). The digital outlining was accompanied by simultaneously checking of the hand specimens to capture the most accurate halite grain shapes. In a final step, the software *Fiji* (Schindelin et al., 2012) was used to analyze the geometry of all particles concerning number, area, ellipticity, long and short axis, axial ratio and errors. The corresponding ellipses for every single halite grain contour (Fig. 2.2c, right) were subsequently used for the reconstruction of the grain shape ellipsoid. A shape factor (T) defines whether the ellipsoid is prolate (< 0), oblate (> 0) or triaxially shaped (± 0), concordantly to the Flinn parameter (Flinn, 1962). An anisotropy parameter (P') gives the degree of deformation and is calculated from the ellipsoid's three main axes (e.g.: $P' = 1.1$ corresponds to 10 % anisotropy). Hence, the determined anisotropy (P') of the grain shape ellipsoid represents an AR in 3D by incorporating the three main axes of an ellipsoid (for calculation of P' , see Jelinek, 1981).

The relative error is given as incompatibility index ($\sqrt{F^{\sim}}$) indicating how the single ellipses are in agreement with the final ellipsoid (see Launeau and Robin, 2005 and Robin, 2002). This index is generally calculated for the final ellipsoid and for every single ellipse and can be described as an estimate of the standard deviation of the population of sectional ellipses (Launeau and Robin, 2005). The Jelinek diagram (Jelinek, 1981) is used to illustrate the ellipsoid parameters plotting the anisotropy (P') versus the shape factor (T). For theory, applications, examples and error estimations, the reader is referred to Launeau and Robin (2005).

Besides the reconstruction and comparison of three-dimensional halite grain shape ellipsoids, the halite grain fabrics were used to analyze halite grain size and axial ratios. The equivalent circle diameter (ECD) of every halite grain was calculated from the grain areas and is further depicted as grain size. The halite

Chapter 2: Microfabrics and 3D grain shape of Gorleben rock salt: constraints on deformation mechanisms and paleodifferential stress

grain shape ellipses, as described above, provide the axial ratios (ARs) calculated by Fiji (Schindelin et al., 2012).

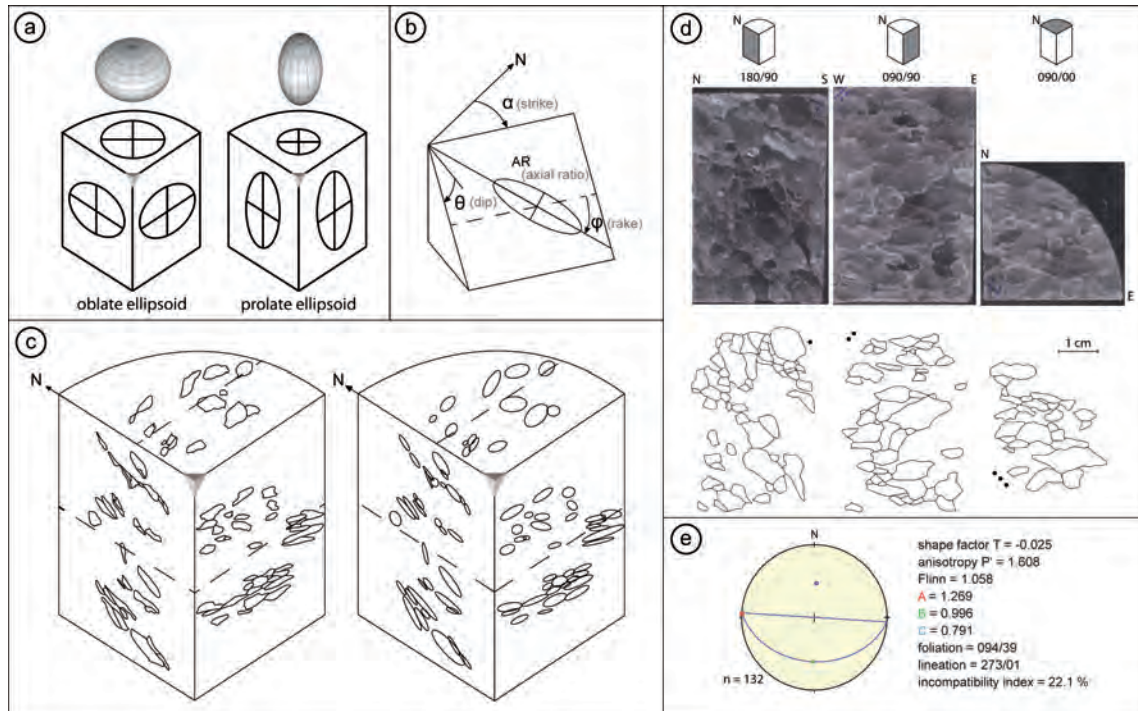


Fig. 2.2: Basic principle of an ellipsoid reconstruction from measured sectional ellipses after Launeau and Robin (2005). a) Example of sectional ellipses resulting in an oblate (left) or prolate (right) ellipsoid depending on ellipse orientation and ellipticity. b) Required geometric parameters for analyzed section and ellipse for the Ellipsoid software (after Launeau and Robin, 2005). c) Exemplary halite grain shape masks (left) transformed into single ellipses by Fiji (right). Dashed horizontal lines are the references for the rake (see b). These ellipses are further used to analyze the axial ratios (ARs). d) Exemplary flat bed scanning images from three perpendicular drill core sections and equivalent halite grain shape masks. e) Stereographic plot of the final ellipsoid with geometric and spatial information. A, B, and C are normalized lengths giving the main axes, from which the shape factor (T) and the degree of anisotropy (P') of the ellipsoid originates. The shape factor ($-1 \leq T \leq 1$) defines, whether the ellipsoid is prolate, triaxial or oblate. The anisotropy (P') gives information about the degree of axis variations (ellipticity). For further explanation see text.

2.3.2. Microstructural investigations

The microstructures of halite and anhydrite in Gorleben z2HS1 and z2HS2 were investigated by light microscopy of thick and thin sections. The main focus was set on grain shape and grain boundary characteristics of halite and anhydrite in order to determine possible grain-shape fabrics and the distribution of fluid phases. Fluorescence microscopy was used to reveal the distribution of hydrocarbons. Overviews of larger thick or thin section areas were digitally generated by merging

Chapter 2: Microfabrics and 3D grain shape of Gorleben rock salt: constraints on deformation mechanisms and paleodifferential stress

numerous microphotographs. For a precise description of very small structures in thick sections, such as grain boundary fluids or single crystals, multiple images of different focus planes were stacked in order to increase the depth of field (z-stack). Anhydrite characteristics and the overall halite grain fabric were further documented by flat bed scanning and digital photography.

In order to determine possible subgrain fabrics of halite, numerous samples were etched with slightly unsaturated NaCl solution and afterwards cleaned with n-hexane according to the method described by Urai et al. (1987).

2.3.3. Paleopiezometry

The subgrain size of halite crystals can be used to determine the approximate differential stress that was present during the deformation of halite (Carter et al., 1993; Schlöder and Urai, 2005; Twiss, 1977). The differential stress σ' ($\sigma_1 - \sigma_3$) is inversely proportional to the subgrain diameter (Carter and Hansen, 1983) obtained from circle equivalents of the analyzed subgrains. This relation can be expressed as

$$d [\mu\text{m}] = 215 \sigma'^{-1,15} [\text{MPa}] \quad (1)$$

or

$$\sigma' [\text{MPa}] = 107d^{0,87} [\mu\text{m}] \quad (2)$$

with d = subgrain size [μm] and σ' = differential stress [MPa] (Carter et al., 1993; Franssen, 1993; Schlöder and Urai, 2005, 2007). The subgrain size has often been used to constrain the differential stress of naturally deformed rock salt (Desbois et al., 2010; Kneucker et al., 2014; Leitner et al., 2011; Schlöder and Urai, 2005, 2007). Experimental deformation of Asse rock salt at 345 °C has shown that the differential stress obtained using Eq. (2) is well in agreement with the actual differential stress recorded by load cells in deformation experiments (Zulauf et al., 2010, 2011).

In the present study, subgrain analyses have been carried out along cross cut 1 West on 21 samples of z2HS1 and on 6 samples of z2HS2 (Fig. 2.1b). Several microphotographs were taken under reflected and transmitted light from subgrain-bearing sections and merged to larger image patches. The outline of subgrains was digitized by retracing the subgrain boundaries using *Adobe Illustrator*. The generated subgrain masks were analyzed with *Fiji* concerning subgrain size giving approximate differential stress values using Eq. (2). The subgrain size is defined as the ECD of one subgrain. The subgrains used for paleopiezometry should not be influenced by mineral inclusions, such as anhydrite (e.g. Zulauf et al., 2010). Therefore, representative areas of relatively homogeneous subgrain distribution were selected for paleopiezometry, especially central parts of larger halite crystals situated remote from grain or phase boundaries.

Chapter 2: Microfabrics and 3D grain shape of Gorleben rock salt: constraints on deformation mechanisms and paleodifferential stress

2.3.4 Electron backscatter diffraction (EBSD)

Textural data were obtained using EBSD, which is a robust method for microstructural studies of rock salt (e.g. Bestmann et al., 2005; Desbois et al., 2010; Kneuker et al., 2014; Pennock and Drury, 2005; Pennock et al., 2006; Schléder and Urai, 2007; Trimby et al., 2000a; Zulauf et al., 2011). We used a scanning electron microscope (JEOL JSM-6490) equipped with an EBSD detector by Oxford Instruments and CHANNEL 5 software (HKL Technology) at the Johann Wolfgang Goethe University Frankfurt am Main with an acceleration voltage of 15 kV and a beam current of 8 nA. EBSD measurements were taken at 20 mm working distance, and the edges of 4-7 Kikuchi bands were detected. For detailed orientation maps, step sizes were 6 μm or 16 μm depending on the magnification. Raw data sets were improved with a 3x3 Kuwahara filter (Humphreys et al., 2001). Wild spikes and zero solutions were replaced by 6 neighboring orientations.

EBSD measurements of a total of four z2HS1 samples are presented. One EBSD mapping set focuses on a large halite crystal (sample RB649UR) to investigate the crystal plastic deformation of halite regarding subgrain rotation, crystal lattice bending and (sub)grain boundary characteristics. An additional map (sample RB657.008) was generated to analyze a particular grain boundary in detail regarding possible GBM.

Furthermore, two samples of z2HS1 (RB647 and RB649) were investigated concerning the grade of a lattice preferred orientation (LPO) evaluating the contribution of crystal plastic deformation for the development of the rock fabric. Due to the relatively large halite grain size, we performed manual EBSD point measurements on several similarly oriented thick sections with numerous grains ($n < 500$) from two drill core samples in order to quantify the LPO.

Inverse (IPF) and normal pole figures (PF) have been used to illustrate the crystallographic orientations of halite. The X0 in IPFs describes the long axis of the thick section and is not related to the strain axis. Uncorrelated misorientation angle distributions give additional information about the statistic distribution of crystal orientations. These distributions are used to calculate the misorientation index (M) after Skemer et al. (2005), which quantifies the strength of the LPO.

Active slip systems (slip plane and slip direction) of halite have been determined from rotation axes, the latter obtained from textural data displayed in pole figures (e.g. Barrie et al., 2008; Prior et al., 2002; Reddy et al., 2007).

2.4. Results

2.4.1. Halite grain size and shape

The analyzed drill core surfaces and the outlined halite grain masks for the ellipsoid reconstruction determined in *Fiji* were used to analyze halite grain sizes and ARs. The mean grain size (ECD) for both

Chapter 2: Microfabrics and 3D grain shape of Gorleben rock salt: constraints on deformation mechanisms and paleodifferential stress

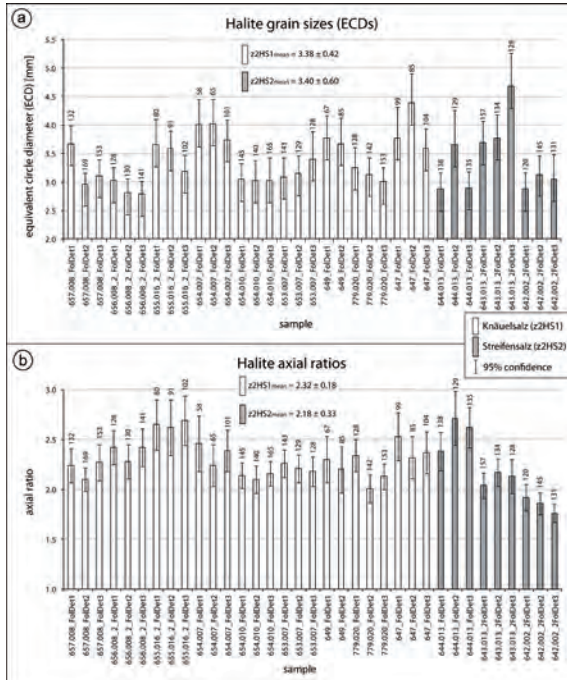


Fig. 2.3: a) Halite grain sizes (ECDs) and b) axial ratios (ARs) of z2HS1 and z2HS2 samples, which represent mean values calculated by numerous halite grains for every sample (vertical numbers). The error bars represent calculated 95% confidence intervals.

salt formations is similar ($z2HS1 = 3.4 \pm 0.4$ mm; $z2HS2 = 3.4 \pm 0.6$ mm; Fig. 2.3a). The average halite AR of both salt formations only slightly differs ($z2HS1 = 2.3 \pm 0.2$; $z2HS2 = 2.2 \pm 0.3$; Fig. 2.3b). The variations of the average grain size and ARs within a single salt formation are relatively small.

The calculated grain shape ellipsoids of 26 z2HS1 and 9 z2HS2 drill core segments reveal a certain variety concerning the shape and anisotropy of the ellipsoids (Table 2.1; Fig. 2.4). The anisotropy ranges from ca. 1.3 to 2.2 with the triaxial to slightly prolate ellipsoids representing the highest values. The shape factor (T) ranges between ca. -0.6 (prolate shape) to ca. +0.9 (oblate shape), the latter prevailing in z2HS1 samples.

Generally, both salt formations show heterogeneous grain shape ellipsoids and no distribution trends regarding anisotropy or

shape factor. A re-orientation of the lineation/foliation is not possible for particular samples, since the drill cores have not been sampled with respect to their original orientation. However, the underground exploration of the Gorleben mine shows that the overall foliation in the central part of the salt dome is relatively steep following the WSW-ENE trend of the overall salt anticline (Bornemann et al., 2008).

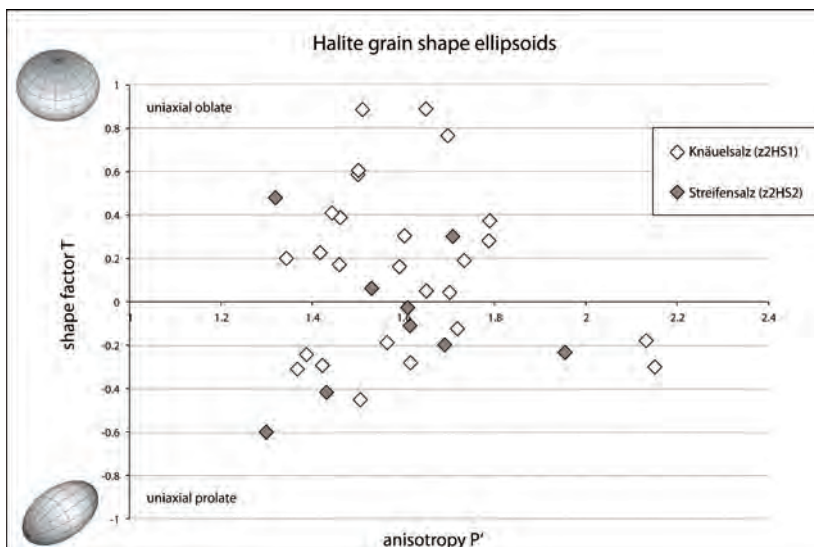


Fig. 2.4: Halite grain shape ellipsoids visualized in the Jelinek diagram (Jelinek, 1981). The halite grain shape fabrics are very heterogeneous regarding anisotropy and shape factor. Error values are listed in Table 1 as incompatibility index ($\sqrt{(|F \sim|)}$). For further discussion see section 5.1. Particular errors for the shape factor (T) and the anisotropy (P') are not available.

Chapter 2: Microfabrics and 3D grain shape of Gorleben rock salt: constraints on deformation mechanisms and paleodifferential stress

or jagged halite boundaries are uncommon (Fig. 2.5e). In a few samples, such boundaries show 90° deflections (Fig. 2.5f). Such clear, partly euhedral grains occur extremely seldom. In some cases, bulged and deflected grain boundaries occur and partially separate halite grains with differing subgrain patterns (Fig. 2.5g, see also section 2.4.3). Moderately to strongly serrated grain boundaries with spikes and edges occur subordinately (Fig. 2.5h,i).

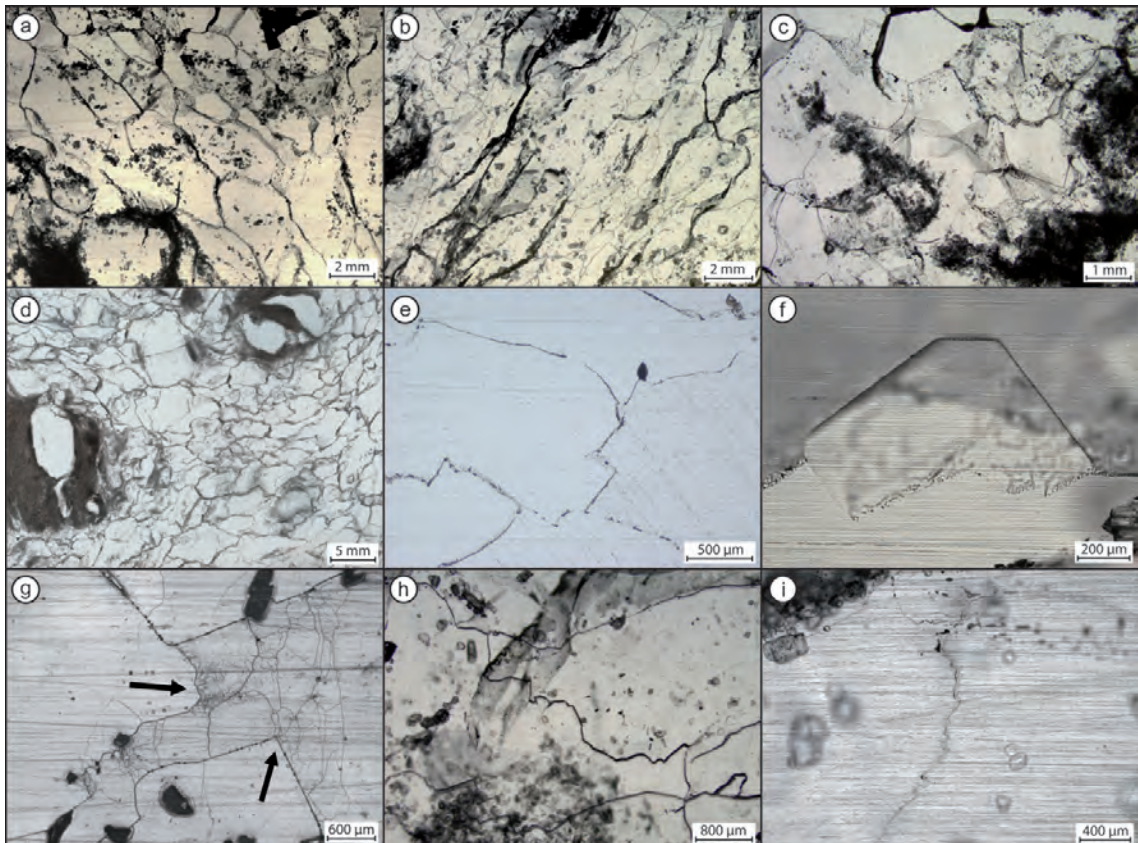


Fig. 2.5: Rock salt fabrics from Gorleben z2HS1 and z2HS2. a) Smoothly curved halite grain boundaries encircling elongated halite grains. The grain shape preferred orientation (SPO) forms a moderate foliation in this sample; transmitted light. b) Microphotograph of z2HS2 thick section illustrating a clear SPO resulting in a foliation; transmitted light. c) Microphotograph of z2HS1 sample with anhydrite impurities. Note the lack of SPO; transmitted light. d) Flat bed scanning photograph of z2HS1 thick section with moderate foliation, which changes its orientation over short distances (steep in the upper right corner). The larger halite grains are covered by anhydrite and are oriented oblique to the average halite grain orientation. e) Jagged and only partly curved halite grain boundaries accommodating small amounts of fluid (black dots). Note the very clear halite grains; transmitted light. f) Partly euhedral halite grain largely free from intracrystalline solid or fluid inclusions; transmitted light. g) Bulged and deflected grain boundaries (arrows) in etched thick section. Note the halite grain on the right-hand side with clearly developed subgrains compared to the other grains; reflected light. h) Serrated halite grain boundary; transmitted light. i) Small-scaled, serrated grain boundary without any fluid phases. Such types of boundaries occur very subordinately; transmitted light.

Chapter 2: Microfabrics and 3D grain shape of Gorleben rock salt: constraints on deformation mechanisms and paleodifferential stress

Most of the halite grain boundaries accommodate fluid inclusions. There are only few fluid inclusions in the rock salt samples studied, which can be interpreted to be of primary type. Chevron shaped fluid bands in halite crystals or pervasive, intracrystalline fluid inclusion bands found in rock salt (Roedder, 1984; Schléder and Urai, 2005; Schoenherr et al., 2007) are lacking. The main fluid and gas phases are distributed along halite grain boundaries retracing their curved morphologies into depth (Fig. 2.6a). Fluid phases decorate the grain boundaries as bubbles or channel-like structures and in rare cases as slightly thicker drops or menisci at halite crystal edges (Fig. 2.6b-d). Rarely, films of grain-boundary fluids are present if the amount of fluid content is elevated. Intragranular trails of fluid and gas inclusions occur subordinately (Fig. 2.6e).

The distribution of hydrocarbons in Gorleben rock salt has been intensely studied during the last years (e.g. Hammer et al., 2012, 2013, 2015; Pusch et al., 2014; Siemann and Ellendorff, 2001; Thiemeyer et al., 2014). Hence, hydrocarbons are mainly located along halite grain boundaries or at halite/anhydrite interfaces giving characteristic channel and island structures (Fig. 2.6f,g). The amount and distribution of fluids in rock salt are strongly controlled by the presence of anhydrite. Besides the phase and grain boundaries, micro capillaries in anhydrite single crystals bear a certain amount of fluid/hydrocarbons (Fig. 2.6h; Hammer et al., 2015; Pusch et al., 2014). The characteristic anhydrite clusters or layers in Gorleben z2HS1 and z2HS2 represent sites, where fluid and gas can be situated particularly due to a slightly elevated microporosity (Fig. 2.6i) (Thiemeyer et al., 2014). The general concentrations of fluids are very low in the Gorleben Hauptsalz group and have been quantified by ≤ 0.017 wt.-% (Bornemann et al., 2008, and references therein).

2.4.3. Halite subgrain fabrics and piezometry

The investigated samples reveal halite subgrains varying in size and shape. Chessboard patterns or equiaxial grains as observed in experimentally deformed samples (Trimby et al., 2000a; Zulauf et al., 2010, 2011) or in weakly-deformed rock salt (Schléder and Urai, 2005) have not been observed. The heterogeneous subgrain size is present in most halite grains resulting in subgrain domains (Fig. 2.7a). Similar subgrain patterns have already been reported from other examples of naturally deformed rock salt (Schoenherr et al., 2007). The etching process after Urai et al. (1987) revealed particular orientations of halite grains by differing gray-shadings of halite crystals. This visual attribute allows identifying a certain misorientation of halite grains or subgrain domains (Fig. 2.7b).

Subgrain sizes become smaller when approaching anhydrite impurities or clusters (Fig. 2.7c). In some cases, subgrain-free halite grains are situated adjacent to subgrain-rich halite grains (Fig. 2.7d). Some subgrains emerge more considerably to others indicated by darker etched boundaries (see Franssen, 1994), whereas other boundaries are fuzzy and hardly visible under the microscope (Fig. 2.7d).

Subgrain boundaries may influence the outline of grain boundaries. In cases where the subgrain boundary is in contact with the grain boundary at an angle of ca. 90° , the grain boundary shows a

Chapter 2: Microfabrics and 3D grain shape of Gorleben rock salt: constraints on deformation mechanisms and paleodifferential stress

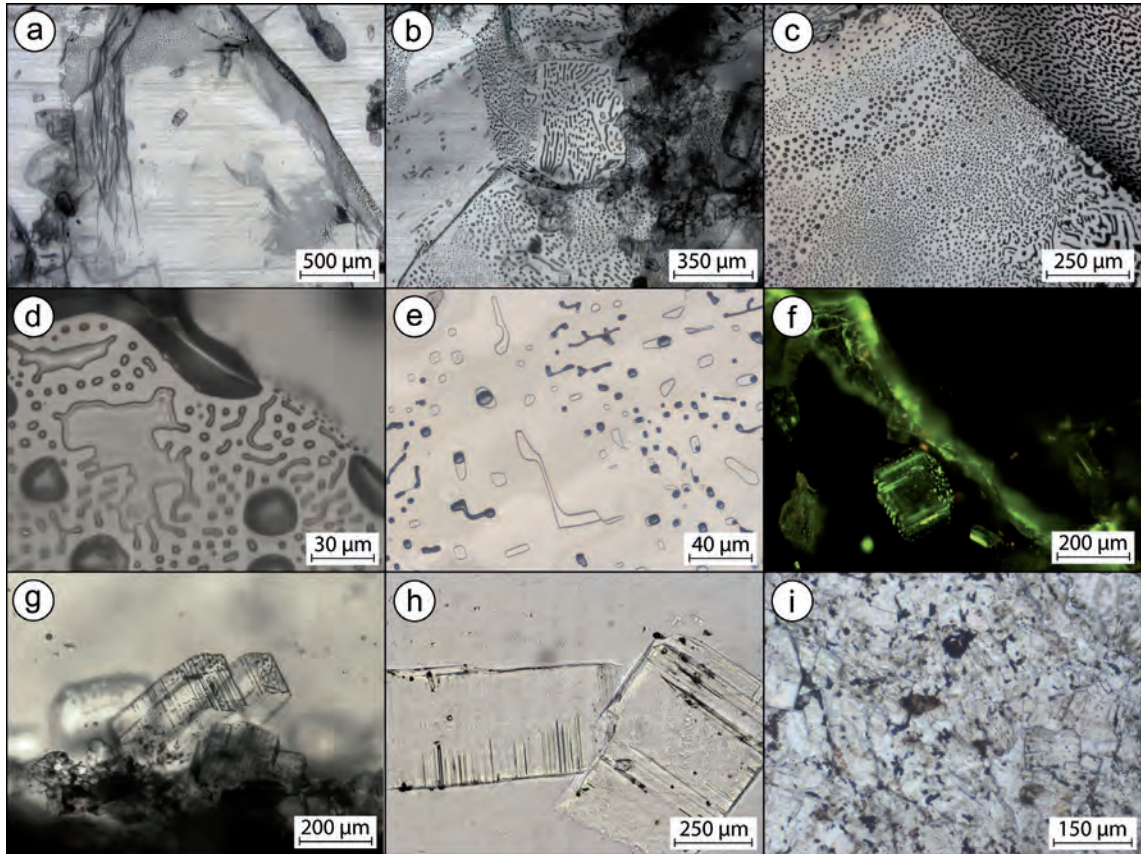


Fig. 2.6: Microphotographs of characteristic fluid inventory of Gorleben rock salt. All images taken under transmitted light (f taken under UV light). a) Stack image of fluid phases decorating halite grain boundaries. Note the wavy trend of the boundary in depth visualized by the black fluid phases. b) Typical stripes and spots of fluids along halite grain boundaries. c) Stacked image of single fluid spots. Increasing amounts of fluid cause dendritic structures or stripes (bottom right). d) Close-up view of grain boundary inclusions containing fluid and gas. e) Intracrystalline fluid inclusions of various shapes containing gas and liquid components. f) Hydrocarbons (green) distributed along grain boundary and cube-shaped anhydrite crystal. g) Anhydrite crystals showing characteristic strips of fluid inclusions, with the orientation of the latter controlled by crystal cleavage. h) Anhydrite crystals with micro capillaries filled with fluid (see also Pusch et al., 2014). i) Anhydrite cluster revealing dark fluid phases and insoluble components. Such anhydrite clusters give slightly elevated porosities and therefore accommodate fluid phases and organic matter.

significant change in orientation (Fig. 2.7e,f). In contrast to high-angle grain boundaries, subgrain boundaries are free from fluid inclusions (Fig. 2.7e,f).

According to equation (2) the paleodifferential stress for several rock salt samples was calculated using the size (ECD) of subgrains. An exemplary subgrain mask is shown in Figure 2.8a. Typical subgrain size histograms show a negative exponential distribution (Fig. 2.8b). All samples of z2HS1 and z2HS2 reveal relatively low differential stress values (Fig. 2.8c). The average differential stress along cross cut 1 West

Chapter 2:
Microfabrics and 3D grain shape of Gorleben rock salt: constraints on
deformation mechanisms and paleodifferential stress

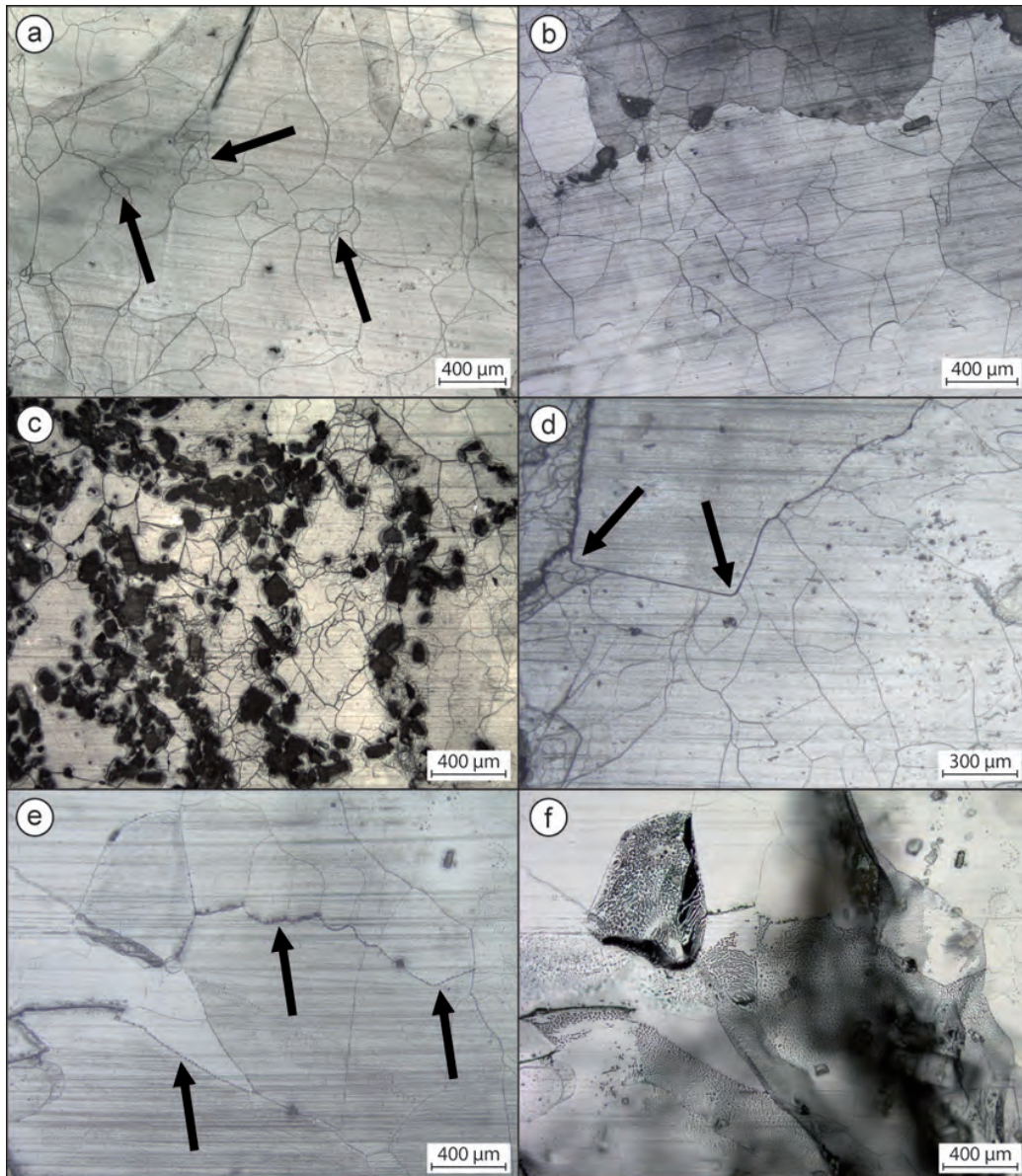


Fig. 2.7: Microphotographs of subgrain fabrics. All images taken from etched thick sections under reflected light (f taken under transmitted light). a) Halite subgrains with heterogeneous size and shape with characteristic domains of smaller subgrains (arrows). b) Gray shades revealing several halite grains with different crystallographic orientations. c) Small subgrains in between disseminated anhydrite crystals (dark fragments). d) Heterogeneous subgrain fabrics separated by deflected high-angle grain boundary (arrows). Some subgrain boundaries are hardly visible. Note that the upper grain is almost free from subgrains. e) Fluid phases are exclusively related to high angle grain boundaries (arrows). Note the partly lobate trend. Tips of this wavy boundary are located at intersections with subgrain boundaries (middle arrow). f) Same image as e) under transmitted light. The stacked image illustrates the fluid distribution along high-angle grain boundaries. Note the lack of fluid phases along subgrain boundaries visible in e) representing the main difference among these two types of boundaries to be seen by light microscopy.

Chapter 2: Microfabrics and 3D grain shape of Gorleben rock salt: constraints on deformation mechanisms and paleodifferential stress

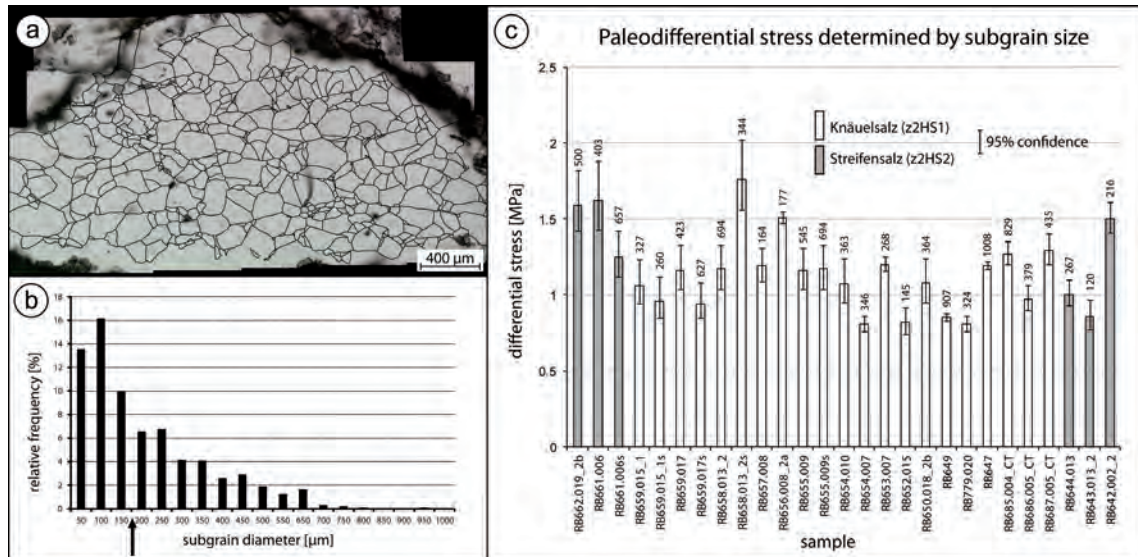


Fig. 2.8: Paleopiezometric data obtained from subgrain size of Gorleben rock salt. a) Exemplary subgrain mask detected in large halite grain. b) Subgrain size histogram determined from subgrains shown in a). Arrow gives the mean ECD for the calculation of the paleodifferential stress in MPa. c) Calculated paleodifferential stress for Gorleben z2HS1 and z2HS2 samples along cross cut 1 West. The data are calculated as mean values and as confidence intervals of 95% due to large standard deviations (see Schlöder and Urai, 2005; Leitner et al., 2011).

is 1.1 ± 0.2 MPa for z2HS1 and 1.3 ± 0.3 MPa for z2HS2. Thus, the calculated differential stress of both salt formations is the same within uncertainties.

2.4.4. Halite texture

One sample of z2HS1 has been investigated concerning halite grain growth and possible GBM. Two adjacent halite grains are separated by a high-angle grain boundary bulging into one of the halite grains (Fig. 2.9). The etched thick section reveals some indistinct subgrain boundaries and etching artifacts (Fig. 2.9a,b), whereas the band contrast image from the EBSD mapping (Fig. 2.9c) clearly illustrates the outline of the grain boundary, disregarding surface artifacts observed under the microscope. The differently oriented halite grains are depicted in the inverse pole figure (IPF) (Fig. 2.9d). The upper right grain (orange) is characterized by a slight variation in the IPF colors and a subgrain boundary (tilt angle $> 1^\circ$) (see Fig. 2.9a and b). In contrast, the lower left grain (green) does not show any IPF color variation or subgrain boundaries. Hence, the IPFs reveal lattice bending in the orange grain, whereas the other grain is free from bending (Fig. 2.9e).

The etched thick section of z2HS1 sample RB649UR shows a large halite grain revealing numerous subgrains of different sizes and shapes (Fig. 2.10a). As typical feature for Gorleben rock salt, the subgrain size and boundary orientations are rather inconsistent. The subgrain diameters range from

Chapter 2: Microfabrics and 3D grain shape of Gorleben rock salt: constraints on deformation mechanisms and paleodifferential stress

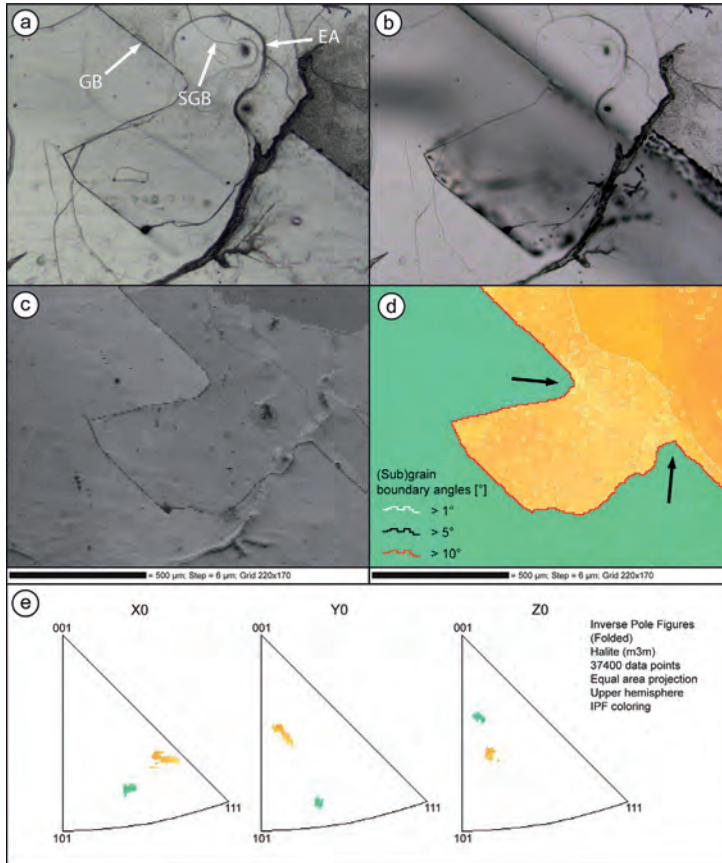


Fig. 2.9: Microphotographs and EBSD mapping of two halite grains. a) Microphotograph of etched thick section under reflected light showing a halite grain boundary (GB), few subgrain boundaries (SGB) and etching artifacts (EA). b) Same image as in a) under transmitted light. The grain boundary is decorated by fluid phases. c) Band contrast (BC) image, obtained by EBSD mapping, illustrating the two halite grains separated by a grain boundary. d) Corresponding EBSD map showing both grains with different crystallographic orientations. The yellow grain is characterized by some internal misorientation of the crystal lattice and a subgrain boundary, whereas the green grain displays homogeneous lattice orientation. The grain boundary bulge suggests grain boundary migration (GBM); arrows indicating the suggested migration direction. e) Corresponding inverse pole figures (IPFs) from EBSD map. IPFs revealing the different grades of crystal lattice bending for the two halite grains. For further explanation see text.

2.10a).

The pole figures of sample RB649UR (Fig. 2.10c) show a clear scattering of the crystallographic axes illustrating the crystal lattice bending and the slight difference in orientation of the subgrains. The

ca. 50 μm to exceptionally 1 mm. Dark fluid phases are distributed along a jagged boundary in the middle of the image (Fig. 2.10a), which extends into the center of the halite grain.

The EBSD map retraces the subgrains observed under the microscope (Fig. 2.10b). Most of the subgrain boundaries reveal misorientation angles $< 5^\circ$. The fluid-bearing boundary, as observed under the microscope, turned out to be a grain boundary with misorientation angles $\leq 24^\circ$. Besides this grain boundary, further small, isolated segments show misorientation angles $> 10^\circ$ (see arrows in Fig. 2.10b). The misorientation angles of the major high-angle boundary decrease toward the upper part of the depicted map, finally dropping below 10° transforming into a subgrain boundary. Thus, the grain boundary is not continuous and the halite grain is not completely split up into two separate halite grains (see also Fig. 2.10a). It has to be emphasized that fluid phases are restricted to those boundaries, where the misorientation angle is $> 10^\circ$ (Fig.

Chapter 2: Microfabrics and 3D grain shape of Gorleben rock salt: constraints on deformation mechanisms and paleodifferential stress

calculated M index for the analyzed halite grain ($M = 0.851$) shows a deviation from a hypothetical, undeformed single crystal ($M = 1$). Usually, this index is calculated to quantify an LPO in rocks for numerous grains (see below). In the case of sample RB649UR the calculated M index for a subgrain

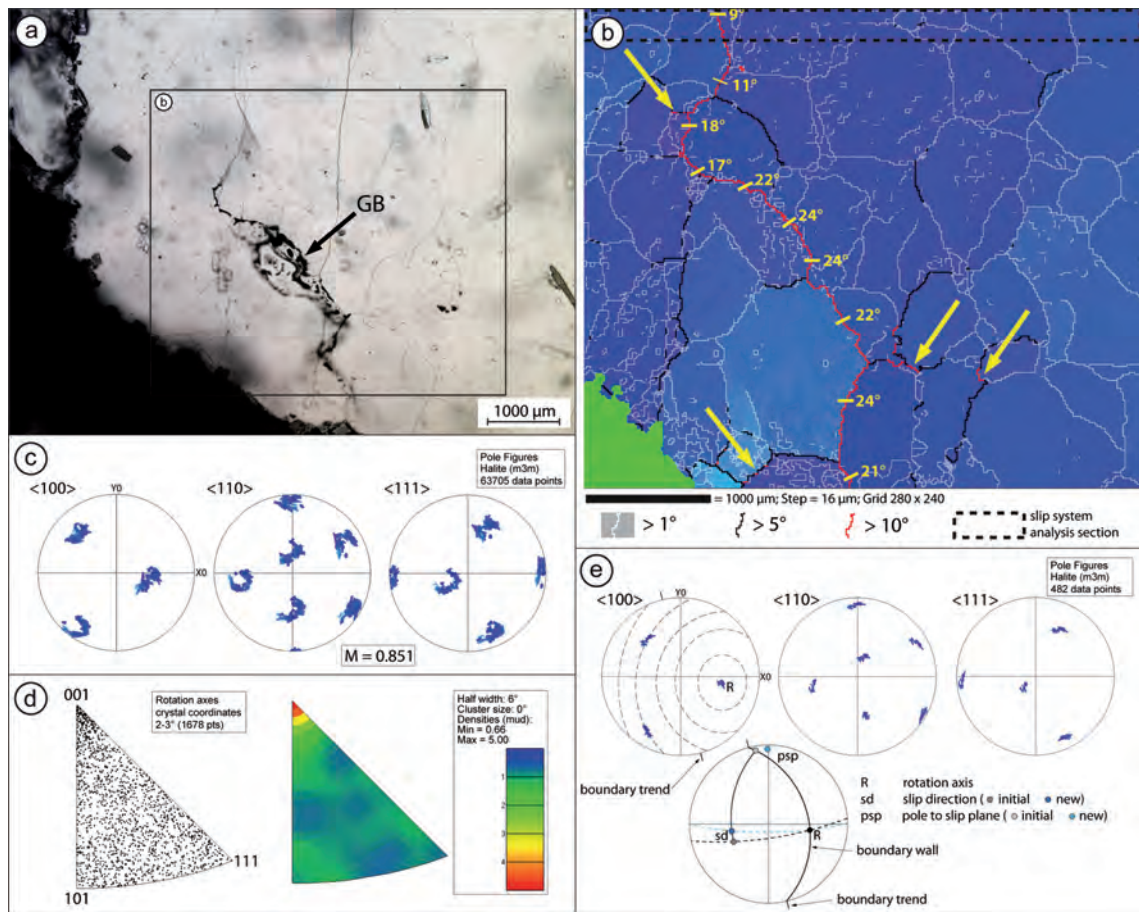


Fig. 2.10: Microphotographs and EBSD analyses of halite. a) Etched thick section revealing subgrains in a large halite grain, which is characterized by a fluid-bearing boundary (GB) in the central part of the transmitted light microphotograph. b) The EBSD map retraces most of the subgrains. Most subgrain boundaries have a misorientation angle $< 5^\circ$. The fluid-bearing structure in a) is a grain boundary (i.e. misorientation angle $> 10^\circ$, see misorientation angles at different locations along the grain boundary). The lower left corner (anhydrite) was not indexed (green). c) Pole figures showing a slight change of the axes orientation within this grain. The calculated M index for the halite grain ($M = 0.851$) demonstrates a deviation of M compared to a hypothetical, undeformed single crystal ($M = 1$). d) Rotation axes orientation plot of the halite grain in IPFs gives a maximum at $\langle 001 \rangle$ for small misorientation angles (2-3°). e) Reconstruction of active slip system for a particular subset shown in b). The orientation of the subgrain boundary is defined as the boundary wall trend and indicated with the thin lines outside the pole figure. In addition, the rotation axis is defined (R). Both, the reconstructed slip direction (sd) and the pole to the slip plane (psp) are congruent with $\langle 110 \rangle$ axes (see $\langle 110 \rangle$ pole figure of e), pointing to the activation of the $\langle 110 \rangle \{110\}$ slip system. The blue psp and sd illustrate the geometric rotation of these poles caused by the tilt boundary. The moving direction is comparable to the $\langle 110 \rangle$ pole figure.

Chapter 2: Microfabrics and 3D grain shape of Gorleben rock salt: constraints on deformation mechanisms and paleodifferential stress

fabric helps to illustrate the overall degree of the lattice misorientation caused by crystal plastic strain. The rotation axes plots reveal a distinct rotation pole, $\langle 001 \rangle$, for low misorientation angles of 2-3° (Fig. 2.10d).

Pole figures from a subset section (dashed box in EBSD map in Fig. 2.10b) allow a reconstruction of the active slip system(s). The $\langle 100 \rangle$ pole figure of the subset reveals a rotation axis (R), which can be used

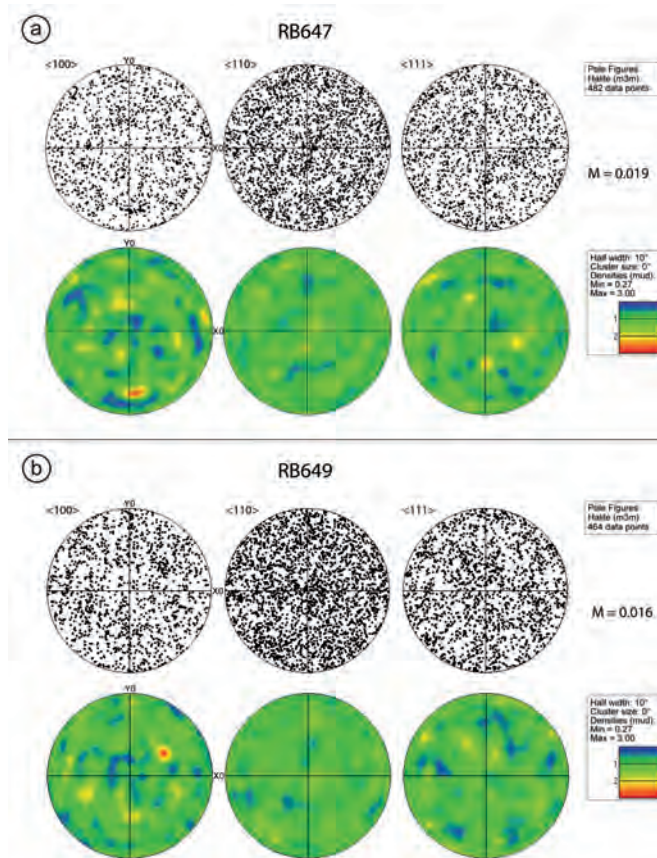


Fig. 2.11: Pole figures and misorientation indices (M) of z2HS1 taken from several oriented thick sections (samples RB647 and RB649). Every point in the pole figures represents a single halite grain. The figures show a random distribution of crystal orientations. No distinct pole maxima can be discerned. Concordantly, the M -indices after Skemer et al. (2005) obtained from uncorrelated misorientation distributions are very low. Pole figures illustrated as upper hemisphere equal area projections

together with the subgrain boundary trend (ca. 76°) to geometrically project the slip direction and the pole to the slip plane. In order to determine the slip system, the subgrain boundary is assumed to be a tilt wall. The derived slip direction and pole to the slip plane are congruent with $\langle 110 \rangle$ axes (Fig. 2.10e). Thus, the $\langle 110 \rangle \{110\}$ slip system should have been active during the accommodation of crystal plastic strain in this particular sample.

The EBSD point analyses of sample RB647 and sample RB649 (both z2HS1) incorporate single orientations of several hundreds of halite grains for each sample ($n_1 = 482$; $n_2 = 464$). For both samples, the pole figures do not show any pole maximum (Fig. 2.11). Thus, a lattice preferred orientation (LPO) is not developed. The uncorrelated misorientation angle distribution of both samples is similar to a random misorientation distribution as illustrated by the calculated, very low misorientation indices (M) of 0.019 (RB647) and 0.016 (RB649).

2.4.5. Macro- and microfabrics of anhydrite

The macroscopic differentiation between the studied salt formations is mainly based on the more distinct layering of anhydrite and halite bands in z2HS2 (Bornemann et al., 2008). In z2HS1 this layering

Chapter 2: Microfabrics and 3D grain shape of Gorleben rock salt: constraints on deformation mechanisms and paleodifferential stress

is rarely preserved due to the strong halokinesis (Fig. 2.12a,b). Only few anhydrite fragments exhibit relics of internal bedding (Fig. 2.12c). The single layers have been broken, dispersed and disrupted during the uplift and the strong deformation of the salt rocks, partly represented as highly complex folding (Fig. 2.12d). Remnants of anhydrite layers are more distinctly preserved in z2HS2 compared to z2HS1.

The overall anhydrite content in these rock salt formations has been previously quantified by ca. 5 vol.-% (Bornemann et al., 2008), while X-ray CT analyses yielded values up to 10 vol.-% for anhydrite-rich samples (Thiemeyer et al., 2015).

The thickness of anhydrite layers ranges from a few mm to a few cm, while thicknesses < 2 cm predominate. The anhydrite layers are broken, folded and disseminated (Bornemann et al., 2008).

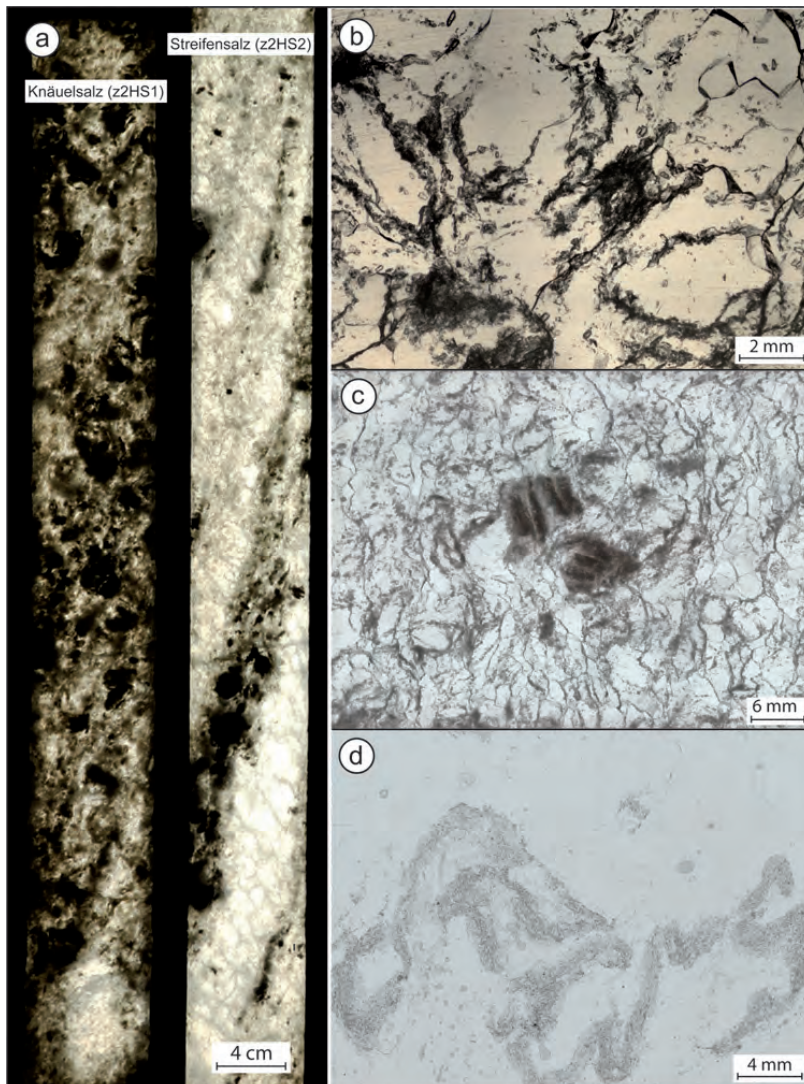


Fig. 2.12: Anhydrite distribution in z2HS1 and z2HS2. a) Representative drill core sections of both formations. The z2HS1 is largely free from a planar fabric and shows characteristic anhydrite nodules and clusters while z2HS2 reveals layers of anhydrite and clear halite bands; transmitted light photograph. b) Microphotograph of z2HS1 illustrating anhydrite crystals disseminated in the halite matrix; transmitted light. c) Flat bed scanning photograph of z2HS1 thick section with two anhydrite fragments. The fragments show relict internal layering d) Flat bed scanning photograph of z2HS2 thin section exhibiting strongly folded anhydrite layer.

Chapter 2: Microfabrics and 3D grain shape of Gorleben rock salt: constraints on deformation mechanisms and paleodifferential stress

In thin anhydrite layers, fine grained anhydrite with grain size $\leq 100 \mu\text{m}$ is dominant. At the rims of the layers, larger euhedral anhydrite crystals (ca. 0.5 mm in size) occur, which are almost free from inclusions and internal deformation structures. A SPO of the anhydrite is noticeable (Fig. 2.13a), and the orientation of the crystal long axis is sub-parallel to the layering. In few cases, large acicular crystals (ca. 1 mm in length) occur and exhibit internal deformation structures and impurities. These crystals

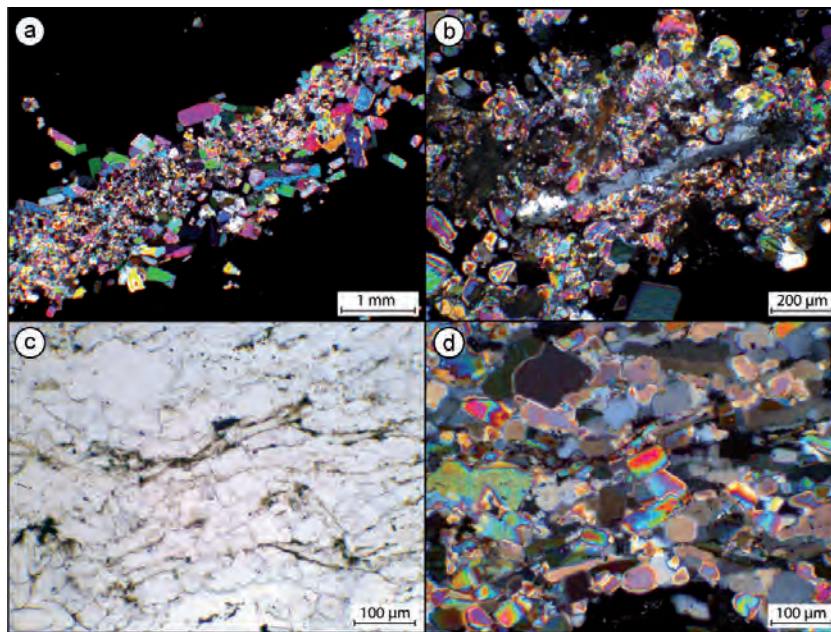


Fig. 2.13: Microstructures in thin anhydrite layer. a) Anhydrite layer in halite matrix. The grain size of anhydrite increases toward the margin of the layer, # polarizers. b) Relicts of large anhydrite crystals, replaced by fine grained anhydrite, # polarizers. c) Seams of opaque material at the grain boundaries of anhydrite, // polarizers. d) Same image as in c) under # polarizers.

have been replaced by fine grained anhydrite (Fig. 2.13b). In single anhydrite fragments, a cleavage developed, which is accentuated by immobile components and by seams of organic matter. Opaque material is dominantly enriched in fold hinges. Grain boundaries of anhydrite are often decorated with organic matter and opaque phases (Fig. 2.13c).

Characteristic features of thicker anhydrite layers are interlayers (Fig. 2.14a), which consist of halite, carbonate (basically dolomite with a size of $\leq 0.5 \text{ mm}$, often euhedral, Fig. 2.14b and c) and anhydrite crystals. In such halite interlayers, euhedral anhydrite crystals reach a size of ca. 0.5 mm. These crystals are oriented parallel to the layer resulting in a shape preferred orientation. They do not show internal deformation and are almost free from inclusions (Fig. 2.14a).

The anhydrite layers consist of different types of anhydrite crystals, which differ in grain size, grain shape and amount of inclusions and impurities (Fig. 2.14d). The largest crystals in these slightly thicker layers

Chapter 2: Microfabrics and 3D grain shape of Gorleben rock salt: constraints on deformation mechanisms and paleodifferential stress

(Fig. 2.14a) have a size of ≤ 0.2 mm and show impurities and fluid inclusions. Undulatory extinction and subgrains (Fig. 2.14e and f) are common microstructures. The grain boundaries are locally bulged (Fig. 2.14f). The large crystals have been replaced by fine grained, massy, granular anhydrite. Seams of opaque material also occur and grain boundaries of fine grained anhydrite are often decorated with organic matter.

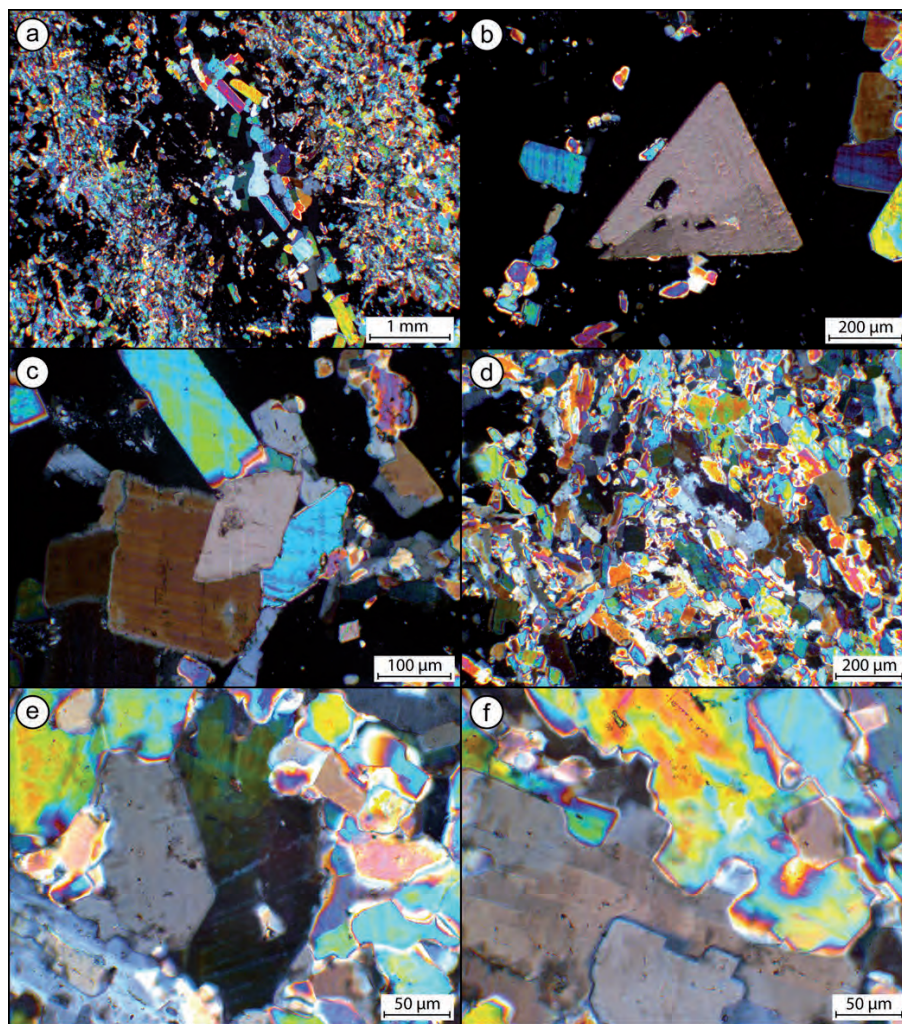


Fig. 2.14: Microstructures in thick anhydrite layer. All images taken under # polarizers. a) Anhydrite layer of ca. 1.5 cm thickness. Note large grain sizes and the shape preferred orientation (SPO) of anhydrite in the halite interlayer. b) Euhedral carbonate crystal in halite matrix. c) Euhedral carbonate crystal in halite interlayer, associated with subhedral anhydrite crystals. d) Different types of anhydrite. Large crystals with internal deformation structures and inclusions are replaced by fine grained, almost inclusion-free crystals. e) Undulatory extinction in anhydrite indicating the bending of crystal lattice. f) Irregular and lobate grain boundaries. Note twins and subgrains in anhydrite (bottom left grain).

Chapter 2: Microfabrics and 3D grain shape of Gorleben rock salt: constraints on deformation mechanisms and paleodifferential stress

2.5. Discussion

2.5.1. Grain size and shape

As there is no information about the initial halite grain size and shape, the geometric information obtained by halite grain shape analyses cannot be used to constrain the finite strain. Neither the determined grain shape ellipsoids, nor the measured ARs represent the real strain ellipsoids (see also Miralles et al., 2001). Several factors, such as initial grain size, impurities, grain boundary characteristics (presence of fluid), halite nucleation and operating deformation mechanisms (including mass transfer) do not allow any quantification of strain. Besides, the dependence between bulk strain and grain size is highly complex (e. g. Ter Heege et al., 2005b) and not straightforward (Miralles et al., 2001). Especially the resetting of deformation structures by healing and recovery processes (see section 2.5.2) operating in halite prohibits any assumptions on bulk strain.

The average halite grain size and axial ratio in Gorleben z2HS1 and z2HS2 (Fig. 2.3) are straddling a reasonable range for collected data on naturally-deformed rock salt (Table 2.2). Highly-strained salt rocks from shear zones (Schléder and Urai, 2007), extruding salt fountains (Desbois et al., 2010, 2012) or tightly folded rock salt (Schléder, 2006; Schléder et al., 2008) show an average halite grain size < 1 mm (Table 2.2). Larger halite grain sizes of few mm to several cm are reported for the Klodawa rock salt (Poland) (Burliga & Czechowski, 2010; Schléder et al., 2007) or partly for the Ara salt diapir in South Oman (Schoenherr et al., 2007).

publication	mean average grain size [mm]	axial ratio (AR)	mean differential stress [MPa]	locality	geological setting
this study	3,4	2.2-2.3	1.1-1.3	Gorleben (Germany)	salt dome
Desbois et al. (2010, 2012)	< 0.5	1.4-1.6	3.1-4.8	Qom Kuh (Iran)	salt fountain
Kneucker et al. (2014)	< 5	1.4-2.1	1.2-2.9	Morsleben (Germany)	salt dome
Leitner et al. (2011)	< 1.5	?	2.0-5.4	Haselgebirge (Austria)	rocksalt-mudrock-tectonite
Mertineit et al. (2014)	0.3-2.5	?	2.28-2.97	Gorleben (Germany)	salt dome
Miralles et al. (2001)	< 2	< 1.73	?	Súria (Spain)	folded salt (shear zone)
Schléder and Urai (2005)	5-25	?	0.45-0.97	Hengelo (Netherlands)	bedded salt
Schléder and Urai (2007)	0,6	0,4	?	Garmsar Hills (Iran)	extrusive salt (mylonite)
	4	1.5-2	1.4-2.0		extrusive salt (protomylonite)
Schléder et al. (2007)	3-25	1-2	0.9-3.1	Klodawa (Poland)	salt dome
Schoenherr et al. (2007)	2-30	< 3	< 2.0	Birba, Harweel (Oman)	salt diapir
Závada et al. (2012)	< 0.3	< 1.61	3.8-4.8	Neuhof (Germany)	folded salt

Table 2.2: Selected rock salt deposits of different geological settings with examined halite grain sizes, axial ratios and differential stress. The single parameters only refer to particular samples examined in the equivalent studies. For more details we refer to the original publications.

The determined anisotropies (P') in 3D for the Gorleben samples are slightly smaller (ca. 1.3-2.2; Table 2.1) than the AR in 2D (ca. 1.8-2.7; Fig. 2.3). The shape factor (T) shows striking variations in shape

Chapter 2: Microfabrics and 3D grain shape of Gorleben rock salt: constraints on deformation mechanisms and paleodifferential stress

ranging from oblate to moderately prolate (Fig. 2.4). Thus, the Gorleben rock salt is not only foliated, but also lineated which is related to the complex and polyphase deformation history of the Gorleben salt dome (Bornemann et al., 2008).

The three-dimensional rock salt fabrics have been previously described for a shear zone by Miralles et al. (2001), who determined a grain shape ellipsoid based on three perpendicular planes oriented in a stratigraphic co-ordinate system of the study area. In contrast, in the studied Gorleben rock salt primary planar and/or linear fabrics, which could have been used as a reference frame, are lacking. For this reason, the axes of the obtained grain shape ellipsoids are not related to an external reference frame. However, the variation from oblate to prolate ellipsoids and the determined anisotropies are in line with the data of Miralles et al. (2001), although the ellipsoid axes were obtained using different methods.

The variations within the reconstructed ellipsoids in our study entail questions about data reliability and error estimation. The incompatibility index ($\sqrt{F^{\sim}}$) is generally an index of misfit between all single grain ellipses and the final ellipsoid (Launeau and Robin, 2005). The authors show that the elimination of few single values of some ellipses, which have been depicted as 'wrong' ($\sqrt{F^{\sim}} > 30\%$), does not change the overall ellipsoid, but only decreases the final index of the reconstructed ellipsoid. In the case of Gorleben rock salt, the heterogeneity of the halite grain shape fabric might cause a certain increase of $\sqrt{F^{\sim}}$ (20.6 - 27.2 %; Table 2.1). However, elevated incompatibility indices do not necessarily reflect unreliable data, because the authors further state that $\sqrt{F^{\sim}}$ can be regarded as an approximate standard deviation of the population of sectional ellipses. Thus, a high number of analyzed grains ($n = 58 - 169$; Table 2.1) might increase the index, although the reconstructed ellipsoid is valid. For a detailed evaluation and discussion of factors influencing the incompatibility index, the reader is referred to Launeau and Robin (2005).

The reconstructed ellipsoids were checked and verified by comparison to the analyzed and digitized sample surfaces. Due to the transparency of clear halite segments, the approximate halite grain shape could be partly obtained in hand specimens, especially at the sample edges. This simultaneous, visual checking already exposed partly pencil-type (prolate) grain shapes according to the heterogeneous halite grain shape ellipsoids (prolate to oblate) calculated by *Ellipsoid*.

Finally, the *Ellipsoid* technique is worth applying for a structural characterization yielding robust geometrical data on rock salt fabrics, such as strength of foliation or lineation and stereoscopic orientations of the fabrics. Both z2HS1 and z2HS2 show similar variations in grain shape ellipsoids pointing to the pervasive and polyphase reworking of the z2HS group in the central part of the Gorleben salt dome. Hence, the term foliation is not always appropriate for Gorleben rock salt, since planar fabrics are not necessarily developed. The *Ellipsoid* technique recruits and enriches traditional techniques for characterizing rock fabrics.

Chapter 2: Microfabrics and 3D grain shape of Gorleben rock salt: constraints on deformation mechanisms and paleodifferential stress

2.5.2. Deformation mechanisms in Gorleben rock salt

The lack of primary structures, such as chevrons, hoppers or primary fluid inclusions in combination with the elongated halite grains and the dissemination of anhydrite (former layers) indicate that this rock salt must have been pervasively deformed.

The determined grain size is small and thus might have supported solution-precipitation creep as deformation mechanism. When taking experimental data of rock salt into account (see Schléder, 2006, and references therein) the average grain size of 3.4 mm of the Gorleben samples and the low paleodifferential stress values ranging from 1.1 to 1.3 MPa are in line with data for domal salt and point to a combination of pressure solution and dislocation mechanisms. Unfortunately, there is no temperature data available for our samples. Since the present-day basis of the Zechstein rock salt in Gorleben is between 3200 and 3400 m (Bornemann et al., 2008), and referring to calculations on sedimentary cover, salt uplift and structural evolution from Zirngast (1996) maximum temperatures can only be roughly estimated by $T \leq 100$ °C.

Regarding the role of pressure solution, the prevalent grain-boundary fluid inclusions might have supported solution-precipitation creep, especially in cases where the water content has exceeded the present-day values. However, the water content for domal salt is generally low (Gies et al., 1990; Urai et al., 1987) related to the “squeezing” of the rocks (Bornemann et al., 2008).

The lack of a LPO in the studied samples (Fig. 2.11) is even reported for strongly deformed rock salt in shear zones (Schléder and Urai, 2007) and for domal salt (Desbois et al., 2010), which is interpreted as evidence for dominant pressure solution processes. However, clear evidence for pressure solution is scarce in the studied samples.

The presence of grain boundary fluids, characteristic grain boundary trends and differing subgrain patterns in adjacent grains (see arrows in Figs. 2.5g and 2.7d) suggest that the rocks have been partly recrystallized by fluid-assisted (and strain-induced) GBM. Moreover, evidence for GBM is indicated by EBSD data (see Fig. 2.10), which reveals a certain degree of lattice bending (see IPF) for only one of two adjacent halite grains. Due to the differing degree of crystal bending, the interfering grain boundary is interpreted to have migrated into the stronger deformed (orange) grain (see arrows in Fig. 2.10d). This particular case gives an example, how EBSD measurements complement evidence for active GBM, which is otherwise only derived from subgrain fabric relations (see arrows in Figs. 2.5g and 2.7d) or grain boundary outlines under the microscope (Fig. 2.7e). Different intensities of subgrain formation in adjacent grains only suggest that the subgrain-rich grain has been invaded by a less-deformed grain (e.g. Franssen, 1994; Küster et al., 2010; Leitner et al., 2011; Schléder and Urai, 2005), and the intensity and appearance of subgrains can also dependent on the crystal orientation (Trimby et al., 2000b). In some cases, grain boundaries are not straight, but show cusps and bulges with sizes directly related to the adjacent subgrains (Fig. 2.7e and f). Such characteristic bulges and cusps have been interpreted as evidence for mobile grain boundaries with small migration distances (Franssen, 1994).

Chapter 2: Microfabrics and 3D grain shape of Gorleben rock salt: constraints on deformation mechanisms and paleodifferential stress

The microfabrics together with the small grain size and the low differential stress suggest a combination of pressure solution and dislocation creep. The latter is displayed by subgrains, which result from glide and climb of dislocations and related recovery (e. g. Carter and Hansen, 1983; Drury and Urai, 1990). The heterogeneous subgrain pattern might have been developed due to the multi-stage deformation. Sub-boundary migration, as suggested by curved subgrain boundaries (Fig. 2.7a), might have contributed to form the present, heterogeneous subgrain fabrics. Moreover, smaller subgrains are related to tips of halite grains (Fig. 2.5g, upper arrow) or anhydrite impurities (Fig. 2.7c), which is taken as indication for locally elevated differential stress.

Subgrain-size based paleopiezometry yielded low differential stress, which is in line with paleopiezometric data obtained from other naturally deformed rock salt (e. g. Carter et al., 1993; Urai and Spiers, 2007; Table 2.2). For Gorleben rock salt, slightly elevated differential stress between 2.3 and 3.0 MPa is only reported for a high-strain domain (Gorleben-Bank, z3OSM) at the southern flank of the main anticline of the salt dome (Mertineit et al., 2014).

A particular EBSD mapping of characteristic subgrain assemblages (Fig. 2.10) can be used to determine the misorientation between the (sub)grains and to reconstruct the operating slip systems. The low M-index of 0.851 reflects crystal lattice deformation, compared to a hypothetical, undeformed single crystal ($M = 1$). The misorientation of the overall subgrains is relatively low ($< 5^\circ$), which has also been observed in subgrain fabrics of strongly deformed, synthetic rock salt (Pennock and Drury, 2005). However, the EBSD analysis of sample RB649UR (Fig. 2.10) reveals (sub)grain boundary segments with increased misorientation $\leq 24^\circ$ (high-angle boundary in the center of Fig. 2.10a and b). Increased misorientation is not restricted to this boundary and occurs at other sites within the subgrain fabric of the halite crystal (see arrows in Fig. 2.10b). These subordinate, isolated high-angle boundaries are linked to boundary segments with angles of $> 5^\circ$, which occur more frequently (black boundaries in Fig. 2.10b). We assume that the misorientation angles $> 10^\circ$ were caused by subgrain rotation. The development of isolated new grain boundary segments with higher misorientations in NaCl crystals has been previously reported from experimentally deformed rock salt (Drury and Pennock, 2007; Guillopé and Poirier, 1979; Pennock et al., 2002, 2005;). The jagged outline of the high-angle boundary (Fig. 2.11a and b) points at least to a subgrain-dependent development by the characteristic intersections between subgrain and high-angle boundary segments (see also Fig. 2.7b and e). As observed by Franssen (1994), the spacing of the boundary bulges depends on the subgrain size.

The grain boundary misorientation angle in the central part of the halite grain (Fig. 2.10a and b) decreases toward the top of the figure to 9° where, by definition, the grain boundary changes to a subgrain boundary. At this site, the high-angle segment is replaced by a subgrain boundary network. Thus, the grain boundary only partially dissects the halite crystal at its rim, which is further illustrated by the limited distribution of the fluid phases along the boundary (see also Fig. 2.10a). The fluid phases only exist where the misorientation is larger than 10° . Possibly, fluid has been distributed by successive

Chapter 2: Microfabrics and 3D grain shape of Gorleben rock salt: constraints on deformation mechanisms and paleodifferential stress

opening of the grain boundary during the deformation of the halite grain. The nearby anhydrite cluster (see dark section of Fig. 2.10a) could represent a potential fluid source.

The presence of subgrain boundaries does not necessarily imply that a rotational component of subgrains is included. Small misorientation angles develop just by the slip and climb of dislocations. Additionally, the migration of subgrain boundaries (Drury and Urai, 1990) can slightly increase the misorientation angles. It remains ambiguous, whether the high-angle boundary has migrated for a short distance causing increased misorientation angles.

SGR should evidently increase misorientation angles, which can be measured using EBSD. However, SGR has only been assumed to be operative in naturally deformed rock salt (e. g. Leitner et al., 2011; Závada et al., 2012) and has never been clearly proven on natural samples, while experimental data on subgrain rotation in halite are available (e. g. Franssen, 1994; Drury and Pennock, 2007, and references therein). The pole figures obtained from EBSD (Fig. 2.10c) illustrate the amount of crystal plastic deformation regarding subgrain rotation or crystal lattice bending. The characteristic scattering trends of different crystallographic directions suggest that the high-angle boundary is a result of continuously-progressive rotation, because otherwise two separate poles should be observable in the pole figure. It should be emphasized that, although we interpret the high-angle grain boundary to be related to SGR, the overall contribution of this mechanism is subordinate as proven by numerous parallel EBSD measurements.

The discovered $\langle 110 \rangle$ $\{110\}$ slip system was reconstructed from a particular subset (dashed box in Fig. 2.10b) in combination with the subgrain boundary outline and a rotation axis (Fig. 2.10d). This reconstruction assumes that the subgrain boundary is a tilt wall. This assumption is based on relatively low differential stress, as determined in our samples. At such low stress the rate-limiting process is the climb of edge dislocations, resulting in tilt walls (subgrain boundaries; Carter et al., 1993). The identified slip system for the particular subset of the EBSD map is in line with previous texture analyses (e. g. Küster et al., 2010; Miralles et al., 2001; Zulauf et al., 2011). However, further slip systems are likely to have been active, as the slip system analysis was restricted to only one subset. Furthermore, in order for homogeneous strain to occur, five independent slip systems need to be active (Von Mises criterion; Von Mises, 1928).

2.5.3. Deformation mechanisms operating in anhydrite

Anhydrite crystals along the margins of thick layers, and crystals forming the thinner anhydrite interlayers, have larger grain size compared to the majority of anhydrite grains and are characterized by weak deformation. The former occur rather isolated and are in some extent completely embedded in halite matrix. Such an isolated position eliminates grain boundary-related deformation mechanisms, such as GBM or solution precipitation creep. In contrast, the overall small grain size of anhydrite within the layers is evident and certainly caused by several mechanisms. Hence, the small grain sizes can be a result of dynamic recrystallization judged by the evidence for GBM, and can be further caused by

Chapter 2: Microfabrics and 3D grain shape of Gorleben rock salt: constraints on deformation mechanisms and paleodifferential stress

solution (re)precipitation creep. The local enrichment of insoluble and organic matter along anhydrite grain boundaries proves that solution precipitation creep was a major deformation mechanism in the studied anhydrite (Bäuerle, 1998; Bäuerle et al., 2000; Zulauf et al., 2010). Crystal plastic deformation is mostly common in larger crystals (Fig. 2.14e), which are interpreted as relicts of sedimentary and post-sedimentary processes such as cementation and gypsum-anhydrite transition (Langbein, 1987; Balzer, 1997).

The role of brittle deformation should be emphasized regarding small grain sizes, as well. Although clear microfractures within the anhydrite layers and clusters have not been observed, brittle shearing and disintegration are possible explanations for the evident grain size differences between the major layers and anhydrite crystals located at the layer rims or those composing the interlayers. Macroscopic anhydrite fragments, displaying a planar shape, point to brittle boudinage of former coherent layers (see Fig. 2.12c). No continuous layers are preserved, and although z2HS2 is named after alternating layers of anhydrite and halite (German language: *Streifen*), anhydrite layers are fragmented and dispersed (Fig. 2.12a, right).

Evidence for different deformation mechanisms are presumably related to the multi-stage deformation history of these rocks during salt diapirism. In this scenario, the anhydrite was affected by GBM recrystallization documented by irregular and bulged anhydrite grain boundaries. In a younger deformation event, where the burial depth was lower due to salt emplacement, anhydrite was affected by solution-precipitation creep, which can operate at lower differential stress. To estimate P-T conditions of different anhydrite types, detailed fluid inclusion analyses are promising methods. Evidence for multi-stage deformation in the Gorleben salt dome was also found in the Gorleben-Bank (z3OSM, Mertineit et al., 2014), a cm to dm thick anhydrite layer of the Leine unit (z3).

Strain-free, euhedral anhydrite crystals could result from new crystal growth (e.g. at the rims of the layer and in halite interlayer). Whether these crystals developed from deformation-related brine, advanced geochemical investigations are necessary (e.g. trace element distribution, Sr, S and O isotope analyses of sulphates, Sr, C and O isotope analyses of euhedral dolomite crystals).

The observed microstructures and deformation mechanisms depending on layer thickness are in line with previous observations in different geological settings (e.g. Bäuerle et al., 2000; Mertineit et al., 2012, 2014; Zulauf et al., 2010). Mechanisms such as subgrain formation, solution reprecipitation creep, macroscopic fracturing and brittle disintegration of grains point to a brittle-ductile deformation regime. The disintegration of anhydrite in combination with viscous flow of halite results in an anhydrite-halite mélange. Potential microfractures within anhydrite clusters are healed by viscous halite ingress (Zulauf et al., 2009, 2010, 2011) or by solution (re)precipitation creep of halite and/or anhydrite. Regarding the fragmentation and dissemination of anhydrite, no continuous layers remained and pathways for fluids have been sealed. Thus, fluid migration, which is often accounted for anhydrite, is an unlikely scenario for z2HS1 and z2HS2.

Chapter 2: Microfabrics and 3D grain shape of Gorleben rock salt: constraints on deformation mechanisms and paleodifferential stress

Despite of the characteristic anhydrite distribution in both formations, deformation experiments revealed that these rocks show higher creep rates compared to other salt formations (Hunsche et al., 2003). Moreover, the Gorleben z2HS rocks show very low permeability values in the range of 10^{-21} m² (Hammer et al., 2012, 2015).

2.5.4. Differences and similarities of the salt formations

Both salt formations studied show distinct similarities regarding grain shape and microfabrics. The macroscopic differences, indicated by drill cores (Fig. 2.12a) or by underground exploration, are related to the distinct layering of the z2HS2 formation compared to the stronger homogenized z2HS1 formation. Our microstructural observations are in line with the definition of the Hauptsalz body depicted as a salt-tectonic breccia (e. g. Bornemann et al., 2008) with gradual transitions leading from one formation into another. The sampling range in our study covers horizontally ca. 300 m cutting the salt anticline axis in cross cut 1 West (see Fig. 1) and the boundary z2HS1/z2HS2. For this area, the (micro)structural differences between both salt formations seem to be less distinct than those reported in the direction toward the northern flank over larger distance (Bornemann et al., 2008). Although there is a macroscopic difference in anhydrite distribution (layering) throughout both salt formations, no microstructural differences can be found. This fact suggests that the larger-scaled distribution of anhydrite had no effect on the development of the halite microstructure and, therefore, no effect on the deformation behavior of the rock salt.

2.6. Conclusions

- 1) Our microfabric data suggest that halite strain was accommodated by different deformation mechanisms, such as dislocation creep (grain boundary migration, subgrain formation) and solution-precipitation creep
- 2) The Gorleben rock salt is characterized by heterogeneous grain shape fabrics with grain shape ellipsoids of halite ranging from oblate to prolate and relatively high average axial ratios (ARs) compared to published data for other salt deposits.
- 3) Anhydrite has been deformed in the brittle-ductile regime. The microfabrics suggest that the most dominant deformation mechanism was solution precipitation creep, although some evidence for crystal plastic deformation is also documented. Brittle disintegration and disruption of anhydrite was absorbed and sealed by the viscous creep of halite ensuring the re-establishing of the rock salt sealing capacity.
Continuous anhydrite layers are not preserved and, therefore, potential migration pathways for fluids do not exist, which is an important fact for nuclear waste disposal.
- 4) The variations in anhydrite distribution had no significant impact on the development of the halite

Chapter 2: Microfabrics and 3D grain shape of Gorleben rock salt: constraints on deformation mechanisms and paleodifferential stress

microfabrics and the deformation behavior of the rock salt, since halite microstructures in both formations are similar.

2.7. Acknowledgements

The constructive comments and suggestions of the two anonymous reviewers and the editor are kindly acknowledged. J Linckens acknowledges funding by DFG (Zu 73/28-1).

2.8. References

- Balzer, D., 1997. Mikrofazies-Analyse von Ca-Sulfatgesteinen des Zechstein. Geologisches Jahrbuch Reihe D, Band D 106, Schweizerbart, Stuttgart, 99 pp.
- Barrie, C. D., Boyle, A. P., Cox, S. F., Prior, D. J., 2008. Slip system and critical resolved shear stress in pyrite: an electron backscatter diffraction (EBSD) investigation. *Mineralogical Magazine* 72 (6), 1181-1199.
- Bäuerle, G., 1998. Sedimentäre Texturen und Stylolithen am Top des Hauptanhydrits (Zechstein 3) im Salzstock Gorleben. Diploma thesis, Hannover University, Hannover, 97 pp. (unpublished).
- Bäuerle, G., Bornemann, O., Mauthe, F., Michalzik, D., 2000. Origin of stylolites in Upper Permian Zechstein anhydrite (Gorleben Salt Dome, Germany). *Journal of Sedimentary Research* 70 (3), 726-737.
- Bestmann, M., Prior, D. J., 2003. Intragranular dynamic recrystallization in naturally deformed calcite marble: diffusion accommodated grain boundary sliding as a result of subgrain rotation recrystallization. *Journal of Structural Geology* 25, 1597-1613.
- Bestmann, M., Piazzolo, S., Spiers, C. J., Prior, D. J., 2005. Microstructural evolution during initial stages of static recovery and recrystallization: new insights from in-situ heating experiments combined with electron backscatter diffraction analysis. *Journal of Structural Geology* 27, 447-457.
- Bornemann, O., Behlau, J., Fischbeck, R., Hammer, J., Jaritz, W., Keller, S., Mingerzahn, G., Schramm, M., 2008. Description of the Gorleben Site Part 3. Results of the geological surface and underground exploration of the salt formation. Bundesanst. Geowiss. Rohstoffe – BGR, Hannover, 223 pp.
- Borns, D. J., Stormont, J. C., 1989. The delineation of the disturbed rock zone surrounding excavations in salt. Rock mechanics as a guide to efficient utilization of natural resources, Proceedings of the 30th US Symposium on rock mechanics, Morgantown, 353-360.
- Bräuer, V., Eickemeier, R., Eisenburger, D., Grisseemann, C., Hesser, J., Heusermann, S., Kaiser, D., Nipp, H.-K., Nowak, T., Plischke, I., Schnier, H., Schulze, O., Sönke, J., Weber, J. R., 2011. Description of the Gorleben site. Part 4: Geotechnical exploration of the Gorleben salt dome. Bundesanst. Geowiss. Rohstoffe – BGR, Hannover, 176 pp.

Chapter 2: Microfabrics and 3D grain shape of Gorleben rock salt: constraints on deformation mechanisms and paleodifferential stress

- Burchardt, S., Koyi, H., Schmeling, H., 2011. Strain pattern within and around denser blocks sinking within Newtonian salt structures. *Journal of Structural Geology* 33, 145-153.
- Burliga, S., Czechowski, F., 2010: Anatomy of hydrocarbon-bearing zones, hydrocarbon provenance and their contribution to brittle fracturing of rock salt in the Klodawa Salt Structure (central Poland). - SMRI Spring 2010 Technical Conference, Grand Junction, USA, 9 pp.
- Carter, N. L., Hansen, F. D., 1983. Creep of rocksalt. *Tectonophysics* 92, 275-333.
- Carter, N. L., Horseman, S. T., Russell, J. E., Handin, J., 1993. Rheology of rocksalt. *Journal of Structural Geology* 15, 1257-1271.
- Chemia, Z., Schmeling, H., Koyi, H., 2009. The effect of the salt viscosity on future evolution of the Gorleben salt diapir, Germany. *Tectonophysics* 473, 446-456.
- Cristescu, N., Hunsche, U., 1998. Time effects in rock mechanics. Series: Materials, modeling and computation. John Wiley & Sons (Oichester), 342 pp.
- Davison, I., 2009. Faulting and fluid flow through salt. *Journal of the Geological Society, London*, 166, 205-216.
- Desbois, G., Závada, P., Schléder, Z., Urai, J. L., 2010. Deformation and recrystallization mechanisms in actively extruding salt fountain: Microstructural evidence for a switch in deformation mechanisms with increased availability of meteoric water and decreased grain size (Qum Kuh, central Iran). *Journal of Structural Geology* 32, 580-594.
- Desbois, G., Urai, J.L., De Bresser, J.H.P., 2012. Fluid distribution in grain boundaries of natural fine-grained rock salt deformed at low differential stress (Qom Kuh salt fountain, central Iran): Implications for rheology and transport properties. *Journal of Structural Geology* 43, 128-143.
- Drury, M. R., Urai, J. L., 1990. Deformation-related recrystallization processes. *Tectonophysics* 172, 235-253.
- Drury, M. R., Pennock, G. M., 2007. Subgrain rotation recrystallization in minerals. *Materials Science Forum* 550, 95-104.
- Flinn, D., 1962. On folding during three-dimensional progressive deformation. *The Quarterly Journal of the Geological Society of London* 118, 385-433.
- Franssen, R. C. M. W., 1993. Rheology of synthetic rock salt with emphasis on the influence of deformation history and geometry on the flow behavior. PhD thesis, Rijksuniversiteit Utrecht.
- Franssen, R. C. M. W., 1994. The rheology of synthetic rocksalt in uniaxial compression. *Tectonophysics* 233, 1-40.
- Gies, H., Herbert, H.-J., Jockwer, N., 1990. Zur Bedeutung der Wassergehalte für die Lithostratigraphie in Steinsalzhorizonten des Zechsteins. *Kali und Steinsalz* 10, 265-271.
- Guillopé, M., Poirier, J. P., 1979. Dynamic recrystallization during creep of single-crystalline halite: an experimental study. *Journal of Geophysical Research* 84, 5557-5567.
- Hammer, J., Pusch, M., Häger, A., Ostertag-Henning, C., Schlömer, S., Mingerzahn, G., Scheeder, G., Shao,

Chapter 2: Microfabrics and 3D grain shape of Gorleben rock salt: constraints on deformation mechanisms and paleodifferential stress

- H., Paul, B., Schulze, O., Zaretzki, B., Hesser, J., 2012. Untersuchungen von Kohlenwasserstoffen im Erkundungsbergwerk Gorleben. Interim report 2012, Federal Institute for Geosciences and Natural Resources, Hannover, 236 pp.
- Hammer, J., Pusch, M., Häger, A., Ostertag-Henning, C., Schlömer, S., Mingerzahn, G., Scheeder, G., Shao, H., Paul, B., Schulze, O., Zaretzki, B., Hesser, J., 2013. Untersuchungen von Kohlenwasserstoffen im Erkundungsbergwerk Gorleben. Interim report 2013, Federal Institute for Geosciences and Natural Resources, Hannover, 207 pp.
- Hammer, J., Pusch, M., Häher, C., Ostertag-Henning, C., Thiemeyer, N., Zulauf, G., 2015. Hydrocarbons in rock salt of the Gorleben salt dome – amount, origin and influence on geomechanical properties. In: Roberts, L., Mellegard, K., Hansen, F. (Eds.). *The Mechanical Behavior of Salt VIII*, Taylor & Francis Group, London, 69-75.
- Humphreys, F. J., Bate, P. S., Hurley, P. J., 2001. Orientation averaging of EBSD data. *Journal of Microscopy* 201, 50-58.
- Hunsche, U., Mingerzahn, G., Schulze, O., 1996. The influence of textural parameters and mineralogical composition on the creep behavior of rock salt. In: Ghoreychi, M., Bérest, P., Hardy Jr., P., Langer, H.-R., (eds.): *The mechanical behavior of salt: Proceedings of the 3rd Conference*. Trans Tech Publications, Clausthal Zellerfeld, 143-151.
- Hunsche, U., Schulze, O., Walter, F., Plischke, I., 2003. Projekt Gorleben 9G2138110000 - Thermomechanisches Verhalten von Salzgestein. Bundesanstalt für Geowissenschaften und Rohstoffe (BGR), Hannover.
- Hunsche, U., Hampel, A., 1999. Rock salt – the mechanical properties of the host rock material for a radioactive waste repository. *Engineering Geology* 52, 271-291.
- Jackson, M. P. A., Talbot, C. J., 1986. External shapes, strain rates and dynamics of salt structures. *Geological Society of American Bulletin* 97 (3), 305-323.
- Jaritz, W., 1980. Einige Aspekte der Entwicklungsgeschichte der Nordwestdeutschen Salzstöcke. *Zeitschrift der Deutschen Geologischen Gesellschaft* 131, 387-408.
- Jelinek, V., 1981. Characterization of the magnetic fabrics of rocks. *Tectonophysics* 79, 63-67.
- Kleber, W., 1983. Einführung in die Kristallographie, VEB (Berlin), 384pp.
- Kneuker, T., Zulauf, G., Mertineit, M., Behlau, J., Hammer, J., 2014. The impact of finite strain on deformation mechanisms of Permian Stassfurt rock salt at the Morsleben site (Germany): constraints from microfabric studies and EBSD analyses. *German Journal of Geosciences* 165 (1), 91-106.
- Küster, Y., Leiss, B., Schramm, M., 2010. Structural characteristics of the halite fabric ‚Kristallbrocken‘ from the Zechstein Basin with regard to its development. *International Journal of Earth Science* 99, 505-526.
- Langbein, R., 1987. The Zechstein Sulphates: The State of the Art. In: Peryt, T.M. (ed.): *The Zechstein*

Chapter 2: Microfabrics and 3D grain shape of Gorleben rock salt: constraints on deformation mechanisms and paleodifferential stress

- Facies in Europe. *Lecture Notes in Earth Sciences* 10, 143-188.
- Launeau, P., Robin, P.-Y. F., 2005. Determination of fabric and strain ellipsoids from measured sectional ellipses – implementation and applications. *Journal of Structural Geology* 27, 2223-2233.
- Leitner, C., Neubauer, F., 2011. Tectonic significance of structures within the salt deposits Altaussee and Berchtesgaden-Bad Dürrenberg, Northern Calcareous Alps. *Austrian Journal of Earth Sciences* 104 (2), 2-21.
- Leitner, C., Neubauer, F., Urai, J. L., Schoenherr, J., 2011. Structure and evolution of a rocksalt-mudrock-tectonite: The haselgebirge in the Northern Calcareous Alps. *Journal of Structural Geology* 33, 970-984.
- Linckens, J., Zulauf, G., Hammer, J., submitted. Experimental ductile deformation of halite to high strain by dislocation creep, without dynamic recrystallization, *Journal of Geophysical Research*.
- Mertineit, M., Behlau, J., Hammer, J., Schramm, M., Zulauf, G., 2012. Mechanical behavior of anhydrite rocks: results of field investigations, mineralogical-geochemical studies and thermomechanical experiments. In: Bérest, P., Ghoreychi, M., Hadj-Hassen, F., Tijani, M. (eds.): *Mechanical behavior of salt VII: Proceedings of the 7th Conference*. Taylor & Francis Group, London, 123-129.
- Mertineit, M., Schramm, M., Hammer, J., Zulauf, G., 2014. Deformation of anhydrite rocks (Gorleben-Bank, z3OSM) in a high-strain domain of the Gorleben salt dome, Germany. *German Journal of Geosciences* 165 (1), 49-62.
- Miralles, L., Sans, M., Galí, S., Santanach, P., 2001. 3-D rock salt fabrics in a shear zone (Súria Anticline, South-Pyrenees). *Journal of Structural Geology* 23, 675-691.
- Pape, T., Michalzik, D., Bornemann, O., 2002. Chevronkristalle im Kristallbrockensalz (Zechstein 2) des Salzstocks Gorleben – Primärgefüge salinärer Flachwassersedimentation im Zechsteinbecken. *Zeitschrift der deutschen geologischen Gesellschaft* 153 (1), 115-129.
- Passchier, C. W., Trouw, R. A. J., 2005. *Microtectonics*. Springer, Berlin, 366 pp.
- Peach, C. J., Spiers, C. J., Trimby, P. W., 2001. Effect on confining pressure on dilatation, recrystallization and flow of rocksalt at 150 °C. *Journal of Geophysical Research* 106 (B7), 13315-13328.
- Pennock, G. M., Drury, M. R., Trimby, R. W., Spiers, C. J., 2002. Misorientation distribution in hot deformed NaCl using electron backscattered diffraction. *Journal of Microscopy* 205 (3), 285-294.
- Pennock, G. M., Drury, M. R., 2005. Low-angle subgrain misorientations in deformed NaCl. *Journal of Microscopy* 217 (2), 130-137.
- Pennock, G. M., Drury, M. R., Spiers, C. J., 2005. The development of subgrain misorientations with strain in dry synthetic NaCl measured using EBSD. *Journal of Structural Geology* 27, 2159-2170.
- Pennock, G.M., Drury, M.R., Peach, C.J., Spiers, C.J., 2006. The influence of water on deformation microstructures and textures in synthetic NaCl measured using EBSD. *Journal of Structural Geology* 28, 588-601.
- Poirier, J. P., 1985. *Creep of Crystals*. Cambridge University Press, 260 pp.

Chapter 2: Microfabrics and 3D grain shape of Gorleben rock salt: constraints on deformation mechanisms and paleodifferential stress

- Popp, T., Wiedemann, M., Kansy, A., Pusch, G., 2007. Gas transport in dry rock salt – implications from laboratory investigations and field studies. In: Wallner, M., Lux, K.-H., Minkley, W., Hardy Jr., H. R. (Eds.). *The Mechanical Behavior of Salt – Understanding of THMC Processes in Salt*, Taylor & Francis Group, 17-26.
- Prior, D. J., Wheeler, J., Peruzzo, L., Spiess, R., Storey, C., 2002. Some garnet microstructures: an illustration of the potential of orientation maps and misorientation analysis in microstructural studies. *Journal of Structural Geology* 24, 999-1011.
- Pusch, M., Hammer, J., Kus, J., Klosa, D., Thiemeyer, N., Mingerzahn, G., 2014. Macro- and microscale distribution of hydrocarbons in the Staßfurt Hauptsalz of the Gorleben salt dome. *German Journal of Geosciences* 165 (1), 3-14.
- Reddy, S. M., Timms, N. E., Pantleon, W., Trimby, P., 2007. Quantitative characterization of plastic deformation of zircon and geological implications. *Contributions to Mineralogy and Petrology* 153, 625-645.
- Robin, P.-Y. F., 2002. Determination of fabric and strain ellipsoids from measured sectional ellipses -theory. *Journal of Structural Geology* 24, 531-544.
- Roedder, E., 1984. The fluids in salt. *American Mineralogist* 69, 413-439.
- Schenk, O., Urai, J. L., 2004. Microstructural evolution and grain boundary structure during static recrystallization in synthetic polycrystals of Sodium Chloride saturated brine. *Contributions to Mineralogy and Petrology* 146, 671-682.
- Schindelin, J., Arganda-Carreras, I., Frise, E., Kaynig, V., Longair, M., Petzsch, T., Preibisch, S., Rueden, C., Saalfeld, S., Schmid, B., Tenevez, J.-Y., White, D.J., Hartenstein, V., Eliceiri, K., Tomancak, P., Cardona, A., 2012. Fiji: an open-source platform for biological-image analysis. *Nature Methods* 9 (7), 676–682.
- Schléder, Z., Urai, J. L., 2005. Microstructural evolution of deformation-modified primary halite from the Middle Triassic Röt Formation at Hengelo, The Netherlands. *International Journal of Earth Sciences* 94, 941-955.
- Schléder, Z., 2006. *Deformation Mechanisms of Naturally Deformed Rocksalt*. PhD thesis, RWTH Aachen, 161 pp.
- Schléder, Z., Burliga, S., Urai, J. L., 2007. Dynamic and static recrystallization-related microstructures in halite samples from the Klodawa salt wall (central Poland) as revealed by gamma-irradiation. *Neues Jahrbuch für Mineralogie-Abhandlungen* 184, 17-28.
- Schléder, Z., Urai, J. L., 2007. Deformation and recrystallization mechanisms in mylonitic shear zones in naturally deformed extrusive Eocene-Oligocene rocksalt from Eyvanekey plateau and Garmsar hills (central Iran). *Journal of Structural Geology* 29, 241-255.
- Schléder, Z., Urai, J. L., Nollet, S., Hilgers, C., 2008. Solution-precipitation creep and fluid flow in halite: a case study of Zechstein (Z1) rocksalt from Neuhof salt mine (Germany). *International Journal*

Chapter 2: Microfabrics and 3D grain shape of Gorleben rock salt: constraints on deformation mechanisms and paleodifferential stress

- of Earth Science 97, 1045-1056.
- Schoenherr, J., Urai, J.L., Kukla, P.A., Littke, R., Schléder, Z., Larroque, J.-M., Newall, M.J., Al-Abry, N., Al-Siyabi, H.A., Rawahi, Z., 2007. Limits to the sealing capacity of rock salt: A case study of the infra-Cambrian Ara Salt from the South Oman salt basin. *AAPG Bulletin* 91 (11), 1541-1557.
- Schulze, O. 2007. Investigations on damage and healing of rock salt, in: Wallner, M., Lux, K.-H., Minkley, W., Hardy Jr., H. R. (Eds.), *The Mechanical Behavior of Salt – Understanding of THMC Processes in Salt*, Taylor & Francis Group, 33-44.
- Schulze, O., Popp, T., Kern, H. 2001. Development of damage and permeability in deforming rock salt. *Engineering Geology* 61, 163-180.
- Schutjens, P. M. T. M., Spiers, C. J., 1999. Intergranular pressure solution in NaCl: Grain-to-grain contact experiments under the optical microscope. *Oil & Gas Science and Technology – Rev. IFP* 54 (6), 729-750.
- Siemann, M. G., Ellendorff, B., 2001. The composition of gases in fluid inclusions of late Permian (Zechstein) marine evaporites in Northern Germany. *Chemical Geology* 173, 31-44.
- Skemer, P., Katayama, I., Jiang, Z., Karato, S-i., 2005. The misorientation index: Development of a new method for calculating the strength of lattice-preferred orientation. *Tectonophysics* 411, 157-167.
- Spiers, C. J., de Meer, S., Niemeijer, A., Zhang, X., 2004. Kinetics of rock deformation by pressure solution and the role of thin aqueous films. In: Nakashima, S., Spiers, C. J., Mercury, L., Fenter, P. A., Hochella, M. F., (Eds.). *Physicochemistry of Water in Geological and Biological Systems – Structures and Properties of Thin Aqueous Films*. Universal Academy Press, Tokyo, 129-158.
- Talbot, C. J., 1981. Sliding and other deformation mechanisms in glacier of salt, S Iran. In: McClay, K. R., Prince, N. J. (Eds.), *Thrust and Nappe Tectonics*. Geological Society, London, Special Publications 9, pp. 173-183.
- Talbot, C. J., Jackson, M. P. A., 1987. Internal kinematics of salt diapirs. *AAPG Bulletin* 71 (9), 1086-1093.
- Talbot, C. J., Medvedev, S., Alavi, M., Shahrivar, H., Heidari, E., 2000. Salt extrusion rates at Kuh-e-Jahani, Iran: June 1994 to November 1997. *Geological Society Special Publication*, London, 174, 93-110.
- Talbot, C. J., Rogers, E. A., 1980. Seasonal movements in a salt glacier in Iran. *Science* 208, 195-197.
- Ter Heege, J. H., De Bresser, J. H. P., Spiers, C. J., 2005a. Rheological behavior of synthetic rock salt: the interplay between water, dynamic recrystallization and deformation mechanisms. *Journal of Structural Geology* 27, 948-963.
- Ter Heege, J. H., De Bresser, J. H. P., Spiers, C. J., 2005b. Dynamic recrystallization of wet synthetic polycrystalline halite: dependence of grain size distribution on flow stress, temperature and strain. *Tectonophysics* 396, 35-57.
- Thiemeyer, N., Pusch, M., Hammer, J., Zulauf, G., 2014. Quantification and 3D visualisation of pore space in Gorleben rock salt: constraints from CT imaging and microfabrics. *German Journal of Geosciences* 165 (1), 15-25.

Chapter 2: Microfabrics and 3D grain shape of Gorleben rock salt: constraints on deformation mechanisms and paleodifferential stress

- Thiemeyer, N., Habersetzer, J., Peinl, M., Zulauf, G., Hammer, J., 2015. The application of high resolution X-ray computed tomography on naturally deformed rock salt: Multi-scale investigations of the structural inventory. *Journal of Structural Geology* 77, 92-106.
- Trimby, P. W., Drury, M. R., Spiers, C. J., 2000a. Misorientations across etched boundaries in deformed rocksalt: a study using electron backscatter diffraction. *Journal of Structural Geology* 22, 81-89.
- Trimby, P. W., Drury, M. R., Spiers, C. J., 2000b. Recognising the crystallographic signature of recrystallisation processes in deformed rocks: a study of experimentally deformed rocksalt. *Journal of Structural Geology* 22, 1609-1620.
- Twiss, R. J., 1977. Theory and applicability of a recrystallized grain size paleopiezometer. *Pure and applied Geophysics* 115, 225-244.
- Urai, J. L., Spiers, C. J., Zwart, H. J., Lister, G. S., 1986a. Weakening of rock salt by water during long-term creep. *Nature* 324, 554-557.
- Urai, J. L., Means, W. D., Lister, G. S., 1986b. Dynamic recrystallization of minerals. In: Hobbs, B. E., Heard, H. C. (Eds.). *Mineral and Rock Deformation: Laboratory Studies – The Paterson Volume*, American Geophysical Union Geophysical Monograph 36, 161-199.
- Urai, J. L., Spiers, C. J., Peach, C. J., Franssen, R. C. M. W., Liezenberg, J. L., 1987. Deformation mechanisms operating in naturally deformed halite rocks as deduced from microstructural investigations. *Geologie en Mijnbouw* 66, 165-176.
- Urai, J. L., Spiers, C. J., 2007. The effect of grain boundary water on deformation mechanisms and rheology of rocksalt during long-term deformation. In: Wallner, M., Lux, K.-H., Minkley, W., Hardy Jr., H. R. (Eds.). *The Mechanical Behavior of Salt – Understanding of THMC Processes in Salt*, Taylor & Francis Group, 149-158.
- Von Mises, R., 1928. Mechanik der plastischen Formänderung von Kristallen. *Zeitschrift für angewandte Mathematik und Mechanik* 8 (3), 161-182.
- Wagner III, B. H., Jackson, M. P. A., 2011. Viscous flow during salt welding. *Tectonophysics* 510, 309-326.
- White, S. H., 1977. Geological significance of recovery and recrystallization processes in quartz. *Tectonophysics* 39, 143-170.
- Závada, P., Desbois, G., Schwedt, A., Lexa, O., Urai, J. L., 2012. Extreme ductile deformation of fine-grained salt by coupled solution-precipitation creep and microcracking: Microstructural evidence from perennial Zechstein sequence (neuhof salt mine, Germany). *Journal of Structural Geology* 37, 89-104.
- Zirngast, M., 1991. Die Entwicklungsgeschichte des Salzstocks Gorleben – Ergebnis einer strukturgeologischen Bearbeitung. *Geologisches Jahrbuch* 132, 3-31.
- Zirngast, M., 1996. The development of the Gorleben salt dome (northwest Germany) based on quantitative analysis of peripheral sinks. In: Alsop, G. I., Blundell, D., Davison, I. (Eds.). *Salt Tectonics*, Special Publication of the Geological Society of London 100, 203-226.

Chapter 2: Microfabrics and 3D grain shape of Gorleben rock salt: constraints on deformation mechanisms and paleodifferential stress

- Zhang, X., Peach, C.J., Grupa, J., Spiers, C.J., 2007. Stress relaxation experiments on compacted granular salt: effects of water. In: Wallner, M., Lux, K.-H., Minkley, W., Hardy Jr., H.R. (Eds.). *The Mechanical Behavior of Salt – Understanding of THMC Processes in Salt*, Taylor & Francis Group, 159-166.
- Zulauf, G., Zulauf, J., Bornemann, O., Kihm, N., Peinl, M., Zanella, F., 2009. Experimental deformation of a single-layer anhydrite in halite matrix under bulk constriction. Part 1: Geometric and kinematic aspects. *Journal of Structural Geology* 31, 460-474.
- Zulauf, G., Zulauf, J., Bornemann, O., Brenker, F., Höfer, H., Peinl, M., Woodland, A., 2010. Experimental deformation of a single-layer anhydrite in halite matrix under bulk constriction. Part 2: Deformation mechanisms and the role of fluids. *Journal of Structural Geology* 32, 264-277.
- Zulauf, J., Zulauf, G., Hammer, J., Zanella, F., 2011. Tablet boudinage of an anhydrite layer in rock-salt matrix: Results from thermomechanical experiments. *Journal of Structural Geology* 33, 1801-1815.

Chapter 3

Deformation of thin layered anhydrite rocks within the Gorleben salt dome, Germany

M. Mertineit, J. Hammer, M. Schramm & T. Kneuker

Federal Institute for Geosciences and Natural Resources (BGR), Hannover, Germany

N. Thiemeyer* & G. Zulauf

Institute of Geosciences, Goethe University Frankfurt, Frankfurt/Main, Germany

Abstract

Strongly deformed halite and anhydrite rocks of the Gorleben-Bank (z3OSM) were investigated in a wide range of outcrops within the Gorleben exploration mine. The deformation behavior of the Gorleben-Bank varies significantly because of its layered composition. Individual zones show variations in deformation style depending on the mineralogical composition, internal structure, thickness and position within the salt dome. A special feature of the Gorleben-Bank is the clayey zone III, that was acting as a shear horizon, de-coupling the foot and the hanging walls of the Gorleben-Bank. Geometrical analyses of extension fractures show a weak correlation of fracture spacing and layer thickness. However, a characteristic aspect ratio does not exist. Mineralogical-geochemical analyses rock salt situated adjacent to the Gorleben-Bank reveal the sedimentary signature and show only local influence of brines. Analyses of the deformation behavior of bedded anhydrite rocks are important for several technical and economic purposes, as anhydrite rocks occur worldwide in salt deposits.

In: Roberts, L., Mellegard, K., Hansen, F. (Eds.). The Mechanical Behavior of Salt VIII, Taylor & Francis Group, London, 99-107. DOI: [10.1201/b18393-14](https://doi.org/10.1201/b18393-14).

*N. Thiemeyer conducted the EBSD measurements regarding crystal plastic strain accommodation in anhydrite and halite.

Chapter 3: Deformation of thin layered anhydrite rocks within the Gorleben salt dome, Germany

3.1. Introduction

Investigations of salt rocks are important for several purposes, e.g. cavern industries, salt mining or the construction of a repository for highly active, heat generating radioactive waste. Anhydrite rocks within a salt repository result from gypsum precipitation and later transition to anhydrite and are a common phenomenon worldwide (Hudec & Jackson, 2007). Due to different deformation behavior compared to rock salt, for longterm safety considerations the deformation of anhydrite layers during salt emplacement and their capacity to store and transmit brines in fissures and faults should receive attention (e.g. Hammer et al., 2014). Furthermore, the analyses of relatively competent layers inside salt bodies enable the reconstruction of the development of salt emplacement (Hudec & Jackson, 2007). In Germany, upper Permian salt rocks of the Gorleben salt dome were investigated in great detail, especially of the Staßfurt (z2) and the Leine unit (z3). The composition, in particular that of the z3 unit, is characterized by stratigraphically and locally varying amounts of anhydrite layers, the latter with thicknesses of a few mm to several 10 m.

The rheology and deformation behavior of anhydrite or halite-anhydrite composites have been investigated in different studies. In experiments with polycrystalline or natural anhydrite samples, evidence for crystal plastic flow was observed at high temperature and confining pressure (e.g. Müller et al., 1981, Dell'Angelo & Olgaard, 1995). Brittle-ductile behavior of anhydrite was observed by other workers under different deformation conditions using different experimental setups (e.g. Peach, 1993, Heidelberg et al., 2001, Liang et al., 2007, Zulauf et al., 2009, 2010, 2011, 2012, Hangx et al., 2011). Textural analyses of anhydrite-rich layers, deformed in a siliciclastic matrix, were performed by e.g. De Paola et al. (2008) and Hildyard et al. (2009). So far, only few microfabric studies of naturally deformed anhydrite (deformed in an evaporitic matrix) were carried out (e.g. Dix & Jackson, 1982, Schindl-Neumayer, 1984, Mainprice et al., 1993, Bäuerle, 2000, Mertineit et al., 2012, 2014).

Fabric analyses of the Gorleben-Bank (z3OSM) offer the opportunity to reconstruct the deformation history as well as the quantification of finite strain and the influence of intrasalinare brines in the Gorleben salt dome.

3.2. Geological setup, sampling and methods

The Gorleben-Bank (z3OSM) is an anhydrite layer and forming the middle part of the Orangesalz (z3OS), characterized by significant variations in thickness from < 10 cm up to 66 cm (Kühnlenz et al., 2014). The Gorleben-Bank has been subdivided into 7 zones (Fig. 3.1, Bäuerle, 2000, modified by Kühnlenz et al., 2014), which consist mainly of halite/carnallite (zones I & IV), anhydrite (zones II, V & VI) and halite/anhydrite composites (zone VII). Within zones I, V and VI, halite clasts occur, which are frequently elongated. A distinctive feature of the Gorleben-Bank is zone III, which consists of clay, organic matter,

Chapter 3: Deformation of thin layered anhydrite rocks within the Gorleben salt dome, Germany

siliceous components and more or less fine grained anhydrite and halite. The mechanically weak zone III is frequently sheared. Open veins caused by bedding-parallel fracturing of zone III were mineralized by carnallite and/or halite (= zone IV).

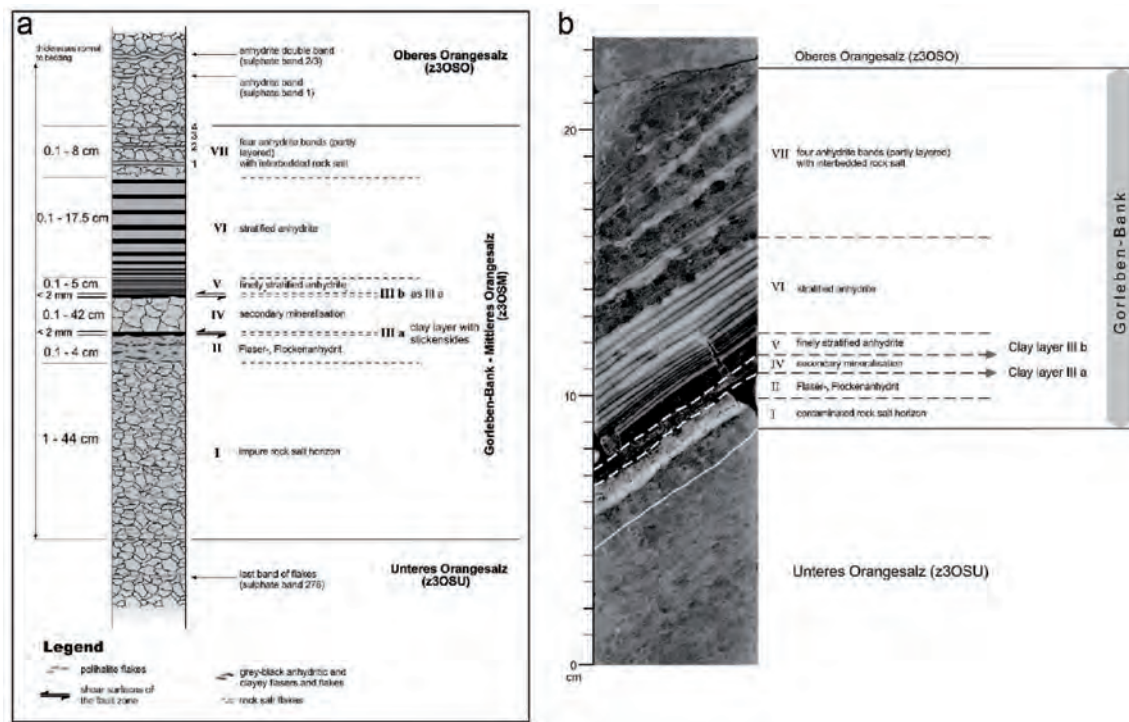


Fig. 3.1: Lithostratigraphic and petrographic composition of the Gorleben-Bank (z3OSM). a) Schematic geological profile of the Gorleben-Bank and surrounding Orangesalz. b) Example of a typical Gorleben-Bank exposure containing zones I – VII. Exploration borehole 02YEA04RB025. From Kühnlenz et al., 2014.

Most Gorleben-Bank outcrops are located within the infrastructure area of the Gorleben exploration mine. The outcrops at the 820 m and 840 m level of the exploration mine are differently affected by a domal structure within the Gorleben salt dome (Kühnlenz et al., in prep.). Outcrops at the 880 m and 930 m levels were not influenced by this domal structure. For fabric and structural analyses, several outcrops situated at different positions with respect to the internal structure of the salt dome were considered. The investigation focus on the layer thickness and the width of fractures and boudin necks. Powder and core samples of anhydrite, boudin neck infill and surrounding rock salt were collected for mineralogical-geochemical and microfabric analyses. Microfabrics of halite were analyzed using light microscopy on thin and thick sections, and electron backscatter diffraction (EBSD) using a JEOL JSM-6490 SEM (Frankfurt University) with an EBSD detector by Oxford Instruments. Analyses were carried out at an accelerating voltage of 20 kV, a current of 26 μ A and a working distance of 20 mm. Kikuchi patterns were indexed automatically using the Channel 5 software by HKL Technology. The angular

Chapter 3: Deformation of thin layered anhydrite rocks within the Gorleben salt dome, Germany

resolution of the obtained data is 1°.

The powder samples were analyzed geochemically using Inductively Coupled Plasma Optical Emission Spectroscopy (ICP-OES; Spectro CIROS ICP-OES) for the cations Na, K, Mg, Ca and Sr, and the anions Cl, SO₄ and Br (for analytical details and limits of detection, see Küster et al., 2009, Mertineit et al., 2014). The quantitative mineralogical composition and the bromide distribution of the sampled rocks were calculated using the software ZECHMIN-7 (Schramm & Bornemann, 2004, Bornemann et al., 2008). The content of Sr in anhydrite and Br in halite, respectively, depends on both, the sedimentary and metamorphic conditions. Thus, content and variations of the trace elements can be used for genetic interpretations of the rocks (e.g. Mattenklott, 1994, Bäuerle, 2000).

3.3. Results

Due to the bedding of the Gorleben-Bank and the different composition of individual beds, the deformation behavior of the Gorleben-Bank is quite complex. Individual beds show different behavior, dependent on thickness, composition and internal structure.

3.3.1. Deformation behavior of individual zones

Zone I (thin anhydrite layer with impure, coarse grained halite) shows differences in the thickness (mm to cm) and is only disclosed in ca. 1/3 of the outcrops. Within the layer, elongated halite crystals with a size of few cm are noticeable. EBSD investigations of these clasts show that they consist of single crystals with a lattice bending of ca. 2°. The bromide content of these single crystals varies between 175 and 200 µg/g halite, which is in line with published data. The surrounding rock salt, on the other hand, shows Br values of 100 - 205 µg/g halite. Except from halite, in zone I polyhalite < 2.8 wt.-%, kieserite < 13.1 wt.-% and carnallite < 3.0 wt.-% were found.

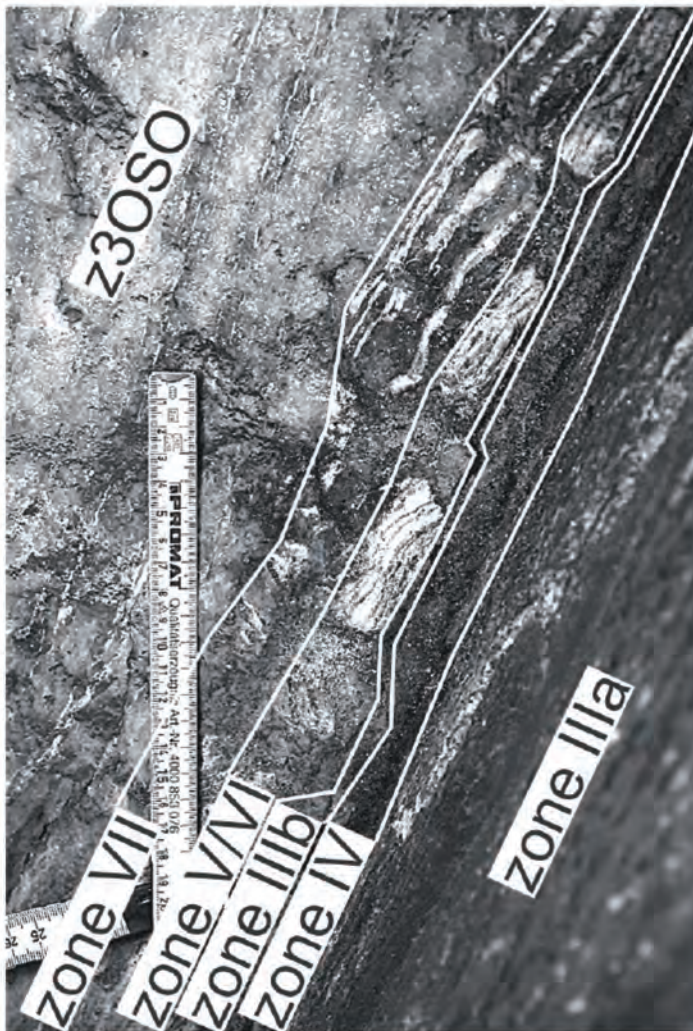
The deformation behavior of zone II depends on the internal structures. Usually zone II has a thickness of 0.1 – 1 cm. In some cases, syndimentary developed slump folds cause a thickening of the layer up to ca. 4 cm (Hammer et al., 2014). In this case, the layer does not seem to be further deformed and behaves rigidly. The microstructures in zone II are variable. Bäuerle (2000) distinguished between fine grained and well sorted anhydrite, and acicular to irregular, coarser grained anhydrite, which is strongly affected by the development of secondary phases like polyhalite, boracites and enrichment of organic matter, which is an evidence for involved K-Mg rich brines.

Zone III plays an important role for the deformation of the Gorleben-Bank. Due to its composition (clay and phyllosilicates, organic matter, fine grained anhydrite and halite), zone III acts as a shear zone, which decouples the foot and the hanging walls of the Gorleben-Bank. Polyphase deformation is documented by different orientations of slickenside. In the clayey parts of zone III, halite filled tension gashes occur. Zone IV consists of halite and/or carnallite and developed during deformation related opening and

Chapter 3: Deformation of thin layered anhydrite rocks within the Gorleben salt dome, Germany

filling of fractures. Zone IV is directly related to movement along zone III and precipitated from a brine, which migrated bedding-parallel to zone III. In this case, zone III is subdivided into zones IIIa and IIIb. Zone IV is basically disclosed as bedding-parallel filling of zone III, but it can also skip into hanging or foot walls of the Gorleben-Bank. Polyphase development is documented by segmented composition of zone IV (halite and carnallite, often separated by thin clayey or sulphate layers).

Zones V and VI are the thickest anhydrite beds within the Gorleben-Bank. Zones V and VI show a similar deformation behavior and can be regarded as one unit in this aspect. Both zones are often strongly deformed by folding or boudinage. It is remarkable, that these zones often show different deformation structures compared to the foot beds beneath zone III, which is caused by the particular mechanical



weakness of this zone. Within the beds, elongated halite clasts with the long axis oriented parallel to the bedding planes are noticeable. Microstructural investigations of these clasts suggest that they consist of both single crystals and polycrystalline aggregates, respectively. At the grain boundaries of the polycrystalline clasts, small anhydrite crystals and fluid inclusions occur. The bromide content of the polycrystalline clasts shows a wide range from 120 – 200 $\mu\text{g/g}$ halite, suggesting a different origin of the aggregates.

Zones V and VI show distinct variations in thickness ranging from mm to several dm. In rare cases, slump folds occur. Microstructural investigations show a strong dependency of layer thickness and microfabrics (Mertineit et al., 2014).

Fig. 3.2: Decoupling and deformation of zones V-VII: view along zone IIIa, which is separated by the development of zone IV in zone IIIa and IIIb. Zones V – VII are boudinaged.

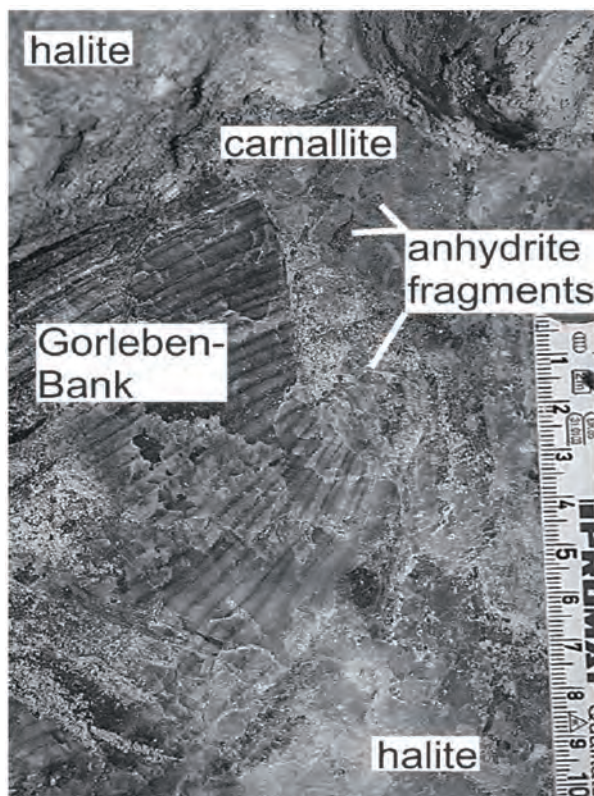
Chapter 3: Deformation of thin layered anhydrite rocks within the Gorleben salt dome, Germany

Thin layers consist of fine grained anhydrite crystals with high amounts of organic matter, indicating solution-precipitation creep as the main deformation mechanism. In thick layers, diagenetic structures like stylolite or large, fan shaped anhydrite crystals (as a result of the gypsum – anhydrite transition) are preserved. Grain boundaries are often lobate and without impurities, indicating grain boundary migration and bulging recrystallization. Single crystals show high amounts of twins with tapering edges, suggesting deformation twinning.

Zone VII consists of four thin anhydrite layers, separated by thin halite beds. Boudinage of this zone only occurs in areas of high finite strain, high total thickness of the Gorleben-Bank and comparatively thick anhydrite layers within zone VII (Fig. 3.2). In most other cases, this zone follows the general shape of the Gorleben-Bank and seems to compensate material movement of zones V & VI by viscous behavior.

3.3.2. General observations

In general, the Gorleben-Bank shows various deformation structures, which are dependent on the position within the salt dome (finite strain, stress regime), composition, internal structure and thickness of the layer. There is evidence for polyphase deformation such as crossing fractures, fractures



crosscutting folds, or reverse movement of material, documented by first folded, then boudinaged anhydrite layers.

Boudinage inside the Gorleben-Bank is supported by the mechanical weakness of zone III. Several outcrops show a complete separation of single Gorleben-Bank fragments, whereas asymmetric boudins developed (Fig. 3.3). The upper zones are particularly affected by shearing. The necks between these blocks are filled with halite and/or carnallite, and often small fragments of anhydrite of zones V/VI. In some cases, zone III acts as a weakening zone and decouples the layers above and beneath. In these cases, basically zones V & VI are separated. Zone VII, a composite of thin anhydrite lines and halite, behaves differently.

Fig. 3.3: Asymmetric boudin of Gorleben-Bank. Boudin neck is filled with carnallite. Note small fragments of anhydrite in boudin neck.

Chapter 3: Deformation of thin layered anhydrite rocks within the Gorleben salt dome, Germany

In some cases, the zone is also separated, but in most cases strain seems to be accommodated by viscous behavior.

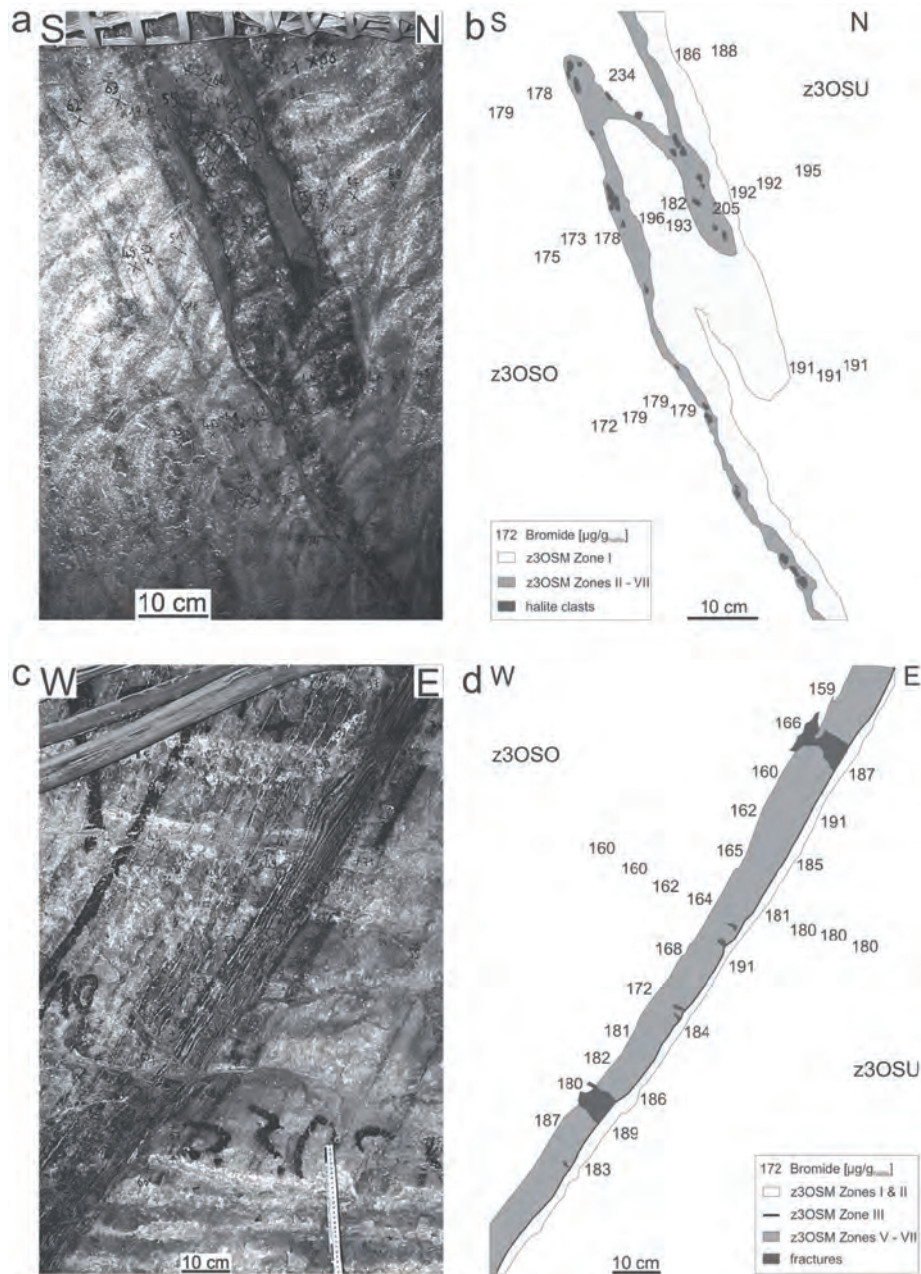


Fig. 3.4: Different outcrops of the Gorleben-Bank in the Gorleben exploration mine. a) Folded and overturned Gorleben-Bank, 840 m level. Note thickened zone I. b) Schematic image of a), with bromide content. All Br data $\pm < 3\%$, except of high value in fold hinge $\pm 7.3\%$. c) Fractures in Gorleben-Bank, 930 m level. d) Schematic image of c), with bromide content. All Br data $\pm < 3\%$. Note fracture development from zone III in direction of hanging zones. Zone IV did not form.

Chapter 3: Deformation of thin layered anhydrite rocks within the Gorleben salt dome, Germany

Folds are tight to isoclinal with distinct thickening of the hinges (Figs 3.4a, b). Usually, disharmonic bending shear folds developed (see also Bornemann et al., 2008). Tension gashes along the crest of the folds, basically observed in zones V and VI, are filled with halite. Pressure solution took place in the central part of the crest and caused the enrichment of insoluble phases.

Fracturing represents the youngest deformation event and affected the Gorleben-Bank independent of the layer thickness. The orientation of fractures is different and perpendicular or oblique to bedding. Fractures can penetrate the whole rock sequence, or only a few zones. Fractures are filled with halite and/or carnallite. In some cases, both types are disclosed in one outcrop and their crosscutting relationship can be used for temporal reconstructions.

During progressive deformation, fractures can enlarge and separate single fragments of the Gorleben-Bank. In this case, the boudin neck infill consists of halite and/or carnallite, which precipitated from deformation related brines. Almost no host rocks and Gorleben-Bank fragments are detectable in the

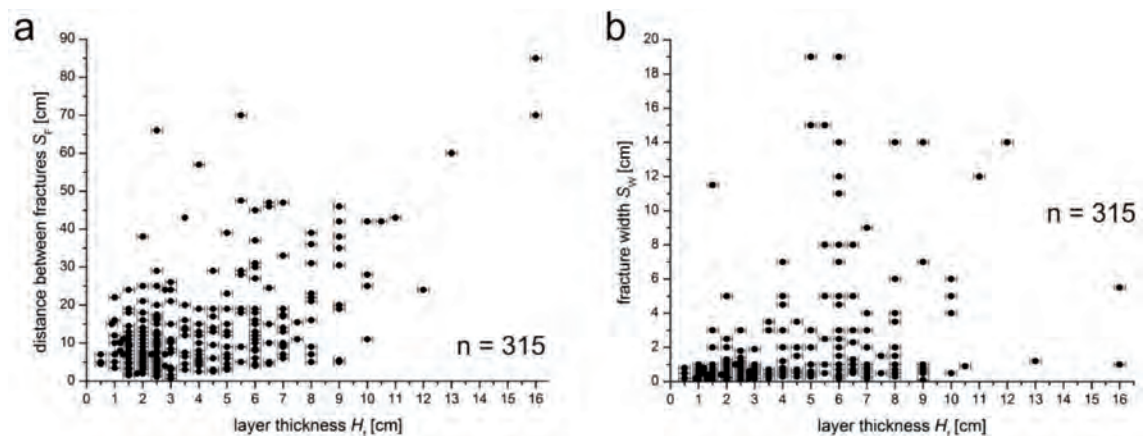


Fig. 3.5: Geometrical analyses of extension fractures oriented perpendicular to bedding in 17 Gorleben-Bank outcrops. a) Distance between fractures S_F vs. layer thickness H_f . n = number of analyzed fractures. b) Fracture width S_W vs. layer thickness H_f . n = number of analyzed fractures.

boudin neck (Figs. 3.4c, d).

Geometrical analyses of 17 Gorleben-Bank outcrops show that the width of fractures S_W is usually few mm to max. 2 cm, with a total maximum of 19 cm (Fig. 3.5b). The distance between single fractures, S_F , depends weakly on the layer thickness (Fig. 3.5a; correlation coefficient $R = 0.541$), and is basically < 20 cm, but can reach 90 cm.

Mineralogical-geochemical analyses of surrounding rock salt show a bromide content of ca. 180 – 190 $\mu\text{g/g}$ halite in the lower, and ca. 160 – 180 $\mu\text{g/g}$ halite in the upper Orangesalz, which are common values. An exception is the lateral increase of bromide content in z3OSO as shown in Figure 3.4d, which is probably caused by an infiltration of z3OSO by metamorphic brine.

Chapter 3: Deformation of thin layered anhydrite rocks within the Gorleben salt dome, Germany

3.3.3. Strain analyses

Geometrical analyses of changes in length of folds, boudins and fractures offer the opportunity to estimate finite strain on outcrop scale. Unfortunately, this method gives only a rough estimation. Furthermore, usually only one direction of movement is observable due to outcrop conditions. However, for exemplary, few outcrops were measured by comparing present and primary lengths of the layer. In case of fracturing and boudinage (Fig. 3.4a, b), extension is approximately +11% perpendicular to bedding. In case of folding (Fig. 3.4c, d), shortening is approximately -21% along bedding.

3.4. Discussion

The origin and deformation history of the halitic part of zone I is not well understood. Bäuerle (2000) suggests a development that is based on recycling processes of pore fluids and first halite precipitates in an early stage of diagenesis and compaction, which explains the strong variations in the bromide content. The presence of salinar brines is supported by carnallite and kieserite, which precipitated in a late stage of evaporation. But these conditions were not fulfilled, as is shown by the bromide content, which is too low for the formation of kieserite and carnallite (e.g. Bornemann et al., 2008). Furthermore, zone I (if developed) was partly affected by the main deformation events judging its pre-tectonic origin. The low amount of subgrains points to very low crystalplastic strain. The lack of a crystallographic preferred orientation (CPO) points to solution-precipitation creep as the main deformation mechanism. The low content of substructures and lack of a preferred orientation suggest an influence of metamorphic brines even during younger deformation events.

The origin and genesis of halite clasts (Figs. 3.4a, b) remains unclear as well. The clasts were observed in halitic parts of zone I, and in anhydrite of zones V/VI. The bromide content of single crystal clasts in zone I is approximately equivalent to that of the surrounding halite, only few samples show differences. In this case, clasts have values of ca. 175 – 200 µgBr/g halite (which is common for halite in zone I), whereas Br content of surrounding rock salt of zone I decreases to ~100 µg/g halite. A possible explanation is, that halite clasts represent an older, boudinaged halite layer, which behaved more rigidly than the surrounding, finer grained halite. A similar explanation is currently given for the formation of the “Kristallbrockensalz” in salt domes in northern Germany (e.g. Bornemann et al., 2008; Küster et al., 2010). To prove this assumption, further microstructural investigations on a broad set of samples are necessary.

For clasts in Zones V/VI, a similar explanation is assumed. Possibly, a thin halite layer developed within the anhydrite zones, which has been mobilized during diagenesis or later deformation. But also in this case, further investigations are recommended.

The geometrical data of extension fractures shows a weak relationship between the distance between single fractures and the layer thickness. But in this evaluation, all outcrops were considered,

Chapter 3: Deformation of thin layered anhydrite rocks within the Gorleben salt dome, Germany

independent of their position within the salt dome, and probably fractures of different deformation events were considered. A stricter differentiation between different environments could improve the results and prove, whether this relation is valid or not. Furthermore, more detailed investigations will be performed to apply the concept of fracture saturation (e.g. Bai & Pollard, 1999, 2000).

The fracture width, on the other hand, does not show any relationship between width and layer thickness, but width seems to depend on the finite strain.

First results of geometrical finite strain estimations show relatively high amounts of strain. These analyses will be expanded with respect to polyphase deformation and position within the salt dome. Furthermore, volumetric strain of anhydrite rocks will be determined using analyses of immobile elements (e.g. Grant, 1986).

Mineralogical-geochemical analyses of z3OS represent dominantly the sedimentary signature and are in line with previous geochemical analyses of z3OS (e.g. Bäuerle, 2000, Bornemann et al., 2008, Mertineit et al., 2014). Local variations (Fig. 3.4d) can be explained by an infiltration of brines into the surrounding halite, where brine might have been migrated at the anhydrite-halite interface. To estimate the origin of these brines, advanced geochemical analyses were successfully applied to characterize Gorleben-Bank related fluids (Kühnlenz et al., in prep.).

The different deformation behavior of the Gorleben-Bank zones is controlled by the total layer thickness, the thickness of each zone, the internal structure of each zone, the composition, and the position in the salt dome (stress regime, finite strain, fluid activity). Due to these numerous variables, it is complex to balance and estimate the importance and influence of each parameter.

However, recent microstructural investigations on strongly deformed anhydrite rocks (e.g. Mertineit et al., 2012, 2014; Schorn et al., 2013) found a distinct relationship between the inventory of microstructures and layer thickness. In thin anhydrite layers, almost the entire rock is deformed by solution-precipitation processes. In thick layers, evidence for diagenetic processes is still preserved, and strain is accommodated locally by crystal plastic deformation of anhydrite (undulose extinction, subgrain formation, grain boundary migration recrystallization, bulging recrystallization, formation of deformation twins).

Based on this knowledge, single zones of the Gorleben-Bank could be investigated. Microstructural and microgeochemical analyses could help to improve the understanding of different deformation behavior. There are several indications for polyphase deformation, e.g. crossing generations of fractures, fractures crosscutting folds, or reverse movement of material, documented by first folded, then boudinaged anhydrite layers. To estimate the history and phases of deformation, age dating of fracture infill is a promising method. Different age dating systems could be applied, e.g. $^{40}\text{Ar}/^{39}\text{Ar}$ (e.g. Leitner et al., 2013) or K-Ar in polyhalite and carnallite (Huff & Wampler, 1990), respectively, depending on the mineralogical composition.

Predictions about the deformation behavior of thick layered anhydrite, e.g. the Hauptanhydrit (z3HA),

Chapter 3: Deformation of thin layered anhydrite rocks within the Gorleben salt dome, Germany

will be difficult and probably only valid for local conditions. The Hauptanhydrit in the Gorleben salt dome reaches a thickness of 80 m and can be subdivided in 13 zones, which are different in composition and fabrics (Bornemann et al., 2008). Investigations on the Gorleben-Bank, a layer which is limited in dimensions, demonstrate the variety of deformation structures in layered anhydrite rocks.

3.5. Conclusions

- The deformation behavior was analyzed in a wide range of outcrops within the Gorleben exploration mine. The deformation behavior of halite and anhydrite rocks of the Gorleben-Bank depends on many parameters, such as composition of the rocks, internal structure, position within the salt dome and layer thickness.
- Each zone of the Gorleben-Bank behaves differently and has to be considered individually.
- A special feature of the Gorleben-Bank is the sheared, clayey zone III, which decouples the foot and the hanging walls of the Gorleben-Bank.
- Analyses of extension fractures show a weak dependence on space between single fractures and layer thickness. An aspect ratio between fracture width and layer thickness, on the other hand, could not be observed.
- Further investigations of single zones will focus on microfabrics and detailed mineralogical-geochemical analyses.
- Predictions about the deformation behavior of thick anhydrite layers (such as the Hauptanhydrit), based on investigations on thin layers, are only valid on a local scale and cannot be generalized.

3.6. Acknowledgements

Thanks to two anonymous referees for their helpful comments. We use the possibility to thank many kind colleagues for the assistance in Gorleben during sampling: The help of L. Fleckenstein, W. Grewe, S. Heydecke, F. Kohnert, J. Kutowski, M. Otto, M. Saßnowski, M. Wietzki, (DBE), C. Dresbach & R. Götze (BGR) is kindly acknowledged. We thank M. Bladt (University Frankfurt), M. Gern & T. Faust (BGR) for the help with the sample preparation. The help of L. Ptock with the photography is acknowledged.

3.7. References

- Bai, T. & Pollard, D.D. 1999. Spacing of fractures in a multilayer at fracture saturation. *International Journal of Fracture* 100, L23-L28.
- Bai, T. & Pollard, D.D. 2000. Fracture spacing in layered rocks: a new explanation based on the stress transition. *J. Struct. Geol.* 22, 43-57.

Chapter 3: Deformation of thin layered anhydrite rocks within the Gorleben salt dome, Germany

- Bäuerle, G. 2000. Geochemisch-mineralogische Untersuchungen zur Genese, Lösungs- und Gasführung der Gorleben-Bank (Zechstein 3) des Salzstocks Gorleben. Dissertation, Technische Universität Clausthal, 147 pp. (unpublished).
- Bornemann, O., Behlau, J., Fischbeck, R., Hammer, J., Jaritz, W., Keller, S., Mingerzahn, G. & Schramm, M. 2008. Description of the Gorleben Site Part 3: Results of the geological surface and underground exploration of the salt formation. *Geologisches Jahrbuch, Reihe C, Heft 73*, E. Schweizerbart'sche Verlagsbuchhandlung, Stuttgart.
- Dell'Angelo, L.N. & Olgaard, D.L. 1995. Experimental deformation of fine-grained anhydrite: evidence for dislocation and diffusion creep. *J. Geophys. Res.* 100 (B8), 15425-15440.
- De Paola, N., Collettini, C., Faulkner, D.R. & Trippetta, F. 2008. Fault zone architecture and deformation processes within evaporitic rocks in the upper crust. *Tectonics* 27, TC4017, 21 pp., doi: 10.1029/2007TC002230.
- Dix, O.R. & Jackson, M.P.A. 1982. Lithology, microstructures, fluid inclusions, and geochemistry of rock salt and of the caprock contact in Oakwood dome, East Texas: Significance for nuclear waste storage. Bureau of Economic Geology, The University of Texas at Austin, Report of Investigations No. 120, 59 pp..
- Grant, J.A. 1986. The Isocon Diagram – A Simple Solution to Gresens' Equation for Metasomatic Alteration. *Economic Geology* 81, 1976-1982.
- Hammer, J., Mertineit, M., Behlau, J., Mingerzahn, G., Kühnlenz, T., Schramm, M., Zulauf, G. & Zulauf, J. 2014. Deformation and geometry of anhydrite rocks in domal salt structures – results of field studies, mineralogical analyses and thermomechanical experiments. In: *Natural Analogues for Safety Cases of Repositories in Rock Salt, Proceedings "Salt Club" Workshop, Braunschweig, 5-7 September 2012*, NEA/RWM/R(2013)10, 147-175, NEA/OECD.
- Hangx, S.J.T., Spiers, C.J. & Peach, C.J. 2011. The mechanical behavior of anhydrite and the effect of deformation on permeability development - implications for caprock integrity during geological storage of CO₂. *Energy Procedia* 4, 5358-5363.
- Heidelbach, F., Stretton, I.C. & Kunze, K. 2001. Texture development of polycrystalline anhydrite experimentally deformed in torsion. *Int. J. Earth Sciences* 90, 118-126.
- Hildyard, R.C., Prior, D.J., Faulkner, D.R. & Mariani, Elisabetta 2009. Microstructural analysis of anhydrite rocks from the Triassic Evaporites, Umbria-Marche Apennines, Central Italy: An insight into deformation mechanisms and possible slip systems. *J. Struct. Geol.* 31, 92-103.
- Hudec, M.R. & Jackson, M.P.A. 2007. Terra infirma: Understanding salt tectonics. *Earth Science Reviews* 82, 1-28.
- Huff, G.F. & Wampler, J.M. 1990. K-Ar geochemistry of carnallite from salt-cycle six of the Paradox-Formation in Utah, U.S.A.. *Chemical Geology (Isotope Geoscience Section)*, 80, 309-318.
- Kühnlenz, T., Sassnowski, M., Hammer, J., Mingerzahn, G. & Kutowski, J. 2014. Evaluation of mapping

Chapter 3: Deformation of thin layered anhydrite rocks within the Gorleben salt dome, Germany

- results of the textural features of the Gorleben-Bank within the Gorleben salt dome, Germany. *Z. Dt. Ges. Geowiss. (German J. Geosci.)*, 165 (1), 63-76.
- Kühnlenz, T., Mingerzahn, G., Sassnowski, M., Hammer, J. & Schramm, M. (in prep.). Variabilität des lithologisch-strukturellen Aufbaus sowie Verbreitung und Lösungsführung der Gorleben-Bank und ihres unmittelbaren Umfeldes. Tätigkeitsbericht 2014, Bundesanstalt für Geowissenschaften und Rohstoffe, Hannover (in prep.).
- Küster, Y., Schramm, M., Bornemann, O. & Leiss, B. 2009. Bromide distribution characteristics of different Zechstein 2 rock salt sequences of the Southern Permian Basin: A comparison between bedded and domal salts. *Sedimentology* 56, 1368-1391.
- Küster, Y., Leiss, B. & Schramm, M. 2010. Structural characteristics of the halite fabric type „Kristallbrocken“ from the Zechstein Basin with regard to its development. *Int J Earth sci (Geol Rundsch)* 99: 505-526.
- Leitner, C., Neubauer, F., Genser, J., Borojevic-Sostaric, S. & Ranitsch, G. 2013. $^{40}\text{Ar}/^{39}\text{Ar}$ ages of crystallization and recrystallization of rock forming polyhalite in Alpine rocksalt deposits. – In: Jourdan, F., Mark, D.F. & Verati, C. (eds.): *Advances in $^{40}\text{Ar}/^{39}\text{Ar}$ dating from Archaeology to planetary Sciences*. Geological society, London, Special Publications 378, 18 p..
- Liang, W., Yang, C., Zhao, Y., Dusseault, M.B. & Liu, J. 2007. Experimental investigation of mechanical properties of bedded salt rock. *International Journal of Rock Mechanics & Mining Sciences* 44, 400-411.
- Mainprice, D., Bouchez, J.-L., Casey, M. & Dervin, P. 1993. Quantitative texture analysis of naturally deformed anhydrite by neutron diffraction texture goniometry. *J. Struct. Geol.* 15 (6), 793-804.
- Mattenklott, M. 1994. Die Bromid- und Rubidiumverteilung in Carnallitgesteinen. Kriterien für die Genese mariner Evaporite. Dissertation, Technische Universität Clausthal, 214 pp. (unpublished).
- Mertineit, M., Behlau, J., Hammer, J., Schramm, M. & Zulauf, G. 2012. Mechanical behavior of anhydrite rocks: results of field investigations, mineralogical-geochemical studies and thermomechanical experiments. – In: Bérest, P., Ghoreychi, M., Hadj-Hassen, F., Tijani, M. (eds.): *Mechanical behavior of salt VII: Proceedings of the 7th Conference*. Taylor & Francis Group, London, 123-129.
- Mertineit, M., Hammer, J., Schramm, M. & Zulauf, G. 2014. Deformation of anhydrite rocks (Gorleben-Bank, z3OSM) in a high-strain domain of the Gorleben salt dome, Germany. *Z. Dt. Ges. Geowiss. (German J. Geosci.)*, 165 (1), 49-62.
- Müller, W.H., Schmidt, S.M., & Briegel, U 1981. Deformation experiments on anhydrite rocks of different grain sizes: Rheology and microfabric. *Tectonophysics* 78, 527-543.
- Peach, C.J. 1993. Deformation, dilatancy and permeability development in halite/anhydrite composites. In M. Ghoreychi, P. Berest, H.R. Hardy, Jr. & M. Langer (eds.), *The Mechanical behaviour of Salt, Proceedings of the Third Conference, Paris 1993*, 153-166, Trans Tech Publications.
- Schindl-Neumayer, M. 1984. Gefügekundliche Studien in alpinen Salzlagern. *Arch. F. Lagerst.forsch.*

Chapter 3: Deformation of thin layered anhydrite rocks within the Gorleben salt dome, Germany

- Geol. B.-A. 5, 135-156.
- Schorn, A., Neubauer, F. & Bernroider, M. 2013. Polyhalite fabrics in an Alpine evaporite mélange: Hallstatt, Eastern alps. *J. Struct. Geol.* 46, 57-75.
- Schramm, M. & Bornemann, O. 2004. Deformationsgrade bzw. -mechanismus des Steinsalzes im Rahmen der Salzstockbildung – Stand der Bearbeitung der Bromidprofile. Tätigkeitsbericht 2003, Bundesanstalt für Geowissenschaften und Rohstoffe, Hannover (unpublished).
- Zulauf, G., Zulauf, J., Bornemann, O., Kihm, N., Peinl, M. & Zanella, F. 2009. Experimental deformation of a single-layer anhydrite in halite matrix under bulk constriction Part 1: Geometric and kinematic aspects. *J. Struct. Geol.* 31, 460-474.
- Zulauf, G., Zulauf, J., Bornemann, O., Brenker, F., Höfer, H., Peinl, M. & Woodland, A. 2010. Experimental deformation of a single-layer anhydrite in halite matrix under bulk constriction, Part 2: Microfabrics and deformation mechanisms. *J. Struct. Geol.* 32, 264-277, doi: 10.1016/j.jsg.2009.12.001.
- Zulauf, J., Zulauf, G., Hammer, J. & Zanella, F. 2011. Tablet boudinage of an anhydrite layer in rock-salt matrix: results from thermomechanical experiments. *J. Struct. Geol.* 33, 1801-1815, doi: 10.1016/j.jsg.2011.09.006.
- Zulauf, G., Zulauf, J., Mertineit, M. & Hammer, J. 2012. Boudinage of anhydrite in rock-salt matrix: The impact of bulk finite strain geometry. In: Bérest, P., Ghoreychi, M., Hadj-Hassen, F., Tijani, M. (eds.): Mechanical behavior of salt VII: Proceedings of the 7th Conference. Taylor & Francis Group, London, 65-70.

Chapter 4

Macro- and microscale distribution of hydrocarbons in the Staßfurt Hauptsalz of the Gorleben salt dome

Maximilian Pusch¹, Jörg Hammer¹, Jolanta Kus¹, Detlef Klosa², Nicolas Thiemeyer^{3*} & Gerhard Mingerzahn¹

¹*Federal Institute for Geosciences and Natural Resources (BGR), GeoZentrum Hannover, Stilleweg 2, 30655 Hannover, Germany*

²*State Authority for Mining, Energy and Geology (LBEG), GeoZentrum Hannover, Stilleweg 2, 30655 Hannover, Germany*

³*Institute of Geoscience, Goethe-University Frankfurt am Main, Altenhöferallee 1, 60438 Frankfurt am Main, Germany.*

Abstract

In context of further exploration of the Gorleben salt dome (March 2011 to November 2012) mineralogical and geochemical investigations have been conducted on hydrocarbon-bearing samples of the “Knäuelsalz” (z2HS1), particularly the oldest part of the “Hauptsalz” (Staßfurt Series z2). Investigations focus on genesis, composition and macro-/microstructural distribution of hydrocarbons. These exploration works continue investigations of Gerling & Faber (2001) and Gerling et al. (2002).

For this purpose 45 entire cored sampling boreholes supplemented with 20 packer boreholes in Crosscuts 1 West (Q1W) and 1 East (Q1E) have been drilled between March 2011 and March 2012 at the 840 m level of the Gorleben exploration mine in order to get new faultless and unaltered samples beyond the excavation damaged zone. Drill cores of hydrocarbon sampling and packer boreholes have been investigated under ultraviolet light ($\lambda = 254 \text{ nm}$) for indications of the existence of fluorescent (aromatic) hydrocarbons. The results were documented and visualised in the geological 3D model of the Gorleben salt dome.

Microscopical studies of thin and thick sections show that hydrocarbons were located at the grain boundaries of halite and/or anhydrite crystals, in newly formed microcracks due to drilling respectively preparational works, in microcapillary tubes of anhydrite crystals and rarely in micro-porous parts of the Hauptsalz.

Keywords: 840 m level, crosscut, Gorleben, hydrocarbon, Knäuelsalz, 3D model, ultraviolet light

[German Journal of Geosciences 165 \(1\), 3-14. DOI: 10.1127/1860-1804/2014/0053](https://doi.org/10.1127/1860-1804/2014/0053)

*N. Thiemeyer analyzed the rock salt microstructures with particular focus on hydrocarbon distributions and rock salt fabrics.

Chapter 4: Macro- and microscale distribution of hydrocarbons in the Staßfurt Hauptsalz of the Gorleben salt dome

4.1. Introduction

Hydrocarbons are a natural constituent of most sedimentary and metamorphic rocks within earth crust and also present in salt formations (Löffler & Schulze 1962, Bornemann et al. 2008). They are common in evaporite rocks in minor quantities as autochthonous constituents – derived from biomass remains – with very low concentrations usually in the ppb range (Gerling et al. 1991, Hammer et al. 2012, 2013). Slightly higher concentrations are observed within the potash seams of the central European Zechstein Formation (Gerling et al. 1988, 1991, 2002).

In addition to the autochthonous hydrocarbons, most salt formations also contain hydrocarbons which have migrated into the salt rocks from the calcareous-argillaceous sediments in the underlying rocks (Cramer 2005) or from the rocks surrounding the evaporites. However, hydrocarbons only migrate into evaporites if temporarily open fracture systems developed during the salt uprise (Bornemann et al. 2008). These are the only conditions which enable hydrocarbons to migrate into salt formations. Such hydrocarbons are then trapped within the salt rocks as a result of recrystallisation and healing processes, and then dragged along or relocated within the structure during the further upward salt movement and salt creep. The distribution of hydrocarbons within a salt dome is therefore strongly dependent on the structural-halokinetic development of the salt structure and its lithological composition.

4.2. Macroscopic observations regarding to the distribution of hydrocarbons in the Gorleben salt dome

Hydrocarbon occurrences in the Gorleben exploration mine are restricted to exposures of the “Hauptanhydrit” (z3HA), “Kaliflöz Staßfurt” (z2SF) and “Hauptsalz” (z2HS1–3) of the Staßfurt Series (z2HS) (Figs. 4.1, 4.2; Bornemann et al. 2008).

Fig. 4.1: Location map of the Gorleben salt dome (black arrow in the enlarged image section; BMWi 2008, modified) in Lower Saxony (Germany).



Chapter 4: Macro- and microscale distribution of hydrocarbons in the Staßfurt Hauptsalz of the Gorleben salt dome

Area	Division	Group	Formation	Thickness [m]	Symbol		
Infrastructure Area	Zechstein 3	Anhydritmittelsalz		60	z3AM	approx. 170 m	
		Buntes Salz		12	z3BT		
		Bank-/Bändersalz		14	z3BK/BD		
		Orangesalz		50	z3OS		
		Linien-salz		31	z3LS		
Exploration Area 1	Zechstein 3	Basissalz		16	z3BS	approx. 80 m	
		Hauptanhydrit		40 bis 80	z3HA		
		Leine-Karbonat		1,5	z3LK		
		Grüner Salzfön		2,5	z3GT		
	boundary Zechstein 2 / Zechstein 3						
	Zechstein 2	Gebänderter Deckanhydrit		1,5	z2DA		
		Decksteinsalz		0,5	z2DS		
		Kaliflöz Staßfurt		0 bis 17	z2SF		
		Kieseritische Übergangsschichten		2,5	z2UE		
		Hangendsalz		10	z2HG		
Exploration Area 1	Zechstein 2	Hauptsalz		700 bis 800	z2HS	approx. 800 m	
		Kristallbrockensalz			z2HS3		
		Streifensalz			z2HS2		
		Knäuelsalz			z2HS1		

Legend		anhydrite
 predominantly rock salt	 anhydrite	 Salztön
 potash	 carbonate	

Fig. 4.2: Simplified stratigraphic table of the salt rocks at the transition zone Zechstein 2 (Staßfurt Series) and Zechstein 3 (Leine Series).

Hydrocarbon occurrences in the underground workings are usually identifiable as dark, light brown, beige-yellowish or olive patches on the walls or roofs.

These patches do not represent large continuously outflowing occurrences, but rather small local isolated outflows of hydrocarbons from the rocks into the drifts for a limited period of time. The outflowing hydrocarbons spread out under the force of gravity to cover large areas over the surface of the rocks around the original outflow point. Therefore the condensate patches give the impression that an apparently large hydrocarbon occurrence has been encountered (Fig. 4.3).

Macroscopic analysis of cores of sampling boreholes in crosscuts 1 West and 1 East under ultraviolet light ($\lambda = 254 \text{ nm}$; Fig. 4.4) revealed that the (aromatic) hydrocarbons contained in the Staßfurt Hauptsalz are mainly located along the grain boundaries of halite and/or anhydrite crystals, and are therefore bound to intercrystalline spaces. Hydrocarbons bound to intracrystalline spaces in the "Knäuelsalz" (z2HS1) were only found rarely and very locally. When viewed in transmitted and reflected artificial light, these cores rarely show any macroscopic visible indication for the presence of hydrocarbons (Fig. 4.5).

Ultraviolet light, however, reveals a heterogenous distribution (variation in size and shape) of hydrocarbons in the cores. It should be noted that the fluorescent light emitted by hydrocarbons is broken and scattered at the grain boundaries of salt minerals. Because of the high transparency of the halite crystals, viewing the hydrocarbon distribution in cores and in thin sections under UV light gives rise to the formation of halos around the hydrocarbon inclusions. As a result, this gives an erroneous impression that the cores are impregnated by a much larger volume of hydrocarbons than it is actually the case.

Chapter 4: Macro- and microscale distribution of hydrocarbons in the Staßfurt Hauptsalz of the Gorleben salt dome



Fig. 4.3: Photo at artificial light (left) and ultraviolet light (right) of drilling station 1.2 in Crosscut 1 West at the 840 m exploration level. View to the SW-corner of drilling station 1.2, located in z2HS2 (Streifensalz); distances between cross-shaped marks about 1 m. The individual condensate outflows are labeled for documentation (e.g. RF 186 in the lower centre). The hydrocarbons appear as a result of the disaggregation of the rocks during drifting, and then spread out on the wall of the drift to form extensive beige-olive coloured patches. On the right photo it is recognisable that the fluorescent hydrocarbons are mainly derived from thin layers of anhydrite or anhydrite-rich halite parallel to bedding (shown by blue dashed lines) and spread under the influence of gravity (photos: DBE).

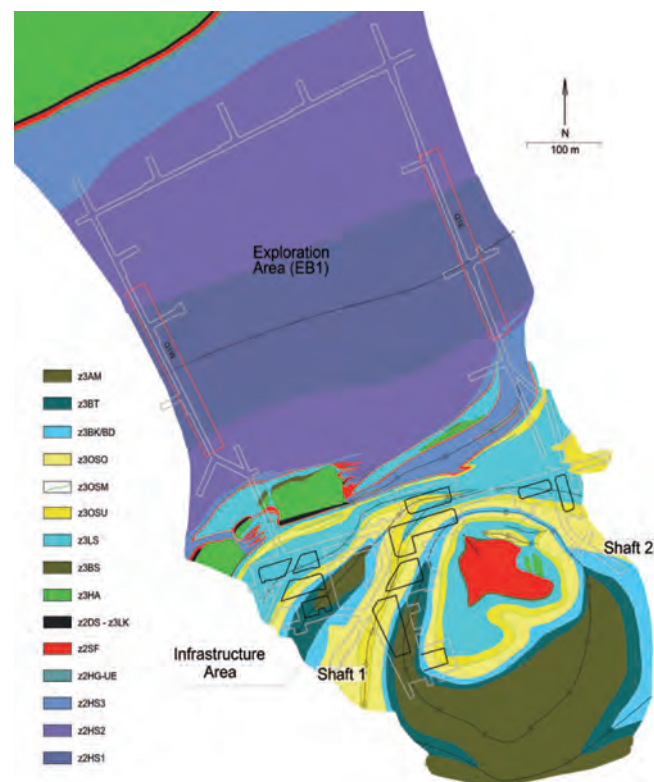


Fig. 4.4: Geological map of exploration area 1 (EB1) at the 840 m level (BGR, modified). The red rectangles represent the areas in Crosscut 1 West and Crosscut 1 East where the hydrocarbon sampling boreholes have been drilled.

Chapter 4: Macro- and microscale distribution of hydrocarbons in the Staßfurt Hauptsalz of the Gorleben salt dome

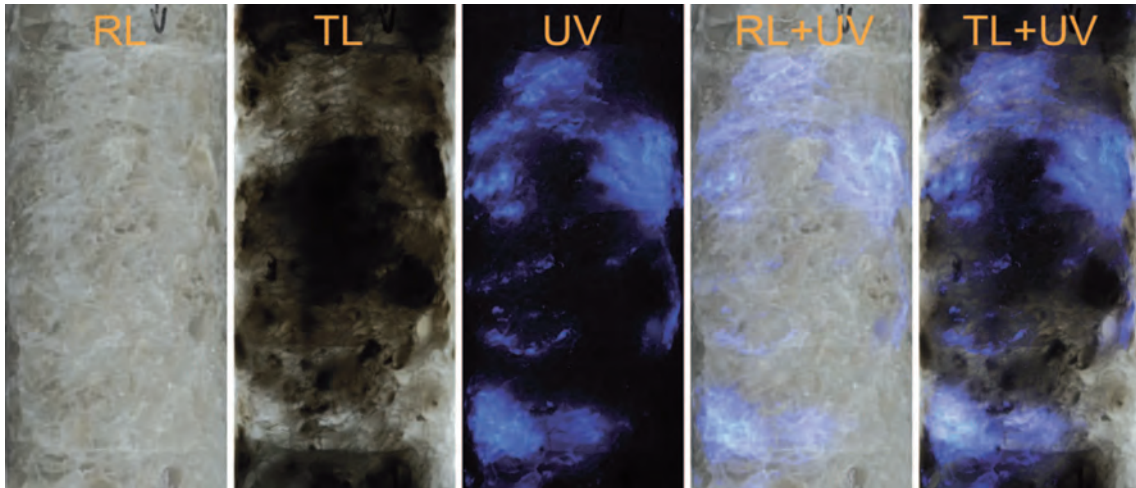


Fig. 4.5: Core segment with a diameter of 72 mm from the hydrocarbon sampling borehole RB652 from depth 1.14 m to 1.29 m at different lighting (core head: top of photo; drilling head: bottom). The core segment doesn't show any noticeable abnormalities in comparison with hydrocarbon-free Hauptsalz samples under reflected artificial light (RL) or transmitted light (TL). Black areas at transmitted light contain more crystals or clews of anhydrite than the translucent halite-rich regions. Under ultraviolet light (UV) aromatic hydrocarbons on grain boundaries of halite and anhydrite crystals fluoresce bluish and trace the grain boundaries, which leads to a halo effect in nearby crystals. Combining the individual pictures into one image (reflected light + UV: RL + UV and transmitted light + UV: TL + UV) reduces the halo effect and reveals the macroscopic structures containing the hydrocarbons.

4.3. 3D visualisation of the hydrocarbon distribution in the Gorleben exploration mine

The cores from the 6 m (Q1W) or 9 m (Q1E) hydrocarbon sampling boreholes in crosscuts 1 West (25 boreholes) and 1 East (20 boreholes) were completely mapped under UV light. The boreholes have been air drilled with nearly identical distances depending on the existing mining infrastructure. The depths of the fluorescing zones were documented in the borehole logs and prepared for three-dimensional visualisation. The fluorescence intensity of the cores was subdivided into “strong” (intensive fluorescence) and “weak” fluorescing zones with the aim of identifying any possible correlations of fluorescence intensity with the hydrocarbon content or salt rock composition.

The results of the UV mapping of the cores were processed with the AutoCAD-based openGEO software for visualisation of the hydrocarbon-enriched zones in the 3D model of the underground workings at the 840 m level (EB1; Figs. 4.6, 4.7). For visualisation reasons, the 3D visualisation only took into consideration zones whose average appearance did not change significantly over a distance of 5 cm. Core zones where hydrocarbon-associated fluorescence only affected part of the core diameter were

Chapter 4: Macro- and microscale distribution of hydrocarbons in the Staßfurt Hauptsalz of the Gorleben salt dome

visualised as hydrocarbon-bearing zones. The core segment of the hydrocarbon borehole RB652 shown in Fig. 4.5 therefore appears in the three-dimensional visualisation as a hydrocarbon-impregnated core section even though the hydrocarbons observed here have a multiple interrupted, streaky distribution. Therefore, the three-dimensional visualisations in Figs. 4.6 and 4.7 only document the core sections containing hydrocarbons but do not provide any information at all on the total content or shape of the hydrocarbon impregnations.

As it can be seen, in z2HS1 the hydrocarbons appear in the form of intersected streaks, clouds, islands and clasts. As a result of the uprising salt during halokinesis and the involved salt tectonic processes the original structure of z2HS1 and the included hydrocarbon enriched zones have been destroyed. As a result of the homogenisation of the z2HS1 during halokinesis it is nearly impossible to correlate the hydrocarbon bearing zones in the boreholes among each other. Along with results of packer tests (Hammer et al. 2012, 2013) the individual hydrocarbon occurrences seem to be isolated of each other.

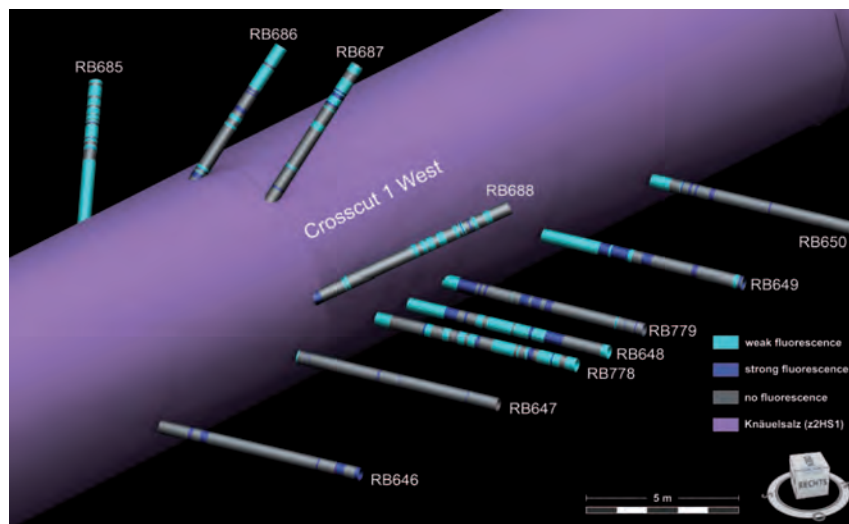


Fig. 4.6: 3D visualisation of the UV core mapping results of the hydrocarbon sampling boreholes in part of the Crosscut 1 West in the vicinity of the large condensate patch (several m² in size) around the hydrocarbon sampling borehole RB648.

In addition to the three-dimensional visualisation of the zones impregnated with hydrocarbons, it is also possible to combine the geometric visualisation with the hydrocarbon concentrations (Fig. 4.8), e.g. total amount of C1–C40 determined with Fast-RGA, HS-GC-FID and GC-FID after dissolving 200 g salt samples in 1 l of water (Hammer et al. 2012). The model part with the large condensate patch in Crosscut 1 West shows the hydrocarbon concentrations (sum C1–C40) for the samples taken from depth zone 4.5 m to 6.0 m at identical depths over all cores (for more details and results see Hammer et al. 2012). The geochemical results show a natural hydrocarbon background for the oldest Hauptsalz (Knäuelsalz, z2HS1) in Crosscut 1 West of <1 mg/kg (C1–C40). The overall concentrations of

Chapter 4: Macro- and microscale distribution of hydrocarbons in the Staßfurt Hauptsalz of the Gorleben salt dome

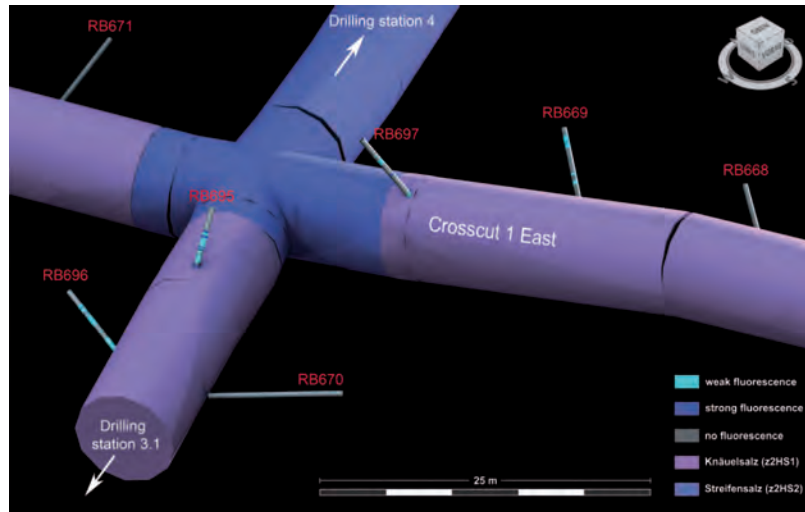


Fig. 4.7: 3D visualisation of the UV core mapping results of the hydrocarbon sampling boreholes in part of the Crosscut 1 East within the area of borehole stations 3.1 and 4 in the central part of Q1E. In Q1E only the cores of hydrocarbon borehole RB669 as well as of packer boreholes RB695, RB696 and RB697 show larger zones with fluorescence under ultraviolet light due to the presence of hydrocarbons.

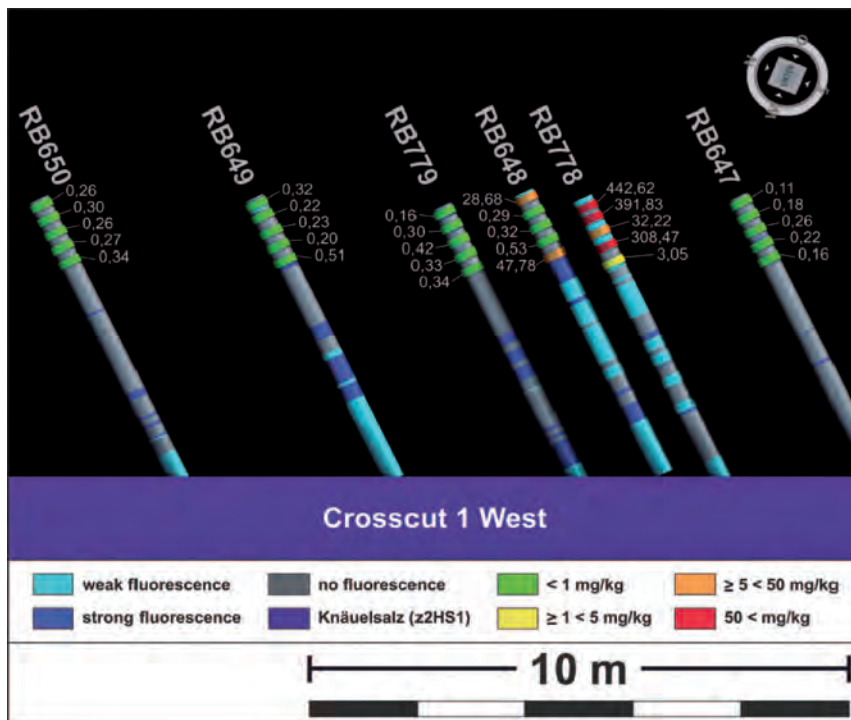


Fig. 4.8: Part of the 3D visualisation of the hydrocarbon boreholes in the vicinity of the large condensate patch in Crosscut 1 West. In addition to the results of the UV mapping of the hydrocarbon boreholes, this image also shows the concentrations of hydrocarbons (C1–C40) in the samples, specified in mg/kg.

Chapter 4: Macro- and microscale distribution of hydrocarbons in the Staßfurt Hauptsalz of the Gorleben salt dome

hydrocarbons (C1–C40) only rise around the large condensate patch, giving a local peak in hydrocarbon sampling borehole RB778 with a maximum concentration of 442 mg/kg (C1–C40).

4.4. Microscopic studies of the hydrocarbon distribution in the Staßfurt Hauptsalz

In addition to the macroscopic analysis, thin sections and thick polished sections (gentle dry preparation), 60 x 40 mm in size, were studied microscopically to determine their mineralogical/ petrographic composition and the fabric-microstructural related distribution of the hydrocarbons within the Hauptsalz. The samples are stratigraphically mainly related to z2HS1 (Knäuelsalz), only a few samples were prepared from z2HS2 (“Streifensalz”). The microscopic studies of the sections reveal that the hydrocarbons in the Hauptsalz are mainly found in intergranular micropores along the grain boundaries of halite crystals (dendritic branched network), i.e. as intercrystalline occurrences respectively as drop-shaped menisci on the surface of anhydrite crystals (Figs. 4.9A, D).

The fluid inclusions in the intergranular pores are frequently joined up to form dendritic fluidic networks which are filled with brines as well as with hydrocarbons (Figs. 4.10A, B), although not continuously joined up to one another. Larger inclusions of brines and hydrocarbons are more common around microfractures or unconsolidated grain boundaries (Fig. 4.10C). The halite crystals themselves are mainly clear, recrystallised and contain no fluid inclusions. Halite crystals with primary, intracrystalline inclusions of hydrocarbons were only observed rarely in drilling station 1.2 within z2HS2 near to the “Hauptanhydrit” (z3HA). In addition to intercrystalline fluid inclusions, hydrocarbons also occur within cleavage-parallel capillaries or planes within anhydrite crystals (Figs. 4.9B, D–H), or in the interparticle spaces of anhydrite clusters/tangles (Fig. 4.9C). Some of the hydrocarbons are also rarely present in z2HS1 as solid bituminous residues of organic matter. Multiphase inclusions are sometimes observed in larger cleavage-parallel capillaries in anhydrite, which, in addition to brines, also contain liquid and/or gaseous hydrocarbons as well as rare solid bituminous organic matter (Figs. 4.9D, G).

Hypidiomorphic to idiomorphic carbonate crystals (Figs. 4.9H–K) or hypidiomorphic to idiomorphic pyrite crystals (Figs. 4.9L, M) are occasionally observed as accessory minerals in the vicinity of anhydrite crystals and anhydrite tangles, or intergrown with them. Carbonates (dolomite, magnesite or calcite) as well as pyrite can be in the form of single crystals or large aggregates (0.1–1 mm) which are already macroscopically visible in some cases within the thin sections and thick polished sections.

4.5. Mineralogical and microstructural analysis of hydrocarbon-bearing rock salt

The macroscopic and polarisation microscopic investigations of hydrocarbon-bearing Hauptsalz samples were supplemented by analysis with an environmental scanning electron microscope (ESEM)

Chapter 4:
Macro- and microscale distribution of hydrocarbons in the Staßfurt
Hauptsalz of the Gorleben salt dome

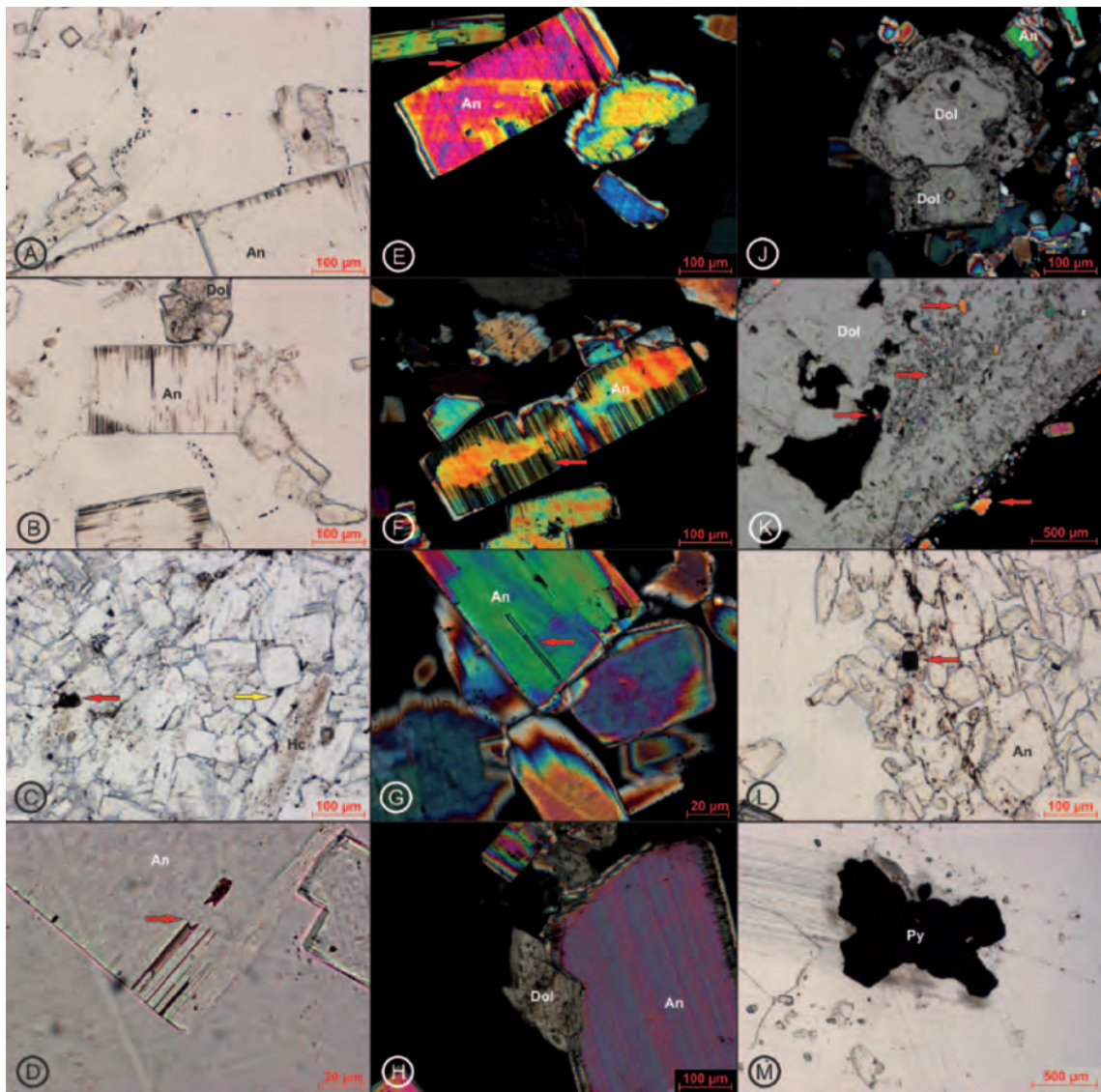


Fig. 4.9: (A) Brownish-black coloured fluid inclusions at the grain boundaries of recrystallised halite crystals or as drop-shaped menisci on anhydrite crystals (An), as well as in cleavage-parallel capillaries in anhydrite crystals (RB659, z2HS1; transmitted light, II polarisers). (B) Idiomorphic anhydrite crystals (An) with cleavage-parallel capillaries next to a rosette-shaped aggregate (Dol) of carbonate (RB659; transmitted light, II polarisers). (C) Tangle of anhydrite with bituminous residues of organic matter (red arrow), as well as condensate filled grain interstices (yellow arrow). Grinding during sample preparation has spread brownish hydrocarbons (Hc) over parts of the section (RB659; transmitted light, II polarisers). (D) Cleavage-parallel capillaries (red arrow) within an anhydrite crystal (An) showing a concave meniscus (iridescent in red to green caused by stacking-process) and residues of organic matter at the bottom (brownish-reddish-black) of the capillary (RB659; stacked image with $z = 5 \mu\text{m}$; transmitted light, II polarisers). (E) Edge-altered anhydrite crystal (An) with cleavage fissures (red arrow) and cleavage-parallel capillaries of similar length partially filled with fluid (RB659; transmitted light, + polarisers). (F) Idiomorphic, edge-altered anhydrite crystal (An) with numerous cleavage-parallel capillaries (red arrow)

Chapter 4: Macro- and microscale distribution of hydrocarbons in the Staßfurt Hauptsalz of the Gorleben salt dome

starting from the grain boundary (RB642, z2HS2; transmitted light, + polarisers). (G) Intact anhydrite crystal (An) with cleavage-parallel capillaries (red arrow) filled with hydrocarbons (convex meniscus; RB648, z2HS1; transmitted light, + polarisers). (H) Intergrowth of an idiomorphic carbonate crystal (Dol) with a large crystal of anhydrite (An) from RB659 (transmitted light, + polarisers). (J) Hypidiomorphic to idiomorphic carbonate crystals (Dol) in halite matrix near to a tangle of anhydrite (An). The crystals show a clean central part alongside a growth margin including organic residues (RB648; transmitted light, + polarisers). (K) Detail of an idiomorphic and porous carbonate crystal (Dol), 6 x 2 mm in size, with trapped and edge-grown anhydrite crystals (red arrows). The gaps are filled with halite and anhydrite crystals (RB648; transmitted light, + polarisers). (L) Idiomorphic, sharp-edged cube of pyrite (red arrow) surrounded by altered anhydrite (An) and organic phases (RB648; transmitted light, // polarisers). (M) 1.2 x 1 mm sized aggregate of an idiomorphic pyrite (Py) crystal (generally pentagondodecahedra) on a grain boundary in halite; RB656, z2HS1; transmitted light, // polarisers).

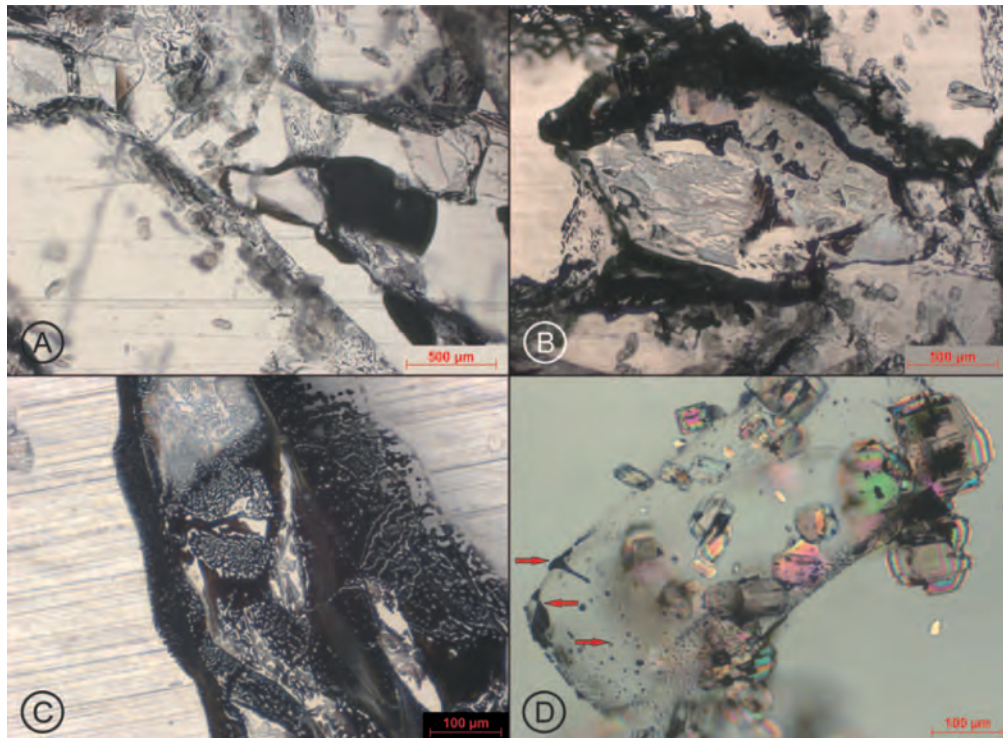


Fig. 4.10: (A) Dendritic network of blackish to brownish (hydrocarbons) and achromatic (brine) fluid inclusions alongside the grain boundaries of halite crystals (RB647, z2HS1; stacked image with $z = 400 \mu\text{m}$; transmitted light, // polarisers). (B) Clear halite crystals surrounded by numerous, extensively interconnected inclusions of brownish-black hydrocarbons and bluish iridescent brine (RB647, stacked image with $z = 400 \mu\text{m}$; transmitted light, // polarisers). (C) Mechanical stress during sample preparation giving rise to a cracked and strongly networked grain boundary covered with blackish to brownish hydrocarbons (RB647; stacked image with $z = 600 \mu\text{m}$; transmitted light, // polarisers). (D) Crystals of anhydrite with streaks to meniscus-shaped hydrocarbons (red arrows) adhering to the crystal surface (RB648; stacked image with $z = 115 \mu\text{m}$; transmitted light, // polarisers).

Chapter 4: Macro- and microscale distribution of hydrocarbons in the Staßfurt Hauptsalz of the Gorleben salt dome

and a confocal laser scanning microscope (CLSM) to determine the accessory minerals within the samples (detected minerals in this work: e.g. carbonates as dolomite and calcite, pyrite, quartz, celestine, etc.), as well as to characterise in more detail the spatial distribution and genesis of the organic phases. To completely determine the mineralogical composition of the hydrocarbon-bearing rocks and any mineral alterations or transformations which may proceeded within the rocks, two 200 g samples from z2HS1 in boreholes RB648 and RB659 (near the condensate patch) were completely dissolved in bi-distilled water. The exemplary samples also served for testing the solution process and its influence on the accessory minerals (especially carbonate and pyrite) in order to gain unaltered mineral grains for isotopic analysis of carbonate and pyrite in terms of the discussion of a passed thermochemical sulphate reduction (TSR). The insoluble/poorly soluble components were filtered off and analysed in ESEM to identify the minerals and to search for traces of dissolution on their surfaces. In addition to small authigenic quartz crystals (main grain component), clay minerals and a few other insoluble minerals mentioned below in more detail, the samples also contained hypidiomorphic to idiomorphic

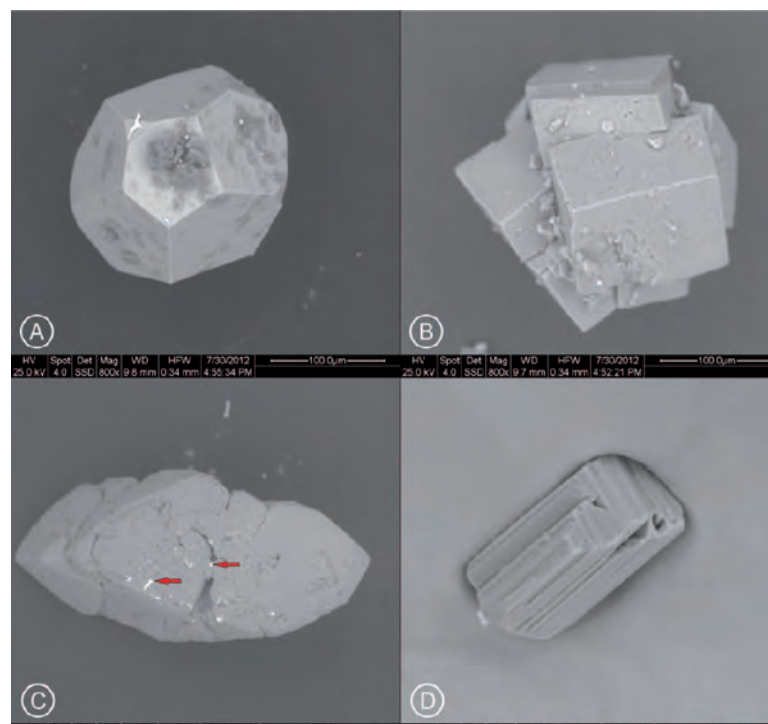


Fig. 4.11: (A) Idiomorphic crystal of pyrite (pentagondodecahedra) with intact and smooth crystal faces as well as sharp crystal edges (RB659). (B) Aggregate of carbonate consisting of intact idiomorphic crystals of dolomite (RB659). (C) Large aggregate of carbonate consisting of hypidiomorphic dolomite crystals, partially fractured and loosely intergrown with trapped idiomorphic crystals of cubic pyrite and aggregates of pyrite (white subjects, marked with red arrows; RB648). (D) Crystal of anhydrite with recognisable openings to single cleavage-parallel capillaries on the surface of the crystal (RB648).

Chapter 4: Macro- and microscale distribution of hydrocarbons in the Staßfurt Hauptsalz of the Gorleben salt dome

and some xenomorphic carbonate crystals (Figs. 4.11B, C), as well as pyrite crystals (Fig. 4.11A) and aggregates. The carbonate as well as the pyrite crystals showed no identifiable solution traces as a result of the dissolution of the rock salt so that they can be used for isotopic analysis. EDX analysis revealed that most of the carbonates contained in the residues are dolomite or magnesite, and that the samples also contained a small portion of pure calcite crystals or magnesium-rich calcite.

Carbonates are present as either idiomorphic single crystals or as aggregates with well-developed crystal surfaces (Fig. 4.11B). The crystal surfaces are usually smooth to slightly porous or locally perforated as a result of the dissolved formerly adhering halite and anhydrite crystals. Hypidiomorphic to idiomorphic quartz and pyrite crystals are sometimes observed which are intergrown with the carbonate aggregates (Fig. 4.11C).

Pyrite is mainly observed in the form of intact single crystals frequently forming pentagondodecahedra (Fig. 4.11A), as well as cubes or cubo-octahedra. Intergrowths of several pyrite crystals to form mm-sized aggregates, or with sphalerite, were also observed. Other accessory minerals confirmed by the ESEM analysis are idiomorphic quartz, celestine and sphalerite as well as rare potassium-feldspar, fluorite, talc and galenite. Some of the rock fragments not used in the dissolution experiments contained anhydrite crystals whose surfaces showed the openings to the cleavage-parallel capillaries (Fig. 4.9D), occasionally occurring in Hauptsalz samples.

	Laser 1	Laser 2	Laser 3
Wavelength used for excitation (AOTF)	458 nm	496 nm	633 nm
Region of detection	460–491 nm	497–628 nm	636–800 nm
Colour coding	blue	green	red

Table 4.1: Excitation wavelengths (AOTF), range of detection and colour coding of the lasers used for the CLSM analysis.

Additionally, investigations of the microscopic to submicroscopic distribution of the hydrocarbons contained in the Hauptsalz were carried out using the CLSM on uncovered samples of a thick section taken from hydrocarbon borehole RB652 (Q1W). In a first test run, the data was recorded,

evaluated and visualised using the LAS AF software from Leica Microsystems. Three different lasers were used to excite the samples and reveal the potential differences in the chemical composition and spatial distribution of the hydrocarbons they contained.

The excitation wavelengths (AOTF) of the lasers in the CLSM, the associated detection range and the colour coding are shown in Table 1.

The CLSM results confirm the core observations as well as the polarisation microscope analysis because it shows that the hydrocarbons within the evaporites are largely present in the form of intercrystalline fluid inclusions bound to the grain boundaries of halite and anhydrite crystals. The hydrocarbons observed by CLSM lie on the grain boundaries either in the form of isolated drops or

Chapter 4: Macro- and microscale distribution of hydrocarbons in the Staßfurt Hauptsalz of the Gorleben salt dome

as dendritic to spatially interlinked structures (Fig. 4.12A). The halite-halite grain boundaries highlight the heterogeneous distribution of hydrocarbons with different compositions shown in different colours in the CLSM photographs. The intensity and colour of emitted fluorescence varies depending on the wavelength used for excitation and composition of hydrocarbons.

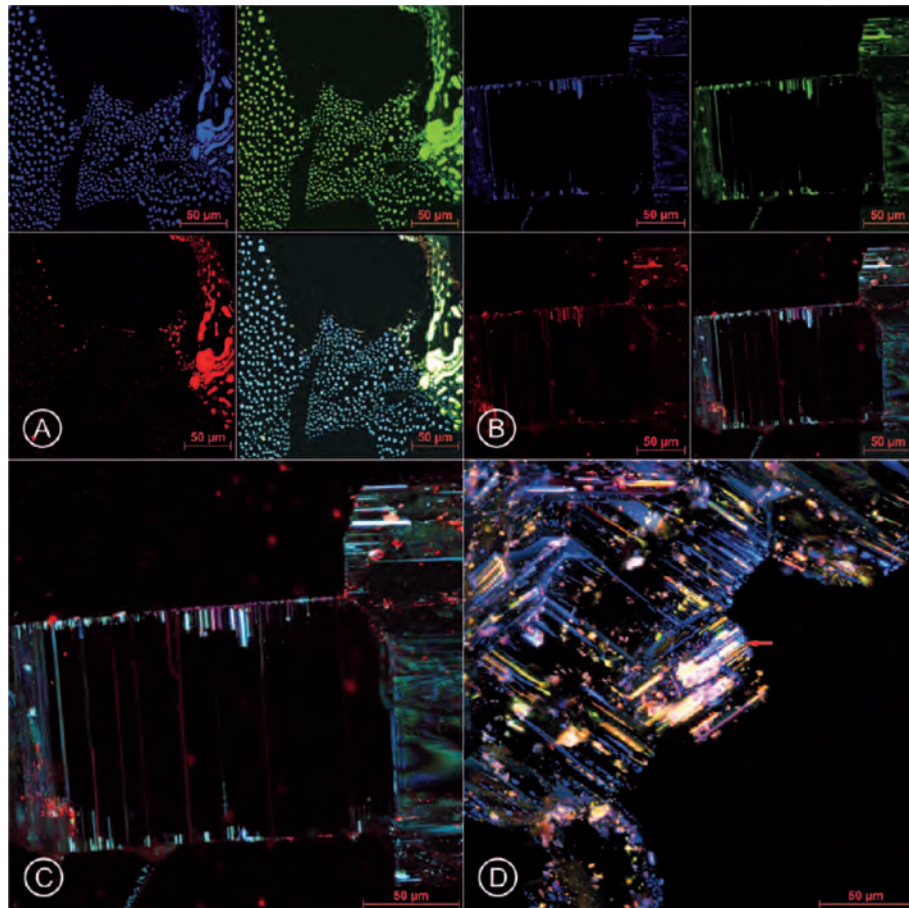


Fig. 4.12: (A) The hydrocarbons on the grain boundaries of the halite crystals show different fluorescence depending on their chemical composition and the laser type (associated colour code: see Table 1). The differences can also be seen in the combined image (bottom right) of all three lasers (RB652, z2HS1). Image size: 246.03 x 246.03 µm; z-penetration depth: 80.99 µm. (B) Intact and slightly edge-altered anhydrite crystal with cleavage-parallel capillaries (RB652; combined image of all wavelengths: bottom right). Image size: 235.86 x 235.86 µm; z-penetration depth: 20.14 µm. (C) Enlarged part of the combined image of Fig. 12B (bottom right). The anhydrite crystal has several cleavage-parallel capillaries extending inwards from the edge of the crystal and filled with hydrocarbons of different compositions (length of the capillaries: 300 nm to 3 µm; diameter 1–30 µm). Image size: 235.86 x 235.86 µm; z-penetration depth: 20.14 µm. (D) Anhydrite cluster (RB652, combined image of all three lasers) with hydrocarbons of different compositions that stick to the surface of the anhydrite crystals and occur in meniscus shapes, linear on cleavage surfaces or pseudo-intercrystalline in capillaries. The capillaries are filled with different fillings (liquid/gaseous hydrocarbons; red arrow in image centre). Image size: 246.03 x 246.03 µm; z-penetration depth: 30.21 µm.

Chapter 4: Macro- and microscale distribution of hydrocarbons in the Staßfurt Hauptsalz of the Gorleben salt dome

As shown by the changing distribution of fluorescence colours, which are dependent on the excitation wavelengths, the chemical composition of the hydrocarbons within the samples changes even over extremely short distances. The hydrocarbons observed along the halite-anhydrite grain boundaries or within anhydrite clusters are usually visible in the form of menisci or streaks on the surface of anhydrite crystals or within the capillaries located along the cleavage of the anhydrite crystals (Figs. 4.12B–D). Under CLSM, there were also occasional observations of capillaries within the anhydrite crystals containing multi-phase fluid inclusions (cf. Figs. 4.9D, G). Although it was only possible to identify capillaries with lengths of up to 100 μm and diameters of 5 μm using polarisation microscopic techniques, CLSM enabled capillaries to be observed with lengths between 300 nm to 3 μm and diameters of 1–30 μm . This allows identifying occurrences and differences in hydrocarbon content in a sub-microscopic scale.

4.6. Conclusions

The results of the investigations on fresh cores from Crosscut 1 West and Crosscut 1 East indicate a very heterogeneous distribution of hydrocarbons. They usually occur in very low concentrations of less than 1 mg/kg (C1–C40) in the Gorleben Hauptsalz (z2HS) located in EB1 at the 840 m level. Most of the occurrences as well as the highest concentration of total hydrocarbons (C1–C40) are located in the oldest part of the Hauptsalz, the Knäuelsalz, in the central anticline of the Gorleben salt dome. The aromatic to long-chain hydrocarbons visible under UV light occur in recrystallised halite rocks and in thin anhydrite or anhydrite-rich halite layers in form of streaks, clouds, islands, clasts, and occasionally also as dissipated or ragged and interrupted layers in the Hauptsalz. Hydrocarbons observed under artificial and UV light on the walls and roof of some drifts locally occur in excavation damaged zones and spread under gravitational influence to cover large surfaces of the drift giving the impression of an apparently large occurrence.

The occurrences of hydrocarbons are limited to intergranular pores or micropores within the rock salt as well as within the capillaries in anhydrite crystals. Although intergranular inclusions form small dendritic branched fluid networks, the individual networks are not interconnected over areas exceeding several crystals. The formation and genesis of the carbonates and sulphides found within the samples is still the subject of continuing research, including isotopic geochemical analysis. Further detailed information about hydrocarbon content of Gorleben Knäuelsalz is described in Hammer et al. (2012, 2013).

4.7. Acknowledgements

The authors would like to thank Stanislaw Burliga and Grzegorz Czapowski for reviewing the article,

Chapter 4: Macro- and microscale distribution of hydrocarbons in the Staßfurt Hauptsalz of the Gorleben salt dome

Maik Gern and Ralf Götze for sample and thin/thick sections preparation, DBE Gorleben for photos from the Q1W, and Lennart Ptock for picture editing.

8. References

- Bornemann, O., Behlau, J., Fischbeck, R., Hammer, J., Jaritz, W., Keller, S., Mingerzahn, G. & Schramm, M. (2008): Description of the Gorleben site, part 3: Results of the geological surface and underground exploration of the salt formation. – Bundesanst. Geowiss. Rohstoffe (BGR): 223 p., Hannover (BGR).
- BMWi (Bundesministerium für Wirtschaft und Technologie) (2008): Endlagerung der hochradioaktiven Abfälle in Deutschland. – Das Endlagerprojekt Gorleben: 64 p., Berlin.
- Cramer, B. (2005): Erdölgeologische 3D-Modellierung des Salzstocks Gorleben. – Final report Bundesanst. Geowiss. Rohstoffe (BGR): 75 p., Hannover (BGR).
- Gerling, P. & Faber, E. (2001): Dokumentation der chemischen Analysen von gasförmigen und flüssigen Kohlenwasserstoffen. – Report Bundesanst. Geowiss. Rohstoffe (BGR), Journal No. 10717/01: 20 p., Hannover (BGR).
- Gerling, P., Whiticar, M.J. & Faber, E. (1988): Extreme isotope fractionation of hydrocarbon gases in Permian salt. – Org. Geochem., 13: 335–341.
- Gerling, P., Beer, W. & Bornemann, O. (1991): Gasförmige Kohlenwasserstoffe in Evaporiten des deutschen Zechsteins. – Kali Steinsalz, 10: 376–383.
- Gerling, P., Faber, E. & Wehner, H. (2002): Interpretation der chemischen Analysen von gasförmigen und flüssigen Kohlenwasserstoffen. – Report Bundesanst. Geowiss. Rohstoffe (BGR), Journal No. 12243/02: 82 p., Hannover (BGR).
- Hammer, J., Pusch, M., Häger, A., Scheeder, G., Shao, H., Paul, B., Ostertag-Henning, C., Mingerzahn, G., Schlömer, S. & Hesser, J. (2012): Untersuchungen von Kohlenwasserstoffen im Erkundungsbergwerk Gorleben. – Interim report 2011, Bundesanst. Geowiss. Rohstoffe (BGR): 236 p., Hannover (BGR).
- Hammer, J., Pusch, M., Häger, A., Scheeder, G., Shao, H., Paul, B., Ostertag-Henning, C., Mingerzahn, G., Schlömer, S. & Hesser, J. (2013): Untersuchungen von Kohlenwasserstoffen im Erkundungsbergwerk Gorleben. – Interim report 2012, Bundesanst. Geowiss. Rohstoffe (BGR): 207 p., Hannover (BGR).
- Löffler, J. & Schulze, G. (1962): Die Kali- und Steinsalzlagerstätten des Zechsteins in der Deutschen Demokratischen Republik. Teil III: Sachsen-Anhalt. – Freiberg. Forschungsh., C 97/III: 347 p.

Chapter 5

Hydrocarbons in rock salt of the Gorleben salt dome – amount, distribution, origin and influence on geomechanical properties

J. Hammer, M. Pusch, A. Häger & C. Ostertag-Henning

Federal Institute for Geosciences and Natural Resources (BGR), Hannover, Germany

N. Thiemeyer* & G. Zulauf

Institute of Geoscience, Goethe University Frankfurt, Frankfurt/Main, Germany

Abstract:

Investigations are focusing on the macro-/microstructural distribution and origin of hydrocarbons as well as on the geomechanical behaviour of hydrocarbon-bearing rock salt of the “Hauptsalz” (z2HS, Staßfurt unit, Zechstein, Upper Permian) in the Gorleben salt dome. Studies of core samples and exposures reveal a heterogeneous distribution of hydrocarbons. They appear mostly in form of streaks, dispersed clouds, clusters and islands. Microscopic studies and computed tomography suggest that hydrocarbons are located 1) along grain boundaries of halite and/or anhydrite crystals, 2) in newly formed artificial microcracks due to drilling and preparation, 3) in microcapillary tubes of anhydrite crystals and 4) rarely in micro-porous parts of the Hauptsalz. Analyses of biomarkers point to the Staßfurt carbonate (z2SK) as source rocks of most hydrocarbons. Creep tests suggest that the content of hydrocarbons determined in the Hauptsalz (up to several hundreds ppm) is too low in order to affect the geomechanical behaviour of the rock salt.

In: Roberts, L., Mellegard, K., Hansen, F. (Eds.). The Mechanical Behavior of Salt VIII, Taylor & Francis Group, London, 69-75. DOI: [10.1201/b18393-10](https://doi.org/10.1201/b18393-10).

*N. Thiemeyer conducted the X-ray CT scans of hydrocarbon-bearing and hydrocarbon-free rock salt samples and visualized the 3D distribution patterns of pore space.

Chapter 5: Hydrocarbons in rock salt of the Gorleben salt dome - amount, distribution, origin and influence on geomechanical properties

5.1. Introduction

Rock salt formations and salt diapirs in particular are well known for their barrier properties and isolation capability to segregate hazardous waste (chemical-toxic and radioactive) permanently away from the biosphere.

To demonstrate the long-term safety of waste disposals in salt rocks, the influence of all relevant parameters and processes on the geomechanic and hydraulic integrity of salt barrier has to be considered. In this context, the distribution and content of hydrocarbons as well as the geomechanical behaviour of hydrocarbon-bearing Staßfurt Hauptsalz (main rock salt, z2HS, Staßfurt unit, Zechstein, Upper Permian) in the Gorleben salt dome were studied. The investigations were conducted from March 2011 to November 2012 as part of the further geological exploration of the salt dome to clarify the suitability of the salt dome for disposal of heat generating radioactive waste. The studies continued investigations of Gerling & Faber (2001) and Gerling et al. (2002).

Hydrocarbons are natural constituents of most sedimentary rocks and are also present in salt formations (e. g. Löffler & Schulze 1962, Tissot & Welte 1984, Popp et al., 2002, Siemann 2007, Bornemann et al., 2008). In evaporitic rocks, hydrocarbons are common as autochthonous constituents with minor quantities, derived from biomass remains, with very low concentrations usually in the ppb range (Gerling et al., 1991).

In addition to these autochthonous hydrocarbons, most salt formations also contain hydrocarbons, which originated from the calcareous-argillaceous sediments in the underlying rocks. Because of the low permeability of halitic rocks under lithostatic pressure, hydrocarbons can only migrate into and inside evaporites if open fractures are present. Such (temporarily) open fractures may result from halotectonic processes during the salt rise. These hydrocarbons are then trapped within the salt rocks as a result of deformation-related and healing processes. Subsequently, the hydrocarbons are dragged along or relocated within the salt structure during the further upward salt movement and salt creep.

5.2. Sampling and analytical methods

2.1. Sampling

In order to get fresh and representative samples beyond the EDZ (excavation damaged zone) for mineralogical-geochemical, microscopic and geomechanical studies of hydrocarbon-bearing salt rocks, 45 boreholes have been drilled at the 840 m level of the Gorleben exploration mine. The boreholes have been air drilled and arranged in nearly equal distances (depending on the mine infrastructure) alongside crosscut 1 West (each 6 m long) and crosscut 1 East (each 9 m long). Cores from the hydrocarbon sampling boreholes were completely mapped under UV light ($\lambda = 254 \text{ nm}$). The results were documented and visualized in the geological 3D model of the Gorleben salt dome (Hammer et al.,

Chapter 5: Hydrocarbons in rock salt of the Gorleben salt dome - amount, distribution, origin and influence on geomechanical properties

2012, 2013, Pusch et al., 2014).

5.2.2. Geochemical, microscopic and tomographic analyses

To study the concentration, composition, distribution and origin of hydrocarbons in the Gorleben Hauptsalz, organic geochemical, microscopic and tomographic analyses were performed.

For organic geochemical analyses, a total of 210 core samples were dissolved in deionised and degased water immediately after the drilling. Hydrocarbon concentrations for the boiling range of C1 – C40 were quantified with different chromatographic analysis methods (Fast-RGA, HS-GC-FID and GC-FID; see Hammer et al., 2012).

To improve knowledge about the origin of hydrocarbons detected in the Gorleben Hauptsalz, organic geochemical analyses of potential source rocks were performed. For this purpose, core samples from 1) Staßfurt carbonate (z2SK), 2) calcareous-argillaceous rocks of the Werra unit (z1) and 3) Upper Permian copper shale of the borehole “Gorleben Z1” were analyzed and compared with hydrocarbon signatures in z2HS.

Additionally, polarisation and fluorescence microscopy as well as confocal laser scanning microscopy (CLSM) were performed. To reveal the microscopic to submicroscopic distribution of the hydrocarbons CLSM (Leica) was carried out on uncovered thick sections. Three different lasers of different wavelength were used to evaluate the potential differences in the chemical composition and spatial distribution of the hydrocarbons.

The non-destructive computed tomography (CT) yields robust quantitative data for the porosity of salt rocks and for 3D reconstructions of the distribution and shape of pores in rock salt (Thiemeyer et al., 2014). The 3D reconstructions can expose spatial distribution anisotropies, amounts, connections and shapes of any visible portion of a scan volume depending on the designated scale. Computed tomography studies were carried out using a Phoenix nanotom s (GE Sensing and Inspection Technologies) equipped with a XS 180 NF tube and a Hamamatsu detector at the Goethe University Frankfurt am Main. The spatial resolution of the obtained data has a major impact on the type of porosity that can be quantified.

5.3. Results

5.3.1. Macroscopic distribution of hydrocarbons

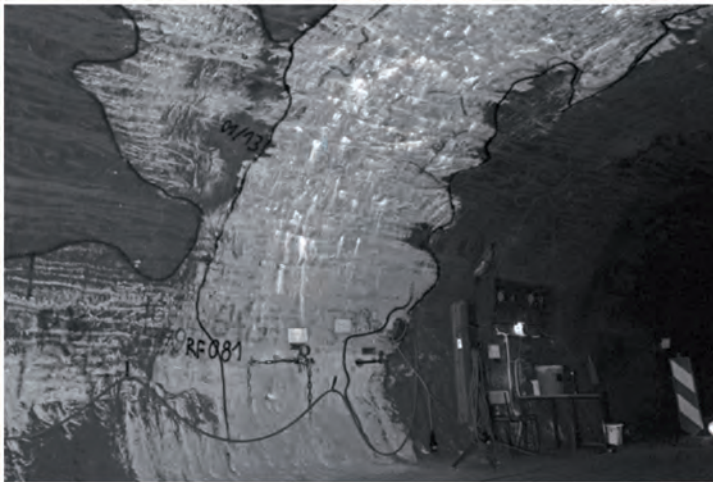
Most excavations and exploration boreholes at the Gorleben exploration mine do not show any macroscopic indications or traces of hydrocarbons (Bornemann et al., 2008). Furthermore, using transmitted and reflected artificial light, cores of hydrocarbon-bearing rock salt rarely show any macroscopic indication for the presence of hydrocarbons.

Relatively rare hydrocarbons in the underground workings occur as dark, light brown, beige-yellowish or olive patches on the walls or roofs. The outflowing hydrocarbons spread out under the force of

Chapter 5: Hydrocarbons in rock salt of the Gorleben salt dome - amount, distribution, origin and influence on geomechanical properties

gravity to cover large areas over the surface of the rocks around the real outflow point. The distribution of hydrocarbons in excavations and drill cores was mapped using ultraviolet light ($\lambda = 254 \text{ nm}$), where aromatic components of hydrocarbons fluoresce. Under UV light, the hydrocarbon patches do not represent large continuously outflowing occurrences, but rather small locally isolated outflows of hydrocarbons from the rocks into the drifts for a limited period of time (Fig. 5.1).

Most of the occurrences as well as the highest concentrations of total hydrocarbons (C1–C40) are



located in the oldest part of the Hauptsalz, the Knäuelsalz (z2HS1), in the central z2 anticline of the Gorleben salt dome. Rarely occurrences of hydrocarbons were found as thin hydrocarbon-bearing layers subparallel to anhydrite layers in stratigraphically upper parts of the Gorleben Hauptsalz, in the Kristallbrockensalz (z2HS3).

Fig. 5.1: Large condensate patch in crosscut 1 West at ultraviolet light (eastern wall, 840 m level). The patch represents many small, isolated outflows of hydrocarbons from Staßfurt Hauptsalz.

Investigations of core samples and underground exposures at ultraviolet light, however, reveal a heterogeneous distribution (variations in size and shape) of hydrocarbons. The core segments of the hydrocarbon sampling boreholes document a multiple interrupted, streaky distribution of the hydrocarbons. Most of the hydrocarbons are present in form of intersected streaks, dispersed clouds, isolated clusters, islands and clasts. As a result of the uprising of salt during the halokinesis and the involved salt tectonic processes, the original structure of Knäuelsalz (z2HS1) and of the included hydrocarbon enriched zones have been destroyed. Therefore, it is nearly impossible to correlate the hydrocarbon bearing zones in the boreholes among each other. In combination with results of packer tests in special boreholes (Hammer et al., 2012, 2013), the individual hydrocarbon occurrences seem to be isolated from each other, even if the distance between boreholes is only 20-30 cm.

Macroscopic analyses of cores at ultraviolet light revealed that the (aromatic) hydrocarbons of the Staßfurt Hauptsalz are mainly located along the grain boundaries of halite and/or anhydrite crystals, and are therefore bound to intercrystalline spaces. Intracrystalline hydrocarbons were rarely and very locally found in the Gorleben Hauptsalz.

Chapter 5: Hydrocarbons in rock salt of the Gorleben salt dome - amount, distribution, origin and influence on geomechanical properties

5.3.2. Microscopic studies of hydrocarbon distribution

In addition to the macroscopic analyses, thin and thick sections were studied using transmitted light microscopy to determine their mineralogical composition and the fabric-microstructural related distribution of the hydrocarbons within the Hauptsalz. The samples show a manifold inventory of fluid inclusions preserved as bubbles, stripes, branching networks, vermicular lines and locally developed fluid films (Fig. 5.2). They mainly occur at halite grain boundaries and along boundaries between halite and anhydrite. Additionally, anhydrite clusters show clear assemblages of fluid phases due to the high surface area.

The microscopic studies of the core sections reveal hydrocarbons in the Hauptsalz mainly distributed in intergranular micropores along the grain boundaries of halite crystals (partly dendritic branched network), i.e. as intercrystalline occurrences, respectively as drop-shaped menisci on the surface of anhydrite crystals. Larger inclusions of brines and hydrocarbons are more common around microfractures or unconsolidated grain boundaries. The halite crystals themselves are mainly clear. Halite crystals with primary, intracrystalline inclusions of hydrocarbons were only rarely observed.

In addition to intercrystalline fluid inclusions, hydrocarbons also occur within cleavage-parallel capillaries or planes within anhydrite crystals (Fig. 5.3), or in the interspaces of anhydrite clusters/tangles. Multiphase inclusions were sometimes present in larger cleavage-parallel capillaries in anhydrite, which, in addition to brines, also contain liquid and/or gaseous hydrocarbons as well as rare solid bituminous organic matter.

5.3.3. Confocal laser scanning microscope (CLSM)

The polarisation microscopic investigations of hydrocarbon bearing Hauptsalz samples were supplemented by analyses with a confocal laser scanning microscope (CLSM) to characterize the spatial distribution of the hydrocarbons in more detail.

The CLSM results confirm the core observations as well as the microscopic data showing the hydrocarbons within the evaporites being present in form of intercrystalline fluid inclusions restricted

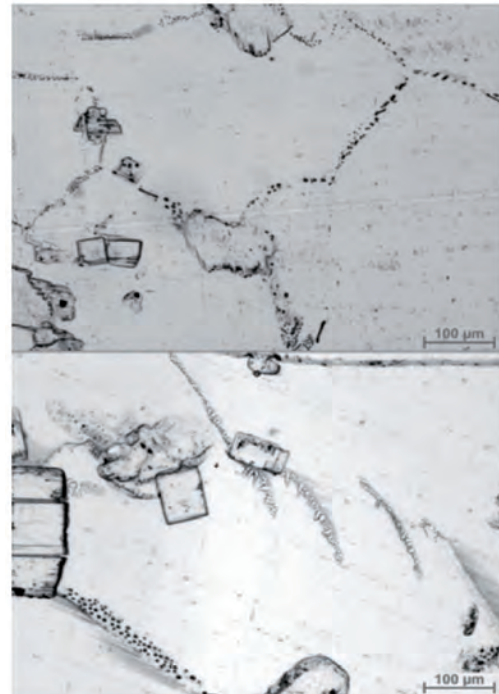


Fig. 5.2: Hydrocarbons and brines at grain boundaries of halite crystals (parallel polarisers, "Knäuelsalz", z2HS1).

Chapter 5: Hydrocarbons in rock salt of the Gorleben salt dome - amount, distribution, origin and influence on geomechanical properties

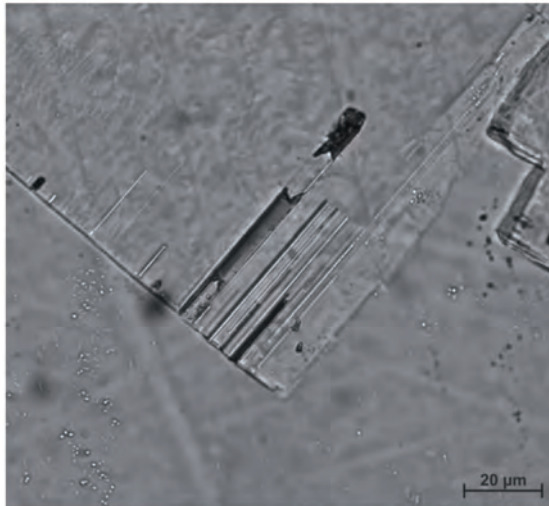


Fig. 5.3: Hydrocarbons in cleavage-parallel capillaries within an anhydrite crystal (parallel polarisers, “Knäuelsalz”, z2HS1).

to the grain boundaries of halite and anhydrite crystals (Pusch et al., 2014). The hydrocarbons observed by CLSM are situated along the grain boundaries either as isolated drops and bubbles or as dendritic to spatially interlinked structures (partly as fluid channels). The halite-halite grain boundaries highlight the heterogeneous distribution of hydrocarbons with different compositions shown in different colours in the CLSM photographs (Fig. 5.4). As shown by the changing distribution of fluorescence colours, which are dependent on the excitation wavelengths, the chemical composition of the hydrocarbons within the samples changes even over extremely short distances. The meniscuses or streaks on the surface of anhydrite crystals or within the capillaries located along the cleavage of the anhydrite crystals. Under CLSM, occasional capillaries within the anhydrite crystals contain multi-phase fluid inclusions (Fig. 5.4). Polarisation microscopy revealed capillaries with lengths of up to 100 μm and diameters of 5 μm. By using CLSM, the resolution increases, so capillaries with lengths between 300 nm to 3 μm and diameters of 1–30 μm can be detected. This allows identifying occurrences and differences in hydrocarbon content on a submicroscopic scale.

5.3.4. Computed tomography

Computed tomography (CT) was applied to visualize the spatial distribution of fluid accumulations and to quantify the porosity of rock salt core samples (Thiemeyer et al., 2014). In combination with 3D visualization software, any structures distinguishable by density contrasts can be visualized and quantified.

The 3D reconstructions reveal the distribution and shape of porous zones in the Hauptsalz samples. The calculated porosities have been acquired by two different digital techniques, presented in Thiemeyer et al. (2014). The volume renderer

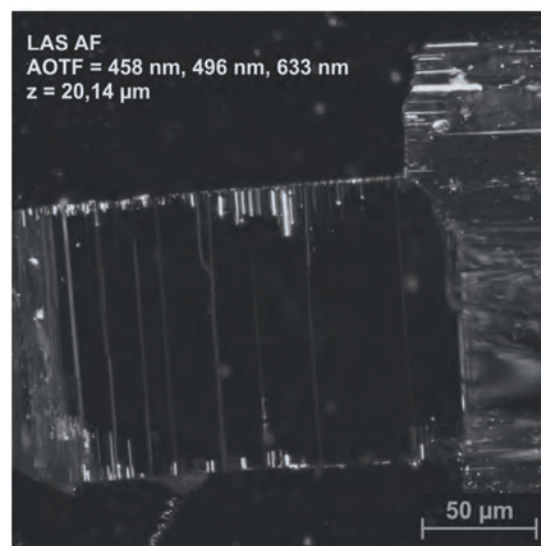


Fig. 5.4: Visualization of hydrocarbons (light) in cleavage-parallel capillaries within an anhydrite crystal. Image generated using confocal laser scanning microscope (“Knäuelsalz”, z2HS1).

Chapter 5: Hydrocarbons in rock salt of the Gorleben salt dome - amount, distribution, origin and influence on geomechanical properties

projections (Fig. 5.5, left) show every pore space in the same intensity, whereby some domains are hidden by others. This projection helps to identify every smallest pore space existing within the data sets. The sum along projection (Fig. 5.5, right) visualizes the thickness of portions by adding the number of portions in the line of sight. This projection is comparable to a density plot. The more portions occur in the line of sight, the brighter the volume will appear, illustrating the three-dimensional distribution as an accentuation of voluminous particles.

The highest porosity of all samples analyzed by non-destructive CT imaging in the present study is 1.26 vol.-% (in a rock salt sample with a hydrocarbon content of ca. 400 mg/kg), whereas the hydrocarbon-free samples show a maximum (mostly artificial) porosity of 0.22 vol.-%. Pores are particularly common along grain boundaries and healed microfractures. In exceptional cases, pores reach up to 7 mm in size.

The porosity values achieved by the 3D reconstructions with VGStudioMAX are slightly higher than those acquired by the ImageJ method. Estimating the error of CT quantifications is difficult because of the lack of alternative porosity measurements upon our samples.

The extracted regions of interest (ROIs) of three samples with macroscopic visible pores show distribution patterns of pore space approximately following the foliation of the rock salt. So, sample RB685.004_CT mainly consists of numerous smaller isolated and few major volumes up to several mm³. The latter are generally rounded, elongated and partially interconnected. Pore space along partly fractured grain boundaries is formed as vesicular patches along one plane. In contrast to some major volumes, most of the extracted particles are not interconnected and appear isolated. However, the exact shape, especially of small volumes, has to be questioned in terms of scan resolution and extraction mode.

The locally increased porosity is an exceptional case of the Gorleben Hauptsalz and presumed to be a remnant of the strong deformation of the hydrocarbon-bearing salt rocks during the salt uprise. The presence of hydrocarbons may be responsible for an incomplete closure and hence a preservation

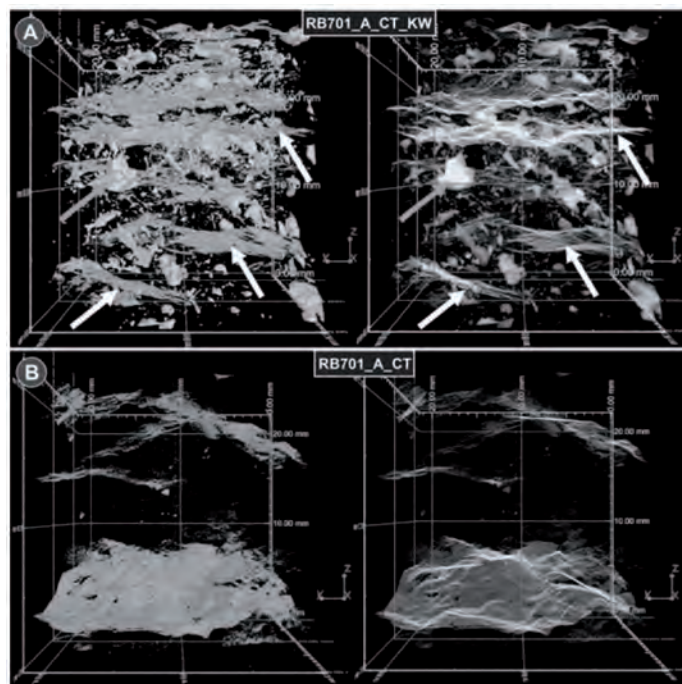


Fig. 5.5: 3D reconstructions of the spatial pore space distributions in a sample with macroscopic visible pores (A, top) and in a sample with planar distribution of porosity (B, below), illustrated by two different projection techniques (“Knäuelsalz”, z2HS1).

Chapter 5: Hydrocarbons in rock salt of the Gorleben salt dome - amount, distribution, origin and influence on geomechanical properties

of these pore structures, which are completely missing in hydrocarbon-free salt rocks. The elevated porosity in naturally deformed rock salt is restricted to hydrocarbon occurrences, which hamper the sealing of open cracks and dilated grain boundaries.

5.3.5. Organic geochemical studies

The quantification of hydrocarbons (C1 to C40) for 210 Hauptsalz samples taken in 2011 and 2012 reveal a background concentration of $< 1 \text{ mg/kg}_{\text{rock}}$. 64% of the samples have a hydrocarbon content $< 1 \text{ mg/kg}$ (i.e. 1 ppm or 0.0001 wt.-%). 70 samples show concentrations between 1 and 50 mg/kg (average 2.66 mg/kg). 5 samples show outlier values up to 443 mg/kg (0.0443 wt.-%, Fig. 5.6, Hammer et al., 2012, 2013).

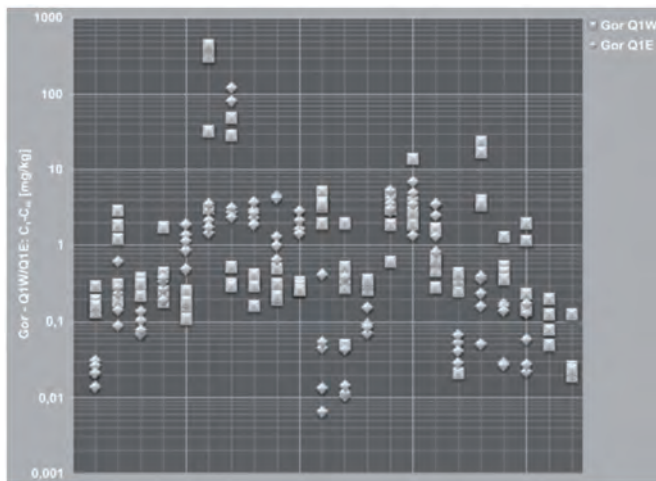


Fig. 5.6: Hydrocarbon content in Gorleben Staßfurt-Hauptsalz. Samples were taken from crosscut 1 West (Gor Q1W) and crosscut 1 East (Gor Q1E).

A visualization of the spatial distribution of hydrocarbon concentrations in adjacent boreholes of crosscut 1 West shows the sum C1–C40 for the samples taken from depth zone 4.5 m to 6.0 m at identical depths over all cores (Fig. 5.7, for more details and results, see Hammer et al., 2012). The visualization confirms the very heterogeneous distribution of hydrocarbons. The geochemical results show a natural hydrocarbon background for the Hauptsalz (z2HS) in crosscuts 1 West and 1 East of $< 1 \text{ mg/kg}$ (C1–C40). The overall concentrations

of hydrocarbons only rise around the large condensate patch (Fig. 5.1), giving a local peak in borehole 02YEQ02RB778 with a maximum concentration of 443 mg/kg (Fig. 5.7).

Analyses of biomarkers (esp. triterpenoid biomarkers) detected in the hydrocarbon mixtures from liquid hydrocarbon occurrences in the Hauptsalz and in nearby potential source rocks (samples were taken from borehole Gorleben Z1), point to the Staßfurt carbonate (z2SK) as source rocks of most or all of the hydrocarbons. The molecular composition of oil in the Gorleben Hauptsalz is significantly different from the extracts of rocks of the Werra unit and of the Upper Permian copper shale, but is consistent with an origin from the organic material in the Staßfurt carbonate (Fig. 5.8).

5.3.6. Laboratory geomechanical tests

To study the influence of the hydrocarbons on creeping and dilatancy of Gorleben Hauptsalz, experimental creep tests were carried out in BGR laboratories. In addition to uniaxial and triaxial tests

Chapter 5:

Hydrocarbons in rock salt of the Gorleben salt dome - amount, distribution, origin and influence on geomechanical properties

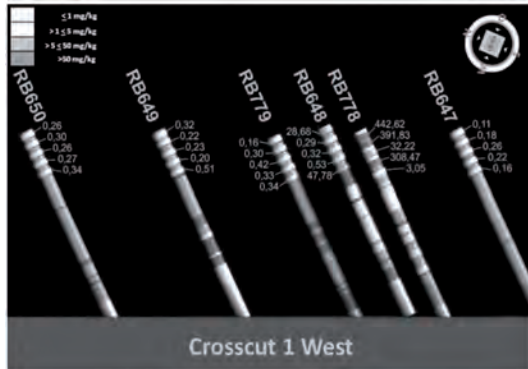


Fig. 5.7: Hydrocarbon content (mg/kg) and distribution in adjacent drillings in Gorleben Staßfurt Hauptsalz (crosscut 1 West).

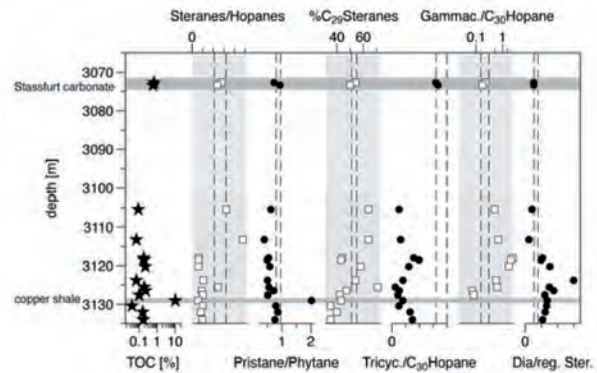


Fig. 5.8: Molecular parameters of selected hydrocarbon biomarkers of oils in the Gorleben Hauptsalz (the hatched areas) and potential source rocks (Staßfurt carbonate and copper shale are indicated) in the Gorleben Z1 borehole.

carried out during the late 1990s (see Schulze 2002, Hunsche et al. 2003, Hammer et al. 2012), new triaxial creep tests at differential stresses of 20 MPa, $T = 30 \text{ }^\circ\text{C}$ and varying confining pressures were carried out to test the influence of hydrocarbons on the beginning of dilatancy. Additionally, the influence of varying temperatures (up to $180 \text{ }^\circ\text{C}$) at differential stresses of 20 MPa on creeping and thermal expansion of Gorleben Hauptsalz were studied in triaxial tests (Schulze 2013).

The experiments demonstrate the lack of any significant influence of hydrocarbons on the creeping or dilatancy of Gorleben Hauptsalz. The position of the dilatancy curve for hydrocarbon-bearing Hauptsalz samples do not change compared to results of Cristescu & Hunsche (1998). After heating experiments at in-situ pressures, no indications of gas fracturing in microstructures could be observed.

Neither the experimental data nor the microscopic studies show any impact of hydrocarbons on the mechanical and hydraulic integrity of the salt barrier in the Gorleben salt dome.

5.4. Summary & Conclusions

The distribution of hydrocarbons within a salt dome depends on the structural-halotectonic development of the salt structure and its lithological composition. Investigations of rock salt of the Gorleben salt dome using ultraviolet light suggest the distribution of fluorescing aromatic hydrocarbons to be very heterogeneous. Isolated, irregular streaks, clusters, clouds and occasionally also dissipated or ragged and interrupted layers of strongly deformed hydrocarbon bearing rock salt are largely restricted to high-strain domains of the Hauptsalz.

Occurrences of hydrocarbons observed at artificial and UV light on the walls and roof of single drifts show that hydrocarbons spread out under gravitational influence. Thus, large patches of hydrocarbons occur, which suggest large domains of hydrocarbons. However, these patches do not represent large,

Chapter 5: Hydrocarbons in rock salt of the Gorleben salt dome - amount, distribution, origin and influence on geomechanical properties

continuously outflowing occurrences, but rather small, locally isolated outflows of hydrocarbons from the rocks into the drifts for a limited period of time.

Thin and thick sections show that hydrocarbons are present as black to brownish fluid inclusions 1) along the grain boundaries of halite; 2) on the surfaces and knuckles or inside microcapillary tubes of anhydrite crystals and anhydrite clusters; 3) in newly formed micro cracks due to drilling or preparation; or 4) very rarely, in micro-porous parts of the Hauptsalz. The occurrences of hydrocarbons are limited to intergranular pores or micropores. Intracrystalline hydrocarbon inclusions were rarely observed. Although intergranular inclusions form small dendritic fluid networks (partly fluid channels), the individual networks are not interconnected over areas exceeding several crystals.

The hydrocarbons usually occur in very low concentrations of less than 1 mg/kg (C1–C40). The Hauptsalz samples with relatively high hydrocarbon concentrations (443 mg/kg as maximum) show enhanced porosities up to 1.26 vol.-%, which is an unusual attribute for Gorleben rock salt. In the Gorleben Hauptsalz, elevated porosities are present only in very few hydrocarbon-bearing rock salt samples, whereas hydrocarbon-free samples are usually characterized by very low porosities and fluid content, which is related to the well-known healing mechanisms of rock salt.

A correlation between hydrocarbon content of samples and their partly elevated porosity indicates that hydrocarbons were responsible for a hampered closure/healing of pore space in deformed halite rocks, which is completely missing in hydrocarbon-free salt rocks. The pore space was mostly generated and incorporated during the polyphasen, halotectonic deformation of salt rocks. Hydrocarbons could inhibit water-halite interaction by coating the solution surfaces as observed by CT studies on Asse rock salt (Zulauf et al., 2010).

The hydrocarbons are mostly autochthonous Zechstein products from thermal alteration of the organic matter of the Staßfurt carbonate (z2SK; see also Gerling et al., 2002, Bornemann et al., 2008). In early phases of halotectonic salt uprise, temporarily elevated permeability could have been caused by uprise-related deformation and accompanied by a release of brines and hydrocarbons from the Staßfurt carbonate (z2SK) into the overlaying Hauptsalz, which was subsequently deformed and reworked.

The total amount of hydrocarbons within the Gorleben Hauptsalz samples is generally low (< 0.05 wt.-%) and not applicable to hydrocarbon-induced fracturing described by Burliga & Czechowski (2010). Based on studies of fault related hydrocarbon occurrences in the Klodawa salt structure (Poland), they emphasize gas and liquid phases to be responsible for the formation and unsealing of shear fractures for longer periods of time.

The geomechanical behaviour of Hauptsalz samples is not significantly affected by the low content of hydrocarbons in the hundred ppm range as maximum.

Chapter 5: Hydrocarbons in rock salt of the Gorleben salt dome - amount, distribution, origin and influence on geomechanical properties

5.5. Acknowledgements

The authors would like to thank L. Fleckenstein, J. Kutowski, M. Saßnowski, S. Heydecke, F. Kohnert, W. Grewe, M. Wietzki, M. Otto (DBE) for the assistance in Gorleben during sampling and documentation, M. Gern, R. Götze and T. Faust (BGR) for sample and thin/thick sections preparation, N. Fitz, G. Scheeder, S. Schlömer, A. Tietjen, S. Krugman, M. Weiß, A. Vidal, J. Poggenburg and D. Graskamp (BGR) for geochemical analyses, DBE Gorleben for photos from excavations, and Lennart Ptock for picture editing.

5.6. References

- Bornemann, O., Behlau, J., Fischbeck, R., Hammer, J., Jaritz, W., Keller, S., Mingerzahn, G. & Schramm, M. 2008. Description of the Gorleben site, part 3: Results of the geological surface and underground exploration of the salt formation. Report Bundesanst. Geowiss. Rohstoffe (BGR), 223 p., Hannover.
- Burliga, S. & Czechowski, F. 2010. Anatomy of hydrocarbon bearing zones, hydrocarbon provenance and their contribution to brittle fracturing of rock salt in the Klodawa Salt Structure (central Poland). SMRI Spring 2010 Techn. Conf., Grand Junction, USA.
- Cristescu, N. & Hunsche, U. 1998. Time effects in rock mechanics. Series: Materials, modeling and computation. John Wiley & Sons, Chichester (UK), 342 pp.
- Gerling, P., Beer, W. & Bornemann, O. 1991. Gasförmige Kohlenwasserstoffe in Evaporiten des deutschen Zechsteins. Kali & Steinsalz, 10, 376– 383.
- Gerling, P. & Faber, E. 2001. Dokumentation der chemischen Analysen von gasförmigen und flüssigen Kohlenwasserstoffen. Report Bundesanst. Geowiss. Rohstoffe (BGR), No. 10717/01, 20 p., Hannover.
- Gerling, P., Faber, E. & Wehner, H. 2002. Interpretation der chemischen Analysen von gasförmigen und flüssigen Kohlenwasserstoffen. Report Bundesanst. Geowiss. Rohstoffe, No. 12243/02, 82 p., Hannover.
- Hammer, J., Pusch, M., Häger, A., Ostertag-Henning, C., Schlömer, S., Mingerzahn, G., Scheeder, G., Shao, H., Paul, B., Schulze, O., Zaretzki, B. & Hesser, J. 2012. Untersuchungen von Kohlenwasserstoffen im Erkundungsbergwerk Gorleben. Interim report 2011. Report, Bundesanst. Geowiss. Rohstoffe, 236 p., Hannover.
- Hammer, J., Pusch, M., Häger, A., Scheeder, G., Shao, H., Paul, B., Ostertag-Henning, C., Mingerzahn, G., Schlömer, S. & Hesser, J. 2013. Untersuchungen von Kohlenwasserstoffen im Erkundungsbergwerk Gorleben. Interim report 2012. Report, Bundesanst. Geowiss. Rohstoffe, 207 p., Hannover.
- Hunsche, U., Schulze, O., Walter, F. & Plischke, I. 2003. Thermomechanisches Verhalten von Salzgestein. Abschlussbericht zum Arbeitspaket 9G213811. Report, Bundesanst. Geowiss. Rohstoffe, Hannover.

Chapter 5: Hydrocarbons in rock salt of the Gorleben salt dome - amount, distribution, origin and influence on geomechanical properties

- Löffler, J. & Schulze, G. 1962. Die Kali- und Steinsalzlagerstätten des Zechsteins in der Deutschen Demokratischen Republik. Teil III: Sachsen-Anhalt. Freiberg. Forschungsh., C 97/III, 347 p.
- Popp, T., Fscher, M. & Kern, H. 2002. Gefügekundliche Untersuchungen zur Verteilung von Kohlenwasserstoffen (KW) in Steinsalz. *Meyniana* 54, 131-154.
- Pusch, M., Hammer, J., Kus, K., Klosa, D., Thiemeyer, N. & Mingerzahn, G. 2014. Macro- and microscale distribution of hydrocarbons in the Staßfurt Hauptsalz of the Gorleben salt dome. *German Journal of Geosciences* 165, 3-14, ISSN-1860-1804.
- Schulze, O. 2002. Auswirkung der Gasentwicklung auf die Integrität geringdurchlässiger Barrieregesteine. Fachbericht zum Arbeitspaket 9Y32130300000, Report, Bundesanst. Geowiss. Rohstoffe, Hannover.
- Schulze, O. 2013. Geotechnische Laborarbeiten im Rahmen der Erkundung Gorleben. Laboruntersuchungen zu den thermo-mechanischen Eigenschaften von Steinsalz mit KW-Imprägnationen. Ergebnisbericht. Report, Bundesanst. Geowiss. Rohstoffe, Hannover, 69 p.
- Siemann, M. G. 2007. Herkunft und Migration mineralgebundener Gase der Zechstein 2 Schichten in Zielitz. *Kali und Steinsalz* 3/2007, 26-41.
- Thiemeyer, N., Pusch, M., Hammer, J. & Zulauf, G. 2014. Quantification and 3D visualisation of pore space in Gorleben rock salt: constraints from CT imaging and microfabrics. *German Journal of Geosciences* 165, 15-25, ISSN-1860-1804.
- Tissot, B. P. & Welte, D. H. 1984. *Petroleum formation and occurrence*. Springer-Verlag, Berlin Heidelberg, 699 p.
- Zulauf, G., Zulauf, J., Bornemann, O., Brenker, F. E., Höfer, H. E., Peinl, M. & Woodland, A. B. 2010. Experimental deformation of a single-layer anhydrite in halite matrix under bulk constriction. Part 2: Deformation mechanisms and the role of fluids. *J. Struct. Geol.* 32, 264-277.

Chapter 6

Quantification and 3D visualisation of pore space in Gorleben rock salt: Constraints from CT imaging and microfabrics

Nicolas Thiemeyer¹, Maximilian Pusch², Jörg Hammer² & Gernold Zulauf¹

¹*Institute of Geoscience, Goethe-University Frankfurt am Main, Altenhöferallee 1, 60438 Frankfurt am Main, Germany.*

²*Federal Institute for Geosciences and Natural Resources (BGR), GeoZentrum Hannover, Stilleweg 2, 30655 Hannover, Germany*

Abstract

Computed tomography (CT) was applied to visualise and to quantify the porosity of hydrocarbon-bearing and hydrocarbon-free Staßfurt rock salt (z2HS) drill cores collected from the Gorleben salt dome. This technique reveals the spatial distribution of porosity and possible fluid accumulations at different scales. Porosity was quantified by calculating greyscale portions of the CT data sets and by virtual extraction and three-dimensional reconstruction of the pore space. The non-destructive CT imaging determines a maximum porosity of 1.26 Vol.-% in a rock salt sample with relatively high hydrocarbon content of several hundred ppm. A locally elevated porosity within some drill cores is an unusual attribute for the Gorleben rock salt and presumed to be a remnant of the strong deformation of the hydrocarbon-bearing salt rocks and specific conditions of healing during the salt uprise. Microstructural investigations of epoxy resin-impregnated samples allowed detailed observations regarding the pore space characteristics. Pores are particularly common along grain boundaries and healed microfractures. In exceptional cases, pores reach up to 7 mm in size. Our observations imply that the presence of hydrocarbons may be responsible for a hampered closure and a preserving of pore structures, which are completely missing in hydrocarbon-free salt rocks.

Keywords: Gorleben, rock salt, CT imaging, porosity, hydrocarbons, fluids

[German Journal of Geosciences 165 \(1\), 15-25. DOI: 10.1127/1860-1804/2013/0050.](#)

Chapter 6: Quantification and 3D visualization of pore space in Gorleben rock salt: constraints from CT imaging and microfabrics

6.1. Introduction

Rock salt is well known for its good barrier properties, particularly the low permeability and the low porosity as well as creeping and healing capacities (Sutherland & Cave 1980, Peach 1991, Stormont & Daemen 1992, De Las Cuevas 1997, Stormont 1997, Popp et al. 2007, Bornemann et al. 2008, Bräuer et al. 2011, Popp et al. 2012). As rock salt is almost impermeable for gases and fluids, it is regarded as a suitable medium for nuclear waste repositories.

The permeability of rock salt depends in a complex way on porosity, pore size and pore structure (Spangenberg et al. 1998). Bulk porosity for both naturally deformed and synthetic rock salt is reported to be mostly < 1 % (Peach 1991, Stormont & Daemen 1992, Stormont 1997). The pores are usually filled with brine or gases (Stormont 1997). De las Cuevas (1997) defined a primary porosity, which means the void structure left after deposition of the rock salt, and a secondary porosity, which means tectonically- or man-induced porosity by fracturing. Stormont (1997) describes permeability and porosity occurring as a result of dilation and sliding along grain boundaries. Initial pathways usually develop along grain boundaries and subsequently along axial intragranular tensile cracks (Stormont & Daemen 1992, Chen et al. 2012). Higher porosities can evolve due to impurities, such as anhydrite or clay minerals (Peach 1991, De las Cuevas 1997), in exceptional cases in synthetic, re-compacted rock salt samples deriving from crushed salt (Salzer et al. 2007) or due to artificial fracturing during sampling (Stormont & Daemen 1992). Deformation has been suggested to substantially influence the porosity in rock salt. By exceeding the dilatancy boundary subsequent microcracking can increase the porosity (Schulze et al. 2001). In the brittle structural level, an increase of the axial strain causes an increase of the porosity and permeability. The confining pressure plays a significant role for porosity and permeability of rock salt (Peach et al. 2001). The higher the confining pressure, the more difficult is the initiation and opening of fractures. In this relation Stormont & Daemen (1992) demonstrate that high confining pressures will cause a slower increase of porosity and permeability during deformation than at lower confining pressure conditions. Generally, the mechanical properties of rock salt (creeping) prevent the conservation of open fractures and pathways (Popp et al. 2007). The ability for self-healing (Stormont & Daemen 1992, Schulze et al. 2001) leads by time to a closure of previously open pathways because of the high ductility of halite (Schulze et al. 2001). The permanent healing reduces the porosity and permeability. It is irreversible and related to plastic flow along grain boundaries (Stormont & Damen 1992). The consolidation of rock salt at hydrostatic pressure counteracts crack propagation and reduces porosity and permeability, including solution, re-precipitation and recrystallization (Schulze 2007).

The permeability of undisturbed rock salt is approximately 10^{-21} m² (Sutherland & Cave 1980, Stormont & Daemen 1992, Stormont 1997, De las Cuevas 1997, Alkan 2009). Furthermore, low (gas) permeability can be caused either by substantial capillary pressure of brine or disconnection of the pore volume (Stormont 1997). A re-established integrity of hydrocarbon-impregnated parts of the Gorleben

Chapter 6: Quantification and 3D visualization of pore space in Gorleben rock salt: constraints from CT imaging and microfabrics

Knäuelsalz (z2HS1) is proven by their low permeability in the range of 10^{-22} m² to 10^{-19} m² (Hammer et al. 2012).

At certain pressure and temperature conditions rock salt loses its sealing capacity as reported by Schoenherr et al. (2007), which is an explanation for hydrocarbons migrating into salt layers at higher depths. As soon as the fluid pressure of reservoirs exceeds the minimal principal stress and the capillary pressure of the surrounding rock ($P_{\text{fluid}} > \sigma_3 + P_{\text{capillary}}$) the sealing capacity of rock salt is disturbed and fluid (or hydrocarbon) migration can be enhanced (Schoenherr et al. 2007, Burliga & Czechowski 2010). Therefore, an elevated porosity in naturally deformed rock salt can be related to hydrocarbon occurrences, which hamper the sealing of cracks and dilated grain boundaries in combination with high fluid pressures (Burliga & Czechowski 2010, Schoenherr et al. 2007).

One accurate and comfortable technique to quantify and visualise pore structures or structural inventories of any solid material without destructing the sample is computed tomography (CT). Nowadays, this technique provides new possibilities, especially in visualisation, for progressive research in the oil industry or in material science. So far, the technique is gradually being established in geoscience (see Mees et al. 2003 and references therein, Füsseis et al. 2009). A field of intensive use of CT techniques are sediment core analyses (Rothwell & Rack 2006) in order to characterise fracture patterns or distribution of mineral parageneses.

In contrast, CT studies of rock salt are rare (e.g. Zulauf et al. 2009, 2012, Burliga & Czechowski 2010, Mertineit et al. 2012). In order to visualise and quantify porosity, this technique has been proved as useful method and was applied by Burliga & Czechowski (2010), who analysed hydrocarbon-bearing zones in the Klodawa Salt Structure (Poland). Thus, in combination with 3D visualisation software, any structures distinguishable by density contrasts can be visualised and quantified. So far, CT imaging offers the possibility to analyse three-dimensional patterns in rock salt at different scales.

The aim of the present study is to visualise, characterise and quantify the geometry and spatial distribution of gas and fluid-filled pore space in Staßfurt rock salt of Gorleben salt dome using computed tomography and microstructural investigations.

6.2. Samples and methodology

6.2.1. Samples

The *Knäuelsalz* (z2HS1) is the lowermost and oldest part of the initial up to 800 m thick Hauptsalz unit of the Staßfurt-Folge (z2HS), which forms the central part of the Gorleben salt dome up to the depth of ca. 3000 m (Bornemann et al. 2008). The Knäuelsalz consists of middle to coarse grained rock salt with relatively rare anhydrite impurities forming characteristic scattered anhydrite nodules and clusters (up

Chapter 6: Quantification and 3D visualization of pore space in Gorleben rock salt: constraints from CT imaging and microfabrics

to 8 Vol.-%; Bornemann et al. 2008). We investigated five rock salt samples from cores of exploration bore holes in Querschlag 1 West in the first exploration area (EB1) at the 840 m level. Three samples (RB685.004_CT, RB686.005_CT and RB687.005_CT; Tab. 6.1) are macroscopically characterised by pores and microcavities up to 7 mm in size as an exceptional characteristic for hydrocarbon-bearing Knäuelsalz samples, which is generally characterised by low water content and low permeability (Bornemann et al. 2008, Hammer et al. 2012). The samples with macroscopic visible pores originate from drill cores of ca. 32 mm in diameter and contain a relatively high (several hundred ppm) amount of hydrocarbons, which are mostly autochthonous Zechstein products from thermal alteration of the organic matter of the Staßfurt-Karbonat (z2SK; Gerling et al. 2002, Bornemann et al. 2008). They are assumed to have migrated from the subjacent Zechstein carbonates during the early halokinetic uprise. Their heterogeneous distribution in Gorleben salt dome is the subject of current research (Hammer et al. 2012). Two samples of Knäuelsalz (RB652.015_CT and RB657.008_CT; Tab. 6.1) are regarded as reference samples of low porosity and without any macroscopic visible pores which were collected from drill cores of 72 mm in diameter.

6.2.2. CT imaging

Computed tomography studies were carried out using a Phoenix nanotom s (GE Sensing and Inspection Technologies) equipped with a XS 180 NF tube and a Hamamatsu detector at the Goethe University of Frankfurt am Main. CT imaging was performed on non-impregnated samples before further preparation. The drill core samples are clamped into a rotating specimen holder between the X-ray source (W filament and Be target) and the detector. The requested number of images defines the rotating angle per step of the holder. At every step, multiple pictures are averaged to one final picture for noise reduction. The number of averaged pictures per step, the requested number of final images and the exposure time of each photo taken affect the quality and the scan time of the scanning process. The dimensions (x, y and z in [mm]) give the edge length of the analysed volumes. Our scan resolution slightly differs from 13.21 μm to 17.68 μm caused by variations in distance between the specimen holder, the detector and the X-ray source during scan procedures. The low-porosity samples are smaller in size leading to an improved resolution in these cases. The final set of pictures is combined and reconstructed to a designated 3D data set with the appropriate regions of interest (ROI). The scan parameters are summarized in Table 6.1.

6.2.3. Data processing

The basic concept of two quantification methods presented in this study involves graphically based differentiation, disconnection and extraction of the relevant volumes. Grey value variations are the basis of every applied processing in order to quantify mineral phases, fluids, pore space or random portions of the data sets.

Chapter 6: Quantification and 3D visualization of pore space in Gorleben rock salt: constraints from CT imaging and microfabrics

Sample	Scan time [min]	Raw images	Dimensions x: y: z [mm]	Scan volume [mm ³]	Resolution [μm]	Macroscopic visible pores	Hydrocarbon content [mg/kg]	Porosity _{abs} [mm ³]		Porosity _{rel} [Vol.-%]	
								VGStudio MAX	ImageJ	VGStudio MAX	ImageJ
RB685.004_CT	185	3000	22.19; 22.60; 38.47	1.93E+04	17.52	+	47.8*	118	91	0.61	0.47
RB686.005_CT	205	3000	21.43; 21.46; 37.69	1.73E+04	17.68	+	443*	218	182	1.26	1.05
RB687.005_CT	205	3000	21.26; 22.14; 36.54	1.72E+04	16.18	+	392*	175	161	1.02	0.94
RB652.015_CT	168	2600	16.08; 13.99; 21.83	4.91E+03	13.33	-	1.96	11	13	0.23	0.28
RB657.008_CT	200	2600	15.54; 13.74; 20.99	4.48E+03	13.21	-	0.02	10	6	0.22	0.13

Table 6.1: Scan parameters and porosity determined by ImageJ and VGStudio MAX. Variations in scan time are caused by different acquiring parameters. The resolution is dominantly predefined by sample size. *Hydrocarbon contents deriving from adjacent, correlated drillcore samples (Hammer et al. 2012).

One method operates with the software VGStudio MAX. This software provides a tool for manual extraction of every region of interest (ROI) by choosing an adjustable greyscale tolerance. Thus, strong material contrasts (grey value contrasts) and good noise reduction are advantageous for distinguishing ROIs (Fig. 6.1). Noise reduction can be supported by filtering the data sets (e.g. Median or Gaussian). The stepwise extracted final ROI can be displayed as a three-dimensional projection in a new data set. The projection can be visualised in different styles and its properties now include accurate information about the dimensions, voxel count, resolution and volume as voxel count or in mm³.

Besides the information on precise volume and size, the 3D reconstruction illustrates the characteristic

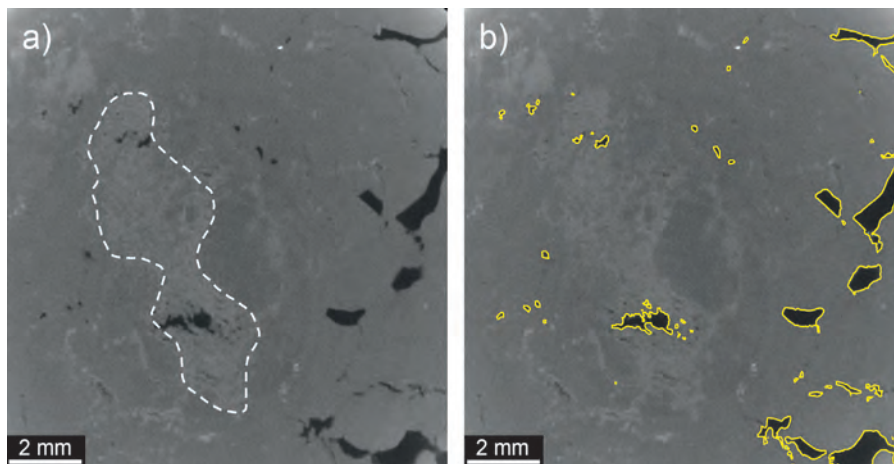


Fig. 6.1: 2D slice of the computer tomography raw scan data set of sample RB686.005_CT. a) Anhydrite is displayed as light grey patches (white dashed line). Pore space (dark fraction) can be located within the anhydrite clusters, along microfractures and grain boundaries and shows irregular voids up to mm in size. b) The yellow portions were manually extracted in VGStudio MAX and form the 3D reconstructions (see Figs. 6.2, 6.3 and 6.7). Very small fractions and diffuse structures cannot be extracted due to the limited grey-value contrast and to data set filtering.

Chapter 6: Quantification and 3D visualization of pore space in Gorleben rock salt: constraints from CT imaging and microfabrics

spatial distribution of the extracted volume (Fig. 6.2). Distribution anisotropies, preferred orientations and shapes of single objects can be studied in detail. Furthermore, the 3D data set can be turned, sliced or magnified in every possible direction in order to follow the complete inventory of objects. Videos of rotating 3D objects or customized camera routes can be generated by VGStudio MAX or by alternative freeware.

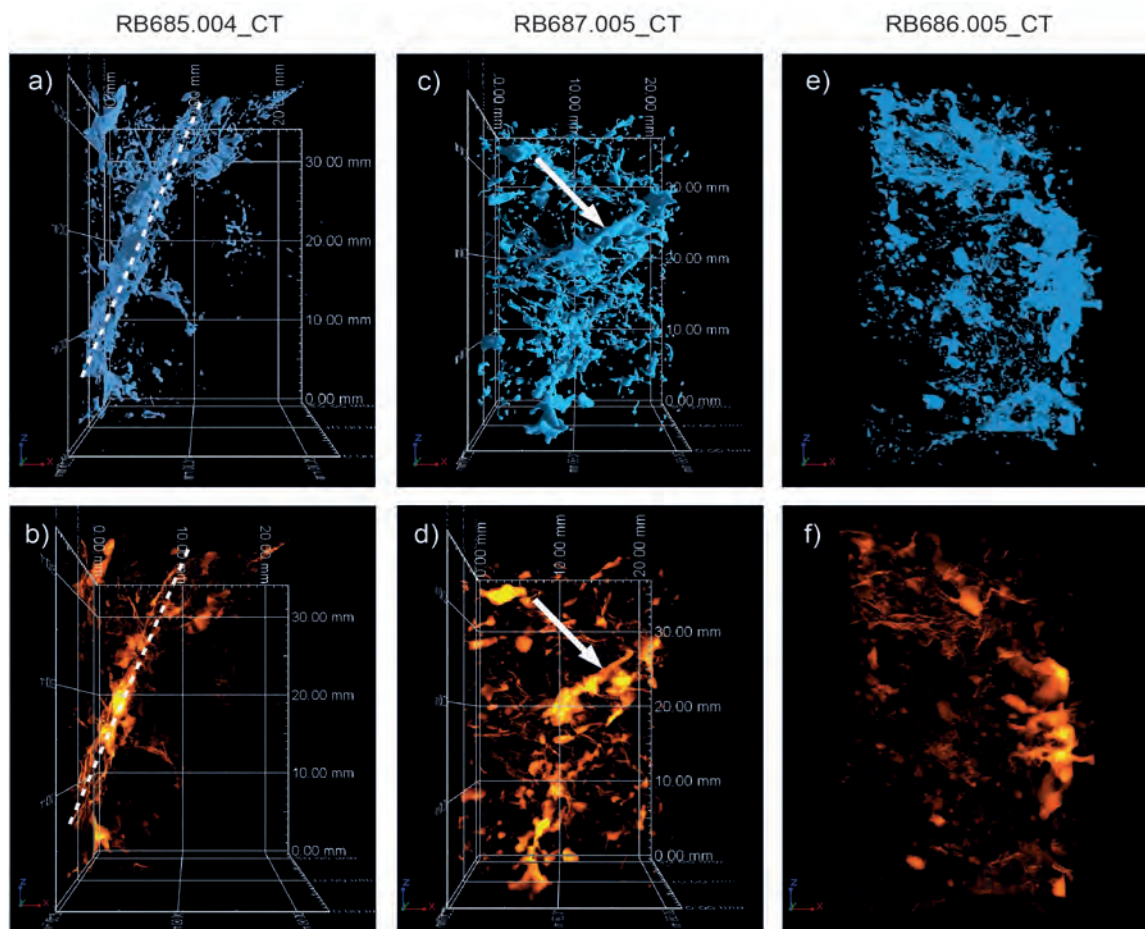


Fig. 6.2: 3D reconstructions of the spatial pore space distributions in samples with macroscopic visible pores. The blue projections (Volume renderer; Figs. 6.2a, c and e) portray the surface of the particles extracted, whereby every particle is displayed in the same intensity. The orange reconstructions (sum along projection; Figs. 6.2b, d and f) show the density distribution of the pore space. Sample RB685.004_CT (Figs. 6.2a and b) shows an alignment of pore space along a steep dipping zone (white dashed line) and its heterogeneous distribution. Sample RB687.005_CT (Figs. 6.2c and d) is characterized by a tube structure in the central part (white arrow) and drop like shapes of few major voids. The pore space distribution in sample RB687.005 is more homogenous than in sample RB685.004_CT. Sample RB686.005_CT (Figs 6.2. e and f) shows a concentration of porosity on the right side (same scale as in RB685.004_CT).

The second method for quantifying volumes is based on the freeware ImageJ. Whereas the previous method has its focus on manual extraction, this method detects all voxels of an image stack in a

Chapter 6: Quantification and 3D visualization of pore space in Gorleben rock salt: constraints from CT imaging and microfabrics

selectable, defined threshold of greyscales. By summarizing the selected threshold voxels, the ratio relating to the total data set voxels gives the percentage of the selected volume, and the total volume can be calculated referring to the known voxel size. Although this method is relatively fast, three-dimensional properties and the visualising aspect with all its advantages remains ambiguous.

6.2.4. Microfabric studies

After CT imaging, the drill cores of the Knäuelsalz were vacuum-impregnated with blue coloured epoxy resin. The aim was to harden the samples for preparation and to reveal the shape, the contact boundaries and the distribution of porosity volumes and fractures at macroscopic and microscopic scales. The drill cores with visible pores are 32 mm in diameter and were cut perpendicular and parallel to the drilling direction. The thick sections of 1 mm thickness were analysed using reflected and transmitted light microscopy and were etched after Urai (1987) to investigate the subgrain fabrics.

6.3. Results

6.3.1. CT imaging, 3D reconstruction and porosity quantification

The distribution of halite, anhydrite and pore space, observed in the thick sections, can be recognised in the 2D slices of the scan volumes (Fig. 6.1). These data sets consist of three major greyscale units.

Anhydrite clusters are portrayed as light grey patches. Since the selected scan parameters result in a lower resolution, single inclusions of anhydrite crystals cannot be precisely detected in shape. However, the clusters show the characteristic shapes observed in thick sections. They can cover halite grains or form large cloudy patches of different shapes and dimensions. Rarely, small inclusions of minerals with high density (such as celestine and pyrite) appear as white spots or microaggregates. They only occur as accessory inclusions and are rarely distributed within the rock salt.

Halite is in the mid-range of the greyscale and forms up to 95 % of the scan volumes. The exact shape of halite grains can only be visible if a contrast with the surrounding phases exists, e.g. with anhydrite accumulations. Fractured grain boundaries or microfractures, generally containing fluid films, are visible as dark grey domains. Our chosen resolution parameters (Tab. 6.1) do not allow the observation of small single grain boundary fluid inclusions.

Pore space is shown by the darkest parts within the raw data sets (Fig. 6.1). High porous domains can be located in the scan volumes at halite grain boundaries or within anhydrite clusters in different shape and size. Although major cavities mostly show wavy and rounded boundaries to the surrounding rock salt, some of them appear as polygons with straight margins indicating the presence of euhedral halite crystals.

The shape of porous portions within the anhydrite clusters can be visualised only indistinctly due to the cloudy and fine-meshed shape. Although not every anhydrite cluster contains a certain amount

Chapter 6: Quantification and 3D visualization of pore space in Gorleben rock salt: constraints from CT imaging and microfabrics

of porosity, some illustrate an irregular, patchy network of pore space. Besides small clear pockets, a granular sparkling of pore space is observable within the anhydrite nests in the scan volumes (Fig. 6.1).

The 3D reconstructions presented in two different visualisation modes reveal the distribution and shape of porous zones in the Knäuelsalz samples. The blue projections (Volume renderer, Figs. 6.2a, c, e) show every pore space in the same intensity, whereby some domains are hidden by others. This projection helps to identify every smallest pore space existing within the data sets. The orange sum along projection (Figs. 6.2b, d, f) visualises the thickness of portions by adding the number of portions in the line of sight. This projection is comparable to a density plot. The more portions occur in the line of sight, the brighter the volume will appear, illustrating the three-dimensional distribution as an accentuation of voluminous particles.

The extracted ROI of the three samples with macroscopic visible pores show distribution patterns of pore space, which approximately follow the foliation of the rock salt in two cases (Figs. 6.2a and c). Sample RB685.004_CT mainly consists of numerous smaller isolated and few major volumes up to several mm³. The latter are generally rounded, elongated and partially interconnected. Pore space along partly fractured grain boundaries is formed as vesicular patches along one plane. In contrast to some major volumes, most of the extracted particles are not interconnected and appear isolated. However, the exact shape, especially of small volumes, has to be questioned in terms of scan resolution and extraction mode. The complete extracted data set of sample RB685.004_CT shows a significant orientation of increased porosity along a 65° steep dipping zone (Figs. 6.2a and b; white dashed line). Most pores are located on one side of the scanned drill core implying a structural control on the distribution of enhanced porosity.

The 3D reconstruction of sample RB687.005_CT displays additional distribution patterns of pore space. Generally, larger pore spaces are observable. Only some vesicular patches occur as a branching network in the central part of the reconstruction. Additionally, a clear developed tube structure in the centre (Figs. 6.2c and d, white arrow) proceeds along several mm to give an apparent microchannel.

The 3D reconstruction of sample RB686.005_CT shows distribution anisotropy of pore space corresponding to sample RB685.004_CT. RB686.005_CT is dominantly composed of smaller vesicular patches, isolated small inclusions and some mm-sized pores which are partly connected. They rather appear as single, randomly distributed isolated volumes. The major volumes show well-rounded shapes and clear smooth surfaces, which is a consequence of good grey value contrasts of the raw data sets. The sum-along projection shows the main volumes located in the central part along one side. The upper part of the reconstruction is more diffuse (Figs. 6.2e and f).

The samples RB657.008_CT and RB652.015_CT are clearly distinct from the porous samples described above. Sample RB657.008_CT shows only one fuzzy planar structure beside some subordinate fragments occurring as cloudy patches (Figs. 6.3a and b). Pores of mm size with sharp edges and smooth surfaces

Chapter 6: Quantification and 3D visualization of pore space in Gorleben rock salt: constraints from CT imaging and microfabrics

are completely missing. Sample RB652.015_CT is characterised by small, homogeneously distributed pores and some patchy films, especially in the upper part of the 3D reconstruction (Figs. 6.3c and d). A preferred orientation of the low pore volume is present.

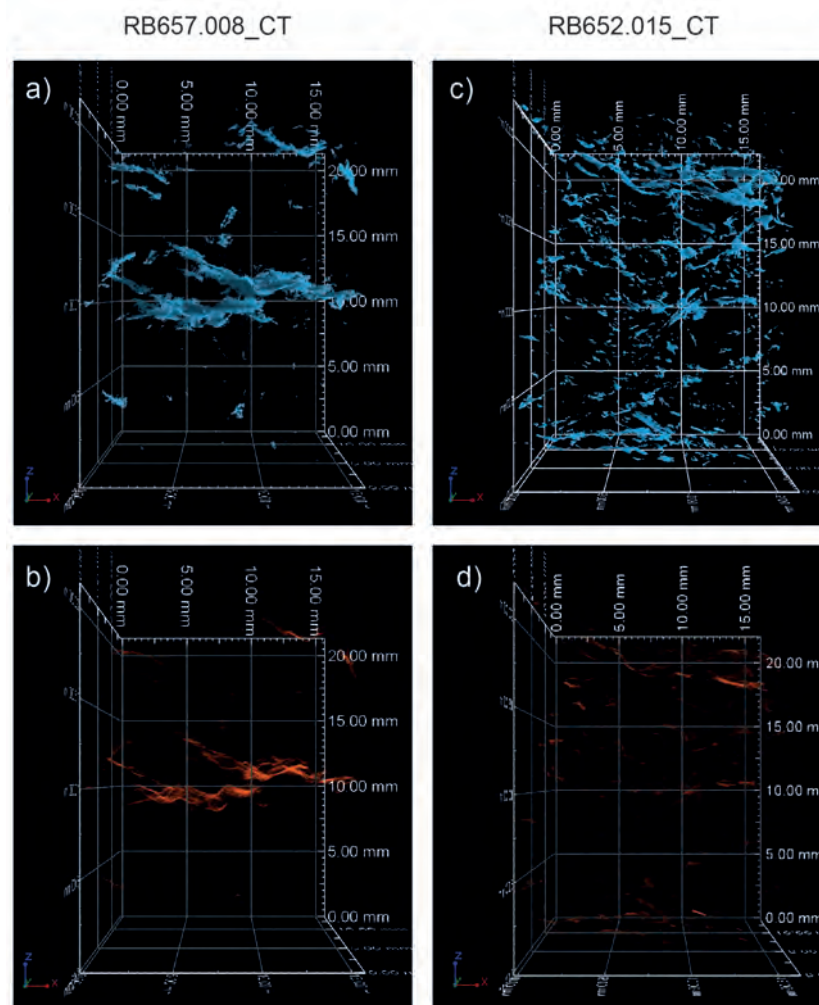


Fig. 6.3: The 3D reconstruction of the spatial pore space for the two less porous samples without macroscopic visible pores show different porosity patterns. Sample RB657.008_CT is characterized by one main penetrative structure (Figs. 6.3a and b) whereas sample RB652.015_CT (Figs. 6.3c and d) shows homogeneously distributed isolated pores and films of small size and volume.

Table 6.1 lists the calculated porosities acquired by the two different digital techniques presented in this study. The hydrocarbon-bearing sample RB686.005_CT contains the highest porosity of all samples analysed in the present study (1.26 Vol.-%), whereas the hydrocarbon-free sample shows a maximum porosity of 0.22 Vol.-%. The porosity values achieved by the 3D reconstructions with VGStudio MAX are

Chapter 6: Quantification and 3D visualization of pore space in Gorleben rock salt: constraints from CT imaging and microfabrics

slightly higher than those acquired by the ImageJ method. Estimating the error of our CT quantifications is difficult because of the lack of alternative porosity measurements upon our samples.

6.3.2. Microfabrics and the distribution of fluids and pore space

Anhydrite characterizes the microstructure of the Knäuelsalz in a distinctive manner (Fig. 6.4a). Single anhydrite crystals range from 20 μm up to 200 μm in diameter and occur as single inter- or intracrystalline solid inclusions or as characteristic clusters and nests consisting of numerous agglutinated anhydrite crystals agglomerated. These clusters can coat halite grains or form patches with diffuse and irregular shapes. Once they follow halite grain boundaries, they emphasise the slight foliation of the Knäuelsalz. The Knäuelsalz usually has a grain shape anisotropy resulting in a moderate foliation. Primary

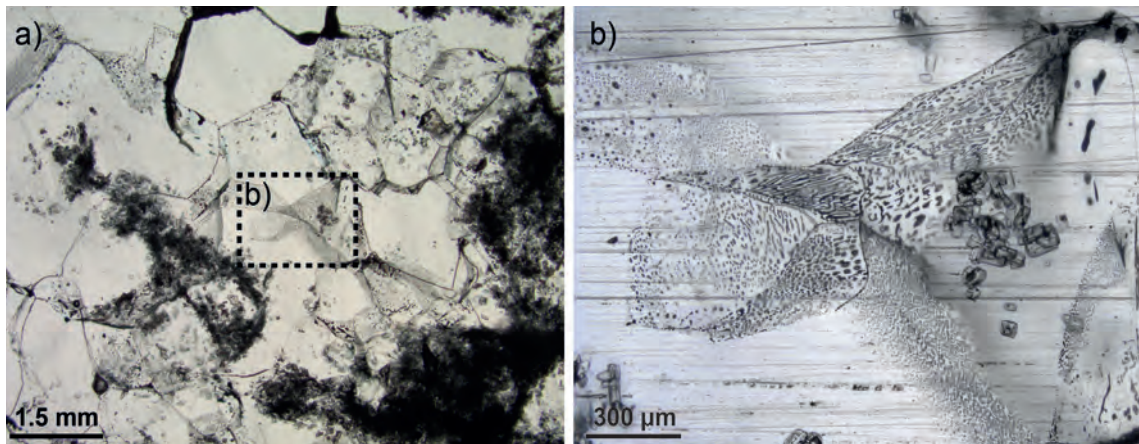


Fig. 6.4: a) Microphotograph of sample RB686.005_CT. Anhydrite clusters (dark nests) are a characteristic attribute for the microstructure of the Knäuelsalz (z2HS1). b) Microphotograph (black dashed box in Fig. 6.4a) of sample RB652.015_CT. Halite grain boundaries decorated with fluid inclusions. The microphotograph results from different images of multiple layers (z-stack) and shows the three-dimensional distribution of grain boundary fluids. Both microphotographs in transmitted light with parallel polarizers.

structures like bedding are generally not or very rarely preserved due to halokinetic deformation and recrystallization. Subgrain fabrics of etched halite crystals (Fig. 6.5b and 5c) indicate climb-accommodated movement of dislocations (Passchier & Trouw 2005). Wavy and irregular halite grain boundaries point to strain-induced grain boundary migration or to pressure solution processes.

The rock salt samples show a manifold inventory of fluid inclusions preserved as bubbles, stripes, branching networks, vermicular lines and fluid films (Fig. 6.4b). They mainly occur on halite grain boundaries and along boundaries between halite and anhydrite (Herrmann & Knipping 1993). Additionally, anhydrite clusters show clear assemblages of fluid phases due to the high surface area.

The amount of pore space capable for fluid (hydrocarbon) storage in three of the five samples studied is clearly revealed by the blue-coloured resin. In this case, the term pore space is used for any void

Chapter 6: Quantification and 3D visualization of pore space in Gorleben rock salt: constraints from CT imaging and microfabrics

structure exceeding the common size of grain boundary fluid inclusions, although they are filled with gas or fluid. Pore space dimensions gradually range from several μm to a maximum of 7 mm. Cutting the samples after impregnation with coloured resin shows that the injection depth is low by trend, attesting either to the high viscosity of resin or the general low permeability of rock salt. Therefore, cutting planes of the impregnated hand specimens reveal fewer coloured pore space than previously expected.

A certain amount of porosity is located within the anhydrite clusters. This porosity is illustrated by a small amount of injected resin, giving a slightly blue shine (Fig. 6.5a). Nevertheless, the abundance of anhydrite constricts a detailed observation of the resin distribution in the pore volume of these clusters. Grain boundaries exhibit pores with different shape. A small amount of resin occurs at triple junctions

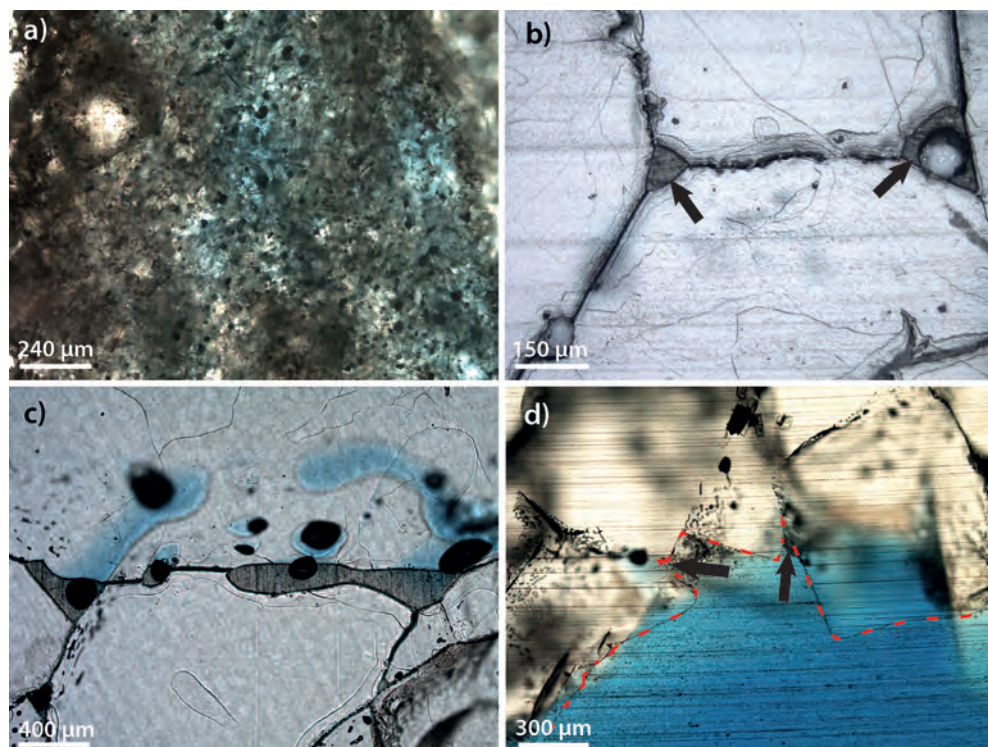


Fig. 6.5: Different sites of enhanced porosity in thick sections of sample RB686.005_CT. Such sites are also visible within the CT raw data sets (see Fig. 6.1). a) Pore space within anhydrite clusters revealed by blue resin; transmitted light. b) Small volumes of resin (black arrows) located at triple junctions of halite grain boundaries. Their size exceeds the usual size of grain boundary fluid inclusions. The right junction shows a bubble filled with powder from polishing, which suggests the pore space was filled with air before preparation; etched sample under reflected light. c) Resin filling of triple junction pore space and along halite grain boundary. Note the partly wavy void structure. Remaining air bubbles from thin section preparation are noticeable as black circles. The blue coloured resin can be tracked at depth; etched sample under transmitted light. d) Partly wavy boundary (red dashed line) of halite and resin filled void of mm size. Resin enters gaps along halite grain boundaries (black arrows) and traces halite crystals; transmitted light.

Chapter 6: Quantification and 3D visualization of pore space in Gorleben rock salt: constraints from CT imaging and microfabrics

of halite crystals or as alignments of small pores of about 50 μm located along grain boundaries (Figs. 6.5b and c). Higher porosities at grain boundaries show stripes or pinching and swelling, leading to a stepwise separation of single halite grains. These stripes can vary in thickness and grow to major volumes of about 1 mm until the former grain boundary-related formation is no longer observable. The main portion of resin was inserted into pores up to several mm^3 in size (Fig. 6.5d). These volumes exceed the usual known pore space of natural rock salt samples from salt domes in size and are visible only in some hydrocarbon-bearing hand specimens. The halite-resin boundaries are usually wavy and undulating (Fig. 6.5d). In some cases these edges seem to be controlled by crystal faces and the orientation of halite crystals.

6.4. Discussion

6.4.1. Limitations and uncertainties of CT quantification

The basis for volume extraction out of CT raw data sets is given by grey value contrasts. Diffuse structures or smaller inclusions cannot be captured properly and show inaccurate shapes. This diffuse appearance is related to the small size of the analysed object and the limited scan resolution. Fig. 6.6 shows the difficulty in selecting diffuse structures with the VGStudio MAX extraction tool. At low magnification, the pore boundary is clearly visible. When magnified, the structure becomes indistinct and shows single voxels with only little variation in grey values. Especially for grain boundaries or fluid films, which only involve very few voxels in diameter and appear more diffuse, it is possible that single voxels are included (or missing) within the ROI. Therefore, a slight inaccuracy of extracted volumes has to be expected, which explains the discrepancy of the acquired volumes by the two different methods. An exact error estimation of our CT study is hard to ascertain and should be determined by additional scanning measurements in comparison to established porosity analyses in order to evaluate a statistical error.

The scan resolutions are predefined by the sample size and range from 13.21 μm up to 17.68 μm . Therefore, objects smaller than approximately 50 μm (equivalent to only 3 voxels) cannot be extracted precisely, because they disappear within the noise of the scan volumes, or indeed after filtering the data sets. Thus, the reconstructed shape of smaller objects consisting of only some few voxels has to be questioned. Finally, the shape of the extracted objects is a matter of scale and contrast quality.

The VGStudio MAX method is based on manual extraction of favoured portions of the scan volume and includes a distinct artificial component. The smaller the greyscale tolerance of the extraction tool is set, the longer it takes to detect diffuse or contrast-poor regions. To keep this method rapid, the greyscale tolerance helps to detect certain greyscale ranges and a larger portion of voxels. Especially in the case of diffuse or contrast-poor structures unsolicited voxels can be detected and therefore lead to a slight overestimation of the ROI. This fact could explain that the porosities determined by VGStudioMAX are slightly higher compared to the porosities determined by the ImageJ method.

Chapter 6: Quantification and 3D visualization of pore space in Gorleben rock salt: constraints from CT imaging and microfabrics

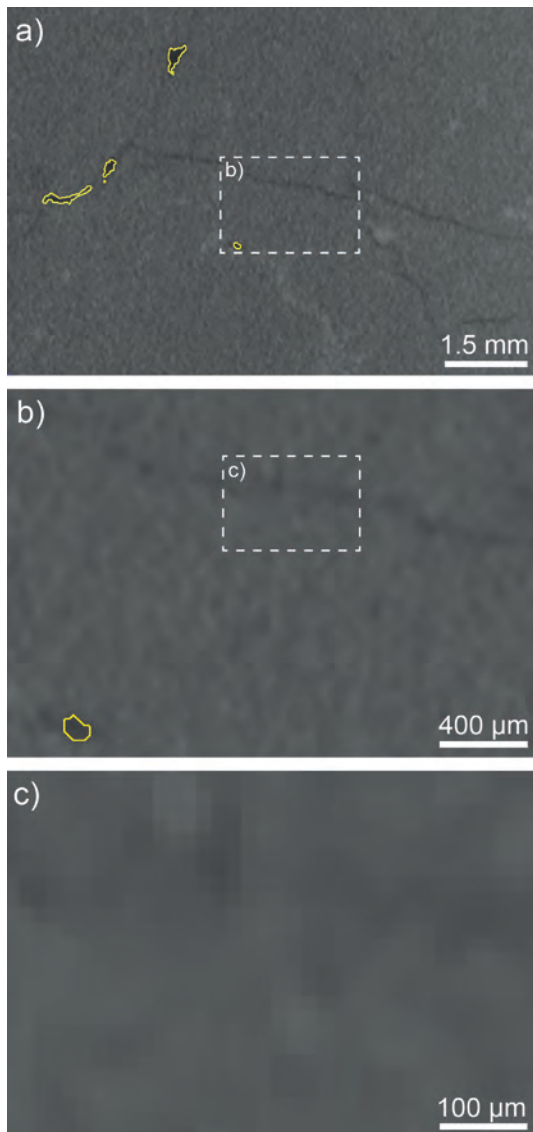


Fig. 6.6: Diffuse structures like grain boundaries or microfractures cannot be extracted properly from the CT raw data sets due to the lack of grey value contrast. a) Major pores along a grain boundary can be marked (yellow areas). b) By magnifying structures become indistinct and untraceable in a detailed view (c).

The ImageJ method considers every voxel in the selected greyscale tolerance and is very accurate in the means of detection. Thus, any uncertainty in the quantification is based only on the greyscale and contrast properties of the scan volume. By setting the requested greyscale range in non-filtered data, single background voxels can be included in the threshold, meaning the noise can affect the extracted volumes. Despite the incorporation of these very few single voxels, there should be no impact on the total amount of porosity. Filtering should not notably affect the quantification, although the structures become more indistinct. However, porosity studies on rock salt by different techniques (see De las Cuevas 1997) show that the main fraction of porosity can be represented by little pore sizes smaller than 7.5 μm. In our porosity determinations the scan resolution prohibits the detection of such small pores. Thus, an overestimation of porosity by our technique is rather unlikely, although artificial fractures can be incorporated. The calculated (ImageJ) and the manually extracted (VGStudioMAX) porosities have to be considered as minimum values.

6.4.2. Application of CT analysis on the relationship between porosity and hydrocarbon content

The presence of porous domains in three of our samples is an unusual feature for the Staßfurt Hauptsalz (z2HS). This fact is well-reputed and confirmed by the underground exploration of the

Gorleben salt dome during the last 30 years and investigations of other salt dome formations related to solution mining.

The CT imaging technique is able to analyse pore space characteristics of the presented rock salt samples. The elevated porosities in three samples were presumed by very rare macroscopic visible

Chapter 6: Quantification and 3D visualization of pore space in Gorleben rock salt: constraints from CT imaging and microfabrics

pores and can be proven and quantified by our CT studies. This fact nicely confirms the application of such modern technique giving supplementary information like spatial distribution, connection of pores (Fig. 6.7) and total volume of pore space.

The elevated porosities correlate with the total amount of hydrocarbons detected in the different rock

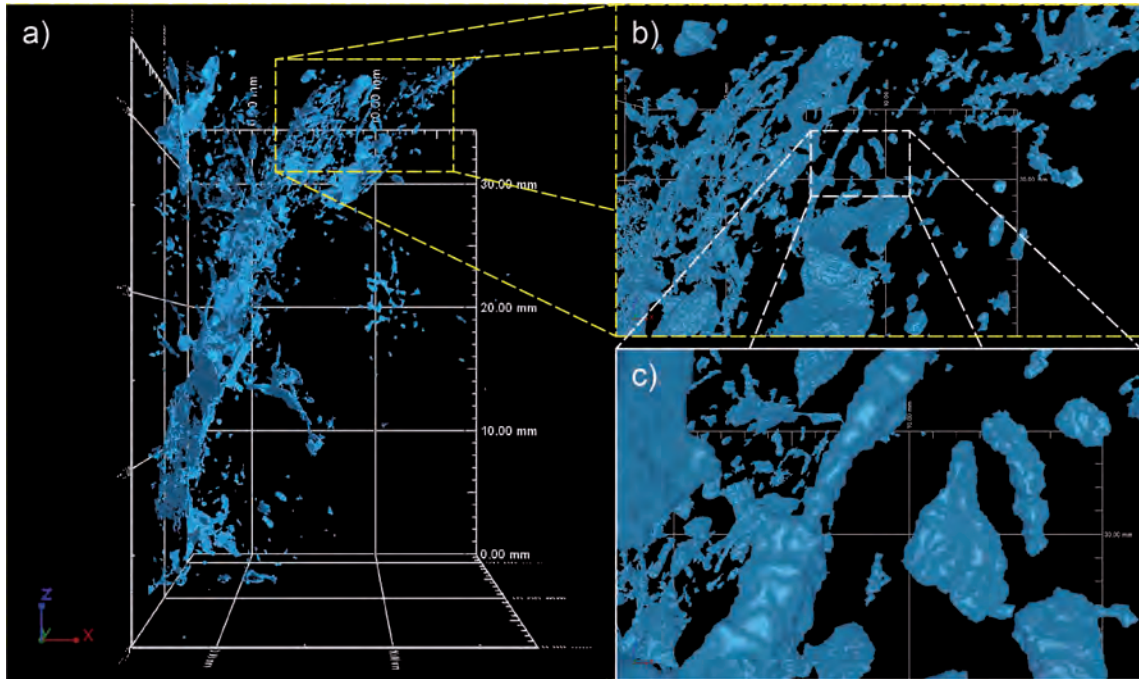


Fig. 6.7: High resolution CT scans allow magnification of designated areas and objects. a) 3D projection of RB685.004_CT (see Figs. 6.2a and b). b and c) Magnified views of image 6.7a show detailed shapes and connections of extracted particles. The true surface shape of small objects is questionable due to resolution limits.

salt samples. Higher permeability could have been caused by uplift-related early deformation and accompanied by a release of brine and hydrocarbons from the Staßfurt-Karbonat (z2SK) into the overlying Hauptsalz, which was subsequently deformed and reworked. The total amount of hydrocarbons within Gorleben Hauptsalz (z2HS) samples is generally low (< 0.05 wt.-%) and not applicable to hydrocarbon-induced fracturing processes described by Burliga and Czechowski (2010). The correlation between elevated porosity and hydrocarbon impregnation implies that they are responsible for hampered closing and healing mechanisms in deformed halite rocks. Burliga & Czechowski (2010) emphasize gas and liquid phases to be responsible for the formation and unsealing of shear fractures for longer periods of time. Moreover, hydrocarbons could inhibit water-halite interaction by coating the solution surfaces as observed by CT studies on Asse rock salt (Zulauf et al. 2010).

In some exposures, the pore space retraces the slight foliation of the Knäuelsalz. This fact suggests that this part of pore space was incorporated during the formation of the foliation. Finally, creeping and self-

Chapter 6: Quantification and 3D visualization of pore space in Gorleben rock salt: constraints from CT imaging and microfabrics

healing processes of the rock salt interrupted fluid migration and subsequently lead to a preservation of fluid accumulations, which could be an explanation for isolated fluid volumes in triple junctions visible f.i. in the CT reconstructions of sample RB652.015_CT (Figs. 6.3c and d). Polyphase reworking of the Knäuelsalz during the halokinetic uprise should have separated and fragmented the hydrocarbon impregnations leading to their overall heterogeneous distribution within the rock salt unit.

Single halite crystals partly extend into the deformation-related pore space (Fig. 6.5d) and exhibit subgrain fabrics. If these crystals are assumed to have grown into the pore space as closing mechanism, the subgrain fabrics suggest that crystal plastic deformation took place during or after the closure of pore space.

6.5. Conclusions

- The non-destructive CT method yields robust quantitative data for porosity of salt rocks and 3D images according to spatial distributions of porosity in rock salt. The 3D reconstructions can expose spatial distribution anisotropies, amounts, connections and shapes of any visible portion of a scan volume depending on the designated scale. The spatial resolution of the obtained data has a major impact on the type of porosity that can be quantified.
- The analysed hydrocarbon-bearing Staßfurt Hauptsalz (Knäuelsalz, z2HS1) samples from Gorleben salt dome show enhanced porosities up to 1.26 Vol.-%, which is an unusual attribute for Gorleben rock salt. The pore space was mostly generated and incorporated during polyphase halokinetic deformation of salt rocks and partly follows the slight foliation of the Knäuelsalz.
- A correlation between hydrocarbon content of samples and their partly elevated porosity indicate that hydrocarbons were responsible for a hampered closure of pore space. In Gorleben Knäuelsalz elevated porosities are determined only in very few hydrocarbon-bearing rock salt samples, whereas hydrocarbon-free samples are usually characterized by very low porosities und fluid content, which is related to the well-known healing mechanisms of rock salt.

6.6. Acknowledgements

We thank S. Piazzolo and F. Neubauer for their constructive comments to improve the manuscript.

6.7. References

- Alkan, H. (2009): Percolation model for dilatancy-induced permeability of the excavation damaged zone in rock salt. - *Int. J. of Rock Mechanics & Mining Sciences* 46: 716-724.
- Bornemann, O., Behlau, J., Fischbeck, R., Hammer, J., Jaritz, W., Keller, S., Mingerzahn, G. & Schramm, M.

Chapter 6: Quantification and 3D visualization of pore space in Gorleben rock salt: constraints from CT imaging and microfabrics

- (2008): Description of the Gorleben Site Part 3. Results of the geological surface and underground exploration of the salt formation. – BGR: 223pp., 50 figures, 7 tables, 5 appendices; Hannover – ISBN 978-3-9813373-6-5.
- Bräuer, V., Eickemeier, R., Eisenburger, D., Grissemann, C., Hesser, J., Heusermann, S., Kaiser, D., Nipp, H.-K., Nowak, T., Plischke, I., Schnier, H., Schulze, O., Sönke, J. & Weber, J.R. (2011): Description of the Gorleben site Part 4: Geotechnical exploration of the Gorleben salt dome. – BGR: 176pp., 96 figures, 13 tables, 2 appendices, Hannover – ISBN 978-3-510-95988-4.
- Burliga, S. & Czechowski, F. (2010): Anatomy of hydrocarbon-bearing zones, hydrocarbon provenance and their contribution to brittle fracturing of rock salt in the Klodawa Salt Structure (central Poland). - SMRI Spring 2010 Technical Conference, Grand Junction, USA.
- Chen, J., Jiang, D.Y., Ren, S., Qiu, H.F. & Yang, C.H. (2012): Analysis of surface cracks growth and damage in salt rock under uniaxial compression. - In: Bérest, P., Ghoreychi, M., Hadj-Hassen, F. & Tijani, M. (Eds.): Mechanical Behavior of Salt VII: 31-36, Taylor & Francis Group, London.
- De las Cuevas, C. (1997): Pore structure characterization in rock salt. - Engin. Geol. 47: 17-30.
- Fusseis, F., Regenauer-Lieb, K., Liu, J., Hough, R. M. & De Carlo, F. (2009): Creep cavitation can establish a dynamic granular fluid pump in ductile shear zones. – Nature 459/7249: 974-977.
- Gerling, P., Faber, E. & Wehner, H. (2002): Interpretation der chemischen Analysen von gasförmigen und flüssigen Kohlenwasserstoffen. - BGR-Bericht, Tagebuch-Nr. 12243/02: 82 S.
- Hammer, J., Pusch, M., Häger, A., Ostertag-Henning, C., Schlömer, S., Mingerzahn, G., Scheeder, G., Shao, H., Paul, B., Schulze, O., Zaretzki, B., & Hesser, J. (2012): Projekt Gorleben. Untersuchungen von Kohlenwasserstoffen im Erkundungsbergwerk Gorleben. - Zwischenbericht 2011. Bericht, Bundesanstalt für Geowissenschaften und Rohstoffe, Hannover: 236 S., 107 Abb., 17 Tab., 3 Anhänge.
- Herrmann, A.G. & Knipping, B. (1993): Waste Disposal and Evaporites – Contributions to Long-Term Safety. - Lecture Notes in Earth Sciences 45: 193 pp., Berlin (Springer).
- Mees, F., Swennen, R., Van Geet, M. & Jacobs, P. (2003): Applications of X-ray Computed Tomography in the Geosciences. - Geological Society, London, Special Publications, 215: 243 pp.
- Mertineit, M., Behlau, J., Hammer, J., Schramm, M. & Zulauf, G. (2012): Mechanical behaviour of anhydrite rocks: Results of field investigations, mineralogical-geochemical studies and thermomechanical experiments. - In: Bérest, P., Ghoreychi, M., Hadj-Hassen, F. & Tijani, M. (Eds.): Mechanical Behavior of Salt VII: 123-130. Taylor & Francis Group, London.
- Passchier, C.W. & Trouw, R.A.J. (2005): Microtectonics: 366 pp., Berlin (Springer).
- Peach, C.J., Spiers, C.J. & Trimby, P.W. (2001): Effect of confining pressure on dilation, recrystallization, and flow of rock salt at 150°C. - J. Geophys. Res. 106: 13315-13328.
- Peach, C.J. (1991): Influence of deformation on the fluid transport properties of salt rocks. - PhD thesis: 238 pp., Universiteit Utrecht.

Chapter 6: Quantification and 3D visualization of pore space in Gorleben rock salt: constraints from CT imaging and microfabrics

- Popp, T., Salzer, K., Wiedemann, M., Kansy, A. & Pusch, G. (2007): Gas transport in dry rock salt – implications from laboratory investigations and field studies. - In: Wallner, M., Lux, K.-H., Minkley, W. & Hardy Jr., H.R. (Eds.): *The Mechanical Behavior of Salt – Understanding of THMC Processes in Salt*: 17-26, Taylor & Francis Group, London
- Popp, T., Minkley, W., Salzer, K. & Schulze, O. (2012): Gas transport properties of rock salt – synoptic view. - In: Bérest, P., Ghoreychi, M., Hadj-Hassen, F. & Tijani, M. (Eds.): *Mechanical Behavior of Salt VII*: 143-154, Taylor & Francis Group, London.
- Rothwell, R.G. & Rack, F.R. (2006): New techniques in sediment core analysis: an introduction. - *Geol. Soc., London, Spec. Pub.* 267: 1-29.
- Salzer, K., Popp, T. & Böhnelt, H. (2007): Mechanical and permeability properties of highly pre-compacted granular salt pricks. - In: Wallner, M., Lux, K.-H., Minkley, W. & Hardy Jr., H.R. (Eds.): *The Mechanical Behavior of Salt – Understanding of THMC Processes in Salt*: 239-248, Taylor & Francis Group, London.
- Schoenherr, J., Urai, J.L., Kukla, P.A., Littke, R., Schlöder, Z., Larroque, J.-M., Newall, M.J., Al-Abry, N., Al-Siyabi, H.A. & Rawahi, Z. (2007): Limits to the sealing capacity of rock salt: A case study of the infra-Cambrian Ara Salt from the South Oman salt basin. - *AAPG Bulletin* 91/11: 1541-1557.
- Schulze, O., Popp, T. & Kern, H. (2001): Development of damage and permeability in deforming rock salt. - *Engin. Geol.* 61: 163-180.
- Schulze, O. (2007): Investigations on damage and healing of rock salt. - In: Wallner, M., Lux, K.-H., Minkley, W. & Hardy Jr., H.R. (Eds.): *The Mechanical Behavior of Salt – Understanding of THMC Processes in Salt*: 33-44, Taylor & Francis Group, London.
- Spangenberg, E., Spangenberg, U. & Heindorf, C. (1998): An experimental study of transport properties of porous rock salt. - *Phys. Chem. Earth* 23/3: 367-371.
- Stormont, J.C. & Daemen, J.J.K. (1992): Laboratory Study of Gas Permeability Changes in Rock Salt During Deformation. - *Int. J. Rock. Mech. Min. Sci & Geomech. Abstr.* 29: 325-342.
- Stormont, J.C. (1997): Conduct and interpretation of gas permeability measurements in rock salt. - *Int. J. Rock Mech & Min. Sci.* 34:3-4, paper No. 303.
- Sutherland, H.J. & Cave, S.P. (1980): Argon gas permeability of New Mexico rock salt under hydrostatic compression. - *Int. J. Rock. Mech. Min. Sci & Geomech. Abstr.* 17: 281-288.
- Urai, J.L., Spiers, C.J., Peach, C.J., Franssen, R.C.M.W. & Liezenberg, J.L. (1987): Deformation mechanisms operating in naturally deformed halite rocks as deduced from microstructural investigations. - *Geol. Mijnbouw* 66: 165–176.
- Zulauf, G., Zulauf, J., Bornemann, O., Kihm, N., Peinl, M. & Zanella, F. (2009): Experimental deformation of a single-layer anhydrite in halite matrix under bulk constriction. Part 1: Geometric and kinematic aspects. - *J. Struct. Geol.* 31: 460-474.
- Zulauf, G., Zulauf, J., Bornemann, O., Brenker, F., Höfer, H., Peinl, M. & Woodland, A. (2010): Experimental

Chapter 6: Quantification and 3D visualization of pore space in Gorleben rock salt: constraints from CT imaging and microfabrics

deformation of a single-layer anhydrite in halite matrix under bulk constriction. Part 2: Microfabrics and deformation mechanisms. - *J. Struct. Geol.* 32: 264-277.

Zulauf, G., Zulauf, J., Mertineit, M. & Hammer, J. (2012): Boudinage of anhydrite in rock-salt matrix: The impact of bulk finite strain geometry. - In: Bérest, P., Ghoreychi, M., Hadj-Hassen, F. & Tijani, M. (Eds.): *Mechanical Behavior of Salt VII*: 65-70. Taylor & Francis Group, London.

Chapter 7

The application of high resolution X-ray computed tomography on naturally deformed rock salt: Multi-scale investigations of the structural inventory

Nicolas Thiemeyer¹, Jörg Habersetzer², Mark Peinl¹, Gernold Zulauf¹, Jörg Hammer³

¹*Institute of Geoscience, Goethe-University Frankfurt am Main, Altenhöferallee 1, 60438 Frankfurt am Main, Germany.*

²*Senckenberg Research Institute and Natural History Museum Frankfurt am Main, Senckenberganlage 25, 60325 Frankfurt am Main, Germany.*

³*Federal Institute for Geosciences and Natural Resources (BGR), GeoZentrum Hannover, Stilleweg 2, 30655 Hannover, Germany.*

Abstract

X-ray computed tomography (CT) represents a useful technique providing new perspectives and insights for the structural investigation of naturally-deformed rock salt. Several samples of Permian rock salt from Gorleben, Asse and Teutschenthal (Germany) were investigated by exploiting the non-destructive nature of micro- and nano-CT techniques particularly for salt rocks. The CT measurements were performed at different scales, including high resolution scanning in the submicron range. CT imaging enabled the visualization and quantification of anhydrite impurities, pore space and fluid phases located along grain-boundaries or trapped as intracrystalline inclusions. Considerations on CT imagery aspects, such as raw data set filtering in combination with image arithmetic are further presented.

Disseminated grains and aggregates of anhydrite in rock salt of the Gorleben salt dome have been visualized and quantified by μ -CT for the first time in order to portray their spatial occurrence. The visualization of anhydrite and pore space shows no correlation between their spatial distributions. This independence excludes the anhydrite to be responsible for elevated porosity (0.87 ± 0.07 vol.-%). High-resolution nCT scans ($\leq 1 \mu\text{m}$ voxel size) of single intracrystalline and grain-boundary fluid inclusions from Gorleben and Asse rock salt allowed the visualization and quantification of their different phase components. A major achievement is the detailed description of the morphology and shape of the fluid inclusions and of their phase components, which has not been conducted in rock salt research by high-resolution X-ray CT imaging before.

Keywords: Computed tomography; Rock salt; Anhydrite; Fluid inclusions; Microstructures

[Journal of Structural Geology 77, 92-106. DOI:10.1016/j.jsg.2015.05.014.](#)

Chapter 7:

The application of high resolution X-ray computed tomography on naturally deformed rock salt: Multi-scale investigations of the structural inventory

7.1. Introduction

7.1.1. CT imaging in the geosciences

CT imaging has gradually entered the realm of geosciences in the past decades. This technique enables non-destructive investigation of a vast range of earth and planetary materials. Overviews of its applications in the geosciences are presented in Ketcham and Carlson (2001), Mees et al. (2003), Carlson (2006) and Cnudde and Boone (2013). Carlsson (2006) suggests high potentials for μ CT and nCT imaging to become essential components in the lineup of future investigational tools. This holds true for various disciplines in the geosciences such as hydrology, soil science, environmental geology, paleontology, petroleum geology, sedimentology, petrology, structural geology, engineering geology, economic geology, and planetary science.

Main fields of CT imaging refer to porosity characterization and pore geometry studies (Coles et al., 1998; Arns et al., 2005; Iassonov et al., 2009; Burliga and Czechowski, 2010; Dewanckele et al., 2012; Wildenschild and Sheppard, 2013; Cnudde and Boone, 2013; Derluyn et al., 2014); rock permeability and fluid migration studies (Fusseis et al., 2009; Cunningham et al., 2013; Alam et al., 2014; Cai et al., 2014), strain determinations or shape analyses (Bay et al., 1999; Godel et al., 2006; Meyer et al., 2011; Adam et al., 2013), quantitative and fabric investigations (Carlson and Denison, 1992; Jerram and Higgins, 2007; Godel et al., 2010; Huddlestone-Holmes and Ketcham, 2010; Boone et al., 2011) or analogue modeling (e.g. Zulauf et al., 2003, 2011a, Pastor-Galán et al., 2012). Moreover, combined studies of CT imaging with micro-X-ray fluorescence (μ XRF) and X-ray diffraction (XRD) (Boone et al., 2011) or thermochronology (Evans et al., 2008) have been carried out. Thus, a leading role of computed tomography is evident to give additional insights and interpretations of results obtained by alternative techniques (Cnudde et al., 2009). The main ambition of μ CT imaging is an ongoing quest on high resolution scans to improve the analytical potential of this technique (Cnudde and Boone, 2013). Based on the Nyquist theorem (Nyquist, 1928) the effective resolution is double the voxel size. In the present paper, the term resolution describes the edge length of the three-dimensional voxel (v) of a generated CT volume, although sometimes resolution refers to the volume of a voxel (e.g. Henderickx et al., 2012) or to the detector dimensions in pixels.

Ketcham and Carlson (2001) define resolution categories of CT scanning ranging from conventional (mm) to microtomography (μ m). CT imaging with resolutions in the range of a few microns or even below 1 μ m voxel size are well established in the geosciences (e.g. Renard, et al., 2004; Arns et al., 2005; Evans et al., 2008; Fusseis et al., 2009; Godel et al., 2010; Henderickx et al., 2012). At present, modern precision-focusing nCT scanners and synchrotron X-ray facilities (see Fusseis et al., 2014) achieve CT resolutions on the nanometer scale, in which case the term nanotomography is appropriate. Especially synchrotron X-ray computed tomography (e.g. Fusseis et al., 2009; Derluyn et al., 2014) can enable high resolutions of $v < 100$ nm (Ogurreck et al., 2013). Fusseis et al. (2014) have summarized the achievements

Chapter 7: The application of high resolution X-ray computed tomography on naturally deformed rock salt: Multi-scale investigations of the structural inventory

of synchrotron micro- and nanotomography for (structural) geology and rock mechanics.

7.1.2. CT imaging of rock salt

Whereas numerous μ CT imaging studies in the diverse fields of geosciences have been published, μ CT imaging studies on rock salt play a subordinate role. Renard et al. (2004) presented synchrotron microtomography on experimentally compacted samples to incrementally monitor changes of the texture and pore space characteristics in halite aggregates. A maximum resolution of $v = 0.7 \mu\text{m}$ revealed changes of halite grain contacts to result in decreasing permeability due to grain indentation and pore connectivity reduction by precipitation on free surfaces of pore throats. Further synchrotron X-ray microtomography studies have analyzed the distribution of salt solution and crystals in porous limestone related to salt weathering cycles (Derluyn et al., 2014). All of these high resolution studies point out the importance of μ CT for the characterization of crystallization processes, textures and changes of pore space in rock salt.

Zulauf et al. (2009) applied clinical CT imaging to separate and visualize experimentally produced anhydrite boudins in rock salt matrix. Further thermomechanical experiments of anhydrite and rock salt set focus on chocolate-tablet boudinage using μ CT (Zulauf et al., 2011b).

CT imaging of natural rock salt samples of the Klodawa Salt Structure (Poland) have been performed by Burliga and Czechowski (2010) in order to visualize and quantify the porosity of hydrocarbon-bearing rock salt in combination with geochemical analyses. Similar μ CT studies have been conducted by Thiemeyer et al. (2014) regarding hydrocarbon impregnations and elevated porosities in the Gorleben salt dome of Northern Germany accompanied by microfabric investigations.

The aim of the present paper is to demonstrate the value of μ CT imaging for the characterization of a typical rock salt inventory. A suite of CT reconstructions will reveal enriching structural data, representing noteworthy progress for the rock salt community. Our presented CT scans in the submicron range are unique and no such data on naturally deformed rock salt exists to this date. Besides the general implications of our results concerning computed tomography on rock salt, conclusions regarding the analyzed samples can be drawn to give new insights pertaining to rock salt from the Gorleben salt dome of northern Germany.

7.2. Geological background and microstructural characteristics of the rock salt samples

7.2.1 Sample localities

All samples of the present study have been collected from Upper Permian salt deposits of northern Germany: (i) the Gorleben salt dome, (ii) the Asse salt structure, and (iii) the Teutschenthal mine (Fig. 7.1).

Chapter 7:

The application of high resolution X-ray computed tomography on naturally deformed rock salt: Multi-scale investigations of the structural inventory

The Gorleben salt dome and the Asse salt structure represent domal salt rocks, which are built up by salt rocks of the Stassfurt Formation (z2) (Bornemann, 1991; Jagsch and Theylich, 1999; Fig. 7.1). In Gorleben, the diapiric uplift of the salt rocks resulted in a vertical rock salt column of approximately 3 km. The lowest sub-unit (Knäuelsalz, z2HS1) of the Stassfurt formation has been interpreted as a halotectonic breccia (Bornemann et al., 2008) because primary bedding features are not preserved due to a relatively strong homogenization during the salt uplift. Comprehensive stratigraphy, lithology and tectonic evolution are given in Bornemann et al. (2008).

The Asse salt structure is situated 200 km W of Berlin and has been used as an underground research laboratory for nuclear waste storage in rock salt since 1965. This salt structure mainly consists of Stassfurt (z2), Leine (z3) and Aller (z4) salt rocks of Upper Permian age forming a steep anticline trending NW-SE (Fig. 7.1).

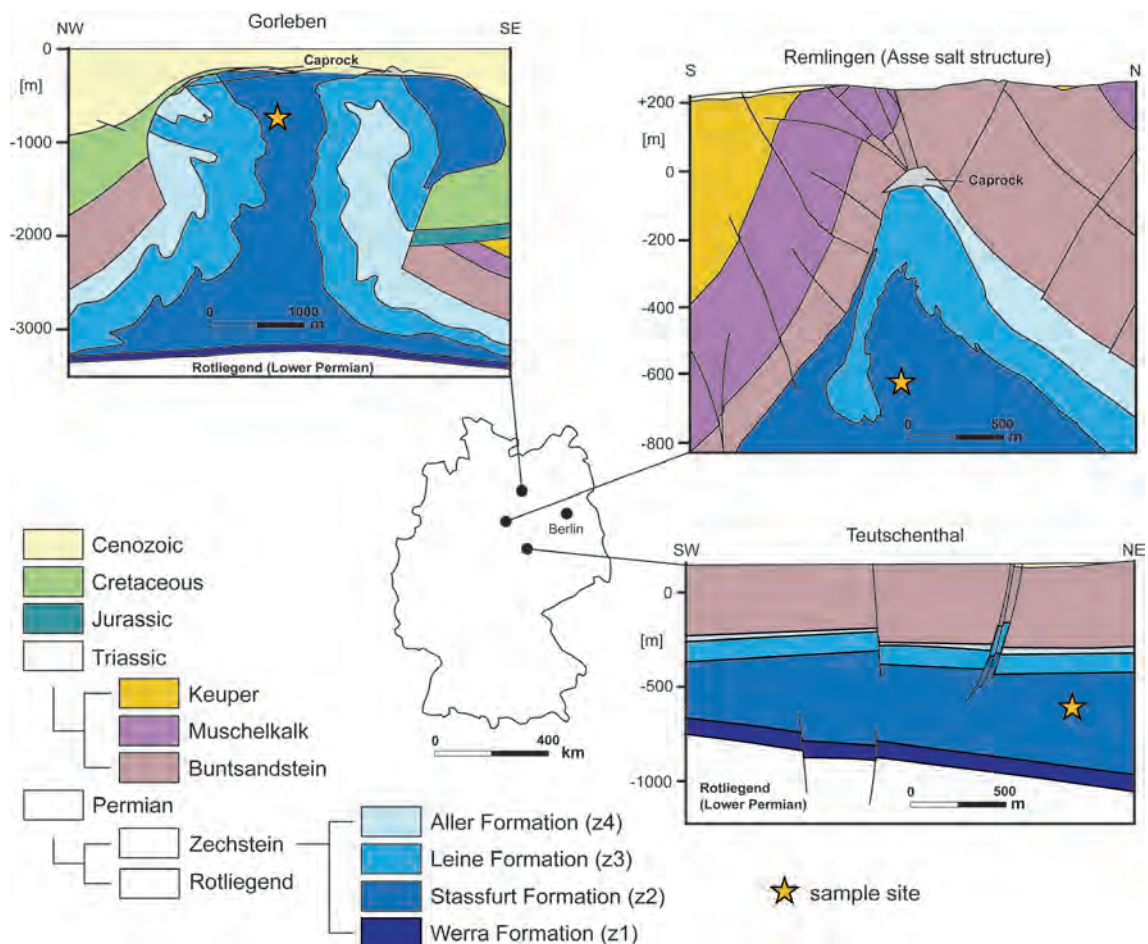


Fig. 7.1: Sampled salt structures in northern Germany according to Bornemann (1991) and Jagsch and Theylich (1999). All samples presented in this paper were collected from the Stassfurt formation (z2). The cross sections only consider the main salt units. For a detailed stratigraphy of the Zechstein and the particular salt formations, the reader is referred to Bornemann et al. (2008).

Chapter 7: The application of high resolution X-ray computed tomography on naturally deformed rock salt: Multi-scale investigations of the structural inventory

In contrast to these domal salt structures, the Teutschenthal deposits consist of stratiform, bedded salt rocks, which have only been moderately deformed compared to the Gorleben and Asse rock salt (Jagsch and Theylich, 1999; Küster, 2011).

The following sections give a brief introduction on general aspects about anhydrite, pore space and fluid phases in rock salt and an introducing summary about microstructural characteristics of the samples.

7.2.2. Anhydrite, pore space and fluid inclusions in rock salt

Anhydrite distribution is important for structural geology and for rock mechanics because rock salt has been suggested to be a suitable medium for nuclear waste repositories (e.g. Hunsche and Hampel, 1999). From large to very small scales, anhydrite intercalations result in mechanical anisotropies and can act as fluid reservoirs (brines and hydrocarbons) or as locally developed pathways for fluids (Bornemann et al., 2008), which can be (re)distributed along fractures or interfaces when deformation is partly accommodated in the brittle-ductile regime (Peach, 1993; Zulauf et al., 2009, 2010, 2011b; Mertineit et al., 2014). During compaction, deformation and recrystallization, primary fluid phases can be trapped and (re)distributed within the halite crystal assemblages along (healing) cracks or by grain-boundary migration and solution-precipitation processes causing the accumulation of fluid inclusions along grain or phase boundaries. The term fluid inclusion implies incorporated vapor and/or fluid potentially including a solid phase of organic or inorganic matter (e.g. Roedder, 1984), such as hydrocarbons or brines, and is not limited to fluids.

There is some evidence that natural fluids might play an important role for rock salt deformation. Even small amounts of brine enable and support solution-precipitation processes and grain-boundary migration under natural conditions resulting in mechanical weakening of rock salt (Urai et al., 1986, Peach et al., 2001; Ter Heege et al., 2005; Pennock et al., 2006; Urai and Spiers, 2007; Zhang et al., 2007). One aim of our study was to visualize and quantify characteristic anhydrite impurities in rock salt collected from various localities. Samples RB648 and RB683 have been collected from the Knäuelsalz unit (z2HS1) in Gorleben at the 840 m level (exploration area 1), which is described as dark-gray to black, medium- to coarse-grained rock salt containing certain amounts of anhydrite (Bornemann et al., 2008). The typical anhydrite distribution is manifested as dispersed anhydrite impurities or as irregular, knotty clusters or nests (the so-called Knäuel in German language) resulting in the term Knäuelsalz for this unit (Fig. 7.2a,b,e,f). The highest amounts of anhydrite are present as larger nodules reflecting former anhydrite layers, which have been separated, folded and disseminated during uprise-related deformation (Bornemann et al., 2008). Sample RB683 (Fig. 7.2e and f, Knäuelsalz, z2HS1, 840 m level) has been studied regarding the correlation between anhydrite and pore space distribution. In very rare cases, rock salt drill cores exhibit small pores leading to slightly elevated porosities (Thiemeyer et al., 2014). The sample is characterized by few pores (< 5 mm), which are even observable in hand specimens. For this type of porosity, the term macroporosity will be used. The sample has been impregnated with

Chapter 7:

The application of high resolution X-ray computed tomography on naturally deformed rock salt: Multi-scale investigations of the structural inventory

blue-coloured resin to accentuate the pore space distribution under the microscope. The thick section reveals a former gas bubble caused by the incomplete ingress of resin during impregnation (Fig. 7.2e) and elevated porosity within the anhydrite clusters (microporosity), which are not visible in hand specimens. However, the main portion of porosity in this particular sample is given by larger pores, although such mm-sized pores are very unusual for naturally deformed rock salt and for the Gorleben Knäuelsalz in particular.

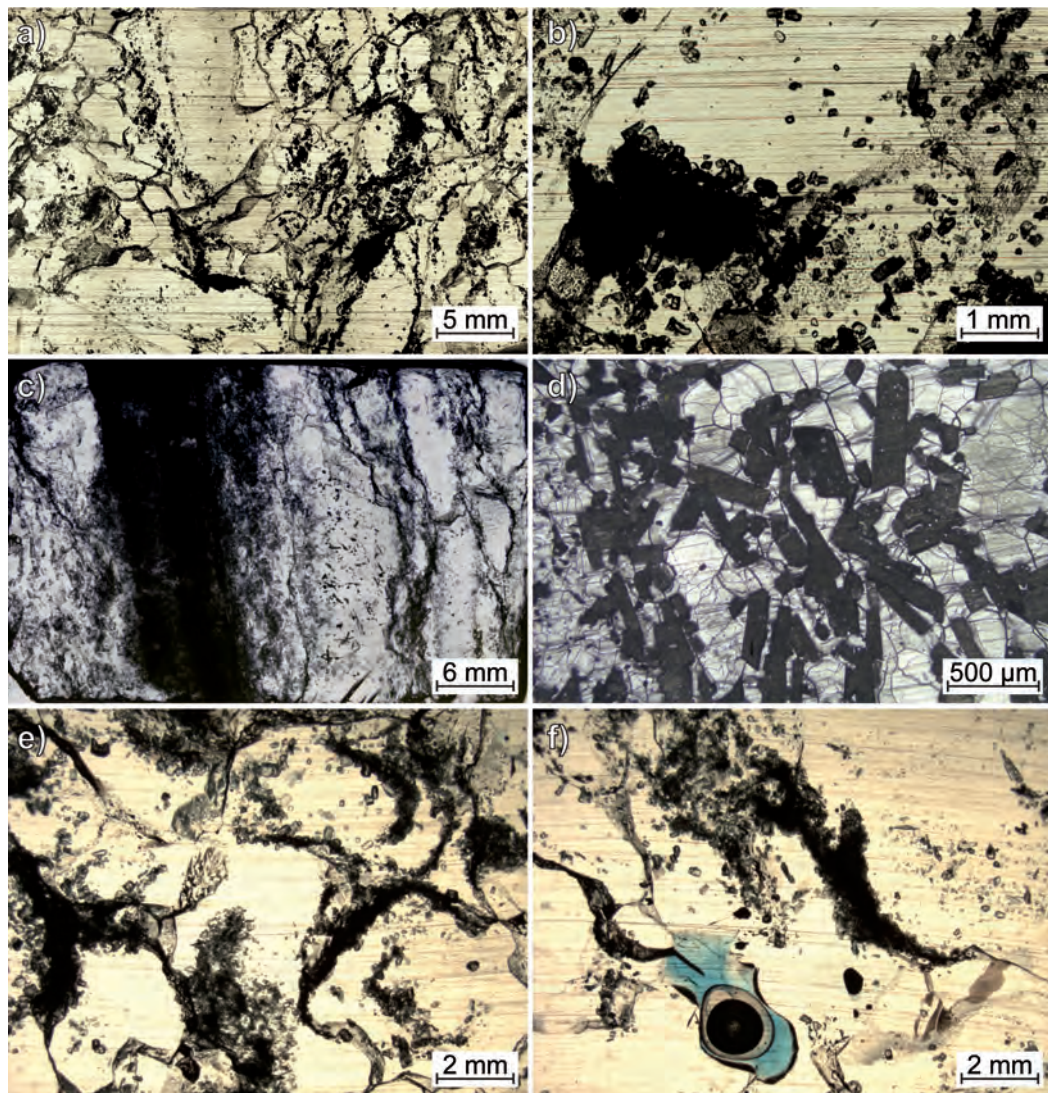


Fig. 7.2: Fabric of rock salt samples presented in this paper. a) and b) Microphotographs showing disseminated dark anhydrite crystals in Gorleben Knäuelsalz (z2HS1; sample RB648, polarizers). c) and d) Microphotographs of Teutschenthal rock salt (sample LT163_1, z2HS) showing a pervasive anhydrite layer (dark band of ca. 8 mm thickness; d) as etched halite thick section under reflected light). e) and f) Microphotographs of sample RB683 (z2HS1, Gorleben) reveal the typical, irregular, dispersed anhydrite clusters. The gas bubble is caused by the incomplete ingress of resin during impregnation.

Chapter 7:

The application of high resolution X-ray computed tomography on naturally deformed rock salt: Multi-scale investigations of the structural inventory

Sample LT163_1 (Hauptsalz unit, z2HS, 759 m drilling depth) from the Teutschenthal salt deposit (see Fig. 7.1) shows intercalations of anhydrite as well (Fig. 7.2c,d) but differing structures compared to the anhydrite distribution of the Gorleben sample. The collected Teutschenthal sample reveals one anhydrite layer of approximately 8 mm thickness intercalated in the halite matrix. Further anhydrite is disseminated as numerous solid inclusions ($\leq 500 \mu\text{m}$) to give an unpurified rock salt, which is supported by primary fluid inclusions. Apart from the anhydrite layer, anhydrite crystals are larger compared to the clusters, lath-shaped and partly idiomorphic (Fig. 7.2d). The halite grain diameters are $> 5 \text{ mm}$ and therefore larger than those of the Gorleben sample(s).

Due to the impact of fluids on the deformation behavior of rock salt (see text above), the investigation of morphologies, volumes, components and distribution patterns of fluid inclusions in synthetic and natural rock salts have been intensively studied in the past (e.g. Roedder, 1984; Urai et al., 1987; Drury and Urai, 1990; Schoenherr et al., 2007; Desbois et al., 2008, 2012; Zulauf et al., 2010; Závada et al., 2012). However, the shape and particular volume of single fluid inclusions in rock salt has not been studied in detail and CT imaging of the fluid inventory of naturally deformed rock salt has not yet been performed. With respect to microstructural characteristics and mechanical properties of Asse rock salt, the natural fluid content has been quantified by 0.04-0.05 vol.-% (Urai et al., 1987; Gies et al., 1990). The fluid characteristics in Asse rock salt has further been presented by Urai et al. (1986, 1987) and Zulauf et al. (2010) concerning the role of brine and hydrocarbon (re)distribution during the deformation of the rocks.

An exemplary fluid distribution pattern of grain-boundary fluids in Asse rock salt (Speisesalz, Na2SP, 600 m drilling depth) is shown in Fig. 7.3a. Characteristic stripes and spots of brine or hydrocarbons decorate halite grain-boundaries in naturally deformed rock salt (e.g. Urai et al., 1987). Further amounts of fluid, gas and solid components can be found in intracrystalline fluid inclusions.

Intracrystalline fluid inclusions can similarly be described for Gorleben rock salt. Sample Bo5 (Kristallbrockensalz, z2HS3, Fig. 7.3b) from the Gorleben salt dome contains two intracrystalline inclusions consisting of various phases. A vapor phase is present as dark bubbles surrounded by fluids composing the overall inclusions. The larger of the two inclusions is elongated and thins out towards the tips. In order to improve the imaging quality, Fig. 7.3b and Fig. 7.3c consist of numerous single images in several focus planes to create z-stack images merging well-focused parts to a digitally-improved final image. However, this method does not provide detailed information about the shape and morphology of the fluid inclusions. Therefore, we performed μCT scans reconstructing the main inclusion to uncover its exact morphology and structure.

The z-stack image of sample Bo5UHR (Fig. 7.3c) shows characteristic fluid inclusion patterns along a halite grain-boundary developed as a branching network with fluid stripes trending horizontally. The fluids are partly blackened due to the amount and thickness of the particular structure and to some extent are linked by very thin, transparent stripes (red arrows, Fig. 7.3c). Additionally, tiny fluid spots

Chapter 7:

The application of high resolution X-ray computed tomography on naturally deformed rock salt: Multi-scale investigations of the structural inventory

decorate the grain-boundary and lie between the main branches (white arrow, Fig. 7.3c). Some parts of the z-stack image remain unfocussed, although the image consists of 26 single images of several focus planes. The corresponding nCT scan was performed with the highest resolution of 700 nm voxel size.

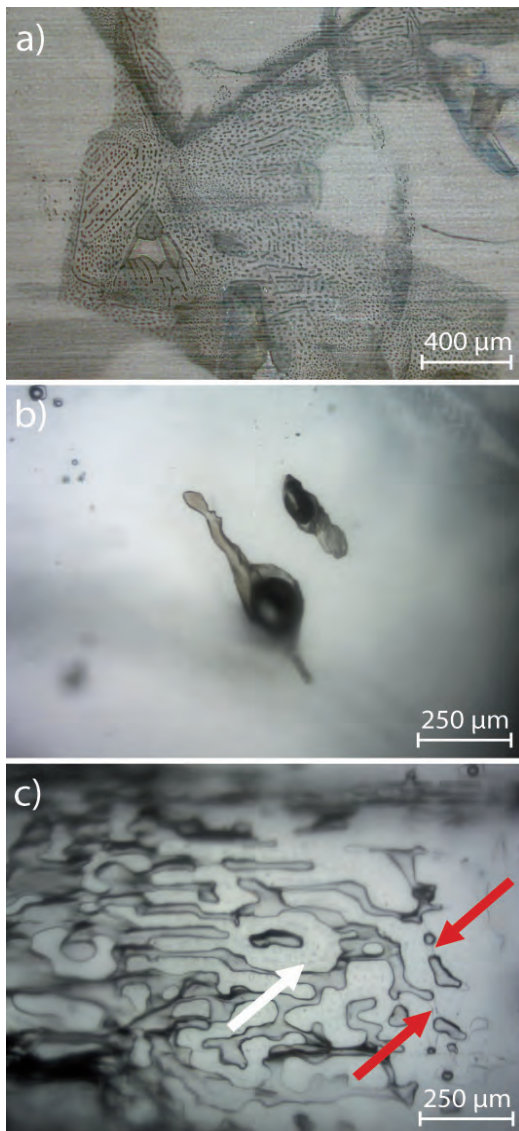


Fig. 7.3: Transmitted light microphotographs of fluid inclusions in Asse Speisesalz (Na₂SP) rock salt (a), and the Gorleben Kristallbrockensalz (z2HS3) samples Bo5 (b) and Bo5UHR (c). The microphotographs result from stacked images to increase the depth of field. a) Typical fluid distribution pattern along halite grain boundaries in Asse rock salt. The fluid pattern reconstructed using CT is not displayed. b) Two intracrystalline fluid inclusions (sample Bo5, z2HS3, Gorleben salt dome) exhibiting gas bubbles surrounded by a fluid phase. c) Grain-boundary fluid inclusion pattern (sample Bo5UHR, z2HS3, Gorleben salt dome). Several main branches of fluids result in a fluid network that is partly linked by transparent, thin stripes (red arrows). Note the very small fluid spots between the main branches (white arrow).

7.3. Methods

7.3.1. Sample preparation

Depending on the designated scales and subject, we analyzed rock salt drill cores (72 and 36 mm in diameter) by means of CT without further cutting. The investigation of characteristic anhydrite distributions in greater detail on the other hand (sample LT163_1) required the preparation of rock salt bricks of ca. 10 cm³. For the highest resolution

scans ($v = 700$ nm), rock salt drill cores and hand specimens were comminuted and then inspected under the microscope for small specimens (ca. 2 mm³) with no artificial cracks..

7.3.2. X-ray computed tomography

CT scanning was performed with a phoenix nanotom s at the Geoscience Department of Goethe University Frankfurt am Main. This CT scanner is equipped with a X-ray nanofocus tube (W-filament and a Be-transmission-target) and a Hamamatsu detector with a resolution of 2240 · 2354 pixels resulting in

Chapter 7:

The application of high resolution X-ray computed tomography on naturally deformed rock salt: Multi-scale investigations of the structural inventory

CT volumes with a maximum resolution of $v < 1 \mu\text{m}$.

A precondition for our high-resolution scans in the submicron range is the multifocus CT ability of the nanotoms. When approaching resolution limits, a very small focal spot is required to capture the smallest structures or objects in samples. A decreasing intensity must be counteracted by longer exposure times for each single image, which produces additional noise. The noise level can be counteracted by averaging more single images per step. To summarize, highest resolution CT scans require longer exposure times per image, more single images per step and exponentially longer scanning times resulting in a trade-off between acquisition time and image quality (Cnudde and Boone, 2013). The relation between sample size, resolution and scanning time is schematically shown in Fig. 7.4.

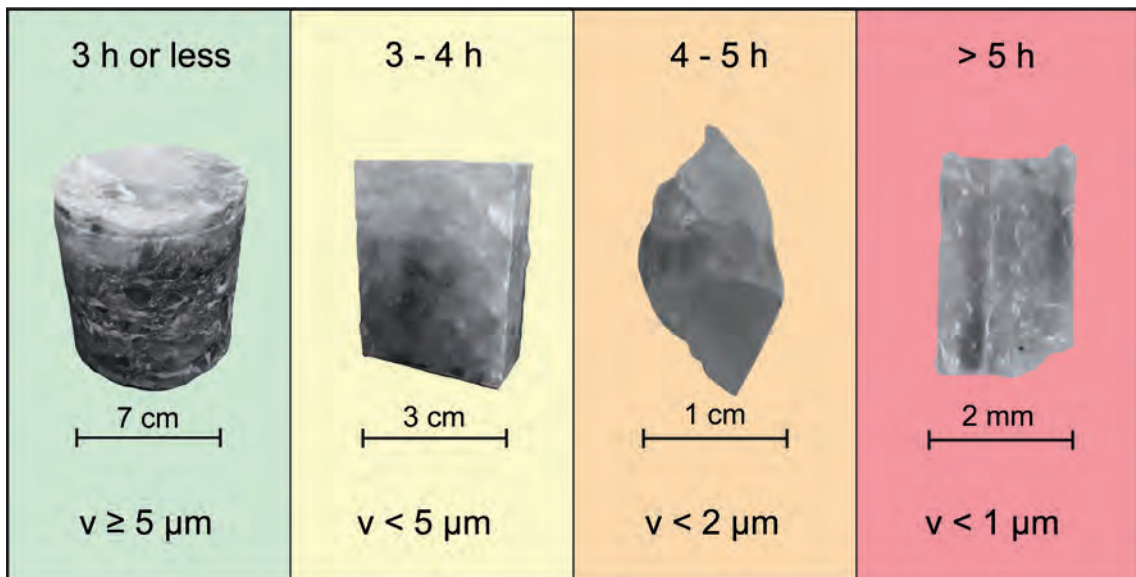


Fig. 7.4: Schematic classification of various scanning regimes concerning sample size, scanning time and resolution. A small voxel size (v) and related high scan resolution are restricted to small samples. All samples shown in this figure are described in the text.

The microstructures of the rock salt samples presented in Fig. 7.2 were scanned with various scanning parameters and resolutions ($v = 700 \text{ nm}$ to $20 \mu\text{m}$) dependent on the sample properties (Table 7.1).

7.3.3. Data processing

The processing of CT rotational data starts with the back projection resulting in a raw data volume with voxels of 8, 16 or 32 bit gray scale. The dimensions of the 3D volume are defined and constructed by a matrix resulting in a certain number of voxels per edge length (x,y,z). As standard case, the dimensions of the volume accord to the detector dimensions. For some special cases, the reconstruction software allows a downscaling of the reconstructing matrix resolution by factor 0.5 or 0.25 to create volumes with reconstructed voxel sizes (v_r) two or four times larger than the original voxel size. The effects are the

Chapter 7:

The application of high resolution X-ray computed tomography on naturally deformed rock salt: Multi-scale investigations of the structural inventory

Sample	locality (stratigraphy)	Sample type (dimensions)	kV	μ A	Mode (beam focus)	Averaged pictures	Skipped pictures	Timing [ms]	Final images	Scanning time [min]	Voxel Size (2Res) [μ m]	Study object
RB648	Gorleben (z2HS1)	cylindric (radius = 7.2 cm)	150	100	0	4	1	1000	3000	256	20	Overall anhydrite distribution
RB683	Gorleben (z2HS1)	cylindric (radius = 3.2 cm)	100	70	0	4	1	1250	2400	255	10.38	Porosity and anhydrite distribution
LT163_1	Teutschenthal (z2HS)	curoid (3x2x2 cm)	100	70	0	4	1	1000	2400	205	8.06	Anhydrite distribution (bedding)
Asse	Asse (NA2SP)	fragmental (2x2x2 mm)	75	280	2	?	?	2000	1800	?	1.7 (0.85)	Distribution of fluid inclusions
Bo5	Gorleben (z2HS3)	fragmental (2x1x1 mm)	70	330	2	5	1	1250	2400	305	1	Distribution of fluid inclusions
Bo5UHR	Gorleben (z2HS3)	fragmental (2x1x1 mm)	70	300	3	4	1	1250	3000	319	0.7 (0.35)	Distribution of fluid inclusions

Table 7.1: Summarized μ CT measurements presented in this paper. X-ray current parameters are given in kV and μ A. The mode describes the focal spot as weak (0) to strong (3) focus. The number of averaged and skipped pictures is given for every rotation increment during the scanning process resulting in one final image. Voxel sizes are given in original and improved reconstruction size (2Res).

same as the well-known pixel-binning for higher signals with reduced noise during real-time scanning and result in reduced resolution and a much smaller data set, which is useful for preliminary checking of the CT data or for easier and faster handling of the data. On the other hand, the software allows an upscaling by the factor 2 (2Res) to achieve a final resolution half the original voxel size. This bisection of the voxel size causes data sets eight times larger than a reconstruction with the original voxel size. The 2Res reconstruction algorithm is a proprietary format of phoenix company and thus not freely available or described. However, the 2Res technique is worth mentioning, because the visual aspect of small particles is clearly increased although resolution is not doubled.

During volume reconstruction the rotation images can be treated with filters and modules for artifact corrections to pre-modify the data set.

We present visualization procedures depending on the data set properties and the designated objects processed by VGStudioMAX 2.2. Based on gray value thresholds of the data volume designated regions of interest (ROIs) can be extracted automatically (fast) or manually (time-consuming) and visualized in different projection modes. The standard surface determination tool of VGStudioMAX was used in order to attain well defined ROIs. Depending on the spatial distribution, capacity or matter of interest, two different projection modes are presented in this paper: (i) the *phong* and (ii) the *sumalong* projection. The *phong* projection displays all reconstructed particles in the same clarity, independent of their size and volume and is best suitable for descriptions of morphologies or animations, especially for very small objects consisting of only few voxels. The *sumalong* projection points out the volumetric distribution depending on the amount of penetrated particles in the line of sight. As a result, larger volumes are highlighted, which is useful in case of numerous, capacious 3D reconstructions. A certain transparency of 3D *sumalong* projections allows the tracing and identification of internal structures or distribution patterns in a 3D reconstruction and is very suitable for ROIs consisting of numerous single particles.

The final 3D reconstructions can be magnified, sliced or turned in every desired direction offering a wide range of perspectives including robust spatial information about size, volume or surface of the objects.

Chapter 7:

The application of high resolution X-ray computed tomography on naturally deformed rock salt: Multi-scale investigations of the structural inventory

Depending on the scanning parameters and the raw data, quantification errors are estimated by slightly shifting the gray value thresholds during volume extraction. This technique applies only to the automated extraction method (see above). When a particular threshold for a single phase component is clearly distinguishable from another, a small shift of the corresponding threshold is used to obtain a quantification error.

7.4. Results

7.4.1. Anhydrite distribution in rock salt on different scales

3D- μ CT reconstruction of extracted anhydrite impurities of sample RB648 (Fig. 7.2a and b) with a voxel size of $v = 20 \mu\text{m}$ are shown in Fig. 7.5. The *sumalong* projection retraces the main portion of the plumes and shreds of anhydrite in the halite matrix. The anhydrite content was quantified as $10.1 \pm 1.0 \text{ vol.-%}$, which is in the range of the overall determined anhydrite content between ca. 5 % and 20 % for the Hauptsalz unit (Bräuer et al., 2011).

Sample RB648 was selected as anhydrite-rich sample, as depending on the analyzed rock salt volume the anhydrite content varies due to its heterogeneous distribution. The CT reconstruction also allows a surface area determination of anhydrite, which yielded the twentyfold (20600 mm^2) of the anhydrite clusters related to a cube surface equivalent (1035.6 mm^2) of the anhydrite volume.

The CT reconstruction of anhydrite in the Teutschenthal sample LT163_1 (Fig. 7.6) differs from the anhydrite pattern of RB648. The anhydrite grains in sample LT163_1 occur in form of three single layers contributing with $7.4 \pm 0.7 \text{ vol.-%}$ to the data volume. One such layer is shown in Fig. 7.2c. The resolution of $v = 8.06 \mu\text{m}$ even allows the identification of single anhydrite crystals, which are slightly larger (up to $500 \mu\text{m}$) than the disseminated anhydrite crystals in the Gorleben sample (RB648, Fig. 7.2a and b).

7.4.2. The relation between pore space and anhydrite distribution

Sample RB683 from the Gorleben Knäuelsalz unit (z2HS1) shows few macroscopically visible pores in the hand specimen and in thick sections (Fig. 7.2e and f). Such voids are an extremely rare feature in Gorleben Hauptsalz formations. They can be correlated with hydrocarbon impregnations and are interpreted as remnants of pore space, which has almost been closed completely during the polyphase deformation and uplift of the Gorleben salt rocks (Hammer et al., 2012, 2013).

This CT scan was acquired with a voxel size of $v = 10.38 \mu\text{m}$. The raw data set of the scan volume reveals dark portions, representing the pore space filled with air or fluids, and light-gray portions representing anhydrite (Fig. 7.7a). Both portions were reconstructed and illustrated as *phong* projections (Fig. 7.7b). The anhydrite (shown in yellow) is present in form of disseminated inclusions within the halite matrix. In contrast to sample RB648 (Fig. 7.5), sample RB683 yields an anhydrite content of only $0.66 \pm 0.25 \text{ vol.-%}$. The pore space, displayed in blue, consists of single pores and fractures, which show a moderate

Chapter 7:

The application of high resolution X-ray computed tomography on naturally deformed rock salt: Multi-scale investigations of the structural inventory

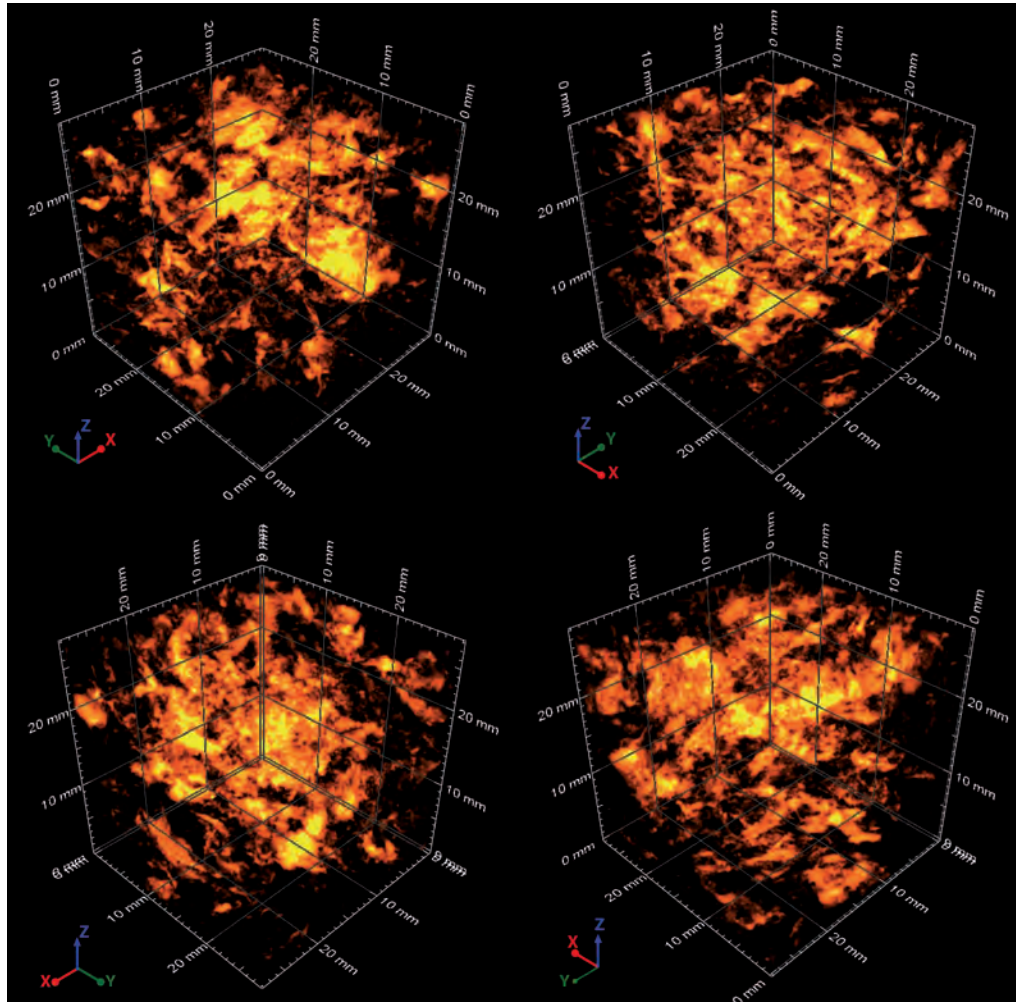


Fig. 7.5: 3D- μ CT anhydrite distribution in Gorleben Knäuelsalz (RB648). The sumalong projection is best suited to visualize the high spatial / 3D complexity and highlights the main portions of extracted objects, which is the 20-fold of the cubic surface. The cloudy visualization retraces the knotty and shredded clusters as a characteristic feature of the Knäuelsalz (z2HS1) yielding 10.1 ± 1.0 vol.-% of anhydrite in RB648; $v = 20$ μ m.

distribution anisotropy resulting in a total porosity of 0.87 ± 0.07 vol.-%. A certain amount of artificial porosity has to be assumed due to the brittle behavior of rock salt during sampling. Despite the low anhydrite content, a pervasive 3D pattern results due to numerous crystals present as single impurities or clusters. The anhydrite content of sample RB683 is low enough to justify the *phong* projection. The raw data slices show that major voids are not associated with anhydrite impurities (Fig. 7.7a). The 3D reconstructions reveal no evident correlation between the spatial distribution of anhydrite and the pore space in general (Fig. 7.7b). The anhydrite cluster in the lower corner includes almost no pore space resolvable with the given voxel size of 10.38 μ m.

Chapter 7:

The application of high resolution X-ray computed tomography on naturally deformed rock salt: Multi-scale investigations of the structural inventory

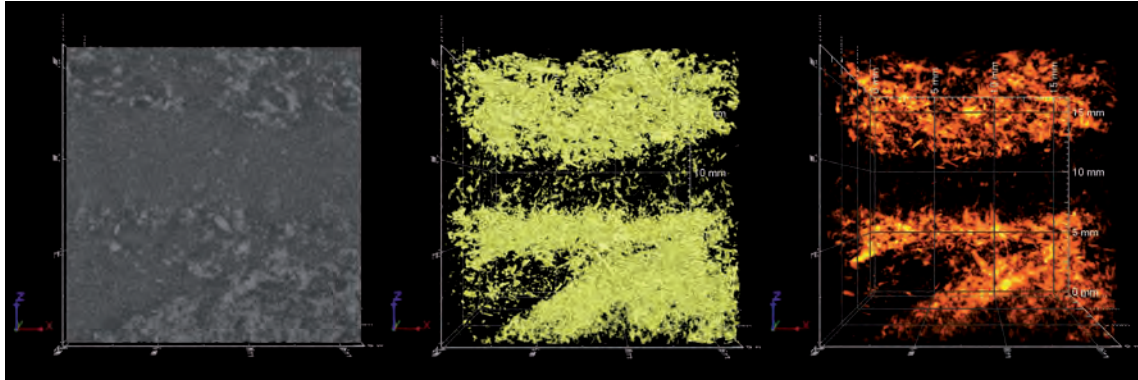


Fig. 7.6: 3D- μ CT reconstruction of mid-scale (slight close-up) anhydrite distribution in Teutschenthal rock salt (LT163_1). The phong projection (yellow) reveals three distinct layers with enriched anhydrite crystals in this rock salt volume reflecting bedding. The sumalong projection (orange) illustrates the volumetric abundance of anhydrite yielding 7.4 ± 0.7 vol.-% of the rock salt volume; $v = 8.06 \mu\text{m}$.

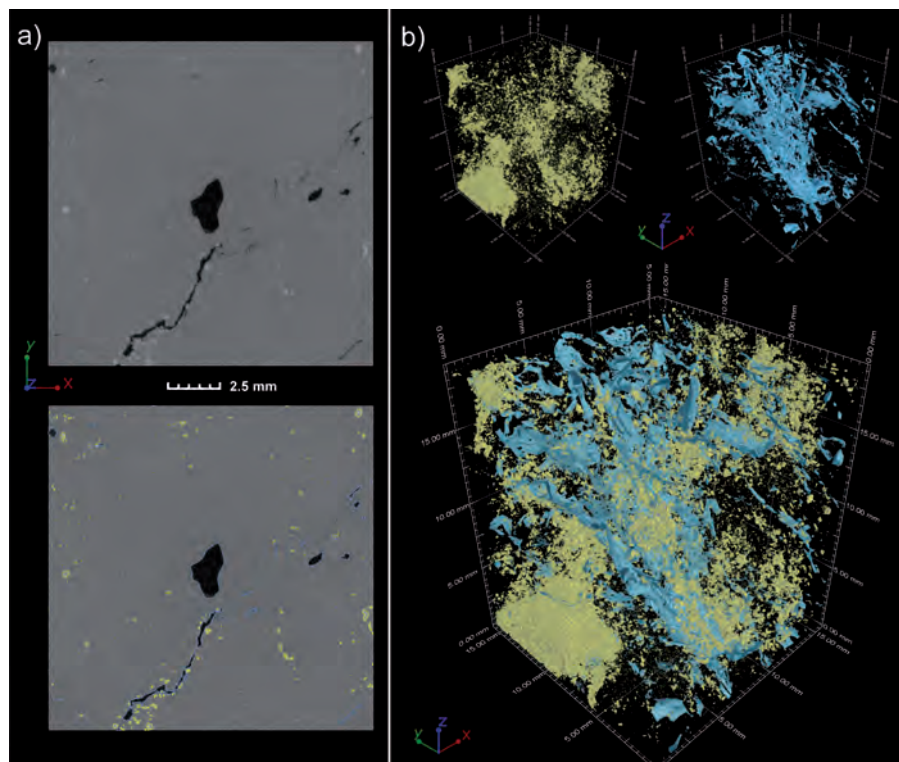


Fig. 7.7: a) Principle of gray-value based extraction in μ CT raw data sets (RB683, top view). Pore space is displayed as dark domains; halite forms the gray matrix. Anhydrite is represented as light gray, small particles. Based on their characteristic gray value thresholds, pore space and anhydrite can be traced and captured in two separate volumes illustrated as blue and yellow masks in the lower part. b) 3D- μ CT reconstruction of pore space (blue) and anhydrite (yellow) based on the raw data set shown in a). Heterogeneously distributed clusters and scattered crystals of anhydrite (yellow) are quantified with 0.66 ± 0.25 vol.-%. The pore space (blue) yields 0.87 ± 0.07 vol.-% of the analyzed volume. Halite contributes > 98 vol.-%. The lower image is a compilation of both anhydrite and pore space; $v = 10.38 \mu\text{m}$.

Chapter 7:

The application of high resolution X-ray computed tomography on naturally deformed rock salt: Multi-scale investigations of the structural inventory

7.4.3. Fluid phase reconstructions

7.4.3.1. Grain-boundary fluids of Asse rock salt

In order to characterize distributions of brines and hydrocarbons in Asse rock salt, nCT analyses were performed with a reconstructed voxel size (v_v) of 0.85 μm . The nCT scan allowed the detailed reconstruction of the fluid distribution and the separation of phase components in a single fluid inclusion. The overall distribution of a reconstructed fluid inclusion inventory is illustrated in Fig. 7.8a. The main volume describes a locally developed film-like sheet of grain-boundary fluid inclusions. The measured thickness (D) of the fluid decoration illustrates the pinching and swelling of the sheet. Some roundly-shaped, partly disconnected inclusions are present. The surface of the extracted volume appears slightly granular, which is caused by noise artifacts. The left part of the CT reconstruction exhibits a steep trail of single fluid inclusions. Such inclusion trails occur intracrystalline and often include a variety of phases (e.g. Roedder, 1984) as described for sample Bo5 (section 7.2.2).

The high scan resolution of the Asse sample allows visual separation of various inclusion components. The raw data slice in 2D as a gray scale image exhibits three different phases inside the inclusion (Fig. 7.8b). The gray scale thresholds suggest a liquid (L), a solid (S) and a vapor phase (V), but provides no information about the presence of organic matter, although parallel microstructural studies revealed the presence of hydrocarbons (Zulauf et al., 2010). The 3D reconstruction allows a spatial analysis of these components and their amounts. The solid phase (projected in yellow, Fig. 7.8b) yields 2.6 vol.-%, the amount of vapor phase (blue) is 23.5 vol.-%, and the liquid phase (cyan) constitutes the majority with 73.9 vol.-%. This type of reconstruction demonstrates how both the vapor and the solid phase are smoothly covered and surrounded by the fluid phase.

7.4.3.2. Fluid inclusions in Gorleben rock salt

The CT reconstruction of sample Bo5 was performed focusing on the main, large inclusion shown in Fig. 7.3b. Particular attention was paid to the shape, morphology, volume and position of the gas bubble. Two exemplary raw data slices exhibit the large intracrystalline, elongated fluid inclusion surrounded by further, smaller inclusions (Fig. 7.9a,b). The main inclusion consists of two different components: a low-density vapor phase portrayed in dark gray and the surrounding liquid material in medium gray. Fluorescence microscopy revealed no evidence for hydrocarbons. The vapor phase is pinched and therefore slightly elongated following the inclusion's morphology. The two components are affected by noise artifacts represented as a granular pattern. Whereas the overall inclusion is quickly reconstructed, the distinction between the liquid and the vapor phase is more difficult. For this reason, the low density contrast and the artifacts preserved by post-processing hinder the automated threshold technique and require manual processing for the vapor component in VGStudioMAX. This technique allows separating both components and enables the quantification and a detailed visualization of the structures. The very

Chapter 7:

The application of high resolution X-ray computed tomography on naturally deformed rock salt: Multi-scale investigations of the structural inventory

small voxel size ($v = 1 \mu\text{m}$) allows a detailed reconstruction of the shape and morphology of the fluid inclusion (Fig. 7.9c-f). By virtual truncating of the liquid portion, the spatial position of the gas bubble can be recognized. A granular surface of the reconstructed vapor volume remains due to the artifacts in the raw data. Finally, the vapor phase is quantified to compose the intracrystalline inclusion with 34.7 vol.-%.

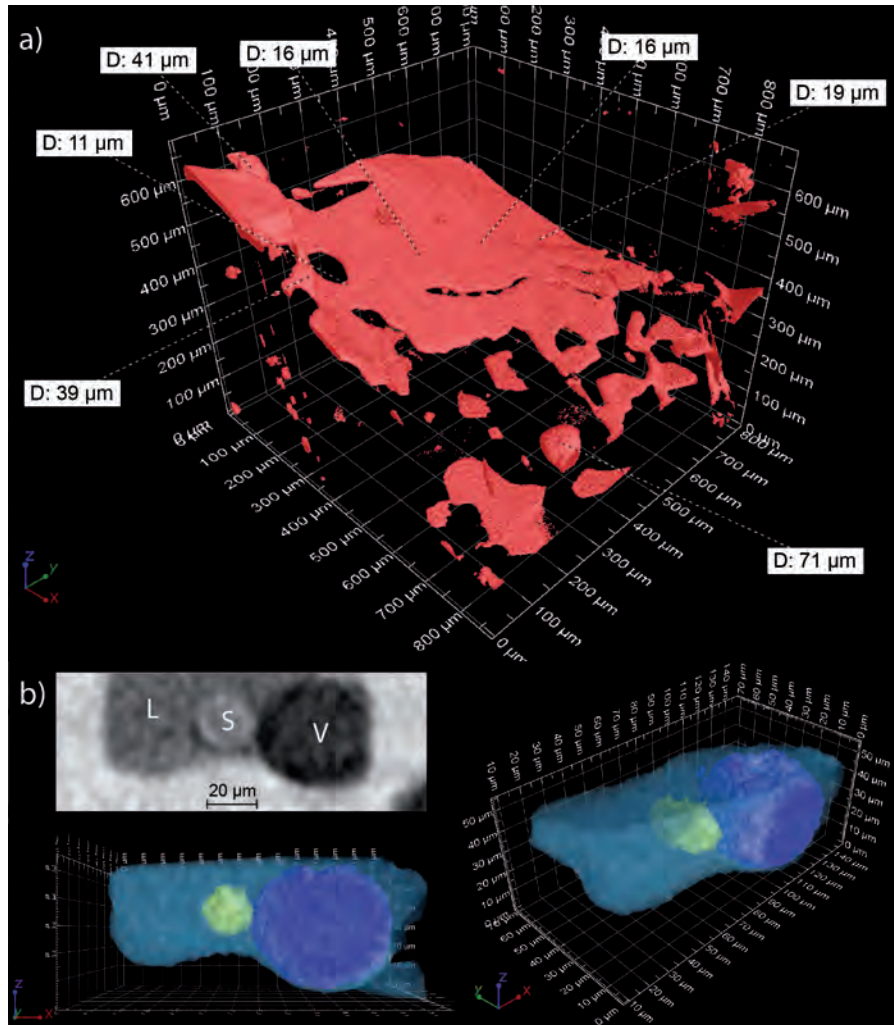


Fig. 7.8: 3D-nCT reconstruction of fluid inclusions in Asse rock salt (Speisesalz). a) The 3D-reconstruction (red) shows various shapes of fluids along a halite grain-boundary. Diameters of fluids (D) are given for single sites to clarify the dimensions of pinching and swelling of some fluids. Some of the isolated inclusions were further analyzed (see below). b) Single fluid inclusion components. The 2D raw data image (gray) reveals three different components (L = liquid, S = solid and V = vapor) which are reconstructed and quantified: The solid phase (shown in yellow in the 3D-nCT reconstruction) yields 2.6 vol.-%, the vapor phase (shown in light blue) represents 23.5 vol.-% and the liquid phase (shown in cyan) is quantified with 73.9 vol.-%; $v = 1.7 \mu\text{m}$; $v_r = 850 \text{ nm}$.

Chapter 7:

The application of high resolution X-ray computed tomography on naturally deformed rock salt: Multi-scale investigations of the structural inventory

The CT reconstruction of Bo5UHR (Fig. 7.10) represents the highest resolution applied so far when analyzing fluid inclusions with nCT ($v = 700$ nm). By reconstructing the original data with the doubled resolution (2Res), the reconstructed voxel size (v_r) was decreased to 350 nm (see section 7.3.3). The scan exhibits the geometry and morphology of the planar fluid network in great detail. Thicknesses (D) are given for single sites to illustrate the pinching and swelling of the fluid structure (Fig. 7.10c). Single objects occur isolated, whereas the main portion is connected giving way from broad patches to fine fluid lines. The main fluid branches can be retraced in Fig. 7.3c, while very small fluid spots and thin fluid

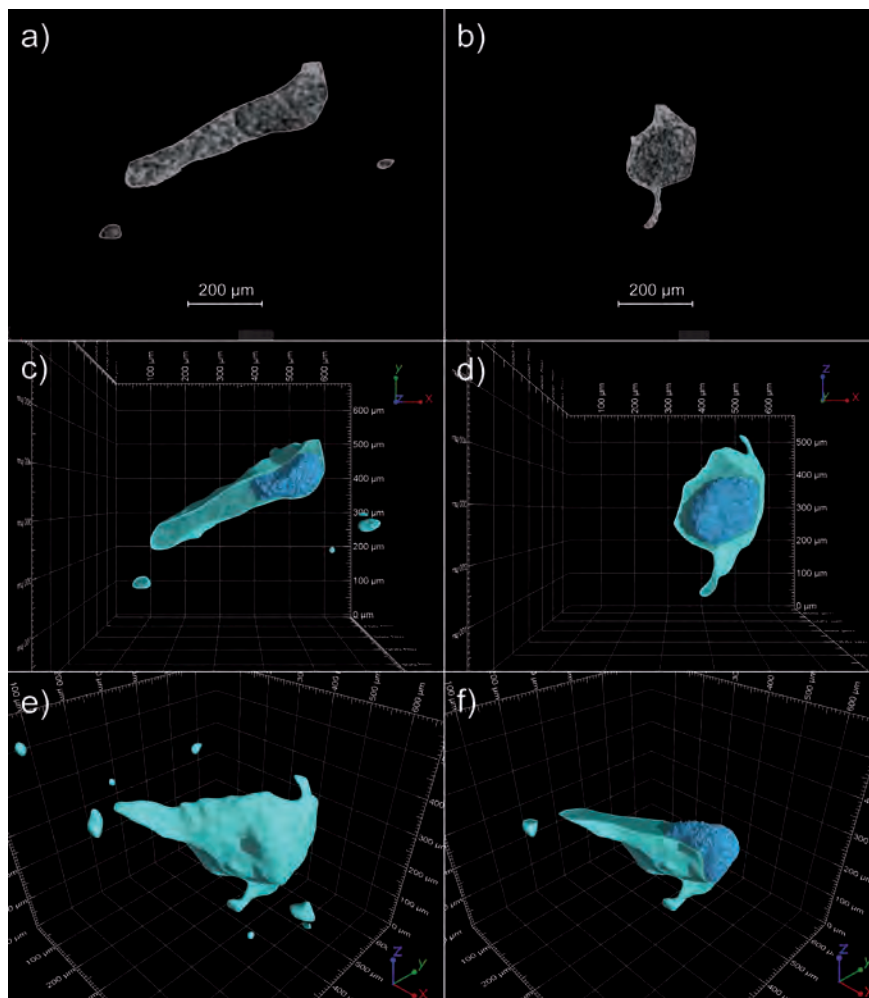


Fig. 7.9: CT scan of an intracrystalline fluid inclusion in Kristallbrockensalz (z2HS3) of Gorleben rock salt (sample Bo5). a) and b) Raw data slices as gray scale images have been limited to the region of interest by excluding the halite matrix illustrating a large low-density vapor phase shown in dark gray surrounded by higher-density fluid shown in medium-gray (including multiple small low-density artifact-particles). c) and d) 3D- μ CT reconstruction of Bo5. The liquid phase volume is virtually truncated to uncover the position of the vapor phase. e) Fully reconstructed morphology of the intracrystalline inclusion. f) Same perspective as e) with truncated liquid phase volume. The vapor phase yields 34.7 vol.-% of the intracrystalline inclusion; $v = 1 \mu\text{m}$.

Chapter 7:

The application of high resolution X-ray computed tomography on naturally deformed rock salt: Multi-scale investigations of the structural inventory

branches could not be reconstructed. A planar network of anastomosed inclusions composes 0.45 ± 0.5 vol.-% of the analyzed rock salt volume.

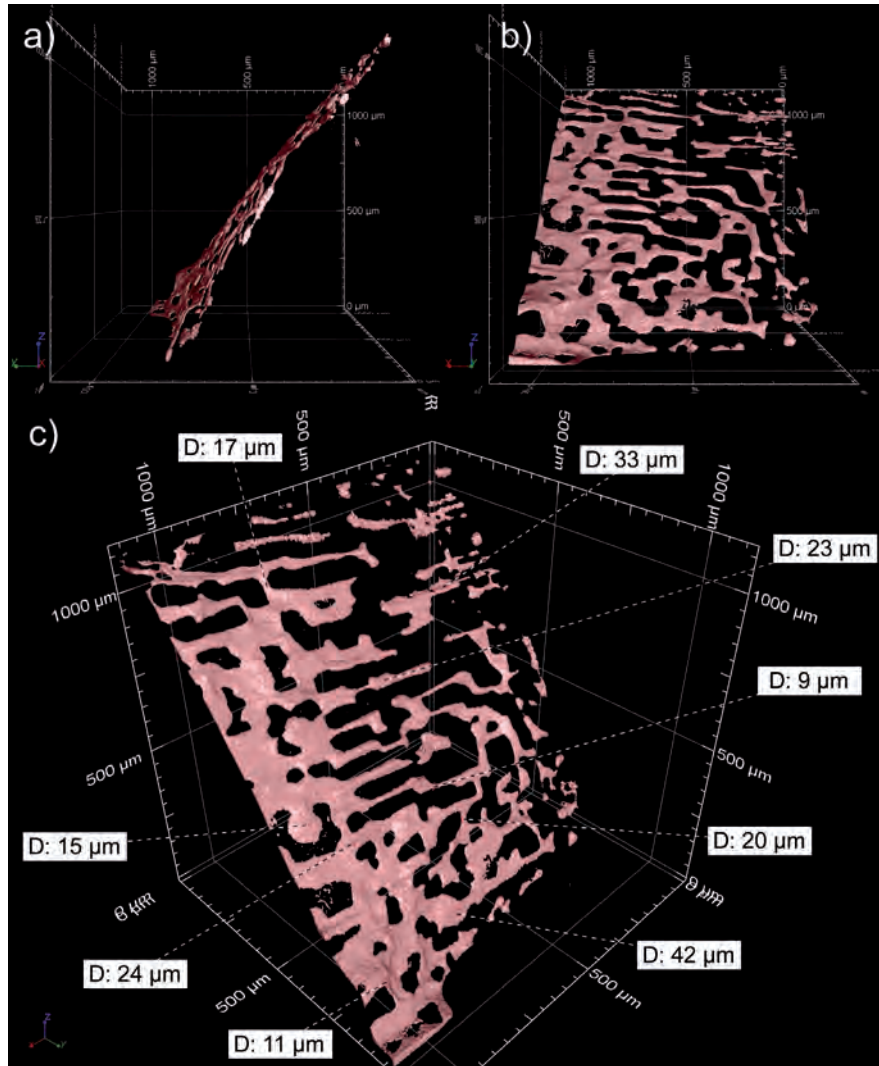


Fig. 7.10: Halite grain-boundary fluid inclusions of sample Bo5UHR in Gorleben Kristallbrockensalz (z2HS3). a) and b) The fluid inclusions yield 0.45 ± 0.05 vol.-% of the analyzed rock salt volume. c) Oblique view of grain-boundary fluid inclusions showing the diameter of the inclusions (D); $v = 700$ nm; $v_r = 350$ nm.

7.5. Discussion

7.5.1. Filtering, image arithmetic and error estimation

Filtering is an important topic in digital imaging and deeply rooted in computed tomography. It symbolizes an essential possibility to counteract a variety of artifacts that are generated during the scanning process by changes of the X-ray spectrum passing through the sample, by detector properties

Chapter 7: The application of high resolution X-ray computed tomography on naturally deformed rock salt: Multi-scale investigations of the structural inventory

(e.g. noise) or by optical aspects (e.g. overlays by beam hardening) of CT imaging. For brief overviews of artifacts and possible corrections, the reader is referred to Ketcham and Carlson (2001) and Cnudde and Boone (2013).

In our study, digital filtering has been used to modify the data set quality in some cases to even enable the reconstruction. Besides noise, the main artifact counteracted in our post-processing is beam-hardening (e.g. Ketcham and Carlson, 2001; Carlson, 2006). The reconstructed phase components in the Asse rock salt (Fig. 7.8b) and in sample Bo5 (Fig. 7.9) were only enabled by 3D Median filtering and noise reduction. Although the single components can be visually distinguished, the weak gray value contrast requires a manual capturing of the structures in VGStudioMAX for any quantitative approach. An automated extraction by gray scale thresholds was not possible due to an overall, limited range of gray values in the raw data.

The anhydrite distribution in sample RB648 (Fig. 7.5) is another example of how filtering can improve or enable the reconstruction of portions in complex CT scans and is illustrated by a stepwise modification of the raw data (Fig. 7.11). The raw data set of RB648 (Fig. 7.11a) is characterized by a certain noise and very weak gray value contrasts of halite and anhydrite. The noise signal denies a proper, automated capturing of the anhydrite portions (light gray). Strong 3D Median filtering (15) reduces the noise signal to a minimum and virtually accentuates the anhydrite volumes. The strong filtering partly erases very small portions of anhydrite resulting in an increased uncertainty of the quantitative data. However, the automated capturing of anhydrite (yellow portions in Fig. 7.11b) uncovers the beam-hardening artifact of the filtered CT volume. The corner and side regions of the halite volume in Fig. 7.11b are represented by higher gray values corresponding to anhydrite. The beam-hardening effect can be generally avoided by various techniques. Firstly, software-related tools allow counteraction of beam-hardening by special algorithms. Secondly, physical filters such as copper plates can be used to split the X-ray spectrum prior to hitting the sample and thus avoiding the beam-hardening effect. Thirdly, the sample can be confined by equivalent material or a cask in order to shield the sample from the hardening effect (Ketcham and Carlson, 2001). Detailed beam-hardening aspects and possible corrections are further presented by Ketcham and Hanna (2014). In sample RB648 outer parts of halite “adopted” the gray values of anhydrite due to the beam-hardening effect (Fig. 7.11b).

In such low contrast raw data sets, physical filtering by copper plates or confining casks decrease the signal intensity at the detector and further lower the gray value contrasts in the data sets. The radial, artificial brightening in the data volume of sample RB648 was solved by image arithmetic performed with Fiji (Schindelin et al., 2012). The CT volume was strongly Gaussian blur filtered (100) in order to reduce the data set information to this particular trend in gray values including the beam-hardening artifact (Fig. 7.11c). In the next step, the Gaussian-filtered volume was inverted and added to the Median-filtered volume afterwards (Fig. 7.11b) in order to produce a data volume in which the background gray scale variation is removed and an improved capturing of the anhydrite is ensured (Fig. 7.11d). Finally, the use

Chapter 7:

The application of high resolution X-ray computed tomography on naturally deformed rock salt: Multi-scale investigations of the structural inventory

of filters (Median and Gaussian blur) in combination with image arithmetic enabled a 3D reconstruction of a raw data set formerly affected by noise and beam-hardening artifact.

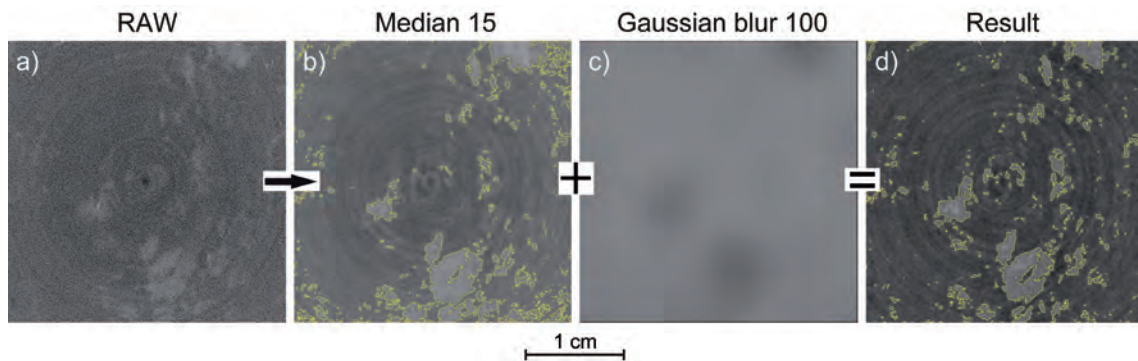


Fig. 7.11: Image quality improvement of sample RB648 (see Fig. 7.2) by different filters and image arithmetic. a) The raw data is affected by noise. b) A Median filter is used to eliminate this noise. Bright parts of halite in the outer regions are included during anhydrite extraction. c) In order to eliminate the outward brightening effect, the raw data volume is strongly Gaussian filtered, inverted and finally added to the Median filtered volume. d) The result shows improved anhydrite extraction and the lack of preferentially selected segments at the corners; $v = 20 \mu\text{m}$.

Generally, the reliability of volume percentages has to be taken with caution and is a complex issue depending on sample type, CT volume quality, data processing and most importantly the maximum resolution (Cnudde and Boone, 2013). The technical limitation (CT resolution) is controlled by the natural limitation (very small structures or low density contrasts). Quantificational studies performed by CT generally give minimum values, for instance in porosity studies due to the resolution limits (e.g. Derluyn et al., 2014; Thiemeyer et al., 2014). The comparison of porosities obtained by laboratory measurements (e.g. noble gas porosimetry) and CT scans are consistent with this observation (e.g. Arns et al., 2005). Possible overestimation is strongly counteracted and certainly prevented by filtering.

As ROIs are extracted and reconstructed by gray value thresholds (automated extraction, see section 7.3.3), the estimated errors can be roughly determined by shifting these thresholds within a reasonable range. The specific range of this shift depends on the gray value contrasts of the raw data set and the designated ROIs. As an example, RB683 (Fig. 7.7) includes anhydrite and pore space. In the same range of gray value shift (± 850 values), both materials give slightly different, relative errors due to the specific density (gray value) contrasts. Higher density contrasts (pore space/halite) therefore attain smaller errors than lower density contrasts (anhydrite/halite). Hence, the particular gray value histograms of the CT scans are the reasons for differing error estimations in the analyzed samples. The largest error of about 10 % was determined in sample RB648 (Fig. 7.5), in which case the weak density contrast was strongly affected by image arithmetic and by the relatively large sample size causing a high penetration depth for the X-ray and thus a very low signal intensity.

However, the stated errors are only related to the extraction and reconstruction technique. The overall

Chapter 7:

The application of high resolution X-ray computed tomography on naturally deformed rock salt: Multi-scale investigations of the structural inventory

limiting factor is given by the CT resolution (voxel size) possibly causing very large errors depending on the spatial and physical properties of the designated phase or material, such as size, distribution and density.

7.5.2. Improving raw data set information in the sub-micron range

For very precise reconstruction of extremely small particles the resolution improvement (2Res) can be generated by a special reconstruction procedure resulting in reconstructed voxel sizes (v_r) half the original (geometrical) voxel size (v) of the CT scan (see section 7.3.3). The 2Res technique is invaluable when very small particles are to be reconstructed, such as grain-boundary fluids. Two preconditions for 2Res reconstruction must be considered: (i) The number of single images in the scanning process should ideally be doubled compared to the standard requirements by the pixel numbers of the detector to provide additional spatial object information; (ii) the spot size should be smaller than the voxel size deduced from the particular projection geometry. If these requirements are fulfilled, the data set improvement enables better constructions of objects by increased numbers of voxels, especially in the submicron range. However, artifacts are equally amplified by the 2Res technique. Thus, it has to be considered whether an improved reconstruction by 2Res is useful or not concerning computing capacities, probe size, noise artifacts or raw data quality in general.

7.5.3. Implications and restricting aspects of rock salt CT measurements

CT imaging was performed on different scales to map characteristic anhydrite impurities, clusters or layers.

The distribution of anhydrite clusters in Knäuelsalz sample RB648 reflects the dynamic reworking of the rock salt during the salt uplift and has been reconstructed in 3D by CT imaging for the first time (Fig. 7.5). The CT reconstruction sheds light upon the distribution of anhydrite in this particular salt formation (Knäuelsalz, z2HS1) and illustrates intense deformation of this particular sample. Primary bedded anhydrite layers and even distinct folds or boudins are no longer recognizable as such. Thus, the three-dimensional anhydrite reconstruction by CT complements macro- and microstructural observations revealing a strongly homogenized halotectonic breccia with primary bedding features being completely destroyed (Bornemann et al., 2008).

The voxel size of 20 μm implies that small anhydrite crystals are not resolved. Digital filtering caused vague phase or gray value transitions and blurred boundaries. Because the main emphasis for sample RB648 pertains to the disseminated clusters, small anhydrite portions were disregarded and a larger volume with a limited resolution was chosen. Although the CT reconstruction is inaccurate in certain aspects, the spatial distribution of the anhydrite clusters was visualized for the first time. The accuracy of the anhydrite quantification is hard to determine. At least the quantification of the anhydrite surface area should be largely underestimated because of the resolution limits and the impact of filtering (see

Chapter 7:

The application of high resolution X-ray computed tomography on naturally deformed rock salt: Multi-scale investigations of the structural inventory

section 7.5.1). However, a large surface area (see section 7.4.1) suggests the object to be composed by a great number of sub-particles.

The Teutschenthal CT volume (sample LT163_1) allows the identification of single anhydrite crystals due to the smaller voxel size and the larger anhydrite crystals compared to sample RB648. The differences in anhydrite distribution obtained by light microscopy (Fig. 7.2a and b) are supported by the CT analyses and clearly reveal the planar distribution of anhydrite crystals in 3D. In contrast to the Gorleben samples, these structures represent distinct layers from deposition. The spatial information provided by CT allows new spatial information on the weak folding or boudinage of the rock salt. This CT reconstruction serves as a counter-example to the strongly deformed Gorleben sample (Fig. 7.5) and clarifies how former bedding features become annihilated by salt tectonics.

Anhydrite often accounts for porosity and related fluid distribution in rock salt. The brittle and brittle-ductile behavior of anhydrite is associated with the formation of microfractures and fissure reservoirs (Bornemann et al., 2008; Zulauf et al., 2010). Due to our CT reconstructions of anhydrite and pore space distribution (sample RB683; Fig. 7.7) this basic assumption can be challenged, because the reconstructed macroporosity shows a differing spatial distribution pattern in respect to the anhydrite. Indeed, the corresponding microfabrics studied under the microscope reveal slightly elevated porosity inside anhydrite clusters, which is in line with the basic assumption mentioned above. However, the macroporosity visualized in the CT reconstruction is the major contributor to the bulk porosity and not related to anhydrite clusters or impurities as illustrated by the corresponding CT patterns. The unequal spatial distribution of such relatively large pores and anhydrite impurities is in agreement with previous macro- and microstructural investigations of Gorleben rock salt, as well (Hammer et al., 2012, 2013). Microporosity within the anhydrite clusters, which subordinately contributes to the bulk porosity in our studied sample, is below the CT resolution and cannot be captured in this data set. Generally, porosity estimations based on CT data must be interpreted as a minimum value because of the resolution limits (e.g. Arns et al., 2005). It has to be emphasized that our determined amount of pore space in sample RB683 is not common for naturally deformed (Gorleben) rock salt, which is generally characterized by very low porosities (e.g. Popp et al., 2007; Bornemann et al., 2008). The differing distribution patterns suggest that anhydrite does not play a significant role in the slightly elevated porosity of this particular sample, which is very important to estimate the influence of anhydrite for assumptions on fluid or gas flow/distribution in rock salt. Generally, μ CT is a potentially highly effective tool in determining genetic relations and dependencies between porosity and solid impurities, such as anhydrite.

The μ CT reconstruction of Asse fluids resulted in a three-dimensional distribution pattern of a grain-boundary fluid film and a separation of solid, liquid and vapor phase in a single inclusion (Fig. 7.8b). The latter was assumed by the lowest density in combination with its circular shape. The liquid phase was deduced by its slightly elevated density and the adaptive shape. Although important information about the chemical properties cannot be obtained by μ CT, the single components can be quantified and

Chapter 7: The application of high resolution X-ray computed tomography on naturally deformed rock salt: Multi-scale investigations of the structural inventory

visualized in three dimensions.

Similarly, the real spatial distribution and morphology of Gorleben fluid inclusions of sample Bo5 and sample Bo5UHR can only be inferred by light microscopy. The CT reconstructions of (Figs. 7.9, 7.10) uncover accurate morphologies and volumes, although little spots and thin linking stripes described in Fig. 7.3c are not captured in the CT scan due to resolution limits. Thus, a combination of light microscopy and CT imaging leads to greater insight concerning inclusions and demonstrates how weak points of one technique can be complemented by the strong points of another. Regarding fluid inclusions in rock salt, light microscopy is limited to a single focus plane causing large parts of the objects to be out of focus. Although the z-stack images of samples Bo5 and Bo5UHR are reduced in blurred areas, some regions of the images remain unfocussed. Stacked image improvement is strongly site-dependent and often influenced by impurities in the samples behind or in front of the objects of interest.

CT imaging is a further method to study fluid inclusions in great detail, which was previously performed by cryogenic vitrification and 3D serial sectioning using high resolution cryo-FIB SEM (see Desbois et al., 2008). Although cryo-FIB SEM allows resolutions not accessible for nCT, high resolution X-ray computed tomography represents a fast, non-destructive method for detailed investigation of single and multiphase fluid inclusions as shown by our reconstructed CT volumes. The potential of the nCT scan of sample Bo5UHR (Fig. 7.10) must be emphasized, because it is the first tomographic investigation of rock salt grain boundary fluid inclusions at such a high magnification in the submicron range. The major advantages relative to other investigational techniques are the unrestricted angles of view and the wealth of supplementary information on thickness, volume, shape, spatial arrangement, etc. of the objects examined.

7.6. Conclusions

- X-ray computed tomography shows its applicability to investigate the structural inventory of rock salt in many ways. The 3D visualization and quantification of phases, pore space or fluid inclusions on different scales give new perspectives for microstructural analyses of rock salt.
- Different projection modes (e.g. *phong* and *sumalong*) precisely carve out morphologies and shapes of the rock salt inventory and allow a characterization of their volumes and characteristic surface determinations.
- The combination of filters with image arithmetic is useful to improve CT raw data volumes in order to counteract noise and beam-hardening artifacts. This procedure enabled the visualization of the eponymous anhydrite distribution, retracing the strong reworking of this rock salt formation.
- The porosity and anhydrite distribution in Gorleben rock salt suggest that the elevated (macro)porosity is not triggered or influenced by anhydrite distribution. This independence is a further argument, that these exceptionally occurring pores (in combination with elevated hydrocarbon and fluid contents)

Chapter 7: The application of high resolution X-ray computed tomography on naturally deformed rock salt: Multi-scale investigations of the structural inventory

represent remnants, which have been generally closed and removed during the complex deformation history of Gorleben rock salt. As anhydrite is generally depicted to represent main pathways and reservoirs for fluids, it is confirmed that rarely occurring elevated porosity in Gorleben rock salt did not arise from anhydrite impurities.

- nCT reconstructions of naturally deformed Gorleben and Asse rock salt fluid inclusions (and their components) have been performed for the first time and illustrates the substantial contribution of CT imaging for intra- and intercrystalline fluid inclusion studies in salt rocks.

7.7. Acknowledgements

The authors are grateful to Maximilian Pusch for providing the numerous rock salt samples. We kindly thank Phoenix/x-ray (General Electric) for performing a CT test scan on the Asse sample. Stuart Clark Fisher-Spurlock is thanked for proofreading the manuscript. We acknowledge constructive reviews from F. Füsseis, F. Neubauer and C. Leitner.

7.8. References

- Adam, J., Klinkmüller, M., Schreurs, G., Wieneke, B., 2013. Quantitative 3D strain analysis in analogue experiments simulating tectonic deformation: Integration of X-ray computed tomography and digital volume correlation techniques. *Journal of Structural Geology* 55, 127-149.
- Alam, A.K.M.B., Niioka, M., Fujii, Y., Fukuda, D., Kodama, J., 2014. Effects of confining pressure on the permeability of three rock types under compression. *International Journal of Rock Mechanics & Mining Sciences* 65, 49-61.
- Arns, C.H., Bauget, F., Limaye, A., Sakellariou, A., Senden, T.J., Sheppard, A.P., Sok, R.M., Pinczewski, W.V., Bakke, S., Berge, L.I., Oren, R.E., Knackstedt, M.A., 2005. Porescale characterization of carbonates using X-ray microtomography. *SPE Journal* 10 (4), 475–484.
- Bay, B.K., Smith, T.S., Fyhrie, D.P., Saad, M., 1999. Digital volume correlation: threedimensional strain mapping using X-ray tomography. *Experimental Mechanics* 39 (3), 217–226.
- Boone, M.N., Dewanckele, J., Boone, M.A., Cnudde, V., Silversmit, G., Van Ranst, E., Jacobs, P., Vincze, L., Van Hoorebeke, L., 2011. Three-dimensional phase separation and identification in granite. *Geosphere* 7 (1), 79–86.
- Bornemann, O., 1991. Zur Geologie des Salzstocks Gorleben nach den Bohrerergebnissen. *BfS-Schriften* 4, 1-67.
- Bornemann, O., Behlau, J., Fischbeck, R., Hammer, J., Jaritz, W., Keller, S., Mingerzahn, G., Schramm, M., 2008. Description of the Gorleben Site Part 3. Results of the geological surface and underground exploration of the salt formation. – BGR: 50 figures, 7 tables, 5 appendices; Hannover, 223pp.

Chapter 7:

The application of high resolution X-ray computed tomography on naturally deformed rock salt: Multi-scale investigations of the structural inventory

- Bräuer, V., Eickemeier, R., Eisenburger, D., Grissemann, C., Hesser, J., Heusermann, S., Kaiser, D., Nipp, H.-K., Nowak, T., Plischke, I., Schnier, H., Schulze, O., Sönnke, J., Weber, J.R., 2011. Description of the Gorleben site Part 4: Geotechnical exploration of the Gorleben salt dome. BGR: 176pp., 96 figures, 13 tables, 2 appendices, Hannover – ISBN 978-3-510-95988-4.
- Burliga, S., Czechowski, F., 2010. Anatomy of hydrocarbon-bearing zones, hydrocarbon provenance and their contribution to brittle fracturing of rock salt in the Klodawa Salt Structure (central Poland). - SMRI Spring 2010 Technical Conference, Grand Junction, USA.
- Cai, Y., Liu, D., Mathews, J.P., Pan, Z., Elsworth, D., Yao, Y., Li, J., Guo, X., 2014. Permeability evolution in fractured coal - Combining triaxial confinement with X-ray computed tomography, acoustic emission and ultrasonic techniques. *International Journal of Coal Geology* 122, 91-104.
- Carlson, W., 2006. Three-dimensional imaging of earth and planetary materials. *Earth and Planetary Science Letters* 249, 133-147.
- Carlson, W.D., Denison, C., 1992. Mechanisms of porphyroblast crystallization: results from high-resolution computed X-ray tomography. *Science* 257, 1236-1239.
- Coles, M.E., Hazlett, R.D., Spanne, P., Soll, W.E., Muegge, E.L., Jones, K.W., 1998. Pore level imaging of fluid transport using synchrotron X-ray microtomography. *Journal of Petroleum Science and Engineering* 19, 55-63.
- Cnudde, V., Silversmit, G., Boone, M., Dewanckele, J., De Samber, B., Schoonjans, T., Van Loo, D., De Witte, Y., Elburg, M., Vincze, L., Van Hoorebeke, L., Jacobs, P., 2009. Multi-disciplinary characterisation of a sandstone surface crust. *Science of the Total Environment* 407 (20), 5417-5427.
- Cnudde, V., Boone, M. N., 2013. High-resolution X-ray computed tomography in geosciences: A review of the current technology and applications. *Earth Science Reviews* 123, 1-17.
- Cunningham, K.J., Sukop, M.C., Huang, H., Alvarez, P.F., Curran, H.A., Renken, R.A., Dixon, J.F., 2013. Prominence of ichnologically influenced macroporosity in the karst Biscayne aquifer: Stratiform “super-K” zones. *Geological Society of American Bulletin* 121/1-2, 164-180.
- Derlyun, H., Dewanckele, J., Boone, M.N., Cnudde, V., Derome, D., Carmeliet, J., 2014. Crystallization of hydrated and anhydrous salts in porous limestone resolved by synchrotron X-ray microtomography. *Nuclear Instruments and Methods in Physics Research B* 324, 102-112.
- Desbois, G., Urai, J.L., Burkhardt, C., Drury, M.R., Hayles, M., Humbel, B., 2008. Cryogenic vitrification and 3D serial sectioning using high resolution cryo-FIB SEM technology for brine-filled grain boundaries in halite: first results. *Geofluids* 8, 60-72.
- Desbois, G., Urai, J.L., De Bresser, J.H.P., 2012. Fluid distribution in grain boundaries of natural fine-grained rock salt deformed at low differential stress (Qom Kuh salt fountain, central Iran): Implications for rheology and transport properties. *Journal of Structural Geology* 43, 128-143.
- Dewanckele, J., De Kock, T., Boone, M.A., Cnudde, V., Brabant, L., Boone, M.N., Fronteau, G., Van Hoorebeke, L., Jacobs, P., 2012. 4D imaging and quantification of pore structure modifications

Chapter 7:

The application of high resolution X-ray computed tomography on naturally deformed rock salt: Multi-scale investigations of the structural inventory

- inside natural building stones by means of high resolution X-ray CT. *Science of the Total Environment* 416, 436–448.
- Drury, M.R, Urai, J.L., 1990. Deformation-related recrystallization processes. *Tectonophysics* 172, 235-253.
- Evans, N.J., McInnes, B.I.A., Squelch, A.P., Austin, P.J., McDonald, B.J., Wu, Q., 2008. Application of X-ray micro-computed tomography in (U-Th)/He thermochronology. *Chemical Geology* 257, 101-113.
- Fusseis, F., Regenauer-Lieb, K., Liu, J., Hough, R.M., De Carlo, F., 2009. Creep cavitation can establish a dynamic granular fluid pump in ductile shear zones. *Nature* 459/7249, 974-977.
- Fusseis, F., Xiao, X., Schrank, C., De Carlo, F., 2014. A brief guide to synchrotron radiation-based microtomography in (structural) geology and rock mechanics. *Journal of Structural Geology* (2014), doi: 10.1016/j.jsg.2014.02.005.
- Gies, H., Herbert, H.-J., Jockwer, N., 1990. Zur Bedeutung der Wassergehalte für die Lithostratigraphie in Steinsalzhorizonten des Zechsteins. *Kali und Steinsalz* 10, 265–271.
- Godel, B., Barnes, S.-J., Maier, W.D., 2006. 3-D Distribution of Sulphide Minerals in the Merensky Reef (Bushveld Complex, South Africa) and the J-M Reef (Stillwater Complex, USA) and their Relationship to Microstructures Using X-ray Computed Tomography. *Journal of Petrology* 47, 1853-1872.
- Godel, B., Barnes, S.J., Barnes, S.-J., Maier, W.D., 2010. Platinum ore in three dimensions: Insights from high-resolution C-ray computed tomography. *Geology* 38/12, 1127-1130.
- Hammer, J., Pusch, M., Häger, A., Ostertag-Henning, C., Schlömer, S., Mingerzahn, G., Scheeder, G., Shao, H., Paul, B., Schulze, O., Zaretzki, B., Hesser, J., 2012. Untersuchungen von Kohlenwasserstoffen im Erkundungsbergwerk Gorleben. Interim report 2012, Federal Institute for Geosciences and Natural Resources, Hannover, 236 pp.
- Hammer, J., Pusch, M., Häger, A., Ostertag-Henning, C., Schlömer, S., Mingerzahn, G., Scheeder, G., Shao, H., Paul, B., Schulze, O., Zaretzki, B., Hesser, J., 2013. Untersuchungen von Kohlenwasserstoffen im Erkundungsbergwerk Gorleben. Interim report 2013, Federal Institute for Geosciences and Natural Resources, Hannover, 207 pp.
- Henderickx, H., Tafforeau, P., Soriano, C., 2012. Phase-contrast synchrotron microtomography reveals the morphology of a partially visible new Pseudogarypus in Baltic amber (Pseudoscorpiones: Pseudogarypidae). *Palaeontologia Electronica* 15 (2).
- Huddleston-Holmes, C.R., and Ketcham, R.A., 2010. An X-ray computed tomography study of inclusion trail orientations in multiple porphyroblasts from a single sample. *Tectonophysics*, 480/1, 305-320.
- Hunsche, U., Hampel, A., 1999. Rock salt – the mechanical properties of the host rock material for a radioactive waste repository. *Engineering Geology* 52, 271-291.
- Iassonov, P., Gebrenegus, T., Tuller, M., 2009. Segmentation of X-ray computed tomography images of

Chapter 7:

The application of high resolution X-ray computed tomography on naturally deformed rock salt: Multi-scale investigations of the structural inventory

- porous materials: A crucial step for characterization and quantitative analysis of pore structures. *Water Resources Research* 45, W09415, doi: 10.1029/2009WR008087.
- Jagsch, R., Theylich, H., 1999. Speicher-geologische und geotechnische Bedingungen an den Kavernenstandorten Teutschenthal und Bernburg. In: Hartmann, O. (Ed.). *Kali-, Steinsalz und Kupferschiefer in Mitteldeutschland*, 115-129.
- Jerram, D.A., Higgins, M.D., 2007. 3D analysis of rock textures: Quantifying igneous microstructures. *Elements* 3, 239–245.
- Ketcham, R.A., Carlson, W.D., 2001. Acquisition, optimization and interpretation of X-ray computed tomographic imagery: applications to the geosciences. *Computers & Geosciences* 27 (4), 381–400.
- Ketcham, R.A., Hanna, R. D., 2014. Beam hardening correction for X-ray computed tomography of heterogeneous natural materials. *Computers & Geosciences* 67, 49-61.
- Küster, Y., 2011. Bromide characteristics and deformation mechanisms of naturally deformed rock salt of the German Zechstein basin. PhD thesis, University of Göttingen, Germany, 221 pp.
- Mees, F., Swennen, R., Van Geet, M., Jacobs, P. 2003. Applications of X-ray Computed Tomography in the Geosciences. Geological Society, London, Special Publications, 215: 243 pp.
- Mertineit, M., Schramm, M., Hammer, J., Zulauf, G., 2014. Deformation of anhydrite rocks (Gorleben-Bank, z3OSM) in a high-strain domain of the Gorleben salt dome, Germany. *German Journal of Geosciences* 165 (1), 49-62.
- Meyer, C., Jébrak, M., Stöffler, D., Riller, U., 2011. Lateral transport of suevite inferred from 3D shape-fabric analysis: Evidence from the Ries impact crater, Germany. *Geological Society of America Bulletin* 123/11-12, 2312-2319.
- Nyquist, H., 1928. Certain topics in telegraph transmission. *Journal of the American Institute of Electrical Engineers* 47, 617-644.
- Ogurreck, M., Wilde, F., Herzen, J., Beckmann, F., Nazmov, V., Mohr, J., Haibel, A., Müller, M., Schreyer, A., 2013. The nanotomography endstation at the PETRA III Imaging Beamline. *J Physics: Conf. Series* 425, 182002.
- Pastor-Galán, D., Gutiérrez-Alonso, G., Zulauf, G., Zanella, F., 2012. Analogue modeling of lithospheric-scale orocline buckling: Constraints on the evolution of the Iberian-Armorican Arc. *Geological Society of America Bulletin* 124/7-8, 1293-1309.
- Peach, C.J., 1993. Deformation, dilatancy and permeability development in halite/anhydrite composites. In: Ghoreychi, M., Berest, P., Hardy, H.R. Jr., Langer, M. (Eds.). *The mechanical behavior of salt: proceedings of the 3rd conference (Trans Tech. Publ.)*, 153-166.
- Peach, C.J., Spiers, C.J., Trimby, P.W., 2001. Effect of confining pressure on dilation, recrystallization and flow of rock salt at 150°C. *Journal of Geophysical Research* 106, 13315-13328.
- Pennock, G.M., Drury, M.R., Peach, C.J., Spiers, C.J., 2006. The influence of water on deformation

Chapter 7:

The application of high resolution X-ray computed tomography on naturally deformed rock salt: Multi-scale investigations of the structural inventory

- microstructures and textures in synthetic NaCl measured using EBSD. *Journal of Structural Geology* 28, 588-601.
- Popp, T., Salzer, K., Wiedemann, M., Kansy, A., Pusch, G., 2007. Gas transport in dry rock salt – implications from laboratory investigations and field studies. In: Wallner, M., Lux, K.-H., Minkley, W., Hardy Jr., H.R. (Eds.). *The Mechanical Behavior of Salt – Understanding of THMC Processes in Salt*, Taylor & Francis Group, 17-26.
- Pusch, M., Hammer, J., Kus, J., Klosa, D., Thiemeyer, N., Mingerzahn, G., 2014. Macro- and microscale distribution of hydrocarbons in the Staßfurt Hauptsalz of the Gorleben salt dome. *German Journal of Geosciences* 165 (1), 3-14.
- Renard, F., Bernard, D., Thibault, X., Boller, E., 2004. Synchrotron 3D microtomography of halite aggregates during experimental pressure solution creep and evolution of the permeability. *Geophysical Research Letters* 31, L07607, doi:10.1029/2004GL019605.
- Roedder, E., 1984. The fluids in salt. *American Mineralogist* 69, 413-439.
- Schindelin, J., Arganda-Carreras, I., Frise, E., Kaynig, V., Longair, M., Petzsch, T., Preibisch, S., Rueden, C., Saalfeld, S., Schmid, B., Tenevez, J.-Y., White, D.J., Hartenstein, V., Eliceiri, K., Tomancak, P., Cardona, A., 2012. Fiji: an open-source platform for biological-image analysis. *Nature Methods* 9 (7), 676–682.
- Schoenherr, J., Urai, J.L., Kukla, P.A., Littke, R., Schléder, Z., Larroque, J.-M., Newall, M.J., Al-Abry, N., Al-Siyabi, H.A., Rawahi, Z., 2007. Limits to the sealing capacity of rock salt: A case study of the infra-Cambrian Ara Salt from the South Oman salt basin. *AAPG Bulletin* 91/11, 1541-1557.
- Ter Heege, J., De Bresser, J. H. P., Spiers, C. J., 2005. Rheological behaviour of synthetic rocksalt: The interplay between water, dynamic recrystallization and deformation mechanisms. *Journal of Structural Geology* 27, 948-963.
- Thiemeyer, N., Pusch, M., Hammer, J., Zulauf, G., 2014. Quantification and 3D visualisation of pore space in Gorleben rock salt: constraints from CT imaging and microfabrics. *German Journal of Geosciences* 165 (1), 15-25.
- Urai, J.L., Spiers, C.J., Zwart, H.J., Lister, G.S., 1986. Weakening of rock salt by water during long-term creep. *Nature* 324, 554–557.
- Urai, J.L., Spiers, C.J., Peach, C.J., Franssen, R.C.M.W., Liezenberg, J.L., 1987. Deformation mechanisms operating in naturally deformed halite rocks as deduced from microstructural investigations. *Geologie en Mijnbouw* 66, 165-176.
- Urai, J.L., Spiers, C.J., 2007. The effect on grain boundary water on deformation mechanisms and rheology of rocksalt during long-term deformation. In: Wallner, M., Lux, K.-H., Minkley, W., Hardy Jr., H.R. (Eds.). *The Mechanical Behavior of Salt – Understanding of THMC Processes in Salt*, Taylor & Francis Group, 149-158.
- Wildenschild, D., Sheppard, A. P., 2013. X-ray imaging and analysis techniques for quantifying pore-scale

Chapter 7:

The application of high resolution X-ray computed tomography on naturally deformed rock salt: Multi-scale investigations of the structural inventory

- structure and processes in subsurface porous medium systems. *Advances in Water Resources* 51, 217-246
- Závada, P., Desbois, G., Schwedt, A., Lexa, O., Urai, J.L., 2012. Extreme ductile deformation of fine-grained salt by coupled solution-precipitation creep and microcracking: Microstructural evidence from perennial Zechstein sequence (Neuhof salt mine, Germany). *Journal of Structural Geology* 37, 89-104.
- Zhang, X., Peach, C.J., Grupa, J., Spiers, C.J., 2007. Stress relaxation experiments on compacted granular salt: effects of water. In: Wallner, M., Lux, K.-H., Minkley, W., Hardy Jr., H.R. (Eds.). *The Mechanical Behavior of Salt – Understanding of THMC Processes in Salt*, Taylor & Francis Group, 159-166.
- Zulauf, G., Zulauf, J., Hastreiter, P. & Tomandl, B., 2003. A deformation apparatus for three-dimensional coaxial deformation and its application to rheologically stratified analogue material. *J. Struct. Geol.*, 25: 469-480.
- Zulauf, G., Zulauf, J., Bornemann, O., Kihm, N., Peinl, M., Zanella, F., 2009. Experimental deformation of a single-layer anhydrite in halite matrix under bulk constriction. Part 1: Geometric and kinematic aspects. *Journal of Structural Geology* 31, 460-474.
- Zulauf, G., Zulauf, J., Bornemann, O., Brenker, F., Höfer, H., Peinl, M., Woodland, A., 2010. Experimental deformation of a single-layer anhydrite in halite matrix under bulk constriction. Part 2: Deformation mechanisms and the role of fluids. *Journal of Structural Geology* 32, 264-277.
- Zulauf, J., Zulauf, G., Kraus, R., Gutiérrez-Alonso, G., 2011a. The origin of tablet boudinage: Results from experiments using power-law rock analogs. *Tectonophysics*, 510, 327–336, doi:10.1016/j.tecto.2011.07.013.
- Zulauf, J., Zulauf, G., Hammer, J., Zanella, F., 2011b. Tablet boudinage of an anhydrite layer in rock-salt matrix: Results from thermomechanical experiments. *Journal of Structural Geology* 33, 1801-1815.

Chapter 8

Summary & Conclusions

Chapter 8: Summary and Conclusions

8. Summary and conclusions

The present thesis examines the microfabrics of Hauptsalz samples from the Gorleben salt dome focusing on hydrocarbon occurrences which have been encountered in the Gorleben exploration mine. Operating deformation mechanisms in both halite and anhydrite have been identified using thick and thin section analyses, EBSD measurements and geometric analyses of the rock salt fabrics. Various rock fabric parameters, such as halite grain size/shape or subgrain size have been compared in hydrocarbon-bearing and hydrocarbon-free samples in order to check whether the heterogeneous hydrocarbon distribution is controlled by local, structural variations within the rock salt fabrics.

Deciphering the distribution of hydrocarbons on the macro- and microscopic scale was a major part of the investigations to evaluate the role of hydrocarbons in the deformation history of the Gorleben salt dome. A major focus was set on the application of high resolution X-ray computed tomography (CT). This modern technique was applied to quantify and visualize pore space patterns in Hauptsalz samples with elevated hydrocarbon concentrations. Moreover, CT imaging was used to display anhydrite distribution patterns and enabled a 3D reconstruction of intra- and intercrystalline fluid inclusions.

Results obtained from geochemical and geomechanical analyses (Hammer et al., 2015b, Chapter 5) complement the microstructural data regarding hydrocarbon provenance and influence on mechanical behavior of Gorleben rock salt.

The microfabrics of the investigated samples point to dislocation creep and strain-induced grain boundary migration (GBM) as operating deformation mechanisms. Unambiguous evidence for pressure solution has not been found and can only be assumed by the low differential stress values (1.1 ± 0.2 MPa for z2HS1 and 1.3 ± 0.3 MPa), the lack of an LPO and the relatively small halite grain size (3.4 ± 0.4 mm in z2HS1 and 3.4 ± 0.6 mm in z2HS2). Crystal plastic deformation is documented in the form of lattice bending, subgrain formation and minor subgrain rotation in halite. The Gorleben samples reveal halite grain shape anisotropies with average axial ratios (ARs) of 2.3 ± 0.2 (z2HS1) and 2.2 ± 0.3 (z2HS2). The heterogeneity of 3D halite grain shapes in both formations is attributed to the polyphase and pervasive deformation of the rock salt during halokinesis (Thiemeyer et al., submitted, Chapter 2).

Anhydrite has been deformed in the brittle-ductile regime. The microstructures reveal solution precipitation creep as dominant deformation mechanism, whereas crystal plastic deformation played only a minor role. The deformation behavior of anhydrite depends on rock composition, internal structure, position within the salt dome or layer thickness (Mertineit et al., 2015, Chapter 3). Brittle deformation of anhydrite in terms of boudinage and fracturing was counteracted by viscous creep of halite which caused a re-sealing of fractures and a re-establishing of the characteristic sealing capacity of rock salt. Continuous anhydrite layers are not preserved and, therefore, potential migration pathways for fluids do not exist, which is an important fact for nuclear waste disposal.

Chapter 8: Summary and Conclusions

The hydrocarbons in the central part of the Gorleben salt dome have been investigated using various techniques. Digital photography of the exploration mine galleries and drill core sections under ultraviolet light concordantly revealed that the distribution of hydrocarbons is very heterogeneous (Pusch et al., 2014, Chapter 4). Macroscopically, the aromatic to long-chain hydrocarbons, visible under UV light, occur in pure halite parts of the salt rock but also in anhydrite clusters or layers. They are further present in the form of streaks, clouds, and occasionally also as dissipated or ragged and interrupted layers in the Hauptsalz. Microscopically, most of the hydrocarbons are bound on halite and anhydrite grain or phase boundaries. Further potential reservoirs for hydrocarbons are intergranular pores or micropores within the rock salt as well as small capillaries in anhydrite crystals. The hydrocarbon-impregnated rock salt samples from cross cut 1 West revealed maximum hydrocarbon contents of 443 mg/kg_{rock} (equivalent to 0.0443 wt.-%), while most of the samples revealed concentrations of < 1 mg/kg_{rock} (equivalent to 0.0001 wt.-%) (Hammer et al., 2012, 2015a, b; Chapter 5). Organic geochemical studies of biomarkers point to the Staßfurt-Karbonat (z2SK) as the source rock of these hydrocarbons, which have migrated into the superjacent salt units during an early stage of the salt uplift (Hammer et al., 2015b).

The heterogeneous distribution of hydrocarbons in the Gorleben Hauptsalz is not related to local variations in the rock salt macro- or microfabrics. A detailed comparison of the hydrocarbon-bearing and hydrocarbon-free rock salt fabrics revealed no correlation between the hydrocarbon content with respect to the (i) paleodifferential stress, (ii) halite grain size, (iii) halite grain elongation or (iv) shape of halite grain shape ellipsoids (see Appendix A). Furthermore, the fabric analyses yielded no microstructural differences between the z2HS1 and z2HS2 rock salt. This finding is in line with the fact that the central part of the Gorleben salt dome represents a strongly deformed and homogenized “salt-tectonic breccia” (Bornemann et al., 2008; Bräuer et al., 2011).

The hydrocarbons have been dismembered and redistributed by the reworking of the Hauptsalz rocks and are nowadays present as local and isolated impregnations as demonstrated by 3D pore space patterns from hydrocarbon-bearing Hauptsalz samples visualized by CT imaging (Thiemeyer et al., 2014, Chapter 6; Hammer et al., 2015b). Hydrocarbons are partly incorporated in the rock salt foliation (Fig. 4.3 in Chapter 4) pointing to an early emplacement and subsequent, contemporaneous reworking of hydrocarbons together with the salt body. Due to the healing mechanisms and viscous flow of rock salt, former migration pathways have vanished.

The partly elevated porosities were correlated to higher hydrocarbon concentrations, suggesting that hydrocarbons were responsible for a hampered closure of pore space. As previously assumed by Burliga and Czechowski (2010) oil and gas could prevent the sealing of open fractures in rock salt. However, the majority of hydrocarbon-bearing samples in Gorleben did not show elevated porosity or permeability (Hammer et al., 2012, 2013) indicating that hydrocarbons have not hampered the self-

Chapter 8: Summary and Conclusions

healing mechanisms in rock salt. Hydrocarbons are rather distributed in the same patterns as brine and show very low concentrations, in general. Presumably, the pure amounts of hydrocarbons are too low to cause any detectable impact on the barrier properties of the rock salt. Moreover, geomechanical laboratory studies revealed no effect of hydrocarbons regarding the creep and deformation behavior of the rock salt (Schulze, 2013; Hammer et al., 2015b).

X-ray computed tomography (CT) was successfully applied for the investigation of the structural inventory of rock salt (Thiemeyer et al., 2014, 2015, Chapters 6 and 7). The 3D visualization of morphologies and the quantification of anhydrite impurities, pore space patterns or fluid inclusions are able to complement traditional microstructural techniques. CT imaging enabled the visualization of the eponymous anhydrite nodules of the Gorleben Knäuelsalz in 3D for the first time (see Fig. 7.5 in Chapter 7). The 3D distribution patterns clarify the strong reworking of the rock salt illustrating the disrupted and balled clusters, which once represented horizontal and continuous layers having been destroyed during salt uplift.

CT imaging was further able to demonstrate that pore space and anhydrite show different 3D distribution patterns. Thus, anhydrite played no decisive role for the elevated porosity found in few Hauptsalz samples. This genetic and structural independence suggests that few larger voids or pores in rock salt rather represent early pore space remnants from deposition or from an early stage of diapirism which have been largely closed during the deformation of the salt body.

The application of high-resolution CT imaging allows new insights into rock salt fluid inclusion analyses by three-dimensional reconstructions of multi-phase intra- or intercrystalline fluid inclusions (Thiemeyer et al., 2015, Chapter 7). Such CT scans of naturally-deformed rock salt fluid inclusions (and their components) were performed for the first time offering new perspectives for microstructural investigations of rock salt. The amount, diameter, surface area or morphology of fluid inclusions can be analyzed and measured accurately.

Assessing the suitability of a geological structure for nuclear waste disposal is a highly complex task and depends on a vast number of aspects. A statement on the suitability of the Gorleben salt dome as final repository would be far beyond the original aims of this thesis and would be virtually unsubstantial. The studies carried out in this thesis only represent a tiny fraction of an enormous amount of crucial factors which are important for delivering a judgment on the suitability of Gorleben salt dome. A further decisive factor might be how to attach value to various, scientific arguments in the framework of the search for a nuclear waste repository.

A major implication of the present thesis is that the Gorleben Hauptsalz has regained its sealing capacity during its deformation history. Although hydrocarbons migrated to some extent into the Gorleben rock salt during an early stage of salt uplift when the sealing capacity was diminished, self-healing

Chapter 8: Summary and Conclusions

mechanisms caused the re-establishing of a quasi-impermeable geological rock salt barrier, which is proven by isolated and disrupted hydrocarbon occurrences, and mainly, by the overall low permeability values measured even for hydrocarbon-bearing Hauptsalz samples.

The intense reworking and “squeezing” of the salt rocks resulted in low water contents (Bornemann et al., 2008). Consequently, in comparison to flat-bedded and weakly deformed rock salt the Gorleben Hauptsalz group represents very dry salt rock. Even the majority of the hydrocarbon concentrations are very low (Hammer et al., 2012, 2013, 2015a, b). Moreover, hydrocarbons show no influence on the mechanical behavior of the rock salt (Hammer et al., 2015b, Schulze, 2013). All these facts suggest that locally occurring hydrocarbons have no negative effect on the rock salt barrier and geomechanical properties.

The present thesis offers new insights in microstructural research on rock salt. Constraining the 3D halite grain shape gives additional information on the rock fabric (Thiemeyer et al., submitted, Chapter 2) and should be considered in such future works. By analyzing other rock salt formations from other localities, 3D grain shape ellipsoids represent an additional fabric parameter for comparison of various localities. At least, this technique allows distinguishing between planar and linear rock fabrics in contrast to 2D analyses of halite grain size and shape. Generally, the investigation of Gorleben Hauptsalz microfibrils is extremely valuable since microstructural data of rock salt deposits in Germany is still scarce.

The application of X-ray CT imaging represents a progressive tool for rock salt research. The 3D aspect is extremely useful for several reasons. Apart from the visualization aspect of single phases, also pore space or fracture patterns, or genetic relations between anhydrite and porosity, for instance, can be identified. There are numerous subjects at which CT imaging can be very useful and therefore, older problems can now be approached with this relatively new technique.

Regarding the suggested hampering effect of hydrocarbons on closing mechanisms of pores and fractures in rock salt (Burliga and Czechowski, 2010; Thiemeyer et al., 2014) future laboratory experiments might help to solve this issue. Synthesizing rock salt by cold pressing NaCl powder (e.g. Ter Heege et al., 2005a, b) with defined amounts of water on the one hand, and n-octane as hydrocarbon equivalent on the other hand (see Hammer et al., 2015a), would represent one possible approach. By deforming the samples under controlled temperature and pressure conditions, subsequent microstructural investigations and comparison of both water- and hydrocarbon-bearing samples, might reveal differences in the deformation behavior and in the particular microfibrils. In such experiments a critical concentration of hydrocarbons could be determined with regard to the impact on the geomechanical behavior of rock salt. This aspect is important to estimate since limits for the sealing capacity of blackish, oil-stained rock salt reported from the Oman (Schoenherr et al., 2007) have not been found in Gorleben Hauptsalz which reveals only low concentrations of hydrocarbons.

Chapter 8: Summary and Conclusions

References

- Bornemann, O., Behlau, J., Fischbeck, R., Hammer, J., Jaritz, W., Keller, S., Mingerzahn, G., Schramm, M., 2008. Description of the Gorleben Site Part 3. Results of the geological surface and underground exploration of the salt formation. – BGR: 50 figures, 7 tables, 5 appendices; Hannover, 223pp.
- Bräuer, V., Eickemeier, R., Eisenburger, D., Grisseemann, C., Hesser, J., Heusermann, S., Kaiser, D., Nipp, H.-K., Nowak, T., Plischke, I., Schnier, H., Schulze, O., Sönke, J., Weber, J. R., 2011. Description of the Gorleben site Part 4: Geotechnical exploration of the Gorleben salt dome. – BGR, Hannover, 176 pp.
- Burliga, S. & Czechowski, F., 2010: Anatomy of hydrocarbon-bearing zones, hydrocarbon provenance and their contribution to brittle fracturing of rock salt in the Klodawa Salt Structure (central Poland). - SMRI Spring 2010 Technical Conference, Grand Junction, USA.
- Hammer, J., Pusch, M., Häger, A., Ostertag-Henning, C., Schlömer, S., Mingerzahn, G., Scheeder, G., Shao, H., Paul, B., Schulze, O., Zaretzki, B., Hesser, J., 2012. Untersuchungen von Kohlenwasserstoffen im Erkundungsbergwerk Gorleben. Interim report 2012, Federal Institute for Geosciences and Natural Resources, Hannover, 236 pp.
- Hammer, J., Pusch, M., Häger, A., Ostertag-Henning, C., Schlömer, S., Mingerzahn, G., Scheeder, G., Shao, H., Paul, B., Schulze, O., Zaretzki, B., Hesser, J., 2013. Untersuchungen von Kohlenwasserstoffen im Erkundungsbergwerk Gorleben. Interim report 2013, Federal Institute for Geosciences and Natural Resources, Hannover, 207 pp.
- Hammer, J., Pusch, M., Ostertag-Henning, C., Haeger, A., Schlömer, S., Scheeder, G., Shao, H., Paul, B., Kus, J., Hesser, J., Blumenberg, M. 2015a. Untersuchungen von Kohlenwasserstoffen im Erkundungsbergwerk Gorleben. Final report 2014, Federal Institute for Geosciences and Natural Resources, Hannover.
- Hammer, J., Pusch, M., Häher, C., Ostertag-Henning, C., Thiemeyer, N., Zulauf, G., 2015b. Hydrocarbons in rock salt of the Gorleben salt dome – amount, origin and influence on geomechanical properties. In: Roberts, L., Mellegard, K., Hansen, F. (Eds.). *The Mechanical Behavior of Salt VIII*, Taylor & Francis Group, London, 69-75.
- Mertineit, M., Hammer, J., Schramm, M., Kneuker, T., Thiemeyer, N., Zulauf, G., 2015. Deformation of thin layered anhydrite rocks within the Gorleben salt dome, Germany. In: Roberts, L., Mellegard, K., Hansen, F. (Eds.). *The Mechanical Behavior of Salt VIII*, Taylor & Francis Group, London, 99-107.
- Pusch, M., Hammer, J., Kus, J., Klosa, D., Thiemeyer, N., Mingerzahn, G., 2014. Macro- and microscale distribution of hydrocarbons in the Staßfurt Hauptsalz of the Gorleben salt dome. *German Journal of Geosciences* 165 (1), 3-14.
- Schoenherr, J., Urai, J.L., Kukla, P.A., Littke, R., Schléder, Z., Larroque, J.-M., Newall, M.J., Al-Abry, N., Al-Siyabi, H.A., Rawahi, Z., 2007. Limits to the sealing capacity of rock salt: A case study of the infra-Cambrian Ara Salt from the South Oman salt basin. *AAPG Bulletin* 91/11, 1541-1557.

Chapter 8: Summary and Conclusions

- Schulze, O. 2013. Geotechnische Laborarbeiten im Rahmen der Erkundung Gorleben. Laboruntersuchungen zu den thermo-mechanischen Eigenschaften von Steinsalz mit KW-Imprägnationen. Ergebnisbericht. Report, Bundesanst. Geowiss. Rohstoffe, Hannover, 69 p.
- Thiemeyer et al., 2014, Thiemeyer, N., Pusch, M., Hammer, J., Zulauf, G., 2014. Quantification and 3D visualisation of pore space in Gorleben rock salt: constraints from CT imaging and microfabrics. *German Journal of Geosciences* 165 (1), 15-25.
- Thiemeyer, N., Habersetzer, J., Peinl, M., Zulauf, G., Hammer, J., 2015. The application of high resolution X-ray computed tomography on naturally deformed rock salt: Multi-scale investigations of the structural inventory. *Journal of Structural Geology* 77, 92-106.
- Thiemeyer, N., Mertineit, M., Linckens, J., Pusch, M., Zulauf, G., Hammer, J., (submitted). Microfabrics of Gorleben rock salt: 3D grain shape, deformation mechanisms and paleodifferential stress. *Tectonophysics*.

Chapter 9

Zusammenfassung und Schlussfolgerungen

Chapter 9: Zusammenfassung und Schlussfolgerungen

9. Zusammenfassung und Schlussfolgerungen

Die vorliegende Arbeit untersucht Mikrostrukturen an Hauptsalz-Proben des Salzstockes Gorleben mit speziellem Fokus auf Kohlenwasserstoffvorkommen, die im Erkundungsbergwerk Gorleben angetroffen worden sind. Aktive Deformationsmechanismen in Halit und Anhydrit wurden mit Hilfe von Dick- und Dünnschliffanalysen, EBSD-Messungen und geometrischen Auswertungen der Steinsalzgefüge ermittelt. Verschiedene Gefügeparameter Kohlenwasserstoff-führender und Kohlenwasserstoff-freier Proben, wie Halit-Korngröße und -form oder Subkorngröße, wurden verglichen, um zu überprüfen, ob die heterogene Kohlenwasserstoffverteilung durch lokale Variationen im Steinsalzgefüge kontrolliert ist.

Die Entschlüsselung der Verteilung der Kohlenwasserstoffe auf makro- und mikroskopischer Skala stellte einen wesentlichen Teil der Untersuchungen dar, um die Rolle der Kohlenwasserstoffe bei der Deformationsgeschichte des Salzstockes bewerten zu können. Ein Hauptaugenmerk wurde auf die Anwendung von hochauflösender Röntgen-Computertomographie (CT) gelegt. Diese moderne Methode wurde unter anderem für die Quantifizierung und Visualisierung von Porenraummustern in Hauptsalz-Proben mit erhöhten Kohlenwasserstoffgehalten verwendet. Weiterhin diente die Computertomographie zur Darstellung von Anhydrit-Verteilungsmustern und 3D-Rekonstruktionen von intra- und interkristallinen Fluideinschlüssen.

Ergebnisse aus geochemischen und geomechanischen Analysen (Hammer et al., 2015b, Kapitel 5) ergänzen die mikrostrukturellen Daten bezüglich der Kohlenwasserstoffherkunft und deren Einfluss auf das mechanische Verhalten des Gorleben-Steinsalzes.

Die Mikrogefüge der untersuchten Proben deuten auf Versetzungskriechen und Strain-induzierte Grenzflächenwanderung als aktive Deformationsmechanismen hin. Klare Anzeichen für Drucklösungsprozesse fehlen in den untersuchten Proben, jedoch deuten geringe Differentialspannungen ($1,1 \pm 0,2$ MPa für z2HS1 und $1,3 \pm 0,3$ MPa), das Fehlen einer kristallographischen Vorzugsorientierung und relativ kleine Korngrößen ($3,4 \pm 0,4$ mm im z2HS1 und $3,4 \pm 0,6$ mm im z2HS2) auf diese Prozesse hin. Die kristallplastische Verformung ist dokumentiert in Form von Gitterverbiegung, Subkornbildung und leichter Subkornrotation im Halit. Die Gorleben z2HS1- und z2HS2-Formationen zeigen Kornformanisotropien mit mittleren Achsenverhältnissen von $2,3 \pm 0,2$ (z2HS1) und $2,2 \pm 0,3$ (z2HS2). Die Heterogenität der 3D Kornformen beider Formationen ist bedingt durch die mehrphasige und umfassende Deformation des Steinsalzes während der Halokinese (Kapitel 2).

Anhydrit wurde im spröde-duktilen Regime deformiert. Die Anhydrit-Mikrostrukturen zeigen Lösungs-Fällungskriechen als dominanten Deformationsmechanismus, während kristallplastische Deformation nur eine untergeordnete Rolle spielt. Das Deformationsverhalten von Anhydrit ist abhängig von der Zusammensetzung, der internen Struktur, der Lage innerhalb des Salzstockes oder der

Chapter 9: Zusammenfassung und Schlussfolgerungen

Schichtmächtigkeit (Mertineit et al., 2015, Kapitel 3). Der spöden Deformation von Anhydrit in Form von Boudinage und Rissbildung wurde durch viskoses Kriechen von Halit entgegengewirkt, was die Verheilung von Rissen sowie eine Wiederherstellung des charakteristischen Abdichtungsvermögens des Steinsalzes bewirkte.

Die Kohlenwasserstoffe im Zentralbereich des Salzstockes Gorleben wurden unter Verwendung verschiedener Methoden untersucht. Digitale Aufnahmen unter UV-Licht von Firste und Stoß sowie von Bohrkernabschnitten des Erkundungsbergwerkes zeigen übereinstimmend, dass die Verteilung der Kohlenwasserstoffe sehr heterogen ist (Pusch et al., 2014, Kapitel 4). Makroskopisch treten die unter UV-Licht sichtbaren, lang-kettigen und aromatischen Kohlenwasserstoffe in reinen Steinsalzpartien aber auch in Anhydrit-Clustern oder Anhydrit-Lagen auf. Des Weiteren liegen sie in Form von Streifen, Wolken und teilweise als zerstreute oder zerrissene, zwischengeschaltete Lagen im Hauptsalz vor. Mikroskopisch sind die meisten Kohlenwasserstoffe an Halit- und Anhydrit-Korn- und Phasengrenzen gebunden. Weitere potenzielle Speicher für Kohlenwasserstoffe sind intergranulare Poren oder Mikroporen im Steinsalz, ebenso wie kleine Kapillaren in Anhydritkristallen. Die Kohlenwasserstoff-imprägnierten Steinsalzproben von Querschlag 1 West weisen maximale Konzentrationen von 443 mg/kg_{rock} (entsprechend 0.0443 Gew.-%) auf, während die meisten Proben Gehalte von < 1 mg/kg_{rock} (entsprechend 0.0001 Gew.-%) aufweisen (Hammer et al., 2012, 2015b; Kapitel 5). Organogeochemische Studien von Biomarkern deuten auf das Staßfurt-Karbonat (z2SK) als das Muttergestein der Kohlenwasserstoffe hin, die während einer Frühphase des Salzaufstieges in die überlagernden Salzeinheiten migriert sind.

Die heterogene Verteilung der Kohlenwasserstoffe im Gorleben-Steinsalz steht in keinem Bezug zu lokalen Variationen der Makro- oder Mikrogefüge des Steinsalzes. Ein detaillierter Vergleich der Kohlenwasserstoff-führenden und Kohlenwasserstoff-freien Steinsalzgefüge zeigte keinerlei Korrelation zwischen Kohlenwasserstoffgehalt und (i) Paläodifferenzialspannung, (ii) Halit-Korngröße, (iii) Halitkorn-Auslängung oder (iv) Form der Halit-Kornformellipsoide (siehe Appendix A). Des Weiteren ergaben die Gefügeanalysen keine mikrostrukturellen Unterschiede zwischen dem Steinsalz aus z2HS1 und z2HS2. Diese Erkenntnis passt zur Tatsache, dass der Zentralteil des Salzstockes Gorleben eine homogenisierte, „salztektonische Brekzie“ darstellt (Bornemann et al., 2008; Bräuer et al., 2011).

Die Kohlenwasserstoffe wurden während der Verknetung der Hauptsalz-Gesteine zerrissen und umverteilt und liegen heute als lokale und isolierte Imprägnationen vor, was durch CT-Visualisierungen von 3D-Porenraummuster Kohlenwasserstoff-führender Hauptsalz-Proben verdeutlicht werden konnte (Thiemeyer et al., 2014, Kapitel 6; Hammer et al., 2015b). Die Kohlenwasserstoffe sind teilweise in die Steinsalz-Foliation mit eingearbeitet (Abb. 4.3 in Kapitel 4), was auf eine frühe Einbringung und anschließende, zeitgleiche Verknetung der Kohlenwasserstoffe mit dem Salzkörper hindeutet. Aufgrund der Verheilungsmechanismen und des duktilen Fließens des Steinsalzes sind die ehemaligen

Chapter 9: Zusammenfassung und Schlussfolgerungen

Migrationspfade ausgelöscht worden.

Die teilweise erhöhten Porositäten konnten mit erhöhten Kohlenwasserstoff-Konzentrationen korreliert werden, was möglicherweise darauf zurückzuführen ist, dass Kohlenwasserstoffe die Schließung von Porenraum verhindert haben. Diese Annahme wurde bereits von Burliga & Czechowski (2010) getroffen, wonach Öl und Gas das Verheilen von offenen Klüften in Steinsalz verhindern könnte. Allerdings zeigt die Mehrzahl der Kohlenwasserstoff-führenden Proben aus Gorleben keine erhöhte Porosität oder Permeabilität (Hammer et al., 2012, 2013), was daraufhin deutet, dass die Kohlenwasserstoffe die Selbstverheilungsmechanismen des Steinsalzes nicht eingeschränkt haben. Kohlenwasserstoffe sind viel eher in den gleichen Mustern wie Salzlösungen verteilt und weisen generell sehr geringe Konzentrationen auf. Vermutlich sind die reinen Gehalte an Kohlenwasserstoffen zu gering, um einen bemerkbaren Einfluss auf die Barriere-Eigenschaften des Steinsalzes zu bedingen. Außerdem zeigen geomechanische Laborstudien keinen Einfluss der Kohlenwasserstoffe auf das Kriech- und Deformationsverhalten des Steinsalzes (Schulze, 2013; Hammer et al., 2015b).

Röntgen-Computertomographie (CT) wurde erfolgreich zur Untersuchung des strukturellen Inventars von Salzgestein verwendet (Thiemeyer et al., 2014, 2015, Kapitel 6 und 7). Die 3D-Visualisierung von Morphologien und die Quantifizierung von Anhydrit-Verunreinigungen, Porenraummustern oder Fluideinschlüssen sind in der Lage traditionell-mikrostrukturelle Methoden zu ergänzen. Mittels CT konnten die namensgebenden Anhydritknäuel des Knäuelsalzes von Gorleben zum ersten Mal in 3D visualisiert werden (siehe Abb. 7.5 in Kapitel 7). Die 3D-Verteilungsmuster verdeutlichen die starke Verknetung des Salzgesteins mit seinen zerrissenen und verknoteten Anhydrit-Clustern, welche als ehemals horizontale und durchgehende Lagen durch den Salzaufstieg zerstört wurden.

Die Computertomographie konnte außerdem zeigen, dass Porenraum- und Anhydrit-Verteilungen verschiedene 3D-Muster aufweisen. Demnach ist Anhydrit nicht für erhöhte Porosität verantwortlich, die in einigen wenigen Hauptsalz-Proben festgestellt wurden. Die genetische und strukturelle Unabhängigkeit deutet darauf hin, dass die wenigen größeren Poren oder Hohlräume im Steinsalz eher als Relikte des Porenraums aus Zeiten der Ablagerung oder dem frühen Diapirismus zu verstehen sind, der während der Deformation des Salzkörpers überwiegend geschlossen wurde.

Die Verwendung von hochauflösender Computertomographie ermöglicht neue Einblicke in die Analyse von Fluideinschlüssen in Steinsalz durch dreidimensionale Rekonstruktionen von mehrphasigen intra- und interkristallinen Fluideinschlüssen (Thiemeyer et al., 2015, Chapter 7). Solche CT-Scans von natürlich-deformierten Steinsalz-Fluideinschlüssen (und deren Komponenten) wurden zum ersten Mal durchgeführt und bieten neue Perspektiven für mikrostrukturelle Untersuchungen von Steinsalz. Mengen, Durchmesser, Oberflächen oder Morphologien von Fluideinschlüssen können somit exakt vermessen werden.

Chapter 9: Zusammenfassung und Schlussfolgerungen

Eine Beurteilung zur Eignung einer geologischen Struktur bezüglich der Einlagerung radioaktiven Abfalls ist eine sehr komplexe Herausforderung und hängt von einer Vielzahl von Aspekten ab. Ein Statement zur Eignung des Salzstockes Gorleben als Endlager geht über die Ziele der vorliegenden Arbeit hinaus und hätte an dieser Stelle zu wenig Substanz, da die in dieser Arbeit durchgeführten Untersuchungen nur einen kleinen Anteil einer Vielzahl von Faktoren repräsentieren, anhand derer über die Eignung des Salzstockes Gorleben geurteilt werden kann. Ein wohl entscheidender Faktor ist auch, wie stark einzelne wissenschaftliche Aspekte im Rahmen der Endlagersuche gewichtet werden.

Eine wichtige Erkenntnis der vorliegenden Arbeit ist, dass das Gorleben-Hauptsalz sein Abdichtungsvermögen während seiner Deformationsgeschichte wiedererlangt hat. Obwohl Kohlenwasserstoffe in einer Frühphase des Salzaufstieges, als das Abdichtungsvermögen verringert war, in das Gorleben-Steinsalz migrierten, konnten die Selbstverheilungsmechanismen eine quasi undurchlässige, geologische Steinsalz-Barriere wiederherstellen, was durch die isolierten und zerlegten Kohlenwasserstoffvorkommen, aber hauptsächlich durch die generell niedrige Permeabilität Kohlenwasserstoff-führender Hauptsalz-Proben unterstrichen wird.

Das intensive Verkneten und „Ausquetschen“ des Steinsalzes führte zu geringen Wassergehalten (Bornemann et al., 2008). Dadurch erweist sich im Vergleich zu flach lagernden und schwach-deformierten Salzgesteinen die Gorleben Hauptsalz-Gruppe als sehr trockenes Salzgestein. Sogar die Mehrheit der Kohlenwasserstoff-Konzentrationen sind sehr gering (Hammer et al., 2012, 2013, 2015a, b). Zusätzlich zeigen die Kohlenwasserstoffe keinen negativen Einfluss auf die Barriere- sowie geomechanischen Eigenschaften.

Die vorliegende Arbeit ermöglicht neue Einblicke in mikrostrukturelle Untersuchungen von Steinsalz. Das Ermitteln von 3D-Kornformanisotropien gibt zusätzliche Informationen über das Gesteinsgefüge (Kapitel 2) und sollte in Zukunft bei solchen Arbeiten stets berücksichtigt werden. Bei Analysen anderer Steinsalz-Formationen stellen 3D-Kornformellipsoide einen weiteren Gefügeparameter dar, der zum Vergleich von verschiedenen Lokalitäten verwendet werden kann. Zumindest erlaubt diese Technik eine Unterscheidung zwischen planaren und linearen Gesteinsgefügen im Gegenteil zu 2D-Analysen von Halit-Korngrößen und -formen. Generell sind die Untersuchungen der Gorleben-Hauptsalz-Mikrogefüge sehr wertvoll, da nur wenig mikrostrukturelle Daten zu Salzgesteinen aus Deutschland existieren.

Die Verwendung von Röntgen-Computertomographie stellt eine fortschrittliche Technik für die Salzforschung dar. Der 3D-Aspekt ist aus verschiedenen Gründen sehr nützlich. Neben dem Visualisierungsaspekt von einzelnen Phasen können auch Poren- oder Rissmuster sowie beispielsweise genetische Beziehungen zwischen Anhydrit und Porosität aufgedeckt werden. Es existiert eine Vielzahl an Themen, bei denen die Verwendung von Computertomographie sehr nützlich sein kann, wodurch alte Fragestellungen mit Hilfe dieser relativ neuen Technik angegangen werden können.

Bezüglich der Annahme, dass Kohlenwasserstoffe einen hemmenden Effekt auf die Schließung

Chapter 9: Zusammenfassung und Schlussfolgerungen

von Porenraum haben (Burliga und Czechowski, 2010; Thiemeyer et al., 2014), könnten zukünftige Laborexperimente Klarheit schaffen. Beispielsweise wäre die experimentelle Herstellung von Steinsalz durch kaltes Pressen von NaCl-Pulver mit definierten Mengen Wasser auf der einen, und n-Octan als Kohlenwasserstoffäquivalent auf der anderen Seite (siehe Hammer et al., 2015a) eine Möglichkeit. Durch die Deformation der Proben bei kontrollierten Temperatur- und Druckverhältnissen könnten anschließende mikrostrukturelle Untersuchungen und Vergleiche zwischen den Wasser- und den Kohlenwasserstoff-führenden Proben Unterschiede im Deformationsverhalten und den spezifischen Mikrostrukturen aufdecken. In solchen Experimenten könnte auch eine kritische Menge von Kohlenwasserstoffen ermittelt werden, bei der sich ein Einfluss auf das geomechanische Verhalten des Steinsalzes feststellen lässt. Dieser Aspekt ist wichtig, da Grenzen für die Abdichtungskapazität, wie sie für geschwärztes, Öl-führendes Steinsalz aus dem Oman beschrieben wurden (Schoenherr et al., 2007), für das Gorleben Hauptsalz nicht festgestellt wurden, da dieses nur sehr geringe Konzentrationen an Kohlenwasserstoffen aufweist.

Literatur

- Bornemann, O., Behlau, J., Fischbeck, R., Hammer, J., Jaritz, W., Keller, S., Mingerzahn, G., Schramm, M., 2008. Description of the Gorleben Site Part 3. Results of the geological surface and underground exploration of the salt formation. – BGR: 50 figures, 7 tables, 5 appendices; Hannover, 223pp.
- Bräuer, V., Eickemeier, R., Eisenburger, D., Grisseemann, C., Hesser, J., Heusermann, S., Kaiser, D., Nipp, H.-K., Nowak, T., Plischke, I., Schnier, H., Schulze, O., Sönnke, J., Weber, J. R., 2011. Description of the Gorleben site Part 4: Geotechnical exploration of the Gorleben salt dome. – BGR, Hannover, 176 pp.
- Burliga, S. & Czechowski, F., 2010: Anatomy of hydrocarbon-bearing zones, hydrocarbon provenance and their contribution to brittle fracturing of rock salt in the Klodawa Salt Structure (central Poland). - SMRI Spring 2010 Technical Conference, Grand Junction, USA.
- Hammer, J., Pusch, M., Häger, A., Ostertag-Henning, C., Schlömer, S., Mingerzahn, G., Scheeder, G., Shao, H., Paul, B., Schulze, O., Zaretski, B., Hesser, J., 2012. Untersuchungen von Kohlenwasserstoffen im Erkundungsbergwerk Gorleben. Interim report 2012, Federal Institute for Geosciences and Natural Resources, Hannover, 236 pp.
- Hammer, J., Pusch, M., Häger, A., Ostertag-Henning, C., Schlömer, S., Mingerzahn, G., Scheeder, G., Shao, H., Paul, B., Schulze, O., Zaretski, B., Hesser, J., 2013. Untersuchungen von Kohlenwasserstoffen im Erkundungsbergwerk Gorleben. Interim report 2013, Federal Institute for Geosciences and Natural Resources, Hannover, 207 pp.
- Hammer, J., Pusch, M., Ostertag-Henning, C., Haeger, A., Schlömer, S., Scheeder, G., Shao, H., Paul, B., Kus, J., Hesser, J., Blumenberg, M. 2015a. Untersuchungen von Kohlenwasserstoffen im Erkundungsbergwerk Gorleben. Final report 2014, Federal Institute for Geosciences and Natural

Chapter 9: Zusammenfassung und Schlussfolgerungen

Resources, Hannover.

- Hammer, J., Pusch, M., Häher, C., Ostertag-Henning, C., Thiemeyer, N., Zulauf, G., 2015b. Hydrocarbons in rock salt of the Gorleben salt dome – amount, origin and influence on geomechanical properties. In: Roberts, L., Mellegard, K., Hansen, F. (Eds.). *The Mechanical Behavior of Salt VIII*, Taylor & Francis Group, London, 69-75.
- Mertineit, M., Hammer, J., Schramm, M., Kneuker, T., Thiemeyer, N., Zulauf, G., 2015. Deformation of thin layered anhydrite rocks within the Gorleben salt dome, Germany. In: Roberts, L., Mellegard, K., Hansen, F. (Eds.). *The Mechanical Behavior of Salt VIII*, Taylor & Francis Group, London, 99-107.
- Pusch, M., Hammer, J., Kus, J., Klosa, D., Thiemeyer, N., Mingerzahn, G., 2014. Macro- and microscale distribution of hydrocarbons in the Staßfurt Hauptsalz of the Gorleben salt dome. *German Journal of Geosciences* 165 (1), 3-14.
- Schoenherr, J., Urai, J.L., Kukla, P.A., Littke, R., Schléder, Z., Larroque, J.-M., Newall, M.J., Al-Abry, N., Al-Siyabi, H.A., Rawahi, Z., 2007. Limits to the sealing capacity of rock salt: A case study of the infra-Cambrian Ara Salt from the South Oman salt basin. *AAPG Bulletin* 91/11, 1541-1557.
- Schulze, O. 2013. Geotechnische Laborarbeiten im Rahmen der Erkundung Gorleben. Laboruntersuchungen zu den thermo-mechanischen Eigenschaften von Steinsalz mit KW-Imprägnationen. Ergebnisbericht. Report, Bundesanst. Geowiss. Rohstoffe, Hannover, 69 p.
- Thiemeyer et al., 2014, Thiemeyer, N., Pusch, M., Hammer, J., Zulauf, G., 2014. Quantification and 3D visualisation of pore space in Gorleben rock salt: constraints from CT imaging and microfabrics. *German Journal of Geosciences* 165 (1), 15-25.
- Thiemeyer, N., Habersetzer, J., Peinl, M., Zulauf, G., Hammer, J., 2015. The application of high resolution X-ray computed tomography on naturally deformed rock salt: Multi-scale investigations of the structural inventory. *Journal of Structural Geology* 77, 92-106.
- Thiemeyer, N., Mertineit, M., Linckens, J., Pusch, M., Zulauf, G., Hammer, J., (submitted). Microfabrics of Gorleben rock salt: 3D grain shape, deformation mechanisms and paleodifferential stress. *Tectonophysics*.

List of Figures and Tables

List of Figures

<i>Fig. 1.1: Salt structures of Northern Germany.</i>	19
<i>Fig. 1.2: Microstructural processes operating during deformation of halite (from Urai and Spiers, 2007).</i>	20
<i>Fig. 1.3: Simplified cross section of the Gorleben salt dome (from Bornemann et al., 2008) with the central part composed by the Staßfurt series (z2).</i>	22
<i>Fig. 1.4: Structural evolution of the Gorleben salt dome (from Bornemann et al., 2008).</i>	23
<i>Fig. 1.5: Retraced halite grain masks from Gorleben Hauptsalz sample analyzed in respect to grain orientation and grain size (from Popp et al., 2002).</i>	25
<i>Fig. 2.1: Geology of the Gorleben salt dome (Northern Germany) in the area of the exploration mine after Bornemann et al. (2008).</i>	41
<i>Fig. 2.2: Basic principle of an ellipsoid reconstruction from measured sectional ellipses after Launeau and Robin (2005).</i>	43
<i>Fig. 2.3: a) Halite grain sizes (ECDs) and b) axial ratios (ARs) of z2HS1 and z2HS2 samples, which represent mean values calculated by numerous halite grains for every sample (vertical numbers).</i>	46
<i>Fig. 2.4: Halite grain shape ellipsoids visualized in the Jelinek diagram (Jelinek, 1981).</i>	46
<i>Fig. 2.5: Rock salt fabrics from Gorleben z2HS1 and z2HS2.</i>	48
<i>Fig. 2.6: Microphotographs of characteristic fluid inventory of Gorleben rock salt.</i>	50
<i>Fig. 2.7: Microphotographs of subgrain fabrics.</i>	51
<i>Fig. 2.8: Paleopiezometric data obtained from subgrain size of Gorleben rock salt</i>	52
<i>Fig. 2.9: Microphotographs and EBSD mapping of two halite grains.</i>	53
<i>Fig. 2.10: Microphotographs and EBSD analyses of halite.</i>	54
<i>Fig. 2.11: Pole figures and misorientation indices (M) of z2HS1 taken from several oriented thick sections (samples RB647 and RB649).</i>	55
<i>Fig. 2.12: Anhydrite distribution in z2HS1 and z2HS2.</i>	56
<i>Fig. 2.13: Microstructures in thin anhydrite layer.</i>	57
<i>Fig. 2.14: Microstructures in thick anhydrite layer.</i>	58
<i>Fig. 3.1: Lithostratigraphic and petrographic composition of the Gorleben-Bank (z3OSM).</i>	76
<i>Fig. 3.2: Decoupling and deformation of zones V-VII: view along zone IIIa, which is separated by the development of zone IV in zone IIIa and IIIb.</i>	78
<i>Fig. 3.3: Asymmetric boudin of Gorleben-Bank.</i>	79
<i>Fig. 3.4: Different outcrops of the Gorleben-Bank in the Gorleben exploration mine.</i>	80

List of Figures and Tables

<i>Fig. 3.5: Geometrical analyses of extension fractures oriented perpendicular to bedding in 17 Gorleben-Bank outcrops.</i>	81
<i>Fig. 4.1: Location map of the Gorleben salt dome (black arrow in the enlarged image section; BMWi 2008, modified) in Lower Saxony (Germany).</i>	89
<i>Fig. 4.2: Simplified stratigraphic table of the salt rocks at the transition zone Zechstein 2 (Staßfurt Series) and Zechstein 3 Leine Series).</i>	90
<i>Fig. 4.3: Photo at artificial light (left) and ultraviolet light (right) of drilling station 1.2 in Crosscut 1 West at the 840 m exploration level.</i>	91
<i>Fig. 4.4: Geological map of exploration area 1 (EB1) at the 840 m level (BGR, modified).</i>	91
<i>Fig. 4.5: Core segment with a diameter of 72 mm from the hydrocarbon sampling borehole RB652 from depth 1.14 m to 1.29 m at different lighting (core head: top of photo; drilling head: bottom).</i>	92
<i>Fig. 4.6: 3D visualisation of the UV core mapping results of the hydrocarbon sampling boreholes in part of the Crosscut 1 West in the vicinity of the large condensate patch (several m² in size) around the hydrocarbon sampling borehole RB648.</i>	93
<i>Fig. 4.7: 3D visualisation of the UV core mapping results of the hydrocarbon sampling boreholes in part of the Crosscut 1 East within the area of borehole stations 3.1 and 4 in the central part of Q1E.</i>	94
<i>Fig. 4.8: Part of the 3D visualisation of the hydrocarbon boreholes in the vicinity of the large condensate patch in Crosscut 1 West.</i>	94
<i>Fig. 4.9: (A) Brownish-black coloured fluid inclusions at the grain boundaries of recrystallised halite crystals or as drop-shaped meniscuses on anhydrite crystals (An), as well as in cleavage-parallel capillaries in anhydrite crystals (RB659, z2HS1; transmitted light, II polarisers).</i>	96
<i>Fig. 4.10: (A) Dendritic network of blackish to brownish (hydrocarbons) and achromatic (brine) fluid inclusions alongside the grain boundaries of halite crystals (RB647, z2HS1; stacked image with z = 400 µm; transmitted light, II polarisers).</i>	97
<i>Fig. 4.11: (A) Idiomorphic crystal of pyrite (pentagondodecahedra) with intact and smooth crystal faces as well as sharp crystal edges (RB659).</i>	98
<i>Fig. 4.12: (A) The hydrocarbons on the grain boundaries of the halite crystals show different fluorescence depending on their chemical composition and the laser type.</i>	100
<i>Fig. 5.1: Large condensate patch in crosscut 1 West at ultraviolet light (eastern wall, 840 m level).</i>	106
<i>Fig. 5.2: Hydrocarbons and brines at grain boundaries of halite crystals (parallel polarisers, “Knäuelsalz”, z2HS1).</i>	107
<i>Fig. 5.3: Hydrocarbons in cleavage-parallel capillaries within an anhydrite crystal (parallel polarisers, “Knäuelsalz”, z2HS1).</i>	108
<i>Fig. 5.4: Visualization of hydrocarbons (light) in cleavage-parallel capillaries within an anhydrite.</i>	108

List of Figures and Tables

<i>Fig. 5.5: 3D reconstructions of the spatial pore space distributions in a sample with macroscopic visible pores (A, top) and in a sample with planar distribution of porosity (B, below), illustrated by two different projection techniques (“Knäuelsalz”, z2HS1).</i>	109
<i>Fig. 5.6: Hydrocarbon content in Gorleben Staßfurt-Hauptsalz.</i>	110
<i>Fig. 5.7: Hydrocarbon content (mg/kg) and distribution in adjacent drillings in Gorleben Staßfurt Hauptsalz (crosscut 1 West).</i>	111
<i>Fig. 5.8: Molecular parameters of selected hydrocarbon biomarkers of oils in the Gorleben Hauptsalz (the hatched areas) and potential source rocks (Staßfurt carbonate and copper shale are indicated) in the Gorleben Z1 borehole.</i>	111
<i>Fig. 6.1: 2D slice of the computer tomography raw scan data set of sample RB686.005_CT.</i>	119
<i>Fig. 6.2: 3D reconstructions of the spatial pore space distributions in samples with macroscopic visible pores.</i>	120
<i>Fig. 6.3: The 3D reconstruction of the spatial pore space for the two less porous samples without macroscopic visible pores show different porosity patterns.</i>	123
<i>Fig. 6.4: a) Microphotograph of sample RB686.005_CT.</i>	124
<i>Fig. 6.5: Different sites of enhanced porosity in thick sections of sample RB686.005_CT.</i>	125
<i>Fig. 6.6: Diffuse structures like grain boundaries or microfractures cannot be extracted properly from the CT raw data sets due to the lack of grey value contrast.</i>	127
<i>Fig. 6.7: High resolution CT scans allow magnification of designated areas and objects.</i>	128
<i>Fig. 7.1: Sampled salt structures in northern Germany according to Bornemann (1991) and Jagsch and Theylich (1999).</i>	136
<i>Fig. 7.2: Fabric of rock salt samples presented in this paper.</i>	138
<i>Fig. 7.3: Transmitted light microphotographs of fluid inclusions in Asse Speisesalz (Na₂SP) rock salt (a), and the Gorleben Kristallbrockensalz (z2HS3) samples Bo5 (b) and Bo5UHR (c).</i>	140
<i>Fig. 7.4: Schematic classification of various scanning regimes concerning sample size, scanning time and resolution.</i>	141
<i>Fig. 7.5: 3D-μCT anhydrite distribution in Gorleben Knäuelsalz (RB648).</i>	144
<i>Fig. 7.6: 3D-μCT reconstruction of mid-scale (slight close-up) anhydrite distribution in Teutschenthal rock salt (LT163_1).</i>	145
<i>Fig. 7.7: a) Principle of gray-value based extraction in μCT raw data sets (RB683, top view).</i>	145
<i>Fig. 7.8: 3D-nCT reconstruction of fluid inclusions in Asse rock salt (Speisesalz).</i>	147
<i>Fig. 7.9: CT scan of an intracrystalline fluid inclusion in Kristallbrockensalz (z2HS3) of Gorleben rock salt (sample Bo5).</i>	148

List of Figures and Tables

<i>Fig. 7.10: Halite grain-boundary fluid inclusions of sample Bo5UHR in Gorleben Kristallbrockensalz.</i>	149
<i>Fig. 7.11: Image quality improvement of sample RB648 (see Fig. 7.2) by different filters and image arithmetic.</i>	151
<i>Fig. A1.1: The determination of grain shape masks based on three sections of a drill core segment.</i>	181
<i>Fig. A1.2: Halite grain shape data of Gorleben rock salt (see Chapter 2) combined with the fluorescence intensities equivalent to hydrocarbon abundance.</i>	187
<i>Fig. A2.1: Calculated paleodifferential stress along cross cut 1 West and cross cut 1 East at the 840 m-level (map sections by DBE and BfS).</i>	192
<i>Fig. A2.2: Paleopiezometric stress data (see chapter 2) related to hydrocarbon abundance.</i>	193
<i>Fig. B1.1: Sequence of CT parameters influencing the scanning time (cost).</i>	195
<i>Fig. B1.2: CT data of sample trace fossil.</i>	198
<i>Fig. B1.3: CT data of sample salt plate.</i>	199
<i>Fig. B1.4: Comparison of CT raw data of trachyte_2 and trachyte_3.</i>	200
<i>Fig. B1.5: 3D reconstruction of trachyte_3.</i>	201
<i>Fig. B1.6: The five central questions mandatory for solid CT imaging.</i>	202
<i>Abb. B2.1: JIMA-Auflösetest mit Streifenmustern verschiedener Breite (15-0,4 µm).</i>	207
<i>Abb. B2.2: Position des JIMA-Tests vor der Röntgenröhre.</i>	208
<i>Abb. B2.3: Snapshot von 0,8 µm-Streifen mit dem Fokuswert +1,5.</i>	209
<i>Abb. B2.4: xs/control mit Focus-Feld zur Kalibrierung der Fokuswerte in 0.5er und 0.1er Schritten (siehe Pfeil).</i>	210
<i>Abb. B2.5: Die Anwendung des Median-Filters am Beispiel von Probe trachyte_3 (siehe Tab. B1.2 sowie Abb. B1.4 und B1.5 in Appendix B1.3.).</i>	211
<i>Abb. B2.6: Der Effekt des Median-Filters auf zwei unterschiedliche Phasen.</i>	212

List of Tables

<i>Table 2.1: Grain shape data determined by ImageJ and Ellipsoid.</i>	47
<i>Table 2.2: Selected rock salt deposits of different geological settings with examined halite grain sizes, axial ratios and differential stress.</i>	59
<i>Table 4.1: Excitation wavelengths (AOTF), range of detection and colour coding of the lasers used for the CLSM analysis.</i>	99
<i>Table 6.1: Scan parameters and porosity determined by ImageJ and VGStudio MAX.</i>	119

List of Figures and Tables

<i>Table 7.1: Summarized μCT measurements presented in this paper.</i>	142
<i>Table A1.1: Geometric data of the halite grain shape masks and reconstructed ellipsoids acquired.</i>	186
<i>Table A2.1: Determined paleopiezometric Hauptsalz data based on subgrain masks.</i>	191
<i>Table B1.1: Focus modes associated to resolution and beam current parameters.</i>	196
<i>Table B1.2: Compilation of exemplary CT scans.</i>	197

Appendices

Appendix A: Halite grain shape and subgrain data

Appendix B: CT imaging at the nanoCT lab

Appendix A: Halite grain shape and subgrain data

A1. Halite grain shape data

The grain shape ellipsoid determination reconstructed by sectional grain shape masks is presented in Chapter 2. The following figures show the acquired halite grain shape masks. Every sample consists of 2-3 ellipsoid reconstructions each frame representing one drill core segment composed of three grain shape masks of perpendicular orientation (see Fig. A1.1 as example). The drill core number is given at the upper left. The complete geometric data is summarized in Table A1.

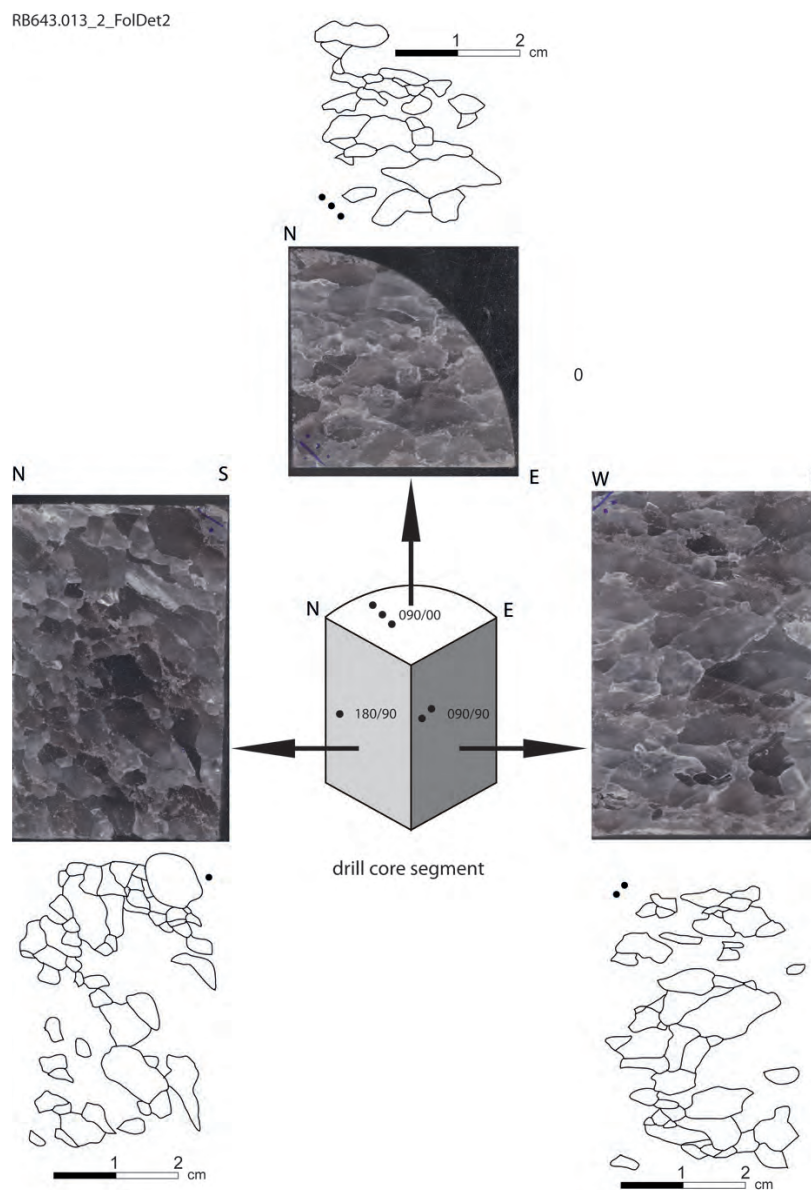
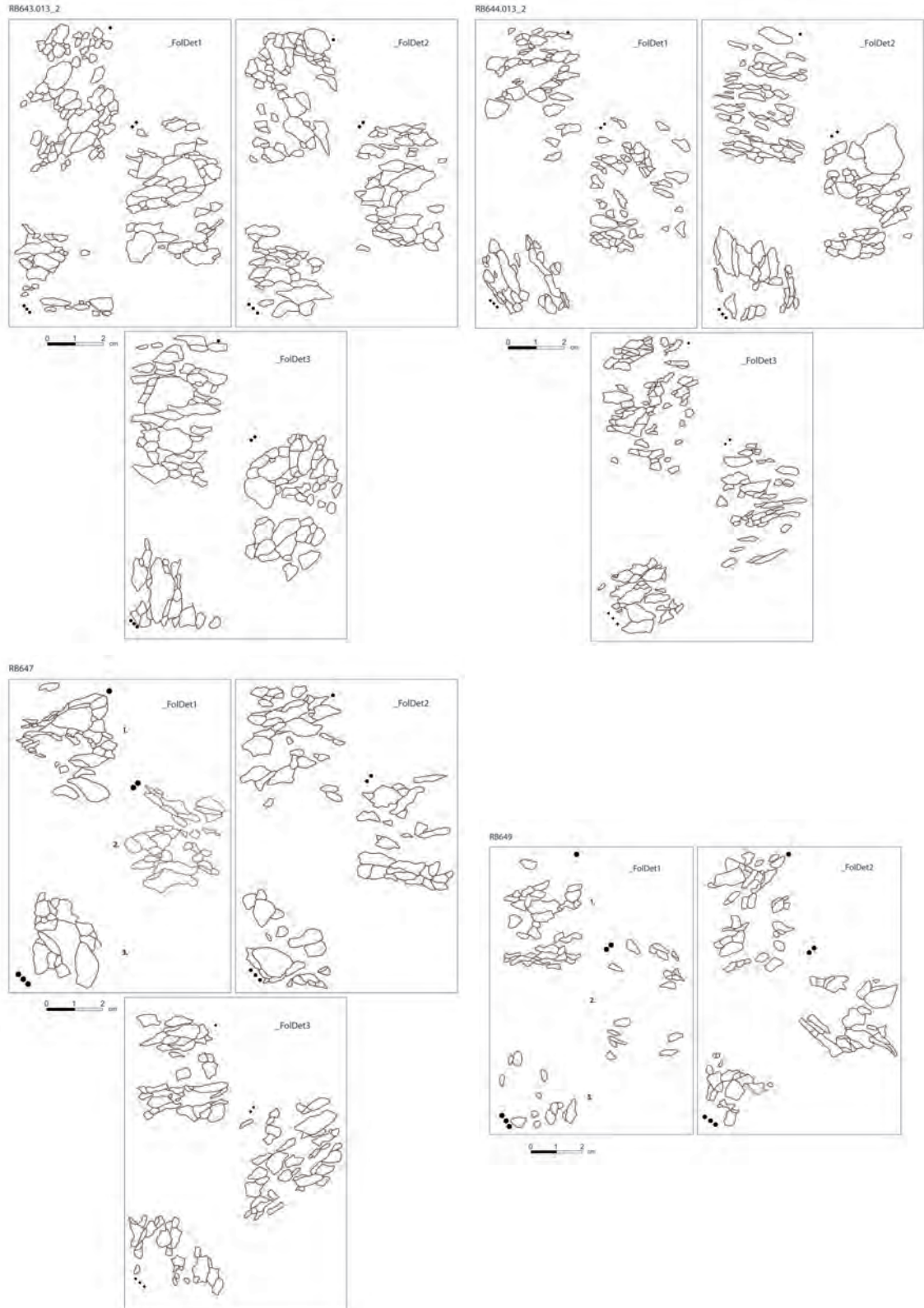
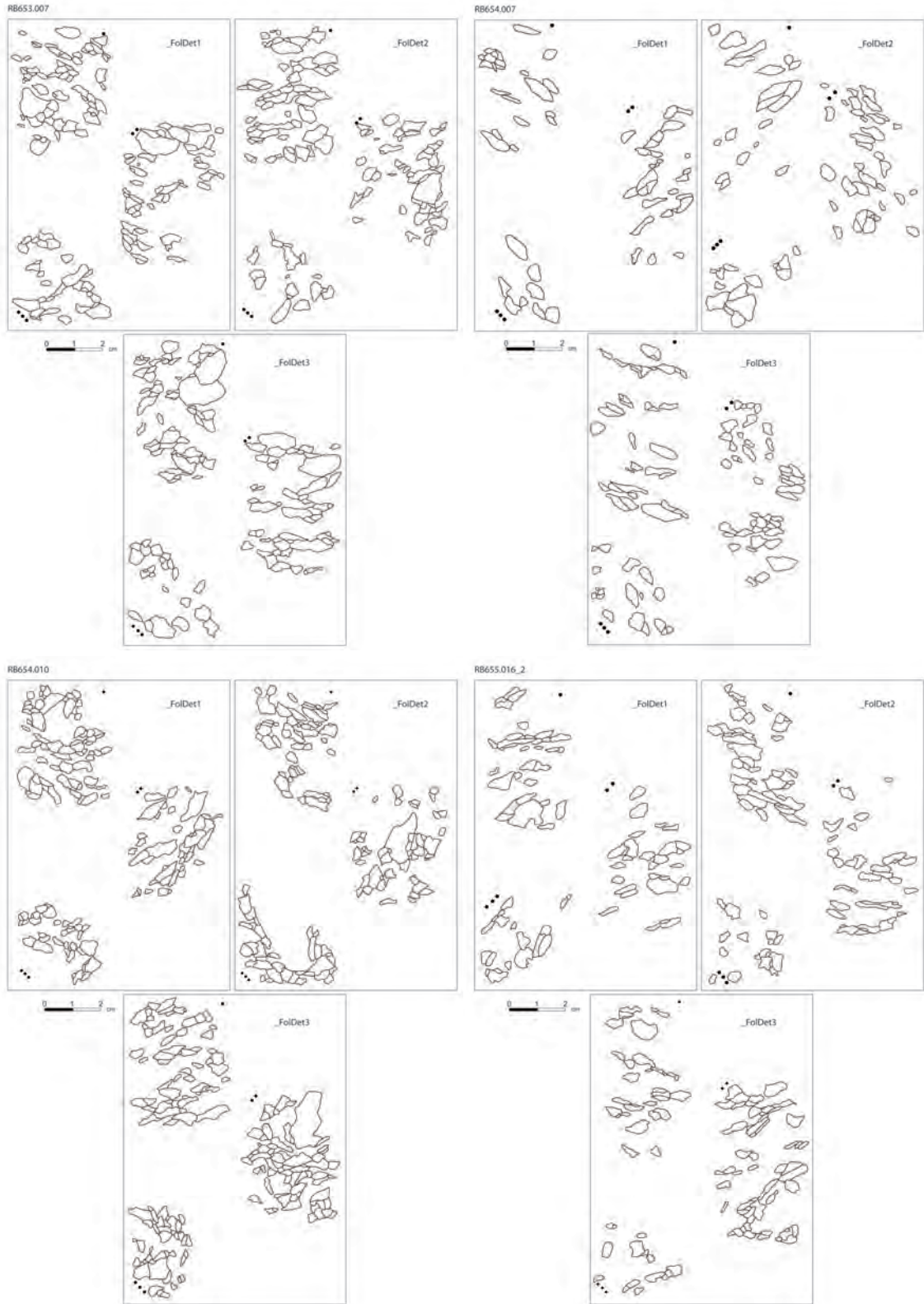


Fig. A1.1: The determination of grain shape masks based on three sections of a drill core segment. Perpendicular sections (planes) are given with strike and dip related to a virtual North (N).

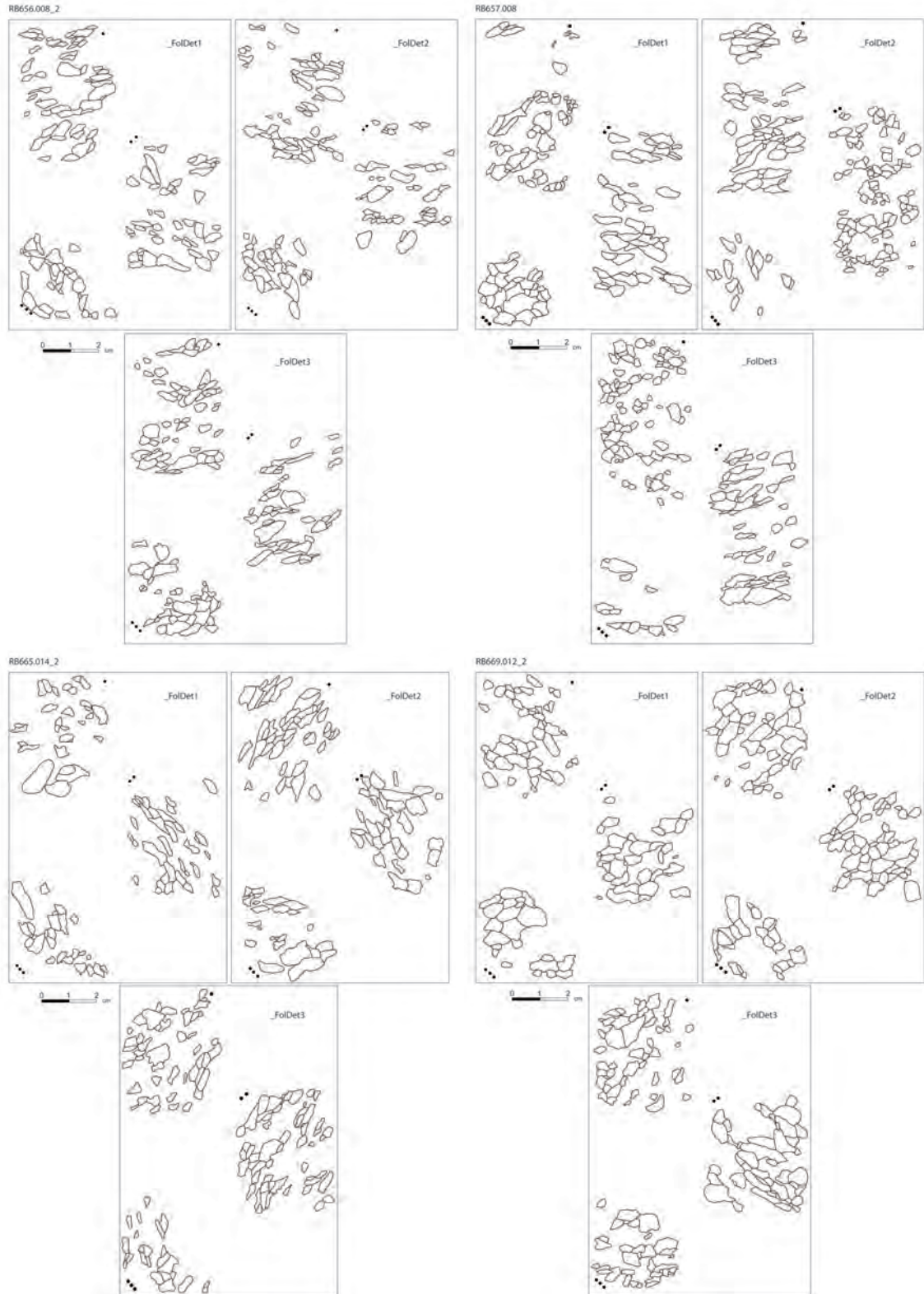
Appendix A: Halite grain shape and subgrain data



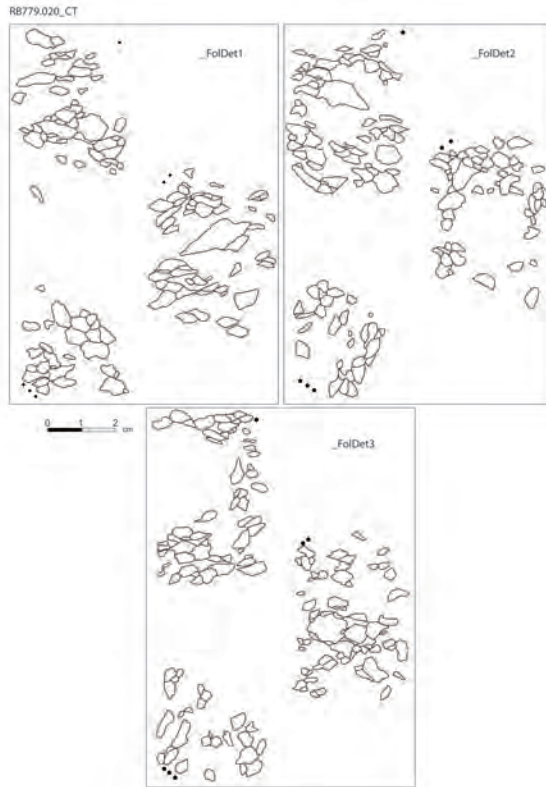
Appendix A: Halite grain shape and subgrain data



Appendix A: Halite grain shape and subgrain data



Appendix A: Halite grain shape and subgrain data



Appendix A: Halite grain shape and subgrain data

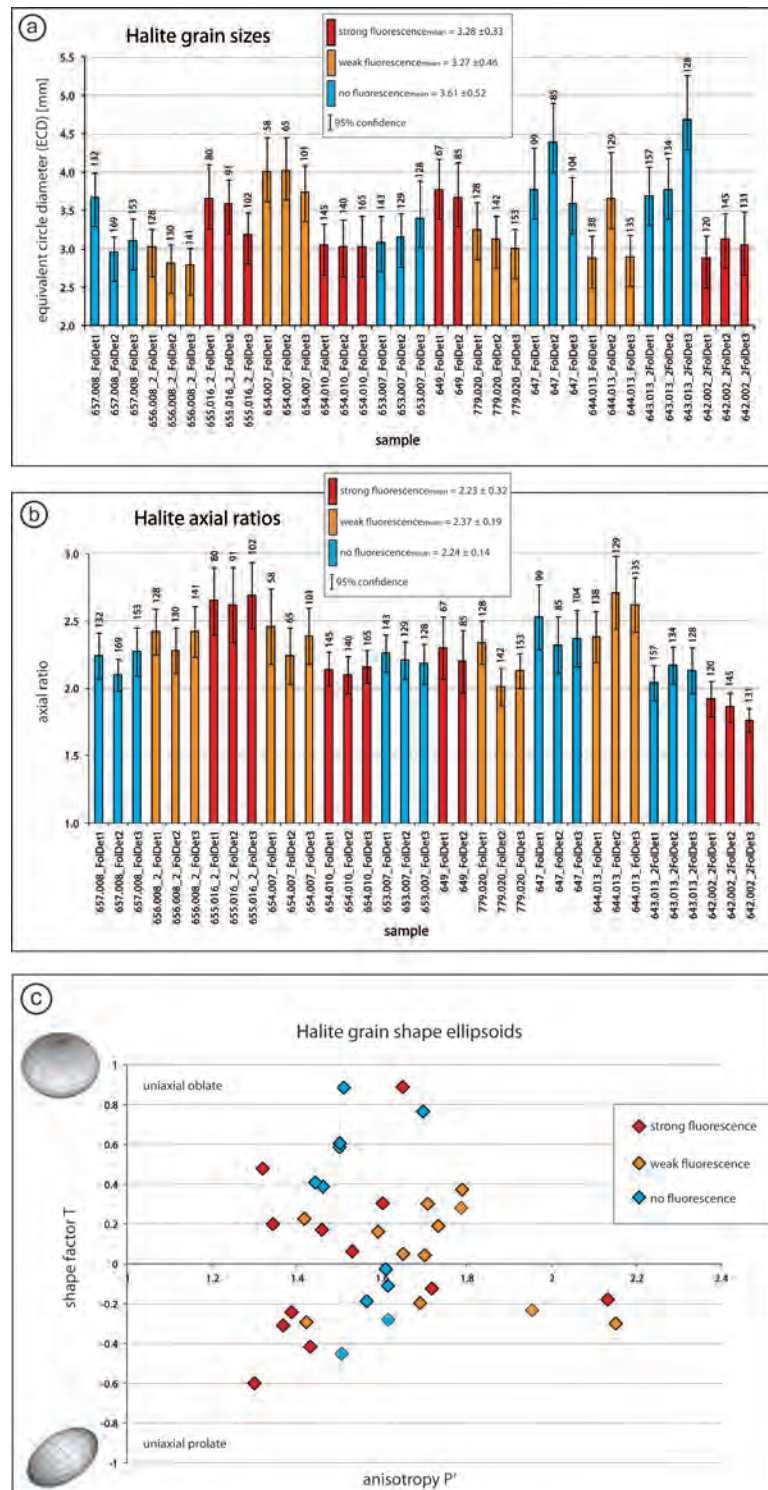
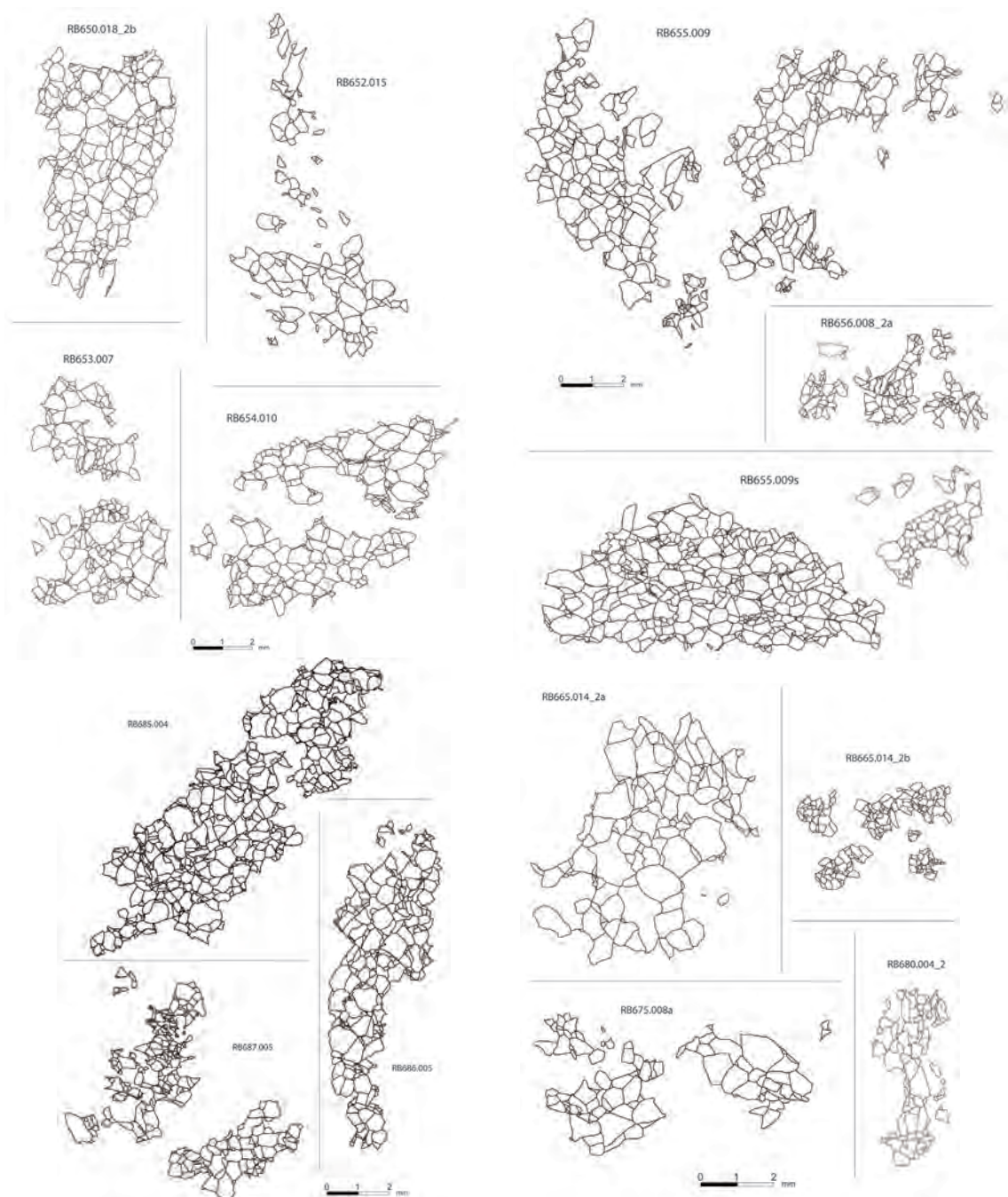


Fig. A1.2: Halite grain shape data of Gorleben rock salt (see Chapter 2) combined with the fluorescence intensities equivalent to hydrocarbon abundance. Hydrocarbon impregnation is independent from grain size (a), axial ratio (b) and grain shape ellipsoid (c).

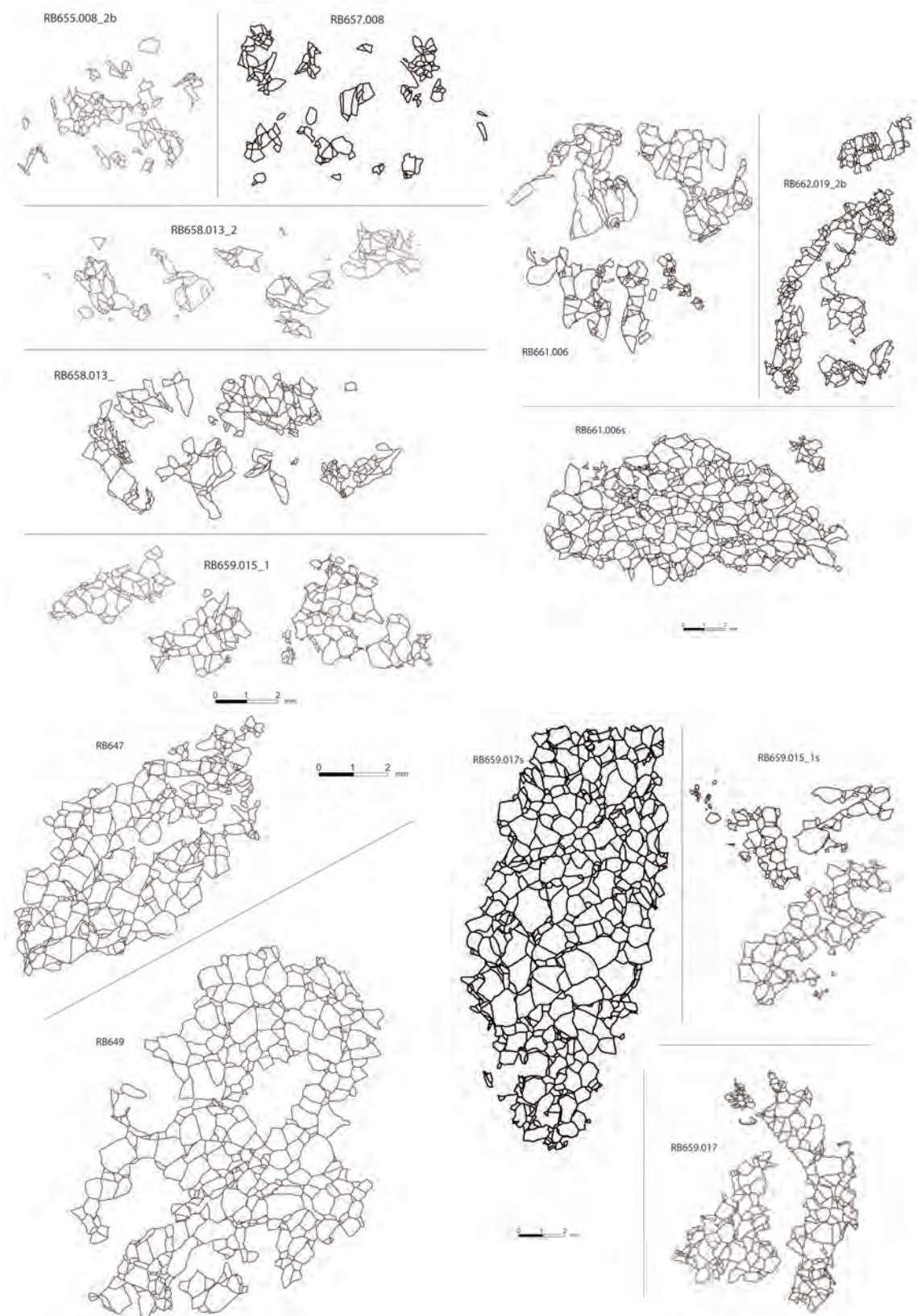
Appendix A: Halite grain shape and subgrain data

A2. Subgrain data

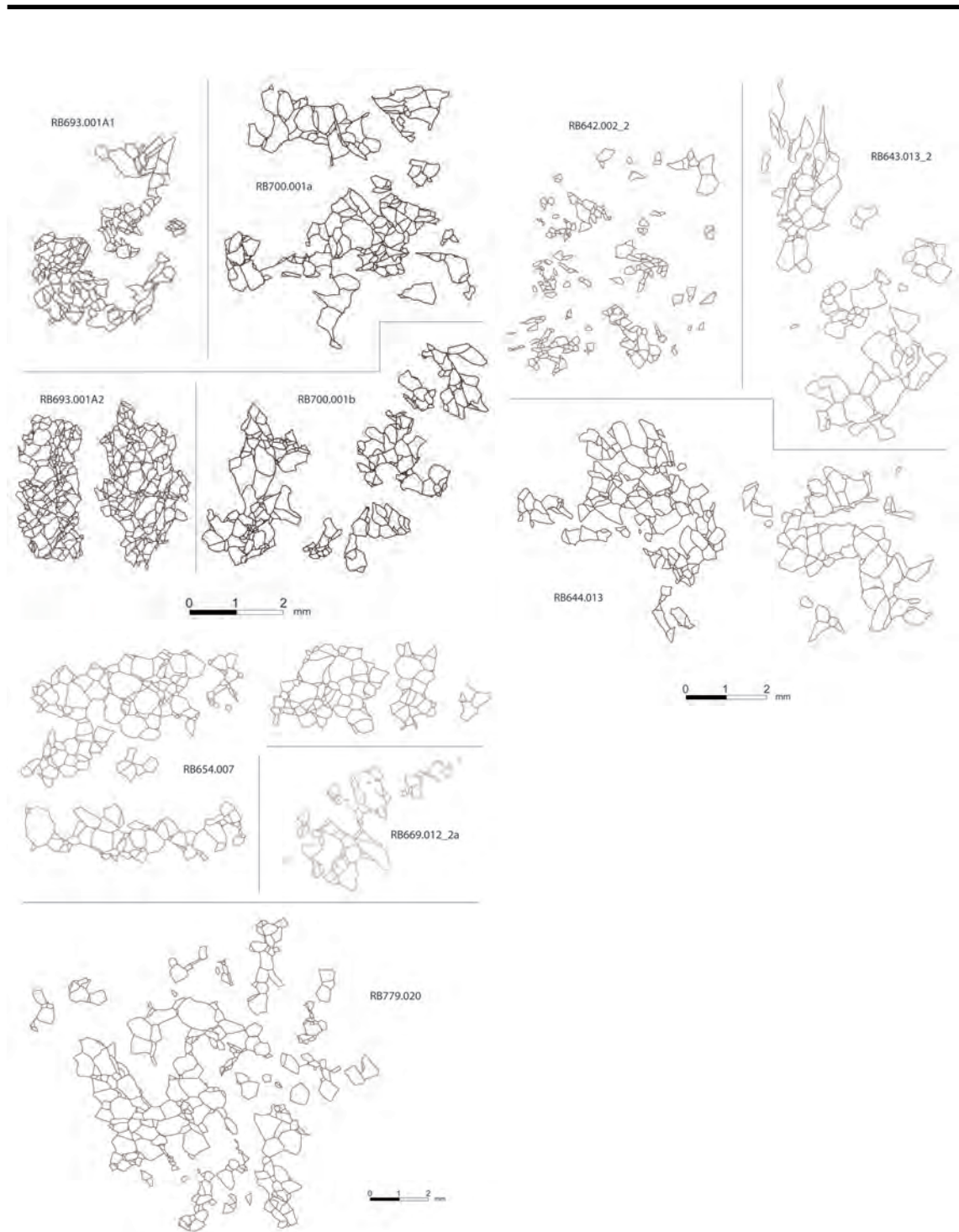
Calculated paleopiezometric stress data is presented and discussed in Chapter 2. The following figures show the complete subgrain masks retraced from subgrain fabrics used for the paleopiezometric calculations. The subgrain data is summarized in Table A2.1. The stress distribution along cross cut 1 West and cross cut 1 East (840 m-level) is shown in Figure A2.1.



Appendix A: Halite grain shape and subgrain data



Appendix A: Halite grain shape and subgrain data



Appendix A: Halite grain shape and subgrain data

sample	formation	cross cut	no. of analyzed subgrains	mean subgrain diameter [μm]	std. dev.	mean values for differential stress [MPa]	mean values for differential stress [MPa] (95% confidence)	strain rate $\dot{\epsilon}_{100}$ at T = 100 °C
RB655.009	z2HS1	1W	545	182	151	1.16	1.04 - 1.31	8.02E-12
RB655.009s	z2HS1	1W	694	180	157	1.17	1.04 - 1.33	8.26E-12
RB658.013_2	z2HS1	1W	694	180	157	1.17	1.04 - 1.33	8.26E-12
RB658.013_2s	z2HS1	1W	344	113	101	1.76	1.56 - 2.02	3.31E-11
RB659.015_1	z2HS1	1W	327	201	193	1.06	0.94 - 1.23	5.90E-12
RB659.015_1s	z2HS1	1W	260	225	199	0.96	0.85 - 1.10	4.22E-12
RB659.017	z2HS1	1W	423	181	159	1.16	1.04 - 1.33	8.02E-12
RB659.017s	z2HS1	1W	627	231	215	0.94	0.83 - 1.08	3.92E-12
RB650.018_2b	z2HS1	1W	364	198	184	1.08	0.95 - 1.24	5.29E-12
RB654.010	z2HS1	1W	363	199	187	1.07	0.95 - 1.24	6.10E-12
RB652.015	z2HS1	1W	145	270	199	0.82	0.74 - 0.92	2.47E-12
RB657.008	z2HS1	1W	164	160	115	1.19	1.09 - 1.31	8.75E-12
RB685.004_CT	z2HS1	1W	829	163	163	1.27	1.20 - 1.35	1.09E-11
RB686.005_CT	z2HS1	1W	379	221	205	0.97	0.90 - 1.06	4.37E-12
RB687.005_CT	z2HS1	1W	435	160	155	1.29	1.20 - 1.40	1.15E-11
RB665.014_2a	z2HS1	1E	159	311	257	0.72	0.65 - 0.82	1.59E-12
RB665.014_2b	z2HS1	1E	250	106	14	1.85	1.82 - 1.88	3.92E-11
RB675.008a	z2HS1	1E	119	253	118	0.87	0.81 - 0.94	3.02E-12
RB647	z2HS1	1W	1008	176	74	1.19	1.17 - 1.22	8.75E-12
RB649	z2HS1	1W	907	258	129	0.85	0.83 - 0.88	2.79E-12
RB653.007	z2HS1	1W	268	174	62	1.2	1.16 - 1.25	9.00E-12
RB656.008_2a	z2HS1	1W	177	134	29	1.51	1.47 - 1.55	1.97E-11
RB654.007	z2HS1	1W	346	276	200	0.81	0.76 - 0.86	2.37E-12
RB779.020	z2HS1	1W	324	275	203	0.81	0.76 - 0.87	2.37E-12
RB669.012_2a	z2HS1	1E	94	217	166	0.99	0.88 - 1.15	4.68E-12
RB661.006	z2HS2	1W	403	123	119	1.62	1.43 - 1.88	2.50E-11
RB661.006s	z2HS2	1W	657	167	139	1.25	1.12 - 1.42	1.03E-11
RB662.019_2b	z2HS2	1W	500	126	112	1.59	1.42 - 1.82	2.34E-11
RB680.004_2	z2HS2	1E	120	166	117	1.26	1.13 - 1.41	1.06E-11
RB700.001a	z2HS2	1E	226	166	53	1.26	1.21 - 1.30	1.06E-11
RB700.001b	z2HS2	1E	263	143	40	1.42	1.38 - 1.47	1.60E-11
RB693.001A1	z2HS2	1E	224	100	17	1.94	1.91 - 1.97	4.61E-11
RB693.001A2	z2HS2	1E	469	86	12	2.23	2.21 - 2.26	7.40E-11
RB643.013_2	z2HS2	1W	120	256	183	0.86	0.77 - 0.97	2.90E-12
RB644.013	z2HS2	1W	267	214	173	1	0.93 - 1.10	4.84E-12
RB642.002_2	z2HS2	1W	216	135	78	1.5	1.41 - 1.61	1.92E-11

Table A2.1: Determined paleopiezometric Hauptsalz data based on subgrain masks. For strain rate calculation, see Carter (1993).

Appendix A: Halite grain shape and subgrain data

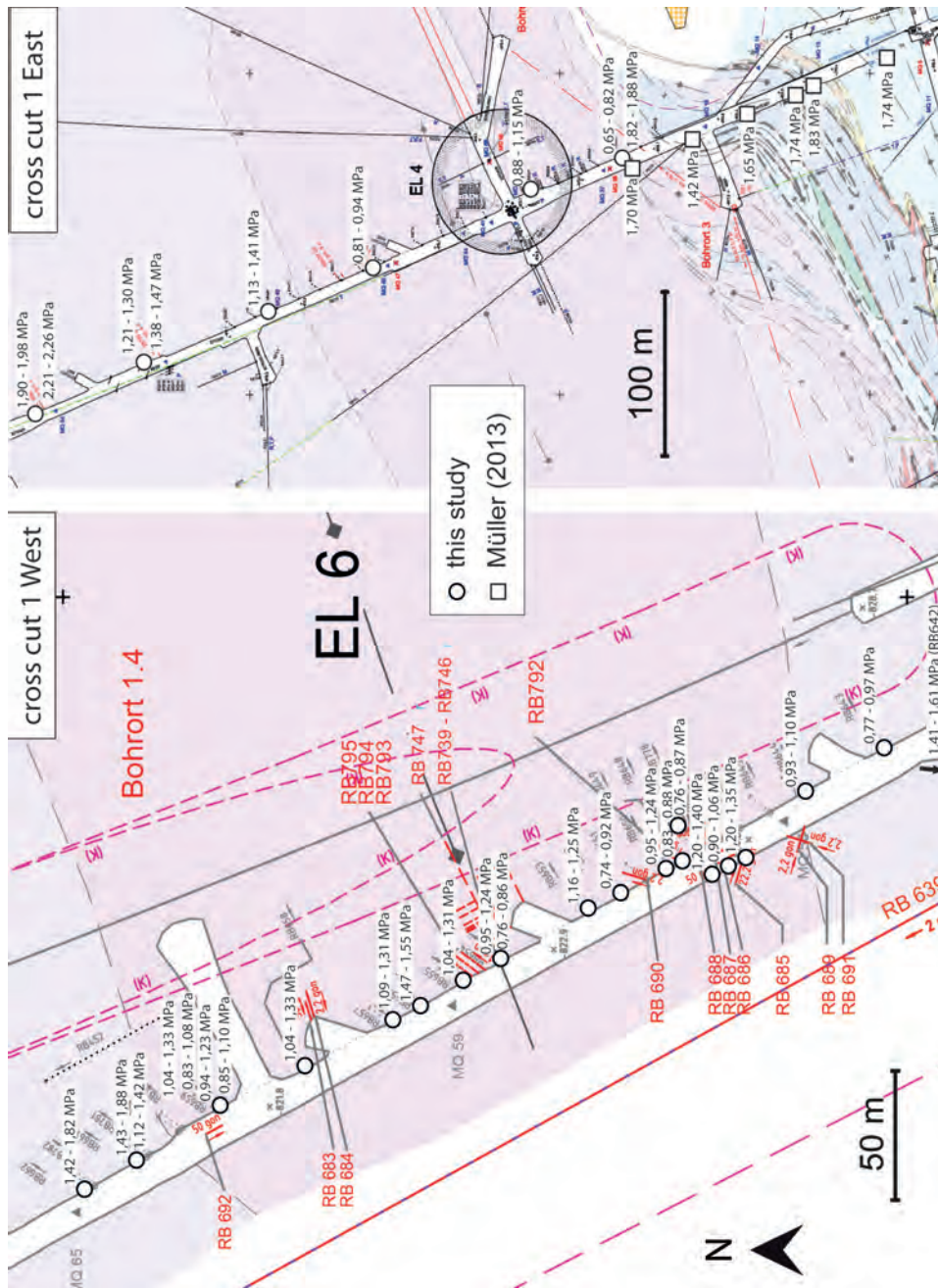


Fig. A2.1: Calculated paleodifferential stress along cross cut 1 West and cross cut 1 East at the 840 m-level (map sections by DBE and Bfs). In cross cut 1 East the calculated data is complemented by data from Müller (2013) *.

* Müller, H.-H., 2013. Mikrostrukturelle Charakterisierung des Hauptsalzes und der Gesteine des Übergangs zu den Leine-Steinsalzen im Querschlag 1 Ost, Gorleben. Unveröff. Masterarbeit, Georg-August-Universität Göttingen.

Appendix A: Halite grain shape and subgrain data

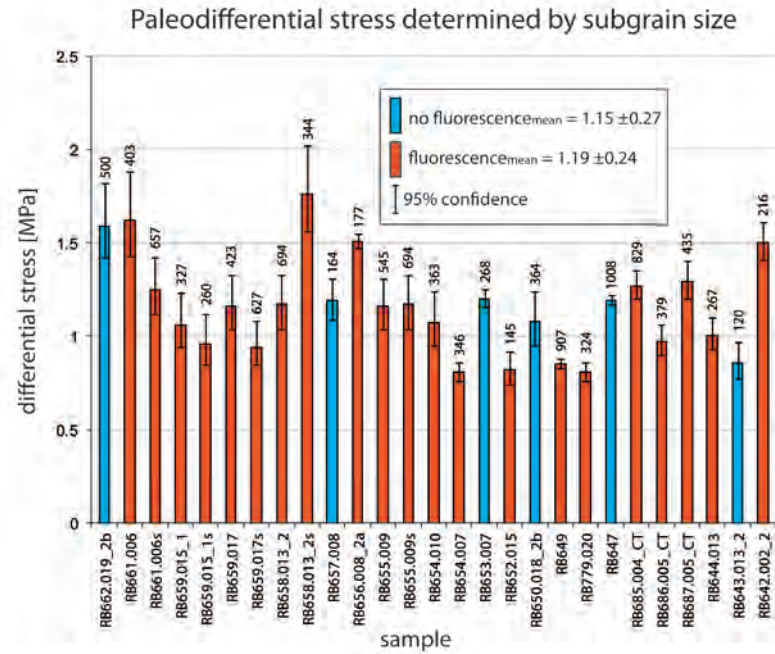


Fig. A2.2: Paleopiezometric stress data (see Chapter 2) related to hydrocarbon abundance (fluorescence). No relation between the subgrain size and hydrocarbon abundance exists.

Appendix B: CT imaging at the nanoCT lab

B1. CT imaging with the nanotom s at the Institute of Geoscience: Basic principles of CT imaging, a guideline for CT data acquisition and specific handling instructions.

Nicolas Thiemeyer¹ & Jörg Habersetzer²

¹*Institute of Geoscience, Goethe-University Frankfurt am Main, Altenhöferallee 1, 60438 Frankfurt am Main, Germany.*

²*Senckenberg Research Institute and Natural History Museum Frankfurt am Main, Senckenberganlage 25, 60325 Frankfurt am Main, Germany.*

1.1. Introduction

The application of X-ray computed tomography has already been presented for modern research on rock salt in general and for specific analyses regarding porosity characteristics in hydrocarbon-bearing rock salt drill cores (Thiemeyer et al., 2014, 2015). All CT measurements (except for one example) presented in these studies have been analyzed at the nanoCT lab at the Institute of Geoscience using a phoenix nanotom s tomograph, which has a maximum specified nominal resolution of ca. 800 nm (ref DIMA-Test in 2D). Apart from several published CT studies carried out at the nanoCT lab (e.g. Zulauf et al., 2011; Habersetzer et al., 2013, 2014; Thiemeyer et al., 2014, 2015; Tkalcec et al., 2015) numerous CT measurements for testing and calibration have been performed during the installation and optimization of the lab in order to enable and ensure CT imaging.

The aim of this essay is to explain essential aspects for understanding μ CT imaging using the nanotom s and further present a guideline addressed to users of the NanoCT lab. Central questions are listed helping the operator to select appropriate scanning parameters in order to acquire high quality CT data depending on the specific sample properties. For a better illustration, we present a number of CT scans including various types of materials and objects, resolutions and scanning modes. Furthermore, we summarize and make note of specific additional information and gained knowledge collected with the nanotom s of the Institute of Geoscience. This internal “hands-on experience” is nowhere else available and hereby saved in written form. The presented facts can lead to CT scans with improved quality enabling and supporting accurate, fast and straight-forward 3D reconstructions.

1.2. The scanning parameter sequence

The dependencies and mutual effects of various scanning parameters (e.g. beam current, brightness, averaged images...) are worth discussing because they represent the basis for solid CT imaging using a nanotom s, since the state of the art for such type of CT scanners can be compared to SEM technology of the 1960s. Thus, there will be a significant technical improvement during the next years and decades

Appendix B: CT imaging at the nanoCT lab

when the manual treatment of the single parameters becomes less complex or even unnecessary. We illustrate the specific parameters as invariable, partly variable (because of a direct dependence to another parameter) and variable (Fig. B1.1). Invariable parameters are the sample size, the sample material and the object geometries including the region of interest (e.g. a fossil) within the entire sample (e.g. epoxy resin or a piece of rock). These invariable parameters predefine the subsequent setting of the other parameters.

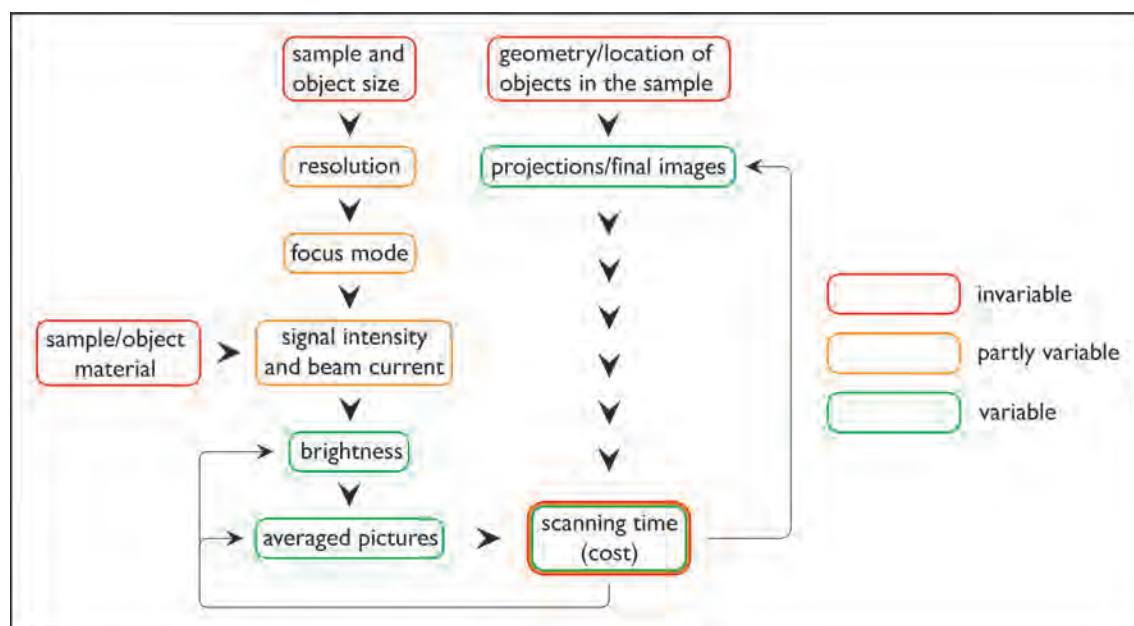


Fig. B1.1: Sequence of CT parameters influencing the scanning time (cost). The time can be mainly controlled by changing the number of projections/final images or the brightness (exposure time) and the number of averaged images (see black lines). The scanning time becomes invariable for CT scans with extreme resolutions of $\leq 1 \mu\text{m}$. For further explanation see text.

Accordingly, the sample and object size is the limiting factor when achieving best resolutions (reconstructed voxel size), because a sample must be placed as close as possible to the X-ray source to achieve great geometric enlargement of a projection captured at the detector. When analyzed samples are relatively large they naturally limit the relative spacing between the detector, the sample and the X-ray source. Depending on the best or designated resolution which is chosen, an associated focus mode should be used (Tab. B1.1). The focus mode classification (0, 1, 2 and 3) literally describes the spot size (or focal spot) of the X-ray current (0 = large, approx. $4 \mu\text{m}$; 3 = very small, less than $1 \mu\text{m}$). Generally, CT imaging requires an X-ray spot size that is similar or even smaller than the reconstructed voxel size, since otherwise information on very fine structures or small objects is not detected. Moreover, the beam current parameters (kV and μA) have to be adjusted depending on which focus mode is used (see Tab. B1.1), because high kV numbers in mode 2 and 3 can cause defocusing effects and a loss of CT data quality. It is of major importance to follow the kV intervals mentioned, whereas the μA numbers can

Appendix B: CT imaging at the nanoCT lab

be adjusted over a large interval depending on the sample properties. However, we recommend using higher μA numbers to guarantee an increase of signal intensity.

focus mode	resolution v (reconstructed voxel size)	kV	μA
0	$v \geq 5 \mu\text{m}$	60 - 150	60 - 100*
1	$5 \mu\text{m} > v \geq 2 \mu\text{m}$	60 - 120	100 - 250*
2	$2 \mu\text{m} > v \geq 1 \mu\text{m}$	60 - 90	200 - 350*
3	$v < 1 \mu\text{m}$	60 - 80	250 - 400*

*can be increased to the maximum possible

Tab. B1.1: Focus modes associated to resolution and beam current parameters. Whereas the μA number is relatively variable and can be set to the maximum possible (software-controlled and -limited), the kV number is restricted to a small interval (60 kV – 80 kV) for mode 2 and 3 due to possible defocusing effects.

Decreasing the X-ray focal spot concurrently causes a decrease in signal intensity captured at the detector forcing high-resolution scans with very small reconstructed voxel size to deal with weak intensities. At this point, the sample material (as invariable parameter) plays a significant role. Usually, decreasing intensity is counteracted by enlarging the brightness (= exposure time) of the single images and, inevitably, a higher number of averaged pictures per rotation increment for noise reduction (see Fig. B1.1). However, when the sample/object material is for example characterized by high dense objects in a low dense matrix, the objects of interest will be still detectable in the reconstructed CT volume due to their high attenuation (high density), although the overall intensity has evidently decreased. On the other hand, when materials with similar density have to be distinguished, it is a must to enlarge the brightness and the number of averaged images in order to guarantee solid CT raw data. This “problem” mainly holds for focus mode 2 and 3 causing large scanning times and increasing costs for high-resolution scans. In such cases, the scanning time is an invariable parameter (see Fig. B1.1). When maximum resolutions of $\leq 1 \mu\text{m}$ must be achieved it is mandatory to use focus mode 3, and the very low intensities require longer exposure times (brightness) and more averaged images. Therefore, we highly recommend aiming for focus mode 2 by a slight increase of the reconstructed voxel size when the objects of interest allow such a modification.

In cases where the scanning time is meant to be limited (costs), the brightness and the number of averaged images (depending on sample/object material) or the number of projections/final images might be reduced (see Fig. B1.1). The latter option is advisable when the geometry/location of the objects in the sample allows this setting, which means: When marginal parts of the scanning volume are going to be disregarded during the subsequent 3D reconstruction after CT raw data acquisition, the number of projections/final images should be reduced (ca. 2200-2400), because a high number of projections/final images is only necessary when outer parts of the projections (or the entire CT volume)

Appendix B: CT imaging at the nanoCT lab

have to be reconstructed. This is because (thinking of a rotating sample) the edges of a sample cover a larger distance for every rotation increment and require more final images for accurate reconstruction than central parts of a sample do; as an example: A small fossil trapped in the middle of a piece of amber covers less distance during the CT scan (rotation scanning) than a point located at the edges of the amber. Since the object of interest is the fossil located in the center and not the surrounding amber, an accurate reconstruction of the surrounding volume (amber) is not requested or necessary by setting a high number of projections/final images of ca. 3000-3500. In contrast, a high number is needed when the entire CT volume including its outer edges belongs to the subject of interest and has to be analyzed.

1.3. Representative CT scans on different scales

In order to clarify the complex relations between the scanning parameters, we give a list of representative CT scans (Tab. B1.2). This list can be used as reference list for CT measurements in different scanning regimes covering a wide range of resolutions and materials. We further present three examples of this list in more detail to explain the chosen parameters dependent on the sample properties.

1) trace fossil:

sample	size of objects of interest	desired objects/ material densities in g/cm ³	sample geometry	resolution v [μm]	focus mode	kV	μA	brightness [ms]	averaged pictures	skipped pictures	final images	scanning time [min]
RB683*	≤ 2 cm	porosity (~0) and anhydrite (~3) in rock salt (2.2)	drill core (3.6 cm in diameter)	10.38	0	100	70	1250	4		2400	255
RB648*	≤ 3 cm	anhydrite clusters (~3.0) in rock salt (2.2)	drill core (7.2 cm in diameter)	20	0	150	100	1000	4		3000	256
trace fossil***	≤ 2 mm	tubes and traces of pyrite (4.9) in black shales (~2.9)	hand specimen, fragmental (7 x 4 x 2 cm)	7.14	0	130	100	500	4		3000	131
salt plate***	≤ 1 mm	anhydrite crystals (~3) in rock salt matrix (2.2)	rock salt plate (2 x 1 x 0.2 cm)	5		100	100	750	4		2300	148
Bo5*	≤ 500 μm	Fluid inclusion (mixture of gas and liquid; 0, 1) in rock salt (2.2)	rock salt plate (2 x 1 x 1 mm)		2	70	330	1250	5		2400	305
trachyte_2**	≤ 100 μm	magnetite (5.2) and amphibole (3-3.6) in feldspar matrix (2.5-2.7)	trachyte cube (1 x 1 x 1 mm)		2	60	400	1250	4		3000	312
trachyte_3***	"	"	"	0.7	3	60	400	1500	4		3000	375

* for 3D reconstructions see Thiemeyer et al. (2015)

** same sample as trachyte_3

*** samples described in the text

Tab. B1.2: Compilation of exemplary CT scans. The coloring is equivalent to Tab. B1.1 illustrating the particular focus modes used.

Appendix B: CT imaging at the nanoCT lab

This sample is a piece of black shale bearing different types of trace fossils present as pyrite (FeS_2). Since the sample was relatively large, the best resolution achievable was a voxel size of $7.14 \mu\text{m}$ which is associated to focus mode 0 (see Tab. B1.1). The beam current parameters were chosen with quite high values (130 kV, $100 \mu\text{A}$) to guarantee the radiation to sufficiently penetrate the sample. Since the object of interest (pyrite) is a high-dense material, it is already clearly distinguishable from its surrounding matrix in X-ray live-view (Fig. B1.2a). Due to the high density contrast the exposure time (brightness) of the projections could remain very low resulting in images with little noise. The aim was to reconstruct an almost entire volume of the rock, so the number of final images (rotating steps) must be relatively high (3000) in order to accurately reconstruct even the edges of the entire volume scanned. Finally, the scanning time was relatively short (131 min) mainly because the high-dense pyrite has a high attenuation clearly emerging the particles within the CT raw data volume (Fig. B1.2b), although a short exposure time for the projections was set.

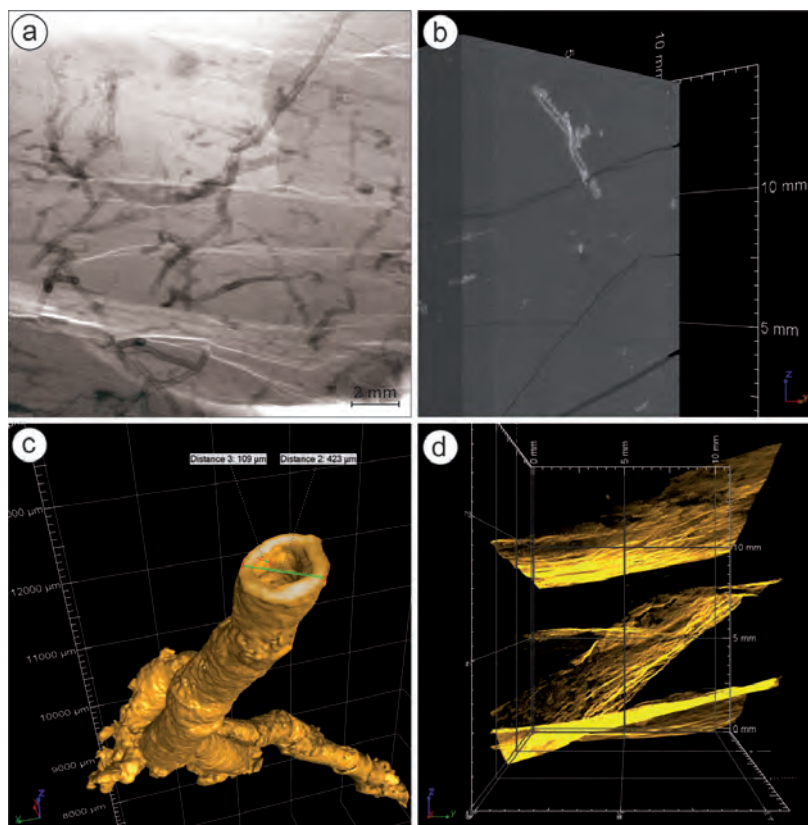


Fig. B1.2: CT data of sample trace fossil. a) Screenshot from live-view during CT scanning. The fossils are easy to trace as dark patterns due to the high density contrast. Fractures are present as white traces. b) Part of the 3D raw data volume reconstructed in VGStudioMAX. Note the clear differentiation between pyrite (white), black shale (gray matrix) and fractures (open space). The voxel size of $7.14 \mu\text{m}$ allows a precise reconstruction of the object of interest. c) Extracted pyrite trace fossil with determined fossil diameter and wall thickness. d) 3D reconstruction of open fracture systems (see b).

Appendix B: CT imaging at the nanoCT lab

2) salt plate

This rock salt sample was relatively small and therefore placed close to the X-ray source enabling a resolution of 5 μm associated to focus mode 1. Since the sample describes a thin plate, the radiation still easily penetrated the sample enabling a differentiation between anhydrite (object of interest) and halite although focus mode 1 caused a slight decrease of signal intensity. However, the remaining intensity only required a slight increase of the brightness. As the main focus was set on the central part of the sample, the number of final images was reduced (2300) leading to a moderate scanning time (148 min). When more scanning time is available or desired, possible improvement of the data quality can be realized by i) an increase of the number of projections/final images (in this type of sample not required) or ii) by an increase of the brightness (exposure time per single image) and the number of averaged images (see Fig. B1.1) in order to intensify the gray value contrast of the different phases in the reconstructed CT raw data set. The gray value intervals enable a differentiation and quantification of various phases (Fig. B1.3).

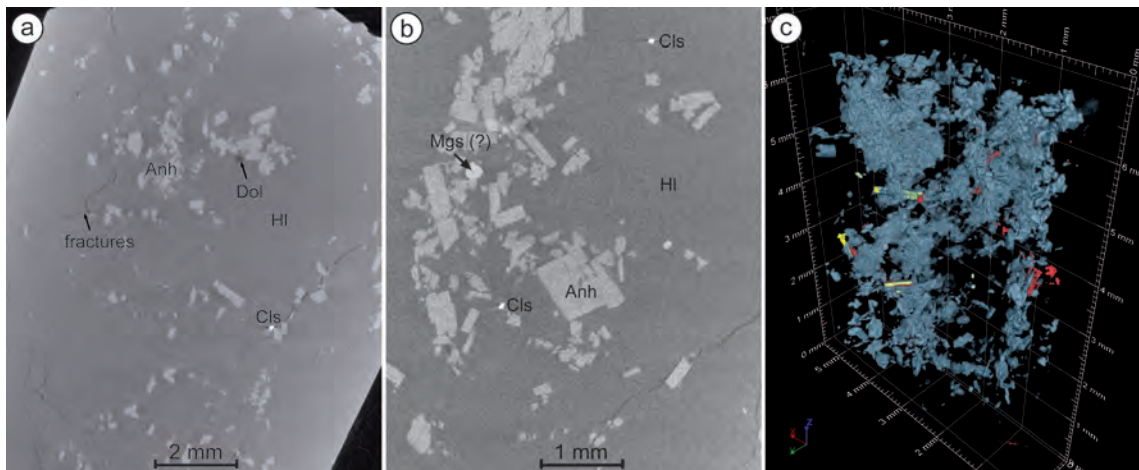


Fig. B1.3: CT data of sample salt plate. a) Various phases can be traced due to density differences: halite (HI; NaCl), anhydrite (Anh; CaSO_4), dolomite (Dol; $\text{CaMg}(\text{CO}_3)_2$), celestine (Cls; SrSO_4) and fractures. b) A slightly higher dense mineral is assumed to be magnesite (Mgs; MgCO_3). c) The well-specifiable phases can be reconstructed in 3D (anhydrite in blue, celestine in yellow and some fractures in red). Note that the fractures are only partly reconstructed due to their very thin planar shape. Anhydrite is quantified by 9.1 vol.-% of the analyzed volume.

3) trachyte_3

This example represents a long-term scan pushing the resolution limits of the nanotom s to a voxel size of 700 nm. The prerequisite was the very small sample size of 1 mm^3 . In focus mode 3 the signal intensity is very weak and required long exposure times (1500 ms) although the current power (μA) is pushed to the maximum. Since the entire CT volume is of interest, 3000 projections are needed to accurately capture the edges. This setting in combination with the long exposure time finally causes a long-term

Appendix B: CT imaging at the nanoCT lab

scan of 375 min. In this example the scanning time turns into an invariable parameter (see Fig. B1.1) because focus mode 3 is used. There is no possibility for reducing the scanning time because of the low signal intensity and the need for a reconstruction of the entire CT volume.

In order to compare the different focus modes this sample was once more scanned with a slightly higher resolution of 1 μm (see trachyte_2 in Tab. B1.2). Note the decrease of the scanning time only by switching into focus mode 2 and the subsequent decrease of the brightness enabled by slightly higher signal intensity. In contrast to focus mode 3 a detection of relatively low density contrasts from sanidine laths (Sn) to the feldspar matrix (Fsp) is still possible using focus mode 2 (Fig. B1.4). However, the use of focus mode 3 is justified when very small and fine structures have to be reconstructed.

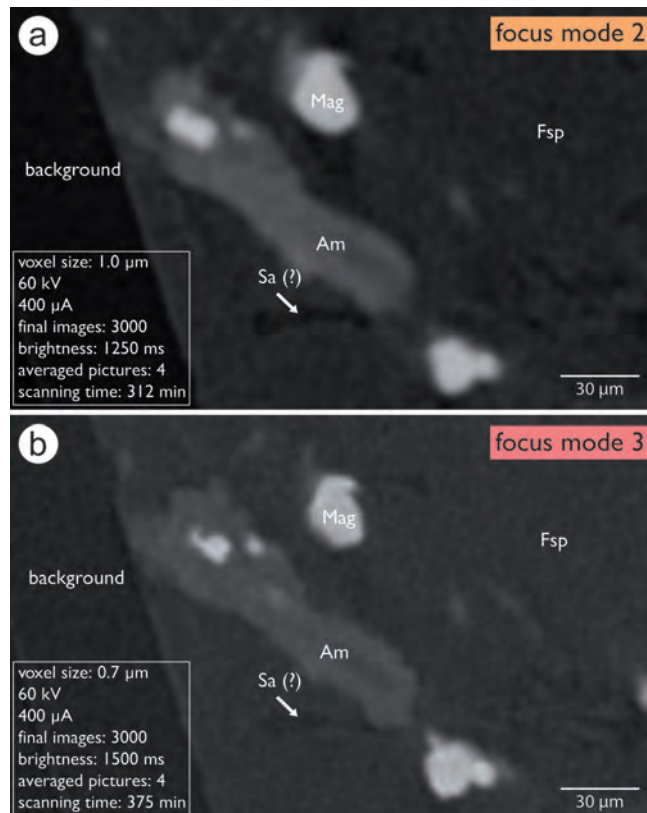


Fig. B1.4: Comparison of CT raw data of trachyte_2 and trachyte_3. a) CT scan trachyte_2 (focus mode 2) allows the differentiation of different mineral phases: magnetite (Mg), amphibole (Am), feldspar (Fsp) and sanidine (Sa). CT scan trachyte_3 (focus mode 3) contains more precise information on the morphologies and exact shape of the minerals as the overall gray value range is reduced.

The raw data of trachyte_3 was filtered with median 5 for noise reduction to simplify the virtual extraction of magnetite and amphibole (Fig. B1.5). The results are valuable for the determination of preferred orientations in the magmatic fabric, particle ellipsoids or volume fractions of different minerals. The CT volume yields an amphibole content of 3.1 vol.-% and a magnetite content of 0.8 vol.-%.

Appendix B: CT imaging at the nanoCT lab

%. The reconstructed voxel size is 0.7 μm .

Although both CT data sets allow the differentiation of three to four mineral phases trachyte_3 allows

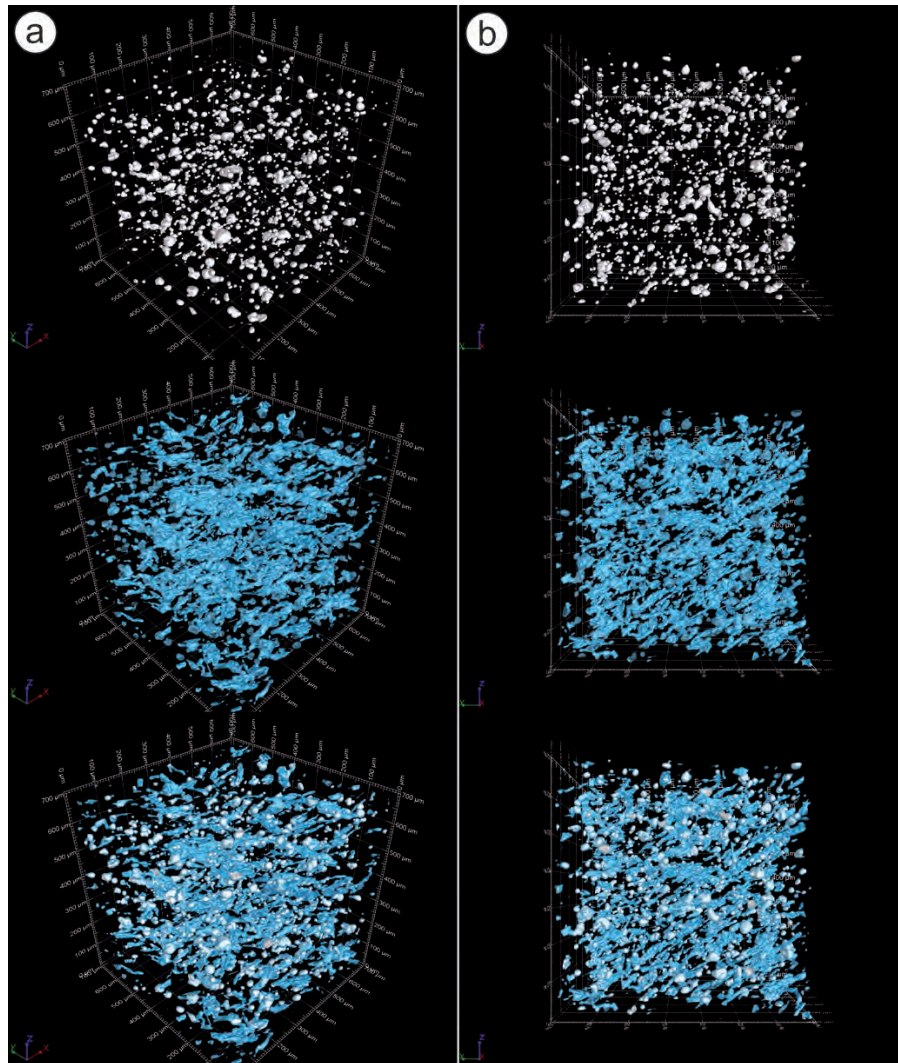


Fig. B1.5: 3D reconstruction of trachyte_3. The volumes show the spatial distribution of magnetite grains (white) and amphibole laths (blue) as top-diagonal view (a) and side view (b). Note the preferred orientation of amphibole minerals representing the typical trachytic fabric retracing magmatic flow.

a more accurate description of the actual shapes. Thus, for a rough estimation on volume fractions trachyte_2 is already sufficient (focus mode 2), whereas trachyte_3 gives supplementary information on morphology and even on a certain amphibole zoning (focus mode 3).

To conclude, the main objective of a CT study and the available financial resources are decisive factors whether to perform such high-resolution scans in focus mode 2 or 3. Generally, shorter CT scans are more reliable than long-term scans regarding the stability of the X-ray tube and the focal spot. Additionally,

Appendix B: CT imaging at the nanoCT lab

3D segmentation of desired objects is easier dealing with a wider spread of gray value ranges for every particular material. High-resolution (long-term) scans are more complex and require a certain amount of time for scanning but also for data processing and the reconstruction of 3D patterns.

1.4. Central questions regarding solid CT data acquisition

Understanding the complex mesh of all the scanning parameters is the basis for reliable CT measurements. To finally complete the outline for CT imaging with the nanotom s, we formulate five central questions which are of major importance for setting the parameters correctly. Accordingly, we give indirect answers to these questions in the context of adjusting the corresponding scanning parameters (Fig. B1.6).

1. What size are the particles or the object(s) of interest?
 - A sufficient **resolution** (voxel size) must be attained.
2. What size is the overall sample placed in the sample chamber?
 - A large sample might prohibit the **resolution** attained (spacing between: detector ◀ sample ▶ X-ray source). The selected resolution defines the **focus mode**.
3. What material are the single phases and the major object(s) of interest?
 - Low material contrast needs an increase of **signal intensity, brightness** and number of **averaged images**. Note that high-dense objects, however, might not require this increase.
4. How is the geometry and the location of the region of interest in the sample?
 - Reconstructing the entire CT volume requires a high number of **projections/ final images**. Reconstructing only the center of the CT data volume allows small numbers.
5. How long is the scanning time? What are the estimated costs?
 - The scanning time can be reduced by decreasing the **brightness** and number of **averaged images** or by a smaller number of **projections/ final images**.

Fig. B1.6: The five central questions mandatory for solid CT imaging. The guiding answers are related to the associated scanning parameters. The coloring is complement as given for the CT parameters sequence (partly variable and variable; see Fig. B1.1).

These fundamental and mandatory questions are addressed to every operator working with the nanotom s.

Appendix B: CT imaging at the nanoCT lab

1.5. References

- Habersetzer, J., Engels, S., Smith, K., 2013. Diverse Strategies for Improving CT Scans of Vertebrate Fossils. *Journal of Vertebrate Paleontology*, SVP Program and Abstracts Book, 2013, Los Angeles Suppl., 138A.
- Habersetzer, J., Engels, S., Gunnell, G. F., Simmons, N., B., 2014. Ecology and Taxonomy of Messel Bats. *Journal of Vertebrate Paleontology*, SVP Program and Abstracts Book, 2014, Berlin Suppl., 142–143A.
- Thiemeyer et al., 2014, Thiemeyer, N., Pusch, M., Hammer, J., Zulauf, G., 2014. Quantification and 3D visualisation of pore space in Gorleben rock salt: constraints from CT imaging and microfabrics. *German Journal of Geosciences* 165 (1), 15-25.
- Thiemeyer et al., 2015 Thiemeyer, N., Habersetzer, J., Peinl, M., Zulauf, G., Hammer, J., 2015. The application of high resolution X-ray computed tomography on naturally deformed rock salt: Multi-scale investigations of the structural inventory. *Journal of Structural Geology* 77, 92-106.
- Tkalcec, B.J., Brenker, F.E., 2015. Asteroidal processes recorded by polyphase deformation in a harzburgitic diogenite NWA 5480. *Journal of Structural Geology* 77, 138-150.
- Zulauf, J., Zulauf, G., Hammer, J., Zanella, F., 2011. Tablet boudinage of an anhydrite layer in rock-salt matrix: Results from thermomechanical experiments. *Journal of Structural Geology* 33, 1801-1815.

Appendix B: CT imaging at the nanoCT lab

B2. CT manual for the nanotom s

B2.1. MICROCENT

Das Programm MICROCENT dient zur permanenten (automatisierten) Zentrierung des Röntgenstrahls während einer Messung. Die Benutzung von MICROCENT sollte bei jeder CT-Messung erfolgen, da so die Intensitätsabfälle speziell bei Langzeitscans in der Vergangenheit verhindert werden konnten. Sollte sich in weiteren CT-Scans ohne MICROCENT zeigen, dass der ausgetauschte Isolator das Problem löst, kann auf MICROCENT zukünftig verzichtet werden. Solange dieser Punkt nicht eindeutig geklärt ist, bietet es sich an, das Programm weiterhin auszuführen.

Bevor ein Scanvorgang final gestartet wird, muss das Programm MICROCENT eingerichtet werden. Dieses läuft im Hintergrund während einer Messung, und die Fokussierung des Strahls zu überprüfen und gegebenenfalls einzustellen.

Komplette Vorbereitungen zum Scan (Position der Probe, Parameter, Detektor kalibrieren...) im datoslx wie gehabt durchführen.

BEVOR ein Scanvorgang endgültig gestartet wird:

1. - MICROCENT öffnen > upgrade.exe
(Ordner: C:\work\programs\KundeV1_5)
Programm auch auf dem Desktop:

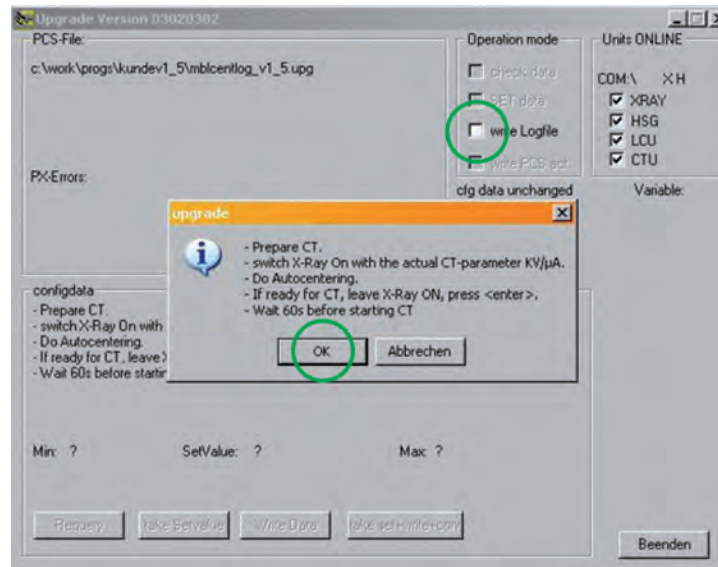
2. - Datei: mblcentlog_v1_

3. 5.upg öffnen
(Ordner: C:\work\programs\KundeV1_5\...)

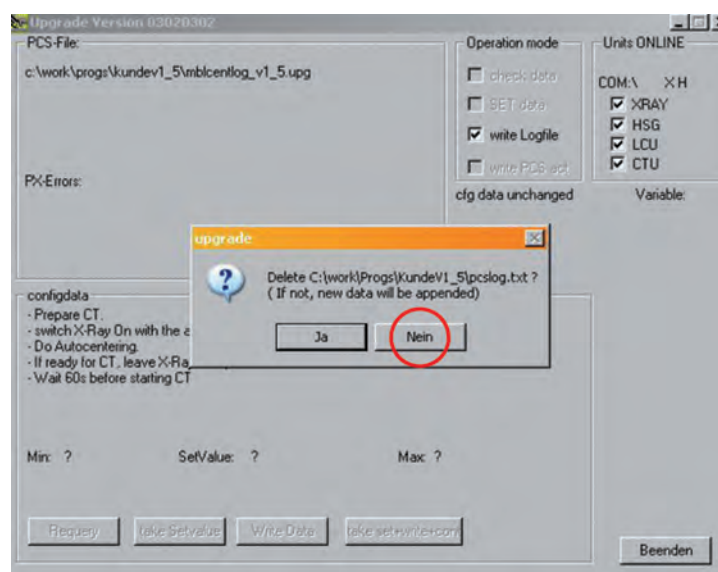
4. - Input of a value 3 OK



Appendix B: CT imaging at the nanoCT lab

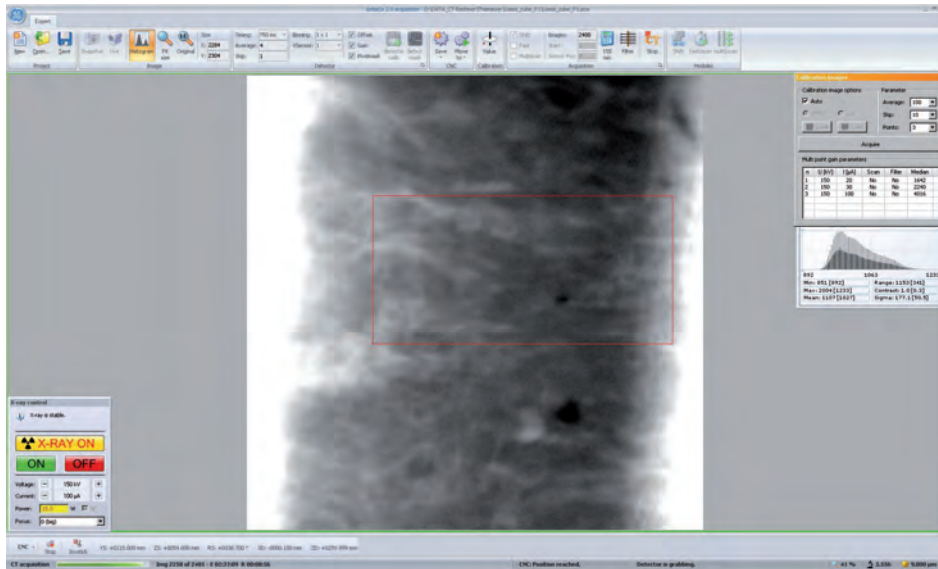


5. - Log-file unter gewünschtem Name (*.dat) speichern (z.B. im Scanordner)
„öffnen“
6. - Im datoslx Röntgenstrahl einschalten: X-Ray ON
7. im MICROCENT: OK und „write Logfile“ Häkchen setzen (trotz Eieruhr)
8. - „Delete...?“ Nein



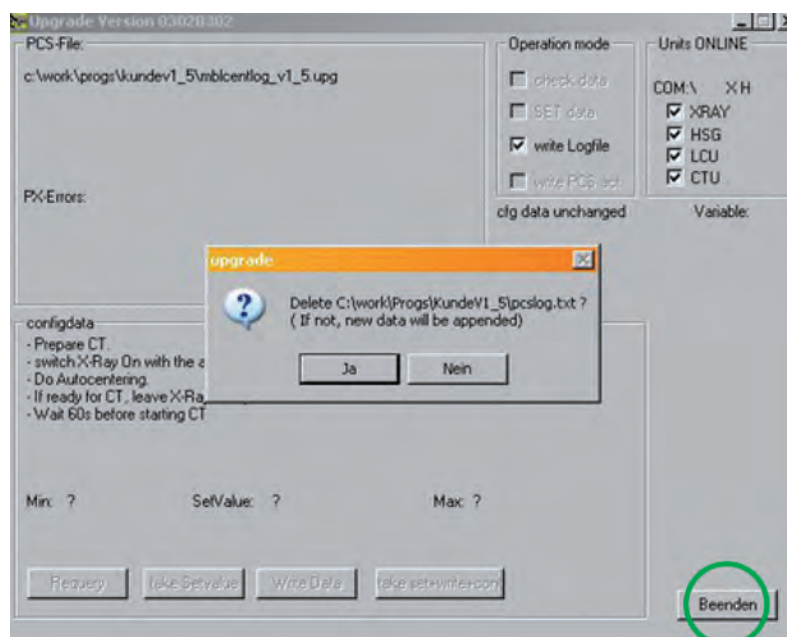
Appendix B: CT imaging at the nanoCT lab

9. - 60 sec warten (Signalton ertönt)
10. - Scanvorgang starten im datoslx
...Scanvorgang...



Falls zyklische Defokussierung („Pumpen“) im Live-Bild zu beobachten ist, Scan abbrechen und ohne MICROCENT neu starten.

11. - Wenn der Scan beendet ist, Programm schließen („Beenden“).



Appendix B: CT imaging at the nanoCT lab

B2.2. Fokussierung des Röntgenstrahls

Die Fokussierung des Röntgenstrahls muss nur selten durchgeführt werden. Es bietet sich zum Beispiel an, vor Langzeitscans bei den gewählten Strahlparametern die aktuelle Fokussierung zu überprüfen und gegebenenfalls zu verbessern. Eine unzureichende Fokussierung führt zu unscharfen Bildern oder dem Verlust feiner Strukturen und verhindert speziell in den Modi 2 und 3 die gewünschte, effektive hohe Auflösung.

Die Fokussierung ist ausschließlich abhängig von der Röhrenspannung (kV). So ist jeder Spannungswert mit exakt einem Fokuswert verbunden, der manuell eingestellt werden kann. Eine Fokussierung ist für hochauflösende CT-Messungen (Modi 2 und 3) weitaus bedeutender als für Scans geringerer Auflösungen. Nach Tab. B1.1 in Appendix B1 fällt die Fokussierungsprozedur für hochauflösende Scans in kV-Bereiche von 60-90 kV, in denen die CT-Messungen der Modi 2 und 3 durchgeführt werden.

Die Fokussierung des Röntgenstrahls geschieht unter Verwendung des JIMA-Auflösetests (Abb. B2.1). Dieser Test beinhaltet eine zentrale Lochblende mit horizontalen und vertikalen Streifenmustern aus Wolfram. Bei der Fokussierung empfiehlt sich die Verwendung der 0,8 μm -Streifen (siehe roter Pfeil in Abb. B2.1), die im Grenzbereich sichtbarer Strukturen des nanotom s liegen.

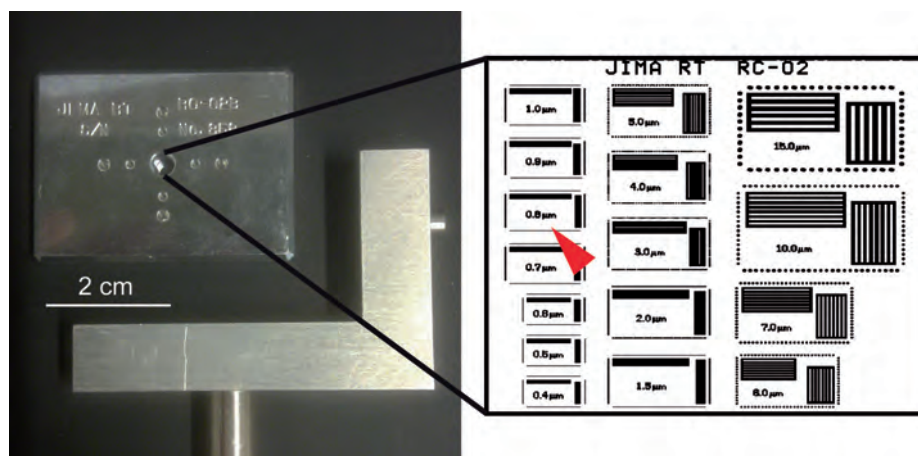


Abb. B2.1: JIMA-Auflösetest mit Streifenmustern verschiedener Breite (15-0,4 μm).

Die Fokussierung mittels JIMA-Auflösetest

1.

- Strahlparameter (kV und μA) ermitteln, bei denen die CT-Probe gescannt werden soll.
- Kollimator vom Target abziehen.
- Den JIMA-Test im dafür vorgesehenen Halter direkt in Kontakt (oberflächenparallel) vor dem Austrittspunkt des Strahls an der Röntgenröhre platzieren (Abb. B2.2). Zur ersten Orientierung sollte hier die zentrale Lochblende in der vertikalen Linie in der Verlängerung des Halterstabes liegen.
- Über die Stellschraube den JIMA-Test horizontal positionieren (siehe rote Markierung in Abb. B2.2). Die vertikale Position durch Heben und Senken des Probenstisches (manuell oder im Scan-Programm

Appendix B: CT imaging at the nanoCT lab

datos/x) eingestellt. Zur groben Orientierung dienen hier die zwei äußeren Schrauben des Targets (blaue Pfeile in Abb. B2.2), die in einer horizontalen Linie mit der Lochblende des JIMA-Tests liegen müssen.

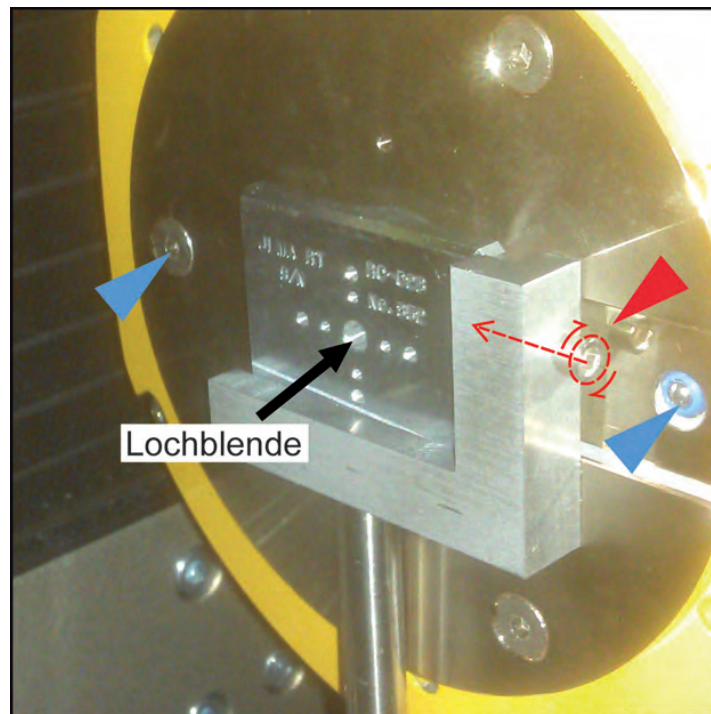


Abb. B2.2: Position des JIMA-Tests vor der Röntgenröhre. Die Lochblende muss zentral vor den Austrittspunkt des Röntgenstrahls gebracht werden.

2.

- Röntgenstrahl einschalten und im Live-Bild die entsprechenden Streifenmusterposition ($0,8 \mu\text{m}$) finden. Als Hilfe zur Orientierung in den Streifenmustern dient hier die Übersicht des gesamten Lochblendenfeldes (siehe Abb. B2.1).

- Die vertikale Feinpositionierung mithilfe des Live-Bildes im datos/x einstellen (Z-Achsen-Werte), während die horizontale Ausrichtung nur manuell mittels der Stellschraube (siehe Abb. B2.2) bei ausgeschaltetem Strahl geändert wird.

3.

- Anhand der $0,8 \mu\text{m}$ -Streifen die Fokussierung durchführen. Hierzu Snapshots des Live-Bildes mit mindestens $\text{Av} = 10$ aufnehmen (Abb. B2.3).

- Bei der Belichtungszeit (brightness) pro Aufnahme 500 ms bis maximal 1000 ms verwenden, da die Wolframstreifen selbst bei geringer Signalintensität deutlich zu erkennen sind. Die Detektordistanz muss bei einer Tomographie im Modus 3 maximal (50 cm) eingestellt werden, allerdings ist die Erkennung der

Appendix B: CT imaging at the nanoCT lab

Streifenmuster im 2-D Betrieb durch die Möglichkeit, das Testobjekt wesentlich dichter an den Fokus heranzuführen, auch bei erheblich geringeren Detektor-Distanzen (20-25 cm) möglich. Dies erleichtert den Fokussierungsvorgang erheblich.

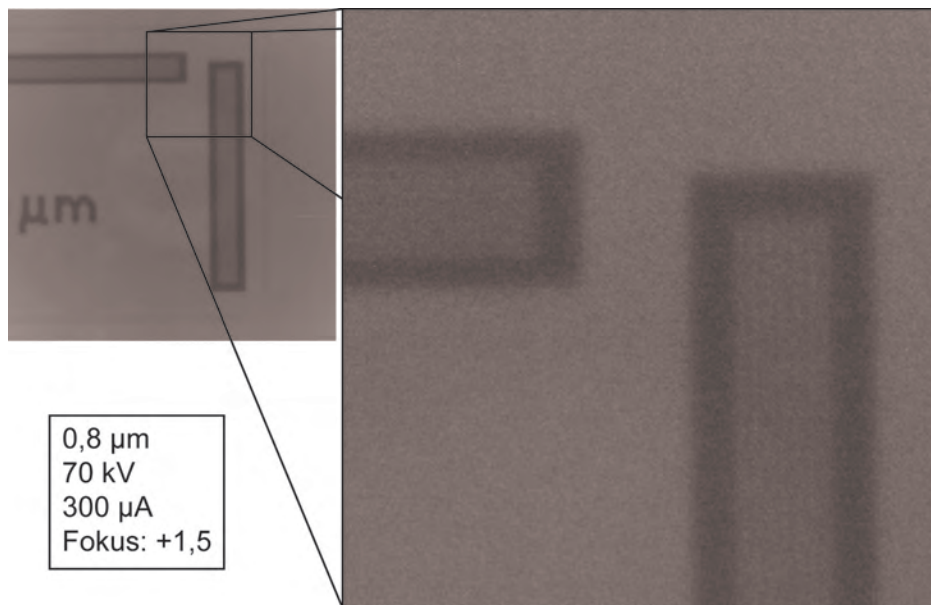


Abb. B2.3: Snapshot von 0,8 µm-Streifen mit dem Fokuswert +1,5. Vertikale Streifenmuster sind deutlicher zu erkennen als horizontale. Dieses Beispiel zeigt die Annäherung an die maximale effektive Auflösung des nanotoms.

- Zu erreichendes Ziel: 7 vertikale und horizontale 0,8 µm-Streifen in den Snapshots erkennen, wobei vertikale Streifen aufgrund von richtungsabhängigen Schwankungen, die möglicherweise auf die Verwendung von MICROCENT zurückzuführen sind, in der Auflösung des nanotoms besser zu erkennen sind als horizontale (Abb. B2.3).
- Das Fokussieren erfolgt in 0,5er Schritten oder 0,1er Schritten im xs/control (Abb. B2.4). Bei den gewünschten Fokuswerten entsprechende Snapshots aufnehmen; erst in 0,5er Schritten, dann über 0,1er Schritten annähern. So kann der optimale Wert schrittweise eingekreist und zum Schluss sehr genau bestimmt werden. Nach jeder Veränderung des Fokus (je Klick) wird das Live-Bild kurz unscharf, bis der neue Fokuswert erreicht ist. Während diesem kurzen Zeitintervall (ca. 5 Sekunden) noch keinen neuen Snapshot starten.
- Den Fokuswert des besten Snapshots (in der Regel zwischen 0.0 und 2.0) im xs/control über den Store-Button (Abb. B2.4) speichern.

Appendix B: CT imaging at the nanoCT lab

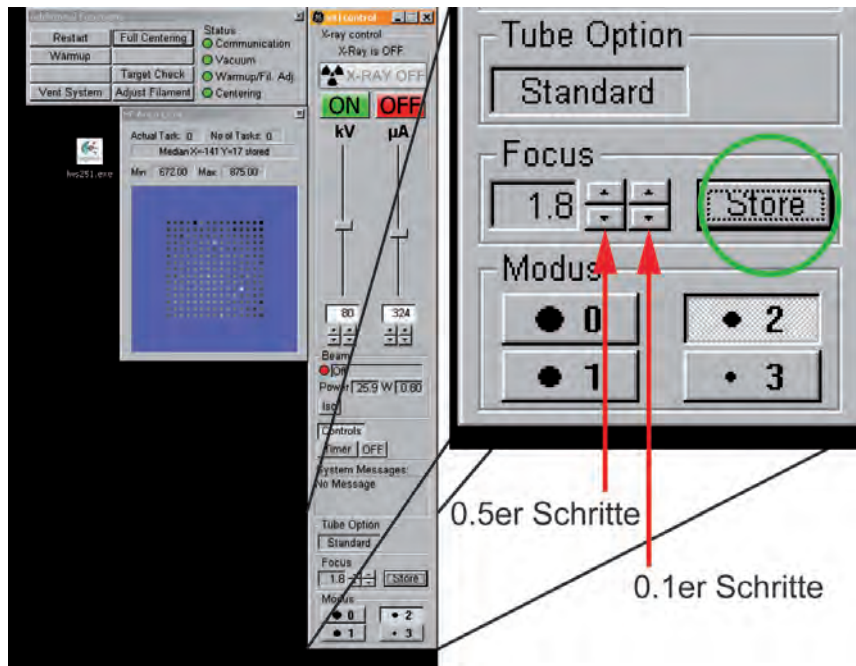


Abb. B2.4: xs/control mit Focus-Feld zur Kalibrierung der Fokuswerte in 0.5er und 0.1er Schritten (siehe Pfeil). Mit dem Store-Button ist der gewünschte Fokuswert zu speichern.

4.

- Den Auflösungstest ausbauen und die Probe in ihrer vorher notierten Position wieder platzieren.
- CT-Messung einrichten und starten.

Merke: Jede kV-Zahl in jedem Modus hat einen individuellen Fokuswert. Eine Interpolation über größere kV-Bereiche wird nicht empfohlen.

Appendix B: CT imaging at the nanoCT lab

B2.3. Digitale Filter

Die Benutzung von digitalen Filtern ist abhängig von den Eigenschaften und der Qualität der CT-Datensätzen. Im Wesentlichen dienen Filter zum Verringern von Rauschartefakten, die speziell bei CT-Aufnahmen mit längeren Belichtungszeiten auftreten.

Gerade bei der automatisierten Extraktion von Objekten (surface determination über spezifische Grauwertebereiche) vereinfacht das vorherige Filtern die schnelle Rekonstruktion von 3D-Mustern. Hierbei bietet sich das Anwenden des 3D Median-Filters an, der das Rauschen reduziert und Phasengrenzen akzentuiert (Abb. B2.5).

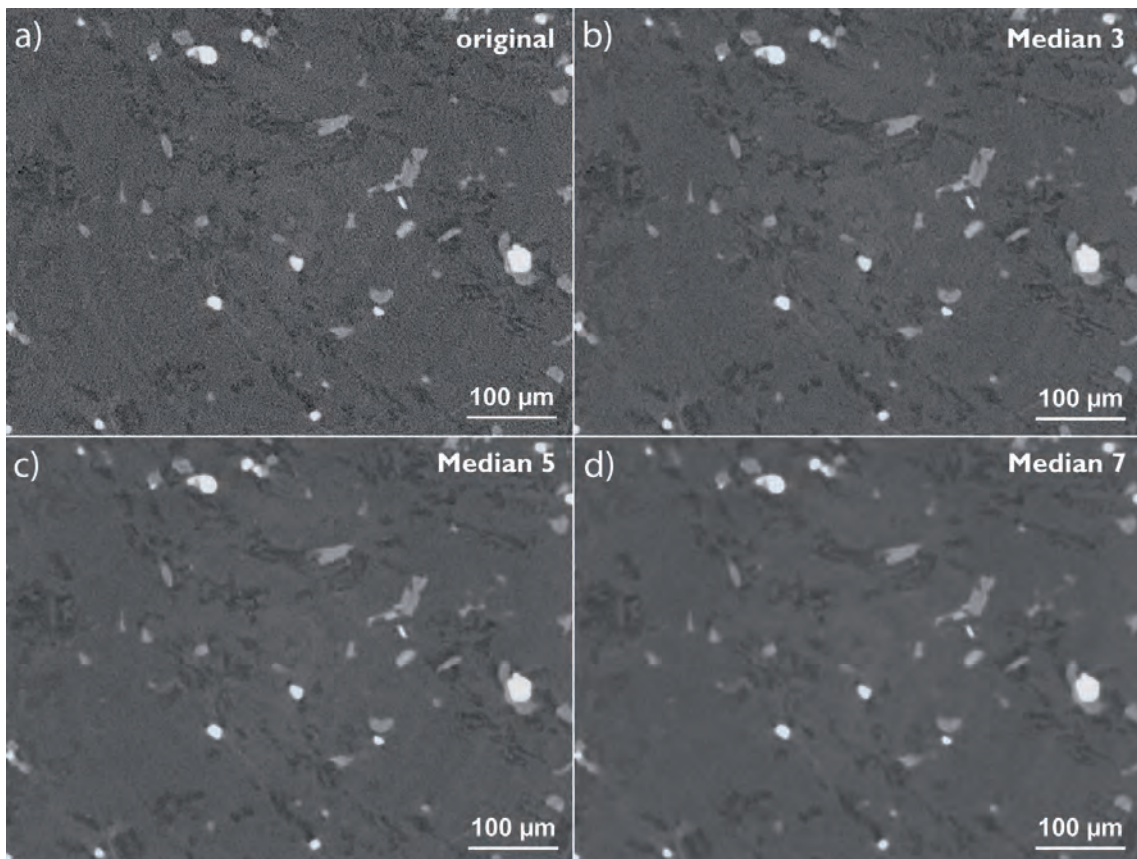


Abb. B2.5: Die Anwendung des Median-Filters am Beispiel von Probe trachyte_3 (siehe Tab. B1.2 sowie Abb. B1.4 und B1.5 in Appendix B1.3.). Das sukzessive Filtern mittels Median 3 (b), 5 (c) und 7 (d) verdeutlicht, wie das Rauschsignal vermindert wird, die Phasen jedoch deutlich unterscheidbar bleiben und insgesamt nur ein geringer Schärfeverlust zu verzeichnen ist.

Der Median-Filter kann im VGStudioMAX angewendet werden (Menü: Filter > Median). Das Filtern erfolgt in X-, Y- und Z-Richtung eines Datensatzes. Merke: Das Filtern eines Datensatzes kann nicht rückgängig gemacht werden. Es empfiehlt sich daher, im Median-Fenster *create new volume* anzuwählen, damit der Originaldatensatz erhalten bleibt. Je stärker der Filter und größer der Datensatz, desto länger dauert

Appendix B: CT imaging at the nanoCT lab

der Vorgang des Filterns.

Es gibt CT-Datensätze, bei denen die Verwendung von digitalen Filtern nötig ist, um eine weitere (schnelle) Bearbeitung der 3D-Volumina überhaupt zu ermöglichen. Eine nützliche Verwendung vom Median-Filter in Kombination mit Bild-Arithmetik zur Beseitigung von Scan-Artefakten (Rauschen und beam hardening) wird in Kapitel 7 (Abschnitt 7.5.1.) präsentiert, ebenso wie Aspekte zur Fehlerabschätzung und den Einfluss auf Phasen-Quantifizierungen mittels CT.

Sollen 3D-Rekonstruktionen von sehr kleinen Objekten oder sehr feinen Strukturen erfolgen (nicht über die automatisierte surface determination, sondern manuell zum Beispiel über selection mode ›

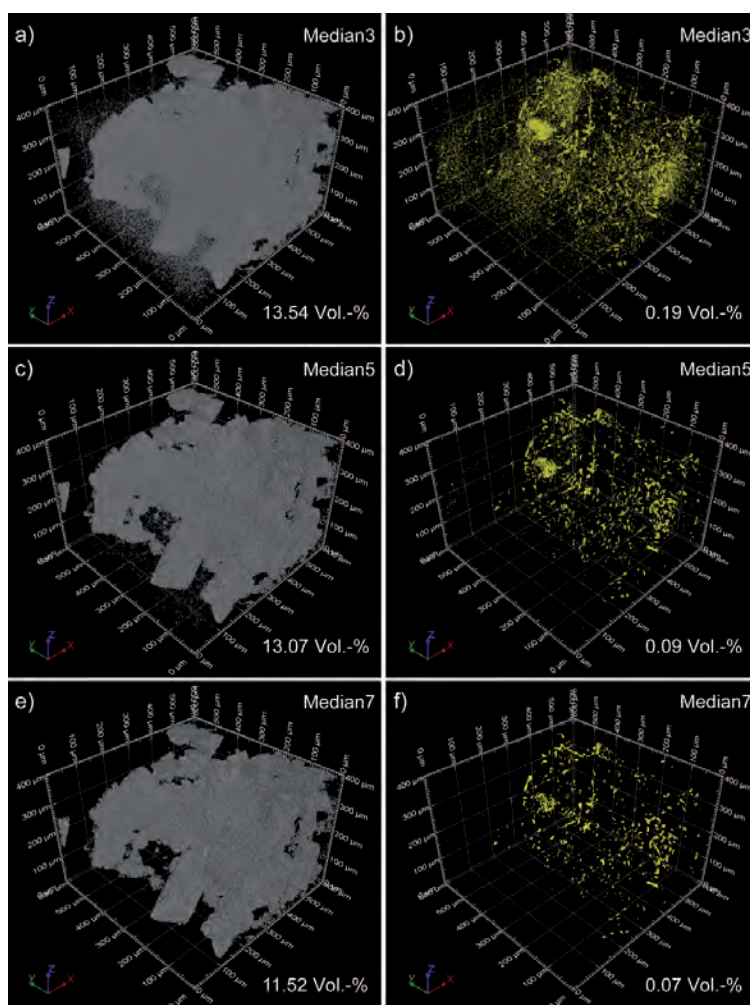


Abb. B2.6: Der Effekt des Median-Filters auf zwei unterschiedliche Phasen. Anhydrit (grau) ist aufgrund seiner Größe resistent gegen das Entfernen des Hintergrundrauschens. Kleine Fluidphasen (gelb) hingegen verschwinden bei der Anwendung des Median-Filters, was eine Unterschätzung der Mengenanteile bedingt.

region growing) kann es bei vorherigem, starkem Filtern zu deutlichen Einbußen der Objektgenauigkeit kommen. Der Verlust besonders feiner und extrem kleiner Objekte (bestehend aus wenigen Voxeln) wirkt sich auf die Quantifizierung von Phasen aus. So zeigt ein gefilterter Datensatz in der Regel geringere Anteile einer Phase als ein ungefilterter, da kleine Objekte (neben fehlerhaften Voxeln) verloren gehen. Je nachdem, wie die zu quantifizierenden Objekte geformt sind, und vor allem wie groß sie sind, beeinflusst ein Filtern die Mengenanteile in unterschiedlichem Maße. Als Beispiel dienen hier Anhydritkristalle und Fluidphasen einer Salzprobe (Abb. B2.6). Ein digitales Filtern (Median 3 › 5 › 7) dient der Beseitigung des Hintergrundrauschens. Im Falle der großen Anhydritkristalle

Appendix B: CT imaging at the nanoCT lab

(grau) scheint die Verwendung des Median 7-Filters gerechtfertigt, da sich die grobe Form nicht verändert. Bei den sehr kleinen Fluidphasen (gelb) hingegen ist nicht zu unterscheiden, ob es sich ausschließlich um Rauschartefakte oder um sehr kleine Fluidphasen handelt. In diesem Fall muss von einer deutlichen Unterschätzung der Mengenanteile ausgegangen werden, da sehr kleine Partikel mit der Beseitigung des Rauschsignals ebenfalls verschwinden. Die relativen Vol.-%-Angaben nehmen stärker ab als im Falle des Anhydrits. Hier zeigt sich die Abhängigkeit einer sinnvollen Anwendung des Median-Filters bezüglich der Objektgröße.

Nicolas Thiemeyer

Personal

Date of birth 24.09.1984
Place of birth Frankfurt am Main
Nationality German
Contact nicolas.thiemeyer@outlook.de



Education

Since 2016 Application engineer
at B & H Schneider GmbH & Co.KG, X-Ray Labor

2011 - 2016 PhD in Structural Geology at the Institute of Geoscience, Johann Wolfgang Goethe-University, Frankfurt am Main
Final mark: magna cum laude
Thesis: „Microfabrics and deformation mechanisms of Gorleben rock salt” in cooperation with the Federal Institute for Geosciences and Natural Resources (BGR)
Supervisor: Prof. Dr. Gernold Zulauf

2008 - 2011 Master of Science in Geosciences, Johann Wolfgang Goethe-University, Frankfurt am Main
Final Mark: 1.0
Thesis: “Gefügekundliche Untersuchungen der Forschungsbohrung Sichenhausen-Eschwald (Vogelsberg)” in cooperation with the Hessian Agency for the Environment and Geology (HLUG)
[Structural analyses of the drilling project Sichenhausen-Eschwald (Vogelsberg)]
Supervisor: Prof. Dr. Gernold Zulauf

2005 - 2008 Bachelor of Science in Geosciences, Johann Wolfgang Goethe-University, Frankfurt am Main
Final mark: 1.6
Thesis: „Tektonische Experimente zu Aufstieg und Platznahme des Salzstockes Morsleben“
[Tectonic experiments of the uplift and emplacement of the salt stock Morsleben]
Supervisor: Dr. habil. Carlo Dietl

